Reconstructing the impact of environmental changes on the river sediment dynamics of the Amazon River and Río de la Plata drainage basins with radiogenic isotopes

Dissertation

zur Erlangung des Doktorgrades der Naturwissenschaften

- Dr. rer. nat. -

Im Fachbereich Geowissenschaften

der Universität Bremen

vorgelegt von

Natalie Höppner

Bremen, Oktober 2017

Erstgutachter: Prof. Dr. Simone A. Kasemann – Universität Bremen

Zweitgutachter: Prof. Dr. Cristiano M. Chiessi – Universität von São Paulo

Erklärung

Hiermit versichere ich, Natalie Höppner, dass ich

1. Die Arbeit ohne unerlaubte fremde Hilfe angefertigt habe,

2. Keine anderen als die von mir angegebenen Quellen und Hilfsmittel benutzt habe und

3. Die den benutzten Werken wörtlich oder inhaltlich entnommenen Stellen als solche kenntlich gemacht habe.

Bremen, den _____

_____

Preface

This PhD thesis is submitted for the doctoral degree in natural sciences (Dr. rer. nat.) at the Faculty of Geosciences, University of Bremen, Germany. The research described herein was conducted under the supervision of Prof. Dr. Simone A. Kasemann at the Isotope Geochemistry group at MARUM – Center for Marine Environmental Sciences and Faculty of Geosciences, University Bremen, Germany between November 2014 and October 2017. The PhD project is part of the MARUM cluster of excellence project OC2 “Land-ocean interaction and climate variability in low latitudes”. The thesis is written in cumulative form and includes the collection of three manuscripts. In total, the dissertation has six chapters and a short summary of each chapter is given below.

Chapter 1 provides a brief introduction to the study areas and the used isotope systems and clarifies the scientific motivation and research aims of this PhD thesis.

Chapter 2 presents a detailed description of the sampling techniques, sample preparation, chemical treatment and analytical procedure.

Chapter 3 is the first manuscript “Holocene provenance shift of suspended particulate matter in the Amazon River basin” that was submitted to *Quaternary Science Reviews*. Radiogenic isotopes (Sr, Nd and Pb) reveal the modern and past sediment supply situation of the Amazon River basin.

Chapter 4 contains the second manuscript “Provenance shift of suspended particulate matter in the Río de la Plata drainage basin over time” that is in preparation to be submitted to *Climate of the Past*. The modern and paleo sediment supply situation of the Río de la Plata drainage basin is presented with radiogenic isotopes (Sr, Nd and Pb).

Chapter 5 is the third manuscript “Chemical leaching of bulk marine sediment under riverine influence – Radiogenic isotope signatures of different fractions and the challenges of interpretation”. Necessary leaching steps to obtain a detrital signal from marine sediments are addressed and problems in leaching signal interpretation are emphasized.

Chapter 6 summarizes the results and provides perspectives for future research.

Table of Contents

Abbreviations i
Abstract iii
Kurzfassung v
Chapter 1 Introduction 1
1.1 Motivation and research aim 3
1.2 Regional setting 5
1.2.1 Amazon River basin 5
1.2.1.1 Hydrological and oceanic setting 6
1.2.1.2 Geological setting 8
1.2.2 Río de la Plata drainage basin 9
1.2.2.1 Hydrological and oceanic setting 10
1.2.2.2 Geological setting 12
1.3 Radiogenic isotope systems 13
1.3.1 Strontium 13
1.3.2 Neodymium 13
1.3.3 Lead 14
1.4 Overview of own research 15
1.5 References 16
Chapter 2 Methodology 23
2.1 Sample collection 25
2.1.1 Amazon River basin 25
2.1.2 Río de la Plata drainage basin (LPDB) 26
2.2 Sample preparation 31
2.2.1 Marine sediment cores 31
2.2.1.1 GeoB16224-1 and GeoB6212-1 31
2.2.1.2 GeoB16223-2, GeoB16217-2, GeoB16216-3, GeoB16212-3, GeoB16212-2 and GeoB16211-3 32
2.2.2 River suspended particulate matter 33
2.2.3 Riverbank and bed sediments 33
2.2.4 Additional methodological tests 34
2.2.4.1 Leaching experiments 34
2.2.4.2 Unsieved vs. sieved 36
2.2.4.3 Fe-Mn oxyhydroxide leaching of river suspended particulate matter 36
2.3 Chemical separation and thermal ion mass spectrometry 36
2.3.1 Strontium 37
2.3.2 Lead 37

2.3.3 Neodymium 38
2.4 Preparation and element analysis 39
2.4.1 Inductively coupled plasma optical emission spectroscopy (ICP-OES) 39
2.4.2 Inductively coupled plasma mass spectroscopy (ICP-MS) 39
2.4.3 X-ray diffraction (XRD) 39
2.4.4 Scanning electron microscopy (SEM) with energy-dispersive X-Ray spectroscopy (EDX) 40
2.5 References 40
Chapter 3 Holocene provenance shift of suspended particulate matter in the Amazon River basin 43
3.1 Abstract 45
3.2 Introduction 45
3.3 Regional setting 47
3.3.1 Geological setting 47
3.3.2 Hydrological setting 48
3.4 Material and methods 50
3.4.1 Material 50
3.4.2 Methods 53
3.4.2.1 ^{14}C ages for GeoB16216-3, GeoB16217-2 and GeoB16223-2 53
3.4.2.2 Sample preparation and dissolution 53
3.4.2.2.1 River SPM 53
3.4.2.2.2 Marine sediment core GeoB16224-1 54
3.4.2.2.3 Marine sediment cores GeoB16212-2, GeoB16212-3, GeoB16216-3, GeoB16217-2 and GeoB16223-2 54
3.4.2.3 Chemical separation and mass spectrometry 54
3.5 Results 55
3.5.1 Pb isotopic composition of the river SPM 60
3.5.2 Sr and Nd isotopic composition of the river SPM 60
3.5.3 Sr, Nd and Pb isotopic composition of marine sediment core GeoB16224-1 62
3.5.4 Sr, Nd and Pb isotopic composition of GeoB16212-2, GeoB16212-3, GeoB16216-3, GeoB16217-2 and GeoB16223-2 62
3.6 Discussion 62
3.6.1 Modern Sr, Nd and Pb isotopic signatures in the Amazon River basin SPM 62
3.6.2 Changes in sediment supply during the last 40 kyr 65
3.6.2.1 Sr isotope signal 66
3.6.2.2 Nd isotope signal 66
3.6.2.3 Pb isotope signal 67
3.6.3 Modern Amazon River SPM and the offset to GeoB16224-1 67
3.6.4 Basin internal shift 68

3.6.5 Possible sediment sources for the Nd shift besides the Amazon River basin.....70
3.7 Conclusions 72
3.8 Acknowledgments 73
3.9 References 73
Chapter 4 Provenance shift of suspended particulate matter in the Río de la Plata drainage basin over time.....85
4.1 Abstract 87
4.2 Introduction.....87
4.3 Regional setting.....89
4.3.1 Geological setting.....89
4.3.2 Hydrological setting 89
4.4 Material and methods 91
4.4.1 Material 91
4.4.2 Methods 92
4.4.2.1 Sample preparation and dissolution 92
4.4.2.1.1 River suspended particulate matter 92
4.4.2.1.2 Riverbank and bed sediment 95
4.4.2.1.3 Marine sediment core GeoB6212-1 95
4.4.2.2 Chemical separation and mass spectrometry.....95
4.5 Results.....96
4.5.1 Pb isotopic composition of the river SPM and river bed sediments 101
4.5.2 Nd and Sr isotopic composition of the river SPM and river bed sediments 101
4.5.3 Sr, Nd, Pb isotopic composition of detrital sediment (core GeoB6212-1).....102
4.6 Discussion.....102
4.6.1 Modern Sr, Nd and Pb isotopic signatures of the Río de la Plata drainage basin102
4.6.2 Changes in sediment supply during the last 30 kyr 104
4.6.2.1 10 cal ka BP shift – Sediment input from southern Argentina 104
4.6.2.2 Sr peak at 13.5 cal ka BP - Strong SASM in the Younger Dryas 105
4.6.2.3 Pb Peak at 15 cal ka BP - Strong SE Trades in the Bølling-Allerød.....106
4.6.2.4 Peaks at 20 to 18 cal ka BP - Strong SASM in the Heinrich Stadial 1 107
4.6.2.5 29 to 28 cal ka BP shift (Strong SE Trades, strong AMOC).....107
4.7 Conclusions 108
4.8 Acknowledgments 109
4.9 References 109
Chapter 5 Chemical leaching of bulk marine sediment under riverine influence – Radiogenic isotope signatures of different fractions and the challenges of interpretation.....115
5.1 Abstract 117
5.2 Introduction.....118

5.3 Regional setting 120
5.3.1 Continental setting 120
5.3.2 Oceanic setting 120
5.4 Material and methods 121
5.4.1 Material 121
5.4.2 Methods 122
5.4.2.1 Sample preparation and dissolution 122
5.4.2.2 Chemical separation and mass spectrometry 125
5.5 Results 126
5.5.1 Major element concentrations 131
5.5.2 Sr, Nd and Pb isotopic compositions 131
5.6 Discussion 131
5.6.1 Detrital (dc) fraction 131
5.6.2 Carbonate (KL) fraction 132
5.6.2.1 Sr isotopic signature 133
5.6.2.2 Nd isotopic signature 133
5.6.3 Fe-Mn oxyhydroxide (FML) fraction 135
5.6.3.1 GeoB16224-1 (Amazon River basin) 135
5.6.3.2 GeoB6212-1 (Río de la Plata drainage basin) 138
5.7 Conclusions 140
5.8 Acknowledgments 141
5.9 References 141
Chapter 6 Conclusion and Outlook 147
6.1 References 151
Acknowledgement 153
Appendices I
A.1 Column Procedure – Separation of Sr and Pb on a single Sr.spec column. III
A.2 Column Procedure – Separation of LREE on TRU.spec columns. IV
A.3 Column Procedure – Separation of Nd on LN.spec columns. IV
B.1 $^{87}Sr/^{86}Sr$ isotope ratios of reference materials. V
B.2 Pb isotope ratios of reference materials. VI
B.3 $^{143}Nd/^{144}Nd$ isotope ratios of reference materials. VII
C.1 XRD results for core GeoB16224-1. VIII
C.2 Major element concentrations for the Río de la Plata drainage basin suspended particulate matter. X
C.3 Rb, Sr, Nd and Pb concentrations for sediment cores GeoB16211-3, GeoB16212-2, GeoB16212-3, GeoB16216-3, GeoB16217-2 and GeoB16223-2. XI
C.4 Sr, Nd and Pb isotopic compositions of GeoB16211-3. XI
C.5 SEM pictures and EDX spectrum for six samples from core GeoB16224-1. XII

Abbreviations

AAIW	Antarctic Intermediate Water
AMOC	Atlantic Meridional Overturning Circulation
BMC	Brazil-Malvinas Confluence
cal a BP	calibrated years before the present
ITCZ	Intertropical Convergence Zone
LPDB	Río de la Plata drainage basin
NADW	North Atlantic Deep Water
NBC	North Brazil Current
PPW	Plata Plume Water
SACZ	South American Convergence Zone
SASM	South American Summer Monsoon
SASW	Subantarctic Shelf Water
SE Trades	Southeast Trade Winds
SPM	Suspended particulate matter
SST	Sea Surface Temperature
STSF	Subtropical Shelf Front
STSW	Subtropical Shelf Water

Abstract

Billions of tons of sediment are transported annually through river systems worldwide. The river sediment dynamics are tightly coupled to the global climate and changes in the precipitation intensity or region generate variations in the transported sediment amount or the source area. Humans have also done severe modification to the river sediment dynamics. Actively by rerouting waterways and damming rivers and passively by enhancing surface erosion through soil destabilization (i.e. deforestation, agriculture). River sediment has an important role in the riverine and coastal ecosystem and changes in physical and chemical properties can have long-lasting consequences. With the prognosis of fast-pacing and drastic climate changes in the near future and the anthropogenic impact proceeding to increase, a study of how past processes have change the river sediment dynamics and a monitoring of the modern situation, is a good approach for predictions about future developments.

This PhD thesis aims to reveal the modern and past sediment supply situation for the Amazon River and Río de la Plata drainage basins, the two biggest river basins of South America that considerably influence the global sediment supply into the world oceans. To achieve this we analyzed radiogenic isotopes (Sr, Nd and Pb) and element concentrations of river sediments and marine sediment cores that archive the last 30,000 to 40,000 years of river sediment supply to the Atlantic Ocean. Radiogenic isotopes are not significantly affected by weathering, transport or depositional processes, making them useful tracers to study sediment provenances.

In agreement with studies of other chemical parameters of the modern Amazon River sediment, two main sediment source areas (the Andes and the cratonic Shield) were identified. Hereby, the Andes were the main sediment supplier in the last 40 kyr, however, a prominent offset between the past and modern radiogenic isotope signatures was determined. A climate induced shift, due to a wetter western or drier eastern basin sector, during the late Holocene is proposed as the cause. Furthermore, a change from a Madeira River to a Solimões River dominated sediment signal is observed in the last decades, implying a possible impact of modern river dams on the sediment dynamics in the Amazon River basin. Additionally, the results also show a shift in the precipitation locus during the second part of the Heinrich Stadial 1 from the Andes to the cratonic Shield areas.

The radiogenic isotope signatures of the modern Río de la Plata drainage basin sediment establish three sediment source areas, i) the upper Paraná River, ii) the Uruguay River and iii) the Andean draining rivers Salado, Pilcomayo and Bermejo. The down-core results reveal several pronounced sediment source changes in the last 30 kyr that are attributed to millennial

scale climate events. A strong South American Summer Monsoon during Heinrich Stadial 1 and the Younger Dryas intensified the sediment supply of the Andean draining rivers. During times of strong SE Trade winds (i.e. the Bølling-Allerød interstadial) the southeastern sector of the basin (i.e. Uruguay River drainage basin) dominated the sediment supply. In addition, the results confirm an external (southern Argentina) sediment deposition in front of the Río de la Plata estuary due to a maximum sea level stand during the late Holocene.

The third manuscript deals with the requirements of the methodology to extract a detrital signature from a marine sedimentation setting. Moreover, it emphasizes that the radiogenic isotope signatures of the carbonate and Fe-Mn oxyhydroxide fraction should be interpreted with caution. Based on the high strontium (Sr) concentration in marine carbonates, on the one hand a decarbonization to obtain a detrital isotopic signature is extremely important, on the other hand the Sr isotopic signature of the carbonate leach fraction is resilient to contamination and does represent a paleo seawater signal. Furthermore, the results suggest that the Fe-Mn oxyhydroxide fraction of marine sediments in river influenced settings does not represent a paleo seawater signal, but rather either a river signature through leaching off pre-formed river-borne Fe-Mn oxyhydroxides (Amazon River basin) or a contamination through the leaching of detrital material (Río de la Plata drainage basin).

Overall, this thesis illustrates the past sediment supply evolution and modern sediment dynamics of the Amazon River and Río de la Plata drainage basins. Additionally, the results extend the current database of radiogenic (Sr, Nd and Pb) isotope signatures on river sediment. Moreover, the study emphasizes the importance of the methodological approach.

Kurzfassung

Milliarden Tonnen an Sediment werden jährlich weltweit durch Flusssysteme transportiert. Die Sedimentdynamik von Flüssen ist dabei eng an das globale Klima gekoppelt und Veränderungen in der Niederschlagsintensität oder -region führen zu Variationen in der transportierten Sedimentmenge oder der -provenienz. Die Menschheit hat die Sedimentdynamik von Flüssen ebenfalls stark verändert. Aktiv durch die Umleitung von Wasserwegen und das Dämmen von Flüssen und passiv durch Verstärkung der Oberflächenerosion durch Bodendestabilisierung (z.B. durch Entwaldung oder Landwirtschaft). Flusssedimente spielen eine wichtige Rolle im Fluss- und Küstenökosystem und Veränderungen in den physikalischen und chemischen Eigenschaften können langanhaltende Konsequenzen haben. Vor dem Hintergrund von rasanten und drastischen Klimaveränderungen in der nahen Zukunft und den zunehmenden anthropogenen Einflüssen ist eine Studie, die untersucht wie vergangene Prozesse die Sedimentdynamik des Flusses verändert haben und die moderne Situation überwacht, ein guter Ansatz um Vorhersagen über zukünftige Entwicklungen treffen zu können.

Diese Dissertation soll den modernen und vergangenen Sedimenteintrag des Amazonas Flussbecken und des Río de la Plata Entwässerungsbecken aufzeigen. Es handelt sich um die zwei größten Flussgebiete Südamerikas, die den globalen Sedimenteintrag in die Weltmeere erheblich beeinflussen. Um dies zu erreichen, haben wir radiogene Isotope (Sr, Nd und Pb) und Elementkonzentrationen von modernen Flusssedimenten und marinen Sedimentkernen, die die letzten 30.000 bis 40.000 Jahre des Flusssedimenteintrags in den Atlantischen Ozean archivieren, analysiert. Radiogene Isotope werden nicht signifikant durch Verwitterungs-, Transport- oder Ablagerungsprozesse beeinflusst und sind daher nützliche Tracer zur Untersuchung der Sedimentherkunft.

In Übereinstimmung mit Untersuchungen anderer chemischer Parameter des modernen Amazonassediments wurden zwei Hauptherkunftsgebiete (die Anden und der kratonische Schild) identifiziert. Die Anden waren in den letzten 40.000 Jahren der Hauptsedimentlieferant, jedoch wurde ein deutlicher Unterschied zwischen der vergangenen und der modernen radiogenen Isotopensignatur festgestellt. Als Ursache wird eine klimabedingte Verschiebung, aufgrund eines feuchteren westlichen oder trockeneren östlichen Sektor des Amazonasbeckens, im späten Holozän vorgeschlagen. Darüber hinaus wurde in den letzten Jahrzehnten ein Wechsel von einem Madeira Fluss dominierten zu einem vom Solimões Fluss dominierten Sedimentsignal beobachtet. Dies lässt auf eine mögliche Auswirkung der Flussdämme auf die Sedimentdynamik im Amazonasbecken schließen. Zusätzlich zeigen die

Ergebnisse eine Verschiebung des Niederschlagsschwerpunktes während des zweiten Teils des Heinrich Stadial 1 von den Anden zu den Gebieten des kratonischen Schildes.

Die radiogenen Isotopensignaturen des modernen Río de la Plata Entwässerungsbeckens zeigen drei Sedimentprovenienzen, i) den oberen Flusslauf des Paranás, ii) den Uruguay Fluss und iii) die Anden entwässernden Flüsse Salado, Pilcomayo und Bermejo. Die Sedimentkernergebnisse zeigen mehrere ausgeprägte Sedimentprovenienzveränderungen in den letzten 30.000 Jahren, die auf Klimaveränderungen in der Größenordnung von Jahrtausenden zurückzuführen sind. Ein starker südamerikanischer Sommermonsun während des Heinrich Stadial 1 und der Jüngeren Dryas verstärkte den Sedimenteintrag der andinen Flüsse. In Zeiten starker SE Passatwinde (z.B. im Bølling-Allerød Interstadial) dominierte der südöstliche Sektor des Beckens (z.B. das Uruguay Entwässerungsbecken) den Sedimenteintrag. Darüber hinaus bestätigen die Ergebnisse eine externe (aus dem südlichen Argentinien) Sedimentablagerung vor der Mündung des Río de la Plata aufgrund eines maximalen Meeresspiegelstandes während des späten Holozäns.

Das dritte Manuskript befasst sich mit den Anforderungen an die Methodik, um aus marinen Sedimentablagerungen ein detritisches Signal zu extrahieren. Außerdem wird betont, dass die radiogenen Isotopensignaturen der Karbonat- und Fe-Mn Oxyhydroxid Fraktionen mit Vorsicht interpretiert werden sollten. Aufgrund der hohen Strontium (Sr) Konzentration in marinen Karbonaten ist einerseits eine Dekarbonatisierung, zum Erhalt einer detritischen Isotopensignatur äußerst wichtig, andererseits ist die Sr Isotopensignatur der Karbonatfraktion weitestgehend kontaminationsresistent und gibt ein Paleo-Meerwassersignal wieder. Darüber hinaus deuten die Ergebnisse darauf hin, dass die Fe-Mn Oxyhydroxid Fraktion von marinen Sedimenten in Gebieten mit starkem Flusseinfluss kein Paleo-Meerwassersignal darstellen. Entweder sie geben, durch das Auflösen von vorgeformtem aus dem Fluss stammenden Fe-Mn Oxyhydroxiden, eine Flusssignatur wieder (Amazonas Flussbecken) oder sind durch detritisches Material kontaminiert (Río de la Plata Entwässerungsbecken).

Insgesamt veranschaulicht diese Arbeit die Entwicklung des Sedimenteintrags und die moderne Sedimentdynamik des Amazonas Flussbeckens und des Río de la Plata Entwässerungsbeckens. Darüber hinaus erweitern die Ergebnisse die aktuelle Datenbank der radiogenen (Sr, Nd und Pb) Isotopensignaturen von Flusssedimenten. Des Weiteren hebt die Studie die Bedeutung des methodischen Ansatzes hervor.

Chapter 1
Introduction

1.1 Motivation and research aim

Riverine sediment input is the main delivery mechanism of solid material into the world oceans (Milliman and Meade, 1983). Changes in its physical and chemical properties, due to source variations, can notably affect coastal organism like benthic communities and coral reefs (Syvitski et al., 2005) and have drastic impacts on the river ecology (Bednarek, 2001). Furthermore, riverine terrestrial organic matter is an important component of the global carbon cycle (Hedges et a., 1997) and therefore closely coupled to global climate evolution. Additionally, a reduction of sediment amount directly enhances coastal retreat, having severe consequences for the human habitat in the coastal region (Syvitski et al., 2005). The riverine sediment discharge is tightly linked to the climate and to human impact (Syvitski and Kettner, 2011). Changes in precipitation patterns influence the sediment transport in river basins. A precipitation intensification leads to higher denudation rates and an increase in the sediment transport of the affected river. Therefore, shifts in the source areas of the river sediment can be used to reconstruct the climate (i.e. precipitation). Areas with high annual rainfall and insufficiently protected soil surfaces are prone to high sediment erosion rates (Favis-Mortlock and Guerra 1999). Humans further increase the soil erosion through i.e. deforestation, agriculture and animal farming and reshape the waterways and river sediment transport through reservoir and dam building (Syvitski and Kettner, 2011). The human impact on the relocation of sediment is in the order of magnitude of the modern global natural fluvial sediment delivery into the oceans (Syvitski et al., 2005). To monitor if humans have affected the Earths processes (i.e. riverine sediment transport) similar to past global geological events, the modern situation needs to be captured and the paleo conditions need to be studied (Syvitski and Kettner, 2011). To understand how the modern anthropogenic impact might influence the river sediment long-term, it is important to study river sediment developments associated with natural changes in the past (Syvitski, 2003; Walling, 2009). In the wake of the predicted climatic changes in the future, a connection of modern and paleo studies improves the predictions of future impacts (Walling 2009). Additionally, humans will keep on shaping the earth surface to match future needs. Therefore, knowledge about the river sediment dynamics (i.e. the source of river sediment) is important for a sustainable management of sediment and water strategies in river basins in the future (Walling, 2005).

The Amazon River basin and Río de la Plata drainage basin are the two largest river basins of South America draining approximately 52 % of the continent. Together they are discharging about 20 % of the world's freshwater into the oceans (Gibbs, 1967; Meybeck and Ragu, 1995) and supply approximately 1.2 to 1.4 x 10^9 tons of sediment into the Atlantic Ocean annually (Depetris et al. 2003; Meade, 1994), making them two very important players in the global land ocean interaction. Furthermore, the tropical rainforest (i.e. in South America) has experienced extreme deforestation (Hansen et al, 2003) and a significant amount of dams being built

(Amsler and Drago, 2009; Lees et al., 2016) in the last decades, having drastic impacts on the sediment regime.

A monitoring of the river sediment is in most cases cost-intensive and, depending on the accessibility of the individual rivers, can be impractical. Tracing sediment sources through physical or geochemical properties is a powerful alternative approach (Walling, 2005). Radiogenic isotopes (Sr, Nd and Pb) are present in almost all materials and therefore, not significantly restricted in spatial coverage like i.e. pollen. They are not affected by weathering, transport or depositional cycles. Given that the radiogenic isotope signatures of the sediment sources are sufficiently different, changes in provenance can be detected. To study river sediment properties and sources of the past, a reliable archive is needed. However, the tropical rainforest does not have the best conditions to archive continuous sediment records (Markgraf, 1989). Therefore, unconventional archives that record past river basin conditions and information about the past river sediment properties are essential. River sediment is deposited in river deltas or along continental margins. Sediment cores of these deposits provide valuable archives with high temporal resolutions. The isotope signatures of their continental sources is recorded and changes in provenance and the past environmental conditions under which they were transported in the river catchment can be detected (Bentahila et al., 2008; Revel et al., 2010, 2014, 2015; Walter et al., 2000; Wei et al., 2013).

The main objective of this thesis is to identify modern and paleo sediment sources in the Amazon River and Río de la Plata drainage basin and to identify possible mechanisms (i.e. climate variations or anthropogenic impact) behind provenance changes. In order to achieve this, the radiogenic (Sr, Nd and Pb) isotopic signatures for sediment from the different river basins tributaries was determined to fingerprint the main sediment supply sources. Marine sediment cores in front of the respective river basin mouth or estuary record the river sediment supply to the ocean for the last 30 to 40 kyr. Therefore, the same isotopic systems were applied to understand how the sediment supply sources varied in the past. This dissertation further provides and enhances the database of radiogenic isotope signatures for river sediment from the Amazon River and Río de la Plata River basin for future provenance studies.

1.2 Regional setting

1.2.1 Amazon River basin

The Amazon River Basin is located in northern South America and encompasses (in decreasing order of surface area) parts of Brazil, Peru, Bolivia, Colombia, Ecuador, Venezuela, Guiana and Suriname (Fig. 1), with about 62 % occupied by Brazil (Wolf et al., 1999). It is the largest river basin in the world with a drainage area of 6.3 x 10^6 km^2 (Gibbs, 1967).

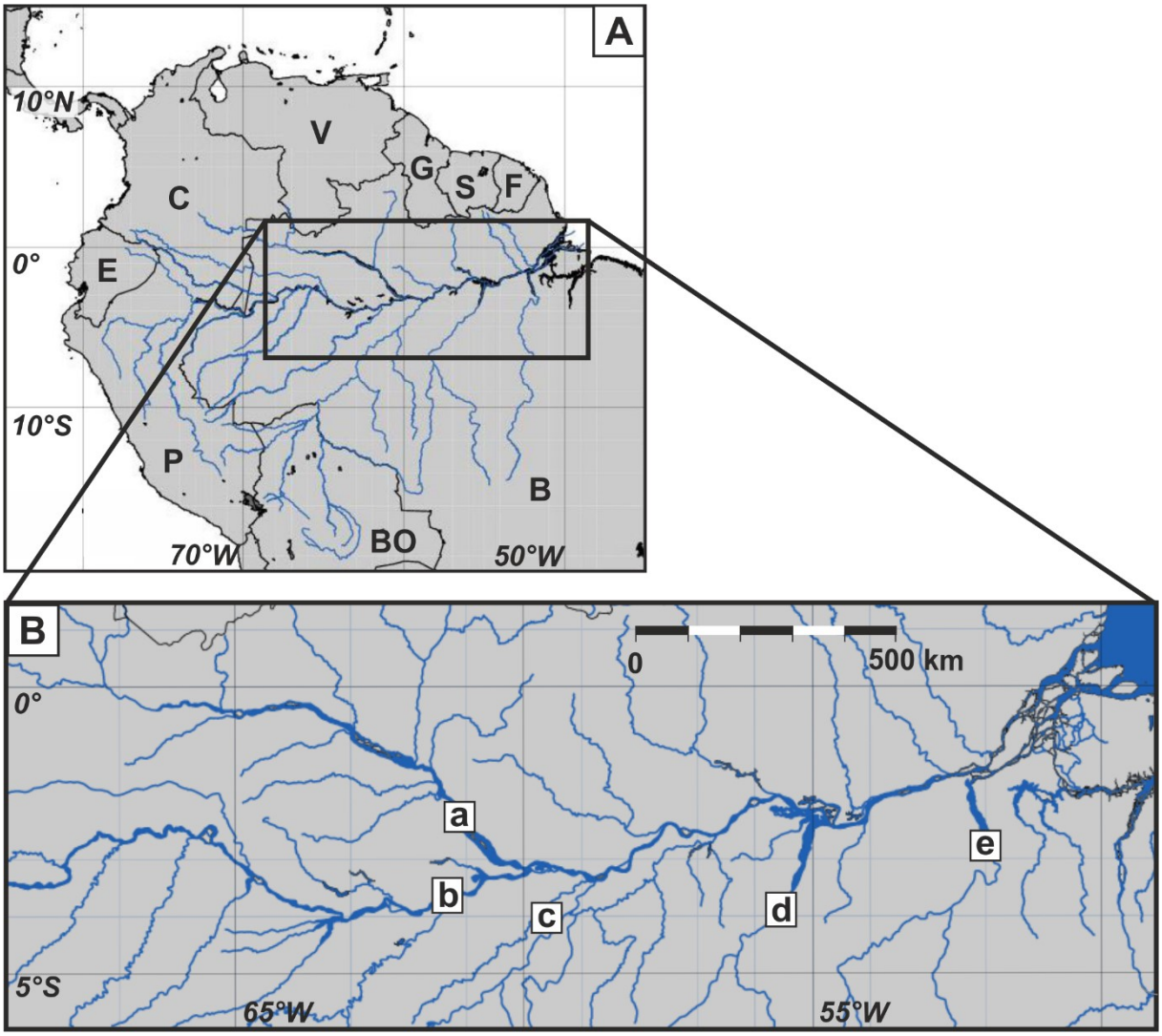

Fig. 1. Panel A: Map of northern South America showing the Amazon River basin and the area expanded in panel B. The countries are marked with black uppercase letters as follows B: Brazil, BO: Bolivia, C: Colombia, E: Ecuador, F: French Guiana, G: Guiana, P: Peru, S: Suriname and V: Venezuela. Panel B: The main tributaries of the Amazon River are marked with black lowercase letters as follows a: Negro River, b: Solimões River, c: Madeira River, d: Tapajós River and e: Xingu River.

1.2.1.1 Hydrological and oceanic setting

Approximately 18 % of the world's river water discharge into the oceans is supplied by the Amazon River basin (Gibbs, 1967). The Amazon River's main channel is formed by the confluence of the Solimões and Negro Rivers near the city of Manaus in Brazil. The other main tributaries of the Amazon River are the Madeira, the Tapajós and the Xingu Rivers (Fig. 1). Almost all of the total water discharge of the Amazon River is supplied by the Solimões River (43 %), the Negro River (29 %) and the Madeira River (20 %) alone (Gibbs, 1967). The rivers of the Amazon basin can be subdivided into three river types based on differences in the river basin topography and vegetation cover (Sioli, 1984). Rivers with a high turbidity and a high suspended particulate matter (SPM) load that drain mountainous areas with a high relief, sparse vegetation and a high seasonality in temperature and precipitation are 'whitewater' rivers like the Solimões and Madeira Rivers. Rivers with a low turbidity and a low SPM load that drain tropical areas with a low to moderate relief, a dense vegetation cover and year-round high temperatures and precipitation are 'clearwater' rivers like the Tapajós and Xingu Rivers. The Negro River has similar properties like the Tapajós and Xingu Rivers, with the addition of having an olive-brown color resulting from a high amount of fulvic and humic acids in the water and is thus being called a 'blackwater' river (Gibbs, 1967; Sioli, 1957). The Amazon River supplies an annual average of 1.1 to 1.3 x 10^9 tons of sediment through its river delta into the North Atlantic Ocean (Fig. 2). Approximately 96 % of this discharge is supplied by the Solimões (41 %) and Madeira (55 %) Rivers (Meade, 1994).

Fig. 2. Satellite image of the Amazon River delta. Credit: Jacques Descloitres, MODIS Land Rapid Response Team, NASA/GSFC.

The water and sediment discharge of the Amazon River basin is transported northwestwards along the coast of Brazil and French Guiana in a density controlled freshwater plume stretching several hundred kilometers (Gibbs and Konwar, 1986). The dominant ocean surface current in front of the Amazon River mouth is the northwestwards flowing North Brazil Current (NBC) (Johns et al., 1998) (Fig. 3). The intermediate and deep water are influenced by the northwards flowing Antarctic Intermediate Water (AAIW) and the southwards flowing North Atlantic Deep Water (NADW). The Amazon River basin has a variety of climate zones, from the tropical rain forest with high average temperatures (26 to 28°C) in the Amazon trough to the arctic mountainous Andes with average low temperatures (< 15°C). The total mean annual precipitation is relatively high with a precipitation maximum on the eastern Andean flank and at the Amazon River mouth (Fig. 3). On average, the rainy season takes place from January to June and is dominated by the South American Summer Monsoon (SASM). The dry season, with less rain, takes place from July to December. Overall the rainy season starts in the south of the basin and moves northwards, causing different precipitation maxima in the individual tributary drainage basins (Gibbs, 1967). The hydrological cycle of South America is closely coupled to the ocean temperature and circulation. The position of the Intertropical Convergence Zone (ITCZ) is influenced by changes in sea surface temperatures (SST) (Broccoli et al., 2006). A cooling of the North Atlantic, i.e. due to a reduced Atlantic Meridional Overturning Circulation (AMOC) shifts the ITCZ southwards (Schmidt and Spero, 2011). This strengthens the convection along the South American Convergence Zone (SACZ), strengthens the SASM (i.e. stronger precipitation) and displaces the summer rainfall belt southwards (Chiessi et al., 2009).

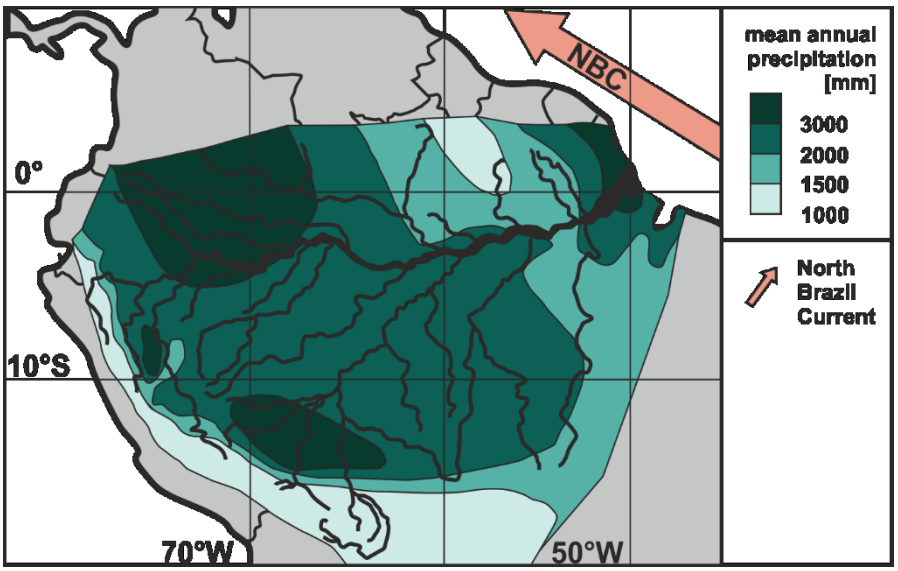

Fig. 3. Mean annual precipitation pattern of the Amazon River basin and the dominant ocean surface current (North Brazil Current, NBC). The red color of the arrow represents warm water and the arrow head indicated the main transport direction. The main tributaries of the Amazon River basin are illustrated as black lines.

1.2.1.2 Geological setting

The eastern two thirds of the Amazon River basin are a broad trough that is flanked by the Precambrian highlands of the Amazon Craton in the north (Guiana Shield) and south (Brazilian Shield) and bordered to the west by the Cenozoic Andes Mountain range with its Subandean foreland (Gibbs, 1967) (Fig. 4). Phanerozoic sedimentary rocks fill the Amazon trough and the upper Neogene and Quaternary units (Dino et al., 2012; Rossetti et al., 2005) are made up of material weathered from the main source areas of the Amazon River (Andes and Shield). The northern (NF) and southern (SF) Subandean foreland basins are mainly composed of Miocene and Pliocene sediments (Roddaz et al., 2005). The mainly granitoid intrusive and metamorphic rocks of the Precambrian Amazon Craton are between 4 and 2 cal Ga BP old (da Rosa-Costa et al., 2006; Tassinara and Macambira, 1999; Tassinari et al., 2000). Paleozoic to Cenozoic plutonic, volcanic and sedimentary rocks make up the main part of the Andes that are drained by the Amazon River basin (Jaillard et al., 2000).

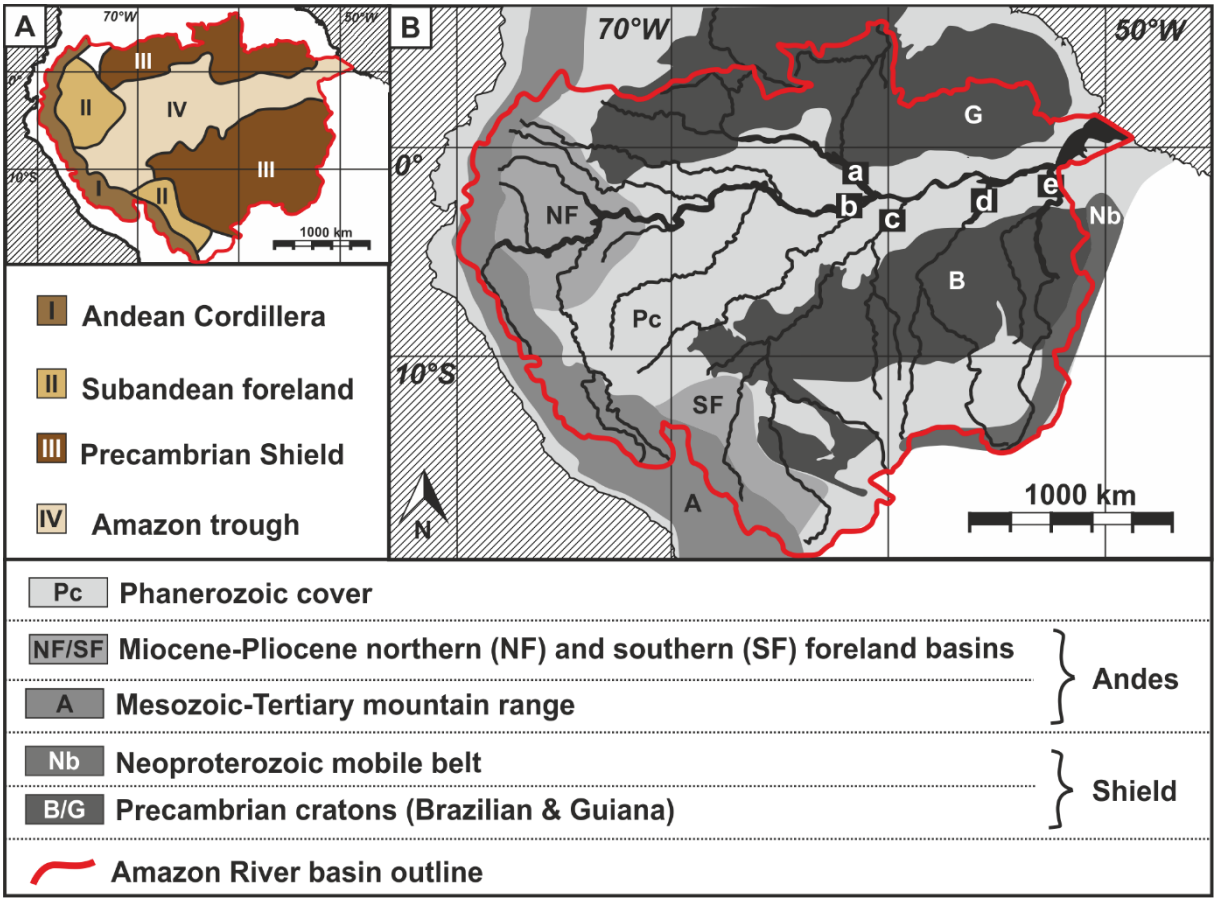

Fig. 4. Panel A: Main morphostructural zones of the Amazon River basin adapted from Stallard and Edmond (1983). Panel B: Major geological units of the Amazon River basin. The outline of the Amazon River basin is shown in red and the main tributaries of the Amazon River are marked with white lowercase letters as follows a: Negro River, b: Solimões River, c: Madeira River, d: Tapajós River and e: Xingu River. Geological units are simplified after Roddaz et al. (2005) and Tassinari and Macambira (1999).

1.2.2 Río de la Plata drainage basin

The Río de la Plata drainage basin (LPDB) is located in southern South America, encompassing (in decreasing order of surface area) the countries of Brazil, Argentina, Paraguay, Bolivia and Uruguay (Wolf et al., 1999) (Fig. 5). It has a drainage area of 3.1 x 10^6 km^2 making it the second largest river basin in South America (Depetris and Griffin, 1968) and the fifth largest in the world (Milliman and Meade, 1983).

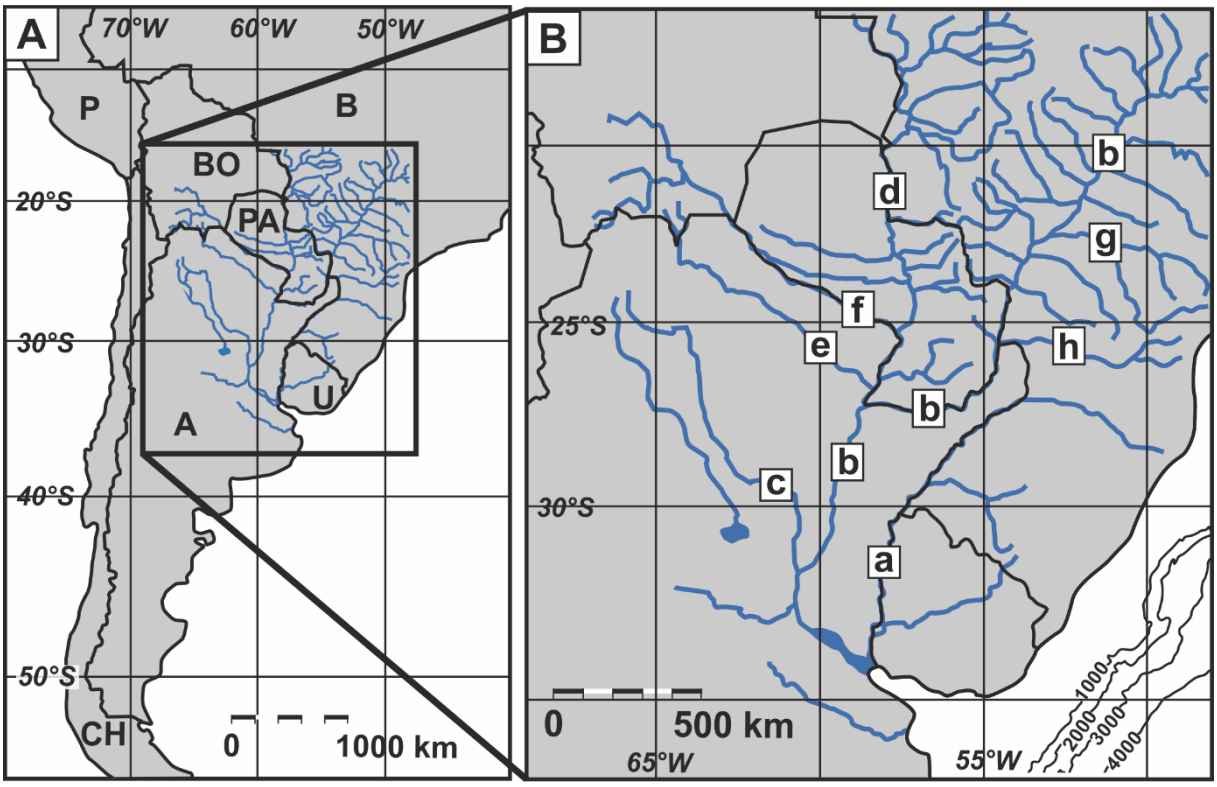

Fig. 5. Panel A: Map of southern South America showing the Río de la Plata drainage basin and the area expanded in panel B. The countries are marked with black uppercase letters as follows A: Argentina, B: Brazil, BO: Bolivia, CH: Chile, P: Peru, PA: Paraguay and U: Uruguay. Panel B: The main tributaries are marked with black lowercase letters as follows a: Uruguay River, b: Paraná River, c: Salado River, d: Paraguay River, e: Bermejo River, f: Pilcomayo River, g: Tietê River and h: Iguaçu River.

1.2.2.1 Hydrological and oceanic setting

The Río de la Plata drainage basin flows into the South Atlantic Ocean in a funnel shaped estuary (Figs. 5 and 6). The estuary has a northwest to southeast orientation, a length of 320 km, a width at the mouth of 230 km and a water depth between 5 and 15 m (Guerrero et al., 1996).

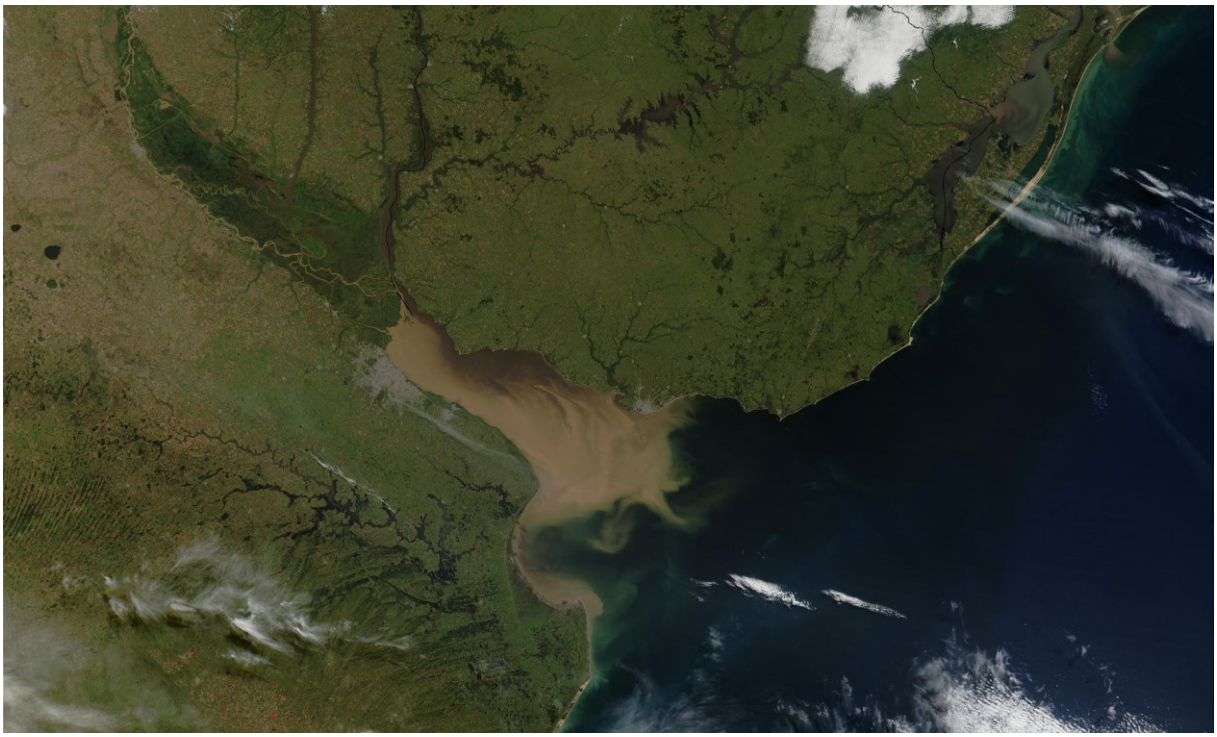

Fig. 6. Satellite image of the Río de la Plata estuary taken from the Terra satellite in May 2002. Credit: Jacques Descloitres, MODIS Land Rapid Response Team, NASA/GSFC.

The Paraná and Uruguay Rivers confluence at the Argentinian and Uruguayan border and form the Río de la Plata estuary (Depetris and Griffin, 1968). The annual water discharge of 470 km^3 (Milliman and Meade, 1983) is supplied to 75 % by the Paraná River (and its tributaries) and to 25 % by the Uruguay River (Depetris and Griffin, 1968). The Paraná River is formed by the confluence of the Grande and Paranaíba River and can be divided into two segments. The part mainly located in Brazil, upstream of the confluence with the Paraguay River, near the city of Corientes, is called the upper Paraná River. The part downstream of this confluence, located in Argentina, up to the confluence with the Uruguay River, is called the lower Paraná River. The western part of the basin is mainly drained by three rivers: The Salado River, a tributary of the lower Paraná River, and the Bermejo and Pilcomayo Rivers tributaries of the Paraguay River (Fig. 5). The Pantanal, a large swamp, accounts for a large section of the Paraguay River drainage basin (Berbery and Barros, 2002). The modern total annual suspended particulate matter (SPM) discharged into the South Atlantic Ocean is 9.2 x 10^7 tons (Depetris et al. 2003) (Fig. 6). Today, the Bermejo River with a percentage proportion of 4 % of the total drainage area is supplying between 50 to 70 % of this SPM discharge alone (Henry

et al., 1996). The Río de la Plata drainage basin is considered a tropical river basin, because approximately 50 % of the basin has a dry and wet tropical climate (Henry et al, 1996). The annual precipitation has a west to east gradient with a drier west and wetter east and an additional precipitation maximum in the northern part of the basin (Berbery and Barros, 2002). The South American Summer Monsoon (SASM) brings a humid climate and high precipitation from northern South America to the Andean foreland and the upper Paraná drainage basin during austral summer (DJF) (Fig. 7). In austral winter (JJA) the Southeast Trade winds (SE Trades) cause a west (wet) to east (dry) precipitation gradient (Piovano et al., 2009) (Fig. 7). Water and suspended particulate matter from the Río de la Plata estuary are transported northeastwards by the Plata Plume Water (PPW) that is mainly driven by wind direction (Piola et al., 2000). The shelf area in front of the estuary is dominated by two ocean currents (Fig. 7), the southwestwards flowing Subtropical Shelf Water (STSW) and the northeastwards flowing Subantarctic Shelf Water (SASW). Their meeting zone is called the Subtropical Shelf Front (STSF), which is assumed as the extension of the Brazil-Malvinas Confluence (BMC) (Lantzsch et al., 2014). The intermediate and deep water in front of the estuary is influenced by the northwards flowing Antarctic Intermediate water (AAIW) and the southwards flowing North Atlantic Deep Water (NADW) (Voigt et al., 2013).

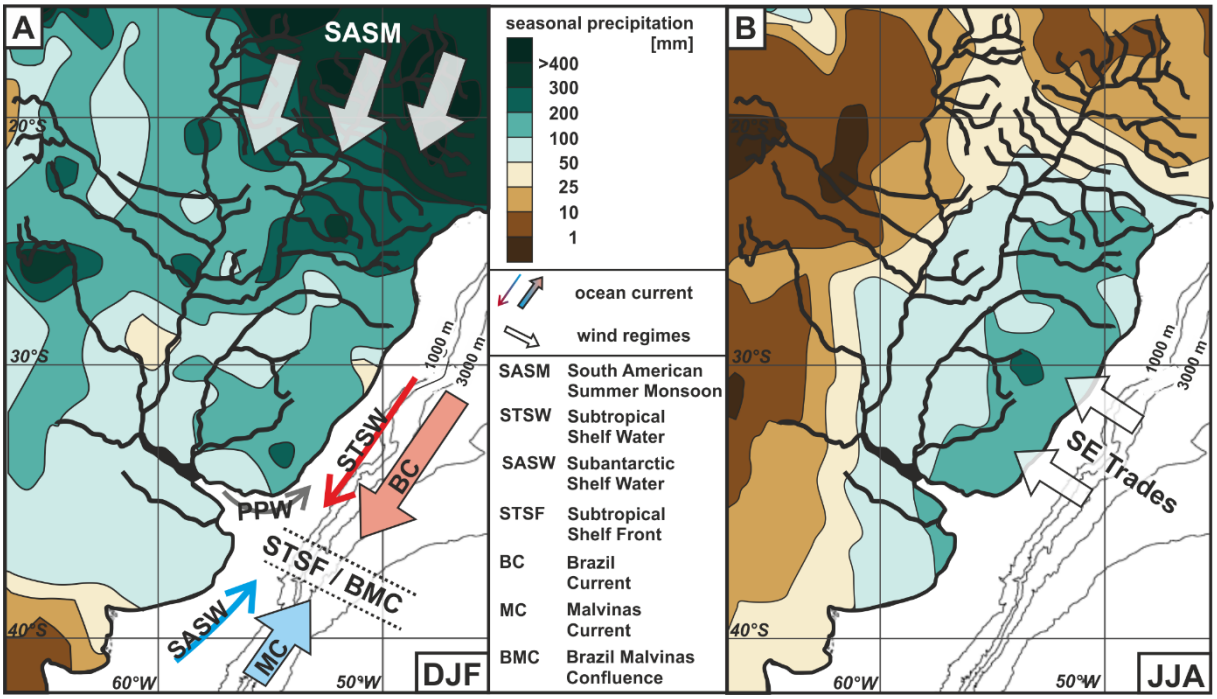

Fig. 7. Seasonal precipitation patterns for austral summer (DJF) and winter (JJA) (after Piovano et al., 2009) and surface ocean currents. Ocean currents are shown in panel A, shelf currents (SASW and STSW) are marked with thin arrows, offshore currents (BC and MC) are marked with thick arrows; a red color represents warm water, a blue color represents cold water; the arrow head indicates the main transport direction; the confluences of the ocean currents (STSF onshore and BMC offshore) is indicated by two dotted lines. Dominant wind regimes are shown in panel A and B for their respective season (DJF: SASM and JJA: SE Trades) indicated with thick white arrows, the arrow head highlights the main wind direction. The main tributaries of the LPDB are illustrated in black lines.

1.2.2.2 Geological setting

The Río de la Plata drainage basin is flanked to the west by the Andes Mountains, bordered to the northeast by the Brazilian Plateau and to the southwest by the Argentinian Pampas (Depetris and Griffin, 1968). The Andes Mountains with their mainly Mesozoic to Tertiary sedimentary and metamorphic rocks are drained by the Bermejo, Pilcomayo and Salado Rivers (Fig. 8). The Paraguay River drains Devonian-Carboniferous sedimentary rocks. The Uruguay River drains primarily tholeiitic flood basalts (Jurassic-Cretatious) and the upper Paraná River drains Jurassic-Cretatious sedimentary rocks. Additionally, both rivers drain parts of Precambrian crystalline basement rock (Río de la Plata Craton and the Brazilian Shield) (Henry et al., 1996).

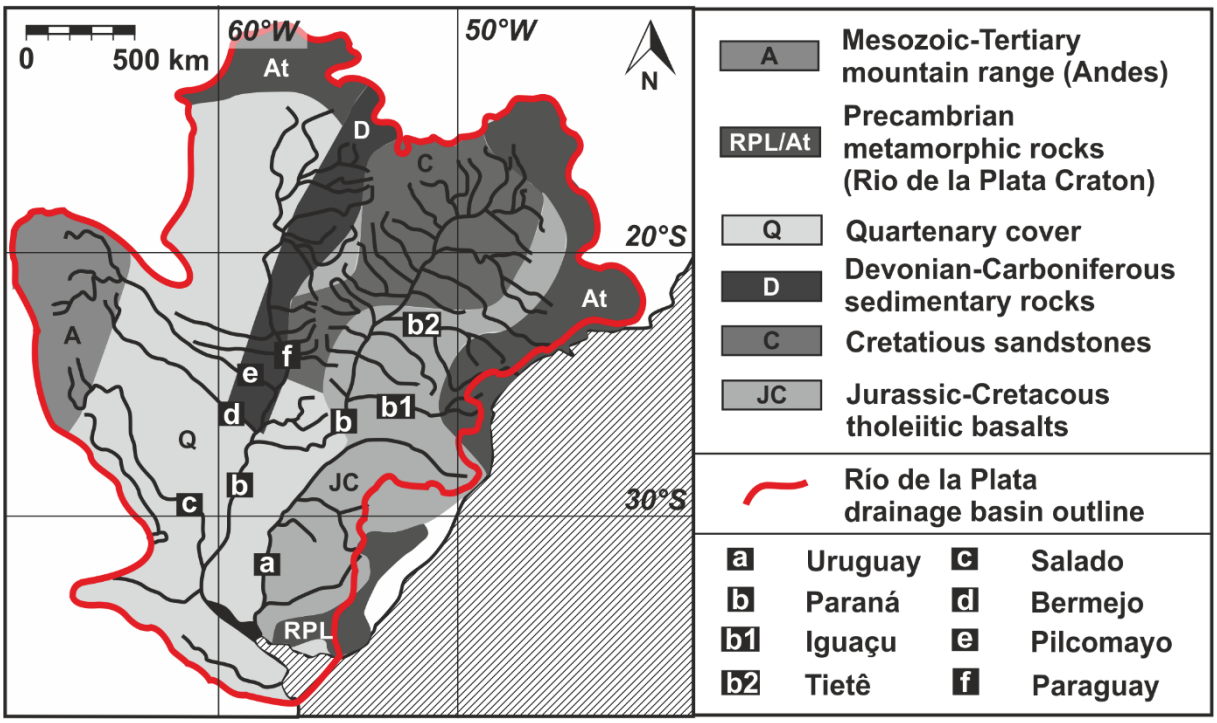

Fig. 8. Major geological units of the Río de la Plata drainage basin. The outline of the Río de la Plata drainage basin is shown in red and the main tributaries are marked with white lowercase letters as follows a: Uruguay River, b: Paraná River, b1: Iguaçu River, b2: Tietê River, c: Salado River, d: Bermejo River, e: Pilcomayo River and f: Paraguay River. Geological units are simplified after Henry et al. (1996).

1.3 Radiogenic isotope systems

1.3.1 Strontium

Strontium (Sr) is an alkaline earth metal with four stable isotopes (^{84}Sr, ^{86}Sr, ^{87}Sr and ^{88}Sr). ^{87}Sr is a radiogenic isotope produced by the β-decay of ^{87}Rb (Rubidium). The Sr isotopic signature is generally expressed as a direct ratio of two isotopes (i.e. $^{87}Sr/^{86}Sr$). The amount of radiogenic ^{87}Sr and thus the Sr isotopic ratio of a rock or mineral is a function of the initial ^{87}Sr amount, the initial Rb/Sr ratio and the age (time for ^{87}Rb to generate ^{87}Sr). Fractionation processes between Sr and Rb during melt crystallization lead to distinct differences in geological reservoirs. The continental crust has a high Rb/Sr ratio with radiogenic $^{87}Sr/^{86}Sr$ ratios of > 0.710. A low Rb/Sr ratio in the residual mantle led to unradiogenic $^{87}Sr/^{86}Sr$ ratios of average 0.703 ± 1 for the present-day mantle and oceanic crust (Veizer, 1989). Weathering, transport or depositional cycles do not significantly affect the Sr isotopic signature, making it possible to identify the provenance and document the contribution of a respective source, if the isotopic signatures of the analyzed materials are sufficiently different.

The oceanic residence time of Sr is much longer (≥ 4 Myr) than the mixing time of the ocean (~ 10^3 yr) (Veizer, 1989), leading to a global $^{87}Sr/^{86}Sr$ isotopic value for the world oceans. The modern $^{87}Sr/^{86}Sr$ value is 0.70917 (Henderson et al., 1994), Phanerozoic seawater values can have a minimum of approximately 0.7068 (Burke et al., 1982). Two main processes supply Sr into the ocean, i) continental input controlled by weathering and tectonics, and ii) hydrothermal input (Edmond, 1992). The Sr isotopic composition of seawater is mainly influenced by changes in the continental input and can therefore be used as a proxy for tectonic evolution (Veizer et al., 1999). Past seawater Sr isotopic compositions can be extracted from marine rocks and carbonate skeletons. Marine calcareous organisms incorporate Sr into their shells, due to the chemical similarity to calcium (Ca), without isotopic fractionation. (Veizer, 1989; Veizer et al., 1999).

1.3.2 Neodymium

Neodymium (Nd) is a light rare earth element (LREE) and has seven stable isotopes (^{142}Nd, ^{143}Nd, ^{144}Nd, ^{145}Nd, ^{146}Nd, ^{148}Nd and ^{150}Nd). ^{143}Nd is a radiogenic isotope produced by the α-decay of ^{147}Sm (DePaolo, 2012). Due to the small fractional differences in the $^{143}Nd/^{144}Nd$ isotopic ratio the Nd isotopic signature is commonly presented in the ε_{Nd} notation ($\varepsilon_{Nd} = \{[(^{143}Nd/^{144}Nd)_{sample} / (^{143}Nd/^{144}Nd)_{CHUR}]-1\}*10000$) relative to the Chondritic Uniform Reservoir (CHUR) with a value of $^{143}Nd/^{144}Nd = 0.512638$ (Wasserburg and DePaolo, 1979). Similar to Sr and Rb, fractionation processes during melt crystallization lead to different Sm/Nd ratios in geological reservoirs. Nd is enriched in the crust and depleted in the residual mantle. The Nd isotopic signature is, analogous to Sr, used as a provenance tracer.

Nd has an ocean residence time of 600 to 2000 years (Frank et al., 2002), shorter than the mixing time of the deep ocean (Wilson et al., 2013). Therefore, there is no globally homogenous ε_{Nd} value. The ocean basins and individual ocean currents have distinct Nd isotopic signatures and Nd is used as a tracer of inter/intra basin water mass mixing (Wilson et al., 2013). Paleo Nd isotopic signature can be obtained from a variety of components, like foraminifera (Howe et al., 2016), fish teeth (Martin and Haley, 2000; Martin et al., 2010), Fe-Mn crusts/noodles (Frank et al., 2002; O'Nions et al., 1998) and Fe-Mn oxyhydroxide coatings (Blaser et al., 2016; Chester and Hughes, 1967; Gutjahr et al., 2007; Pahnke et al., 2008; Wilson et al., 2013). Fe-Mn oxyhydroxides scavenge ions from seawater (Goldberg, 1954) and record the Nd (Bayon et al., 2002) isotopic composition of seawater during the time of formation.

1.3.3 Lead

Lead (Pb) is a post-transition metal that has four stable isotopes. ^{204}Pb is the only non-radiogenic isotope, while ^{206}Pb, ^{207}Pb and ^{208}Pb are radiogenic isotopes produced by the decay of ^{238}U, ^{235}U and ^{232}Th, respectively (Doe, 2012). The Pb isotopic composition is commonly expressed as the ratio between radiogenic and non-radiogenic isotopes (i.e. $^{206}Pb/^{204}Pb$) (Komárek et al., 2008). Most of the ^{235}U on earth has already decayed and the abundance of ^{207}Pb has changed only slightly. In comparison, ^{238}U, and thus ^{206}Pb, has a high abundance (Erel et al., 2001). Similar to Sr and Nd, the Pb isotopic signature is not significantly affected by weathering, transport or depositional cycles and is used as a source tracer (Komárek et al., 2008).

The mixing time of the ocean is much longer than the oceanic residence time of Pb with approximately 20 to 30 years in the North Atlantic Ocean (Henderson and Maier-Reimer, 2001) and 200 to 400 years in the Pacific Ocean (Schaule and Patterson, 1981). Therefore, the Pb isotopic signature is used in studies of local continental input (i.e. freshwater input from glacier retreat) and as a proxy for chemical weathering rates (Kurzweil et al., 2010 and therein). No modern-day natural Pb isotopic signature can be measured, due to anthropogenic pollution. However, ferromanganese deposits provide paleo pre-anthropogenic signals (Reynolds et al., 1999).

1.4 Overview of own research

The research goals described in section 1.1 were addressed in two individual manuscripts (Chapter 3 and 4). An additional manuscript (Chapter 5) focusses on the methodological background of the applied preparation techniques. One manuscript has been submitted to a peer-reviewed international journal and the other two are in preparation for submission. Data generation in respect to core sampling, preparation for all analyses and measurement of radiogenic isotopes (Sr, Nd and Pb) was done by me. The marine sediment cores were provided by the MARUM GeoB core repository, the SPM samples from the Amazon River were provided by Prof. Dr. C. M. Chiessi, the sediment samples from the Río de la Plata drainage basin were provided by Prof. Dr. S. A. Kasemann and Dr. G. M. Paula-Santos. I participated in the organization and execution of the sampling campaign of the SPM samples for the Brazilian part of the Río de la Plata drainage basin. Element concentration data was provide by Silvana Pape and Dr. Patrick Monien, XRD data was provided by Dr. Christoph Vogt and SEM data was provided by Petra Witte. The writing and design of all manuscripts and figures was done by myself. All co-authors contributed to the discussion and interpretation of data and provided comments and suggestions on the manuscripts. In the following, a brief summary of the outcome of each individual manuscript is given.

Chapter 3

"Holocene provenance shift of suspended particulate matter in the Amazon River basin"

Höppner N., Lucassen F., Chiessi C.M., Sawakuchi A.O., Kasemann S.A.

The manuscript reports the modern sediment supply conditions and the past evolution (the last 40 kyr) of the Amazon River basin. The data confirms two modern main sediment sources (Andes and Shield), with the Andes being the main sediment supplier. A sediment source change during the second part of the Heinrich Stadial 1 (HS1) from Andes to Shield areas can be observed and is attributed to a precipitation locus shift. Additionally, the study reveals a prominent offset between the modern and past radiogenic isotope signature. We suggest that this offset results from a permanent change to an even more Andean dominated signature of the river sediment during the late Holocene. We further hypothesize that the effect of the damming of the Madeira River might be visible in core top samples of the last decades.

Chapter 4

"*Provenance shift of suspended particulate matter in the Río de la Plata drainage basin over time"*

Höppner N., Lucassen F., Chiessi C.M., Becchio R.A., Kasemann S.A.

The manuscript presents the last 30 kyr of the sediment supply evolution and the modern supply conditions of the Río de la Plata drainage basin. The study provides the first extensive

data set of radiogenic isotope signatures for the river sediment of the Río de la Plata drainage basin and reveals the possibility to differentiate between the main tributaries. Several prominent source changes of the river sediment in the past are identified. We suggest climate and ocean circulation as the prominent driver behind these shifts. A weaker Atlantic Meridional Overturning Circulation (AMOC) shifts the Inter Tropical Convergence Zone (ITCZ) southward and strengthens the South American Summer Monsoon (SASM). Subsequently, a higher precipitation in the influenced areas leads to higher surface erosion (i.e. river sediment transport) shifting the sediment source. A stronger SASM can be observed in the HS1 and Younger Dryas, and a weaker SASM during the Bølling-Allerød interstadial. Additionally, a sea level high stand during the late Holocene allowed for the deposition of external sediment (from southern Argentina) at the core site, changing the radiogenic isotope signature.

Chapter 5

"*Chemical leaching of bulk marine sediment under riverine influence – Radiogenic isotope signatures of different fractions and the challenges of interpretation"*

Höppner N., Lucassen F., Kasemann S.A.

The manuscript aims to illuminate the necessary and dispensable steps of sample treatment to obtain a detrital signal from marine sediments for provenance studies. It presents the radiogenic isotope signatures of different sediments and leaching fractions and discusses the trustworthiness of the obtained signal. The Sr isotopic signature of marine sediment is heavily influenced by the unradiogenic Sr signature of marine seawater preserved in the carbonate fraction. A decarbonation to extract the detrital signature is of utmost importance. The study reveals that the Fe-Mn oxyhydroxide fraction of the two analyzed marine sediment cores, with heavy riverine influence, does not represent a paleo seawater signal. Furthermore, no Fe-Mn oxyhydroxides could be detected in the core in front of the Río de la Plata drainage basin, while the Fe-Mn oxyhydroxides of the Amazon River basin were river borne. Additionally, the difference between the decarbonated and Fe-Mn oxyhydroxide leached sediment fractions was insignificant and we suggest that a Fe-Mn oxyhydroxide leaching on marine sediments under strong riverine influence is redundant.

1.5 References

Amsler, M. L., Drago, E. C. (2009). A review of the suspended sediment budget at the confluence of the Paraná and Paraguay Rivers. *Hydrological Processes*, **23(22)**, 3230-3235.

Bayon, G., German, C. R., Boella, R. M., Milton, J. A., Taylor, R. N., Nesbitt, R. W. (2002). An improved method for extracting marine sediment fractions and its application to Sr and Nd isotopic analysis. *Chemical Geology*, **187(3)**, 179-199.

Bednarek, A. T. (2001). Undamming rivers: a review of the ecological impacts of dam removal. *Environmental management*, **27(6)**, 803-814.

Bentahila, Y., Othman, D.B., Luck, J.M. (2008). Strontium, lead and zinc isotopes in marine cores as tracers of sedimentary provenance: A case study around Taiwan orogen. *Chemical Geology*, **248(1)**, 62-82

Berbery, E. H., Barros, V. R. (2002). The hydrologic cycle of the La Plata basin in South America. *Journal of Hydrometeorology*, **3(6)**, 630-645.

Blaser, P., Lippold, J., Gutjahr, M., Frank, N., Link, J. M., Frank, M. (2016). Extracting foraminiferal seawater Nd isotope signatures from bulk deep sea sediment by chemical leaching. *Chemical geology*, **439**, 189-204.

Broccoli, A. J., Dahl, K. A., Stouffer, R. J. (2006). Response of the ITCZ to Northern Hemisphere cooling. *Geophysical Research Letters*, **33(1)**.

Burke, W. H., Denison, R. E., Hetherington, E. A., Koepnick, R. B., Nelson, H. F., Otto, J. B. (1982). Variation of seawater 87Sr/86Sr throughout Phanerozoic time. *Geology*, **10(10)**, 516-519.

Chester, R., Hughes, M. J. (1967). A chemical technique for the separation of ferro-manganese minerals, carbonate minerals and adsorbed trace elements from pelagic sediments. *Chemical geology*, **2**, 249-262.

Chiessi, C. M., Mulitza, S., Pätzold, J., Wefer, G., Marengo, J. A. (2009). Possible impact of the Atlantic Multidecadal Oscillation on the South American summer monsoon. *Geophysical Research Letters*, **36(21)**.

da Rosa-Costa, L.T., Lafon, J.M., Delor, C. (2006). Zircon geochronology and Sm–Nd isotopic study: further constraints for the Archean and Paleoproterozoic geodynamical evolution of the southeastern Guiana Shield, north of Amazonian Craton, Brazil. *Gondwana Research*, **10(3)**, 277-300.

DePaolo, D. J. (2012). Neodymium isotope geochemistry: an introduction (Vol. 20). Springer Science & Business Media.

Depetris, P. J., Griffin, J. J. (1968). Suspended load in the Río de la Plata drainage basin. *Sedimentology*, **11(1-2)**, 53-60.

Depetris, P. J., Probst, J. L., Pasquini, A. I., Gaiero, D. M. (2003). The geochemical characteristics of the Paraná River suspended sediment load: an initial assessment. *Hydrological Processes*, **17(7)**, 1267-1277.

Dino, R., Soares, E.A.A., Antonioli, L., Riccomini, C., Nogueira, A.C.R. (2012). Palynostratigraphy and sedimentary facies of Middle Miocene fluvial deposits of the Amazonas Basin, Brazil. *Journal of South American Earth Sciences*, **34**, 61-80.

Doe, B. R. (2012). Lead isotopes (Vol. 3). Springer Science & Business Media.

Edmond, J. M. (1992). Himalayan tectonics, weathering processes, and the strontium isotope record in marine limestones. SCIENCE-NEW YORK THEN WASHINGTON-, 258, 1594-1594.

Erel, Y., Dubowski, Y., Halicz, L., Erez, J., Kaufman, A. (2001). Lead concentrations and isotopic ratios in the sediments of the Sea of Galilee. *Environmental science & technology*, **35(2)**, 292-299.

Favis-Mortlock, D. T., Guerra, A. J. (1999). The implications of general circulation model estimates of rainfall for future erosion: a case study from Brazil. *Catena*, **37(3)**, 329-354.

Frank, M., Whiteley, N., Kasten, S., Hein, J. R., O'Nions, K. (2002). North Atlantic Deep Water export to the Southern Ocean over the past 14 Myr: Evidence from Nd and Pb isotopes in ferromanganese crusts. *Paleoceanography*, **17(2)**.

Gibbs, R.J. (1967). The geochemistry of the Amazon River system: Part I. The factors that control the salinity and the composition and concentration of the suspended solids. *Geological Society of America Bulletin*, **78(10)**, 1203-1232.

Gibbs, R.J., Konwar, L. (1986). Coagulation and settling of Amazon River suspended sediment. *Continental Shelf Research*, **6(1-2)**, 127-149.

Goldberg, E. D. (1954). Marine geochemistry 1. Chemical scavengers of the sea. *The Journal of Geology*, **62(3)**, 249-265.

Guerrero, R. A., Acha, E. M., Framin, M. B., Lasta, C. A. (1997). Physical oceanography of the Río de la Plata Estuary, Argentina. *Continental Shelf Research*, **17(7)**, 727-742.

Gutjahr, M., Frank, M., Stirling, C. H., Klemm, V., Van de Flierdt, T., Halliday, A. N. (2007). Reliable extraction of a deepwater trace metal isotope signal from Fe–Mn oxyhydroxide coatings of marine sediments. *Chemical Geology*, **242(3)**, 351-370.

Hansen, M. C., Potapov, P. V., Moore, R., Hancher, M., Turubanova, S., Tyukavina, A., Thau, D., Stehman, S. V., Goetz, S. J., Loveland, T. R., Kommareddy, A., Egorov, A., Chini, L., Justice, C. O., Townshend, J. R. G. (2013). High-resolution global maps of 21st-century forest cover change. *Science*, **342(6160)**, 850-853.

Hedges, J. I., Keil, R. G., Benner, R. (1997). What happens to terrestrial organic matter in the ocean?. *Organic geochemistry*, **27(5)**, 195-212.

Henderson, G. M., Martel, D. J., O'Nions, R. K., Shackleton, N. J. (1994). Evolution of seawater 87Sr86Sr over the last 400 ka: the absence of glacial/interglacial cycles. *Earth and Planetary Science Letters*, **128(3-4)**, 643-651.

Henderson, G. M., Maier-Reimer, E. (2002). Advection and removal of 210 Pb and stable Pb isotopes in the oceans: a general circulation model study. *Geochimica et Cosmochimica Acta*, **66(2)**, 257-272.

Henry, F., Probst, J. L., Thouron, D., Depetris, P. J., Garçon, V. (1996). Nd-Sr isotopic compositions of dissolved and particulate material transported by the Parana and Uruguay rivers during high (december 1993) and low (september 1994) water periods. *Sciences Géologiques, Bulletin*, **49(1-4)**, 89-100.

Howe, J. N., Piotrowski, A. M., Oppo, D. W., Huang, K. F., Mulitza, S., Chiessi, C. M., Blusztajn, J. (2016). Antarctic intermediate water circulation in the South Atlantic over the past 25,000 years. *Paleoceanography*, **31(10)**, 1302-1314.

Jaillard, E., Hérail, G., Monfret, T., Díaz-Martínez, E., Baby, P., Lavenu, A., Dumont, J.F. (2000). Tectonic evolution of the Andes of Ecuador, Peru, Bolivia and northernmost Chile. In: Cordani, U.G., Thomaz-Filho, A., Campos, D.A. (Eds.) Tectonic Evolution of South America. Acad. Bras. Cienc. Spec. Publ. 31st Int. Geol. Cong., pp. 41-95.

Johns, W.E., Lee, T.N., Beardsley, R.C., Candela, J., Limeburner, R., Castro, B. (1998). Annual cycle and variability of the North Brazil Current. *J. Phys. Oceanogr*. **28(1)**, 103–128.

Komárek, M., Ettler, V., Chrastný, V., Mihaljevič, M. (2008). Lead isotopes in environmental sciences: a review. *Environment International*, **34(4)**, 562-577.

Kurzweil, F., Gutjahr, M., Vance, D., Keigwin, L. (2010). Authigenic Pb isotopes from the Laurentian Fan: Changes in chemical weathering and patterns of North American freshwater runoff during the last deglaciation. *Earth and Planetary Science Letters*, **299(3)**, 458-465.

Lantzsch, H., Hanebuth, T. J., Chiessi, C. M., Schwenk, T., Violante, R. A. (2014). The high-supply, current-dominated continental margin of southeastern South America during the late Quaternary. *Quaternary Research*, **81(2)**, 339-354.

Lees, A. C., Peres, C. A., Fearnside, P. M., Schneider, M., Zuanon, J. A. (2016). Hydropower and the future of Amazonian biodiversity. *Biodiversity and conservation*, **25(3)**, 451-466.

Markgraf, V. (1989). Palaeoclimates in Central and South America since 18,000 BP based on pollen and lake-level records. *Quaternary Science Reviews*, **8(1)**, 1-24.

Martin, E. E., Haley, B. A. (2000). Fossil fish teeth as proxies for seawater Sr and Nd isotopes. *Geochimica et Cosmochimica Acta*, **64(5)**, 835-847.

Martin, E. E., Blair, S. W., Kamenov, G. D., Scher, H. D., Bourbon, E., Basak, C., Newkirk, D. N. (2010). Extraction of Nd isotopes from bulk deep sea sediments for paleoceanographic studies on Cenozoic time scales. *Chemical Geology*, **269(3)**, 414-431.

Meade, R.H. (1994). Suspended sediments of the modern Amazon and Orinoco rivers. *Quaternary International*, **21**, 29-39.

Meybeck, M., Ragu, A. (1995). River discharges to the oceans: an assessment of suspended solids, major ions and nutrients. UNEP.

Milliman, J. D., Meade, R. H. (1983). World-wide delivery of river sediment to the oceans. *The Journal of Geology*, **91(1)**, 1-21.

O'nions, R. K., Frank, M., Von Blanckenburg, F., Ling, H. F. (1998). Secular variation of Nd and Pb isotopes in ferromanganese crusts from the Atlantic, Indian and Pacific Oceans. *Earth and Planetary Science Letters*, **155(1)**, 15-28.

Pahnke, K., Goldstein, S. L., Hemming, S. R. (2008). Abrupt changes in Antarctic Intermediate Water circulation over the past 25,000 years. *Nature Geoscience*, **1(12)**, 870.

Piola, A. R., Campos, E. J., Möller, O. O., Charo, M., Martinez, C. (2000). Subtropical shelf front off eastern South America. *Journal of Geophysical Research: Oceans*, **105(C3)**, 6565-6578.

Piovano, E. L., Ariztegui, D., Córdoba, F., Cioccale, M., Sylvestre, F. (2009). Hydrological variability in South America below the Tropic of Capricorn (Pampas and Patagonia, Argentina) during the last 13.0 Ka. In Past climate variability in South America and surrounding regions (pp. 323-351). Springer Netherlands.

Reynolds, B. C., Frank, M., O'nions, R. K. (1999). Nd-and Pb-isotope time series from Atlantic ferromanganese crusts: implications for changes in provenance and paleocirculation over the last 8 Myr. *Earth and Planetary Science Letters*, **173(4)**, 381-396.

Revel M., Ducassou E., Grousset F. E., Bernasconi S. M., Migeon S., Revillon S., Mascle J., Murat A., Zaragosi S., Bosch D. (2010). 100,000 years of African monsoon variability recorded in sediments of the Nile margin. *Quaternary Science Reviews*, **29(11)**, 1342-1362.

Revel, M., Colin, C., Bernasconi, S., Combourieu-Nebout, N., Ducassou, E., Grousset, F.E., Rolland, Y., Migeon, S., Bosch, D., Brunet, P., Zhao, Y., Mascle, J. (2014). 21,000 Years of Ethiopian African monsoon variability recorded in sediments of the western Nile deep-sea fan. *Regional environmental change*, **14(5)**, 1685-1696.

Revel, M., Ducassou, E., Skonieczny, C., Colin, C., Bastian, L., Bosch, D., Migeon, S., Mascle, J. (2015). 20,000 years of Nile River dynamics and environmental changes in the Nile catchment area as inferred from Nile upper continental slope sediments. *Quaternary Science Reviews*, **130**, 200-221.

Roddaz, M., Viers, J., Brusset, S., Baby, P., Hérail, G. (2005). Sediment provenances and drainage evolution of the Neogene Amazonian foreland basin. *Earth and Planetary Science Letters*, **239(1)**, 57-78.

Rossetti, D.F., Toledo, P.M., Góes, A.M. (2005). New geological framework for Western Amazonia (Brazil) and implications for biogeography and evolution. *Quaternary Research*, **63**, 78–89.

Schaule, B. K., Patterson, C. C. (1981). Lead concentrations in the northeast Pacific: evidence for global anthropogenic perturbations. *Earth and Planetary Science Letters*, **54(1)**, 97-116.

Schmidt, M. W., Spero, H. J. (2011). Meridional shifts in the marine ITCZ and the tropical hydrologic cycle over the last three glacial cycles. *Paleoceanography*, **26(1)**.

Sioli, H. (1957). Sedimentation im Amazonasgebiet. *Geologische Rundschau*, **45(3)**, 608-633.

Sioli, H. (1984). The Amazon and its main affluents: Hydrography, morphology of the river courses, and river types, in: Sioli, H. (Ed.), The Amazon: Limnology and Landscape Ecology of a Mighty Tropical River and Its Basin. Springer Netherlands, Dordrecht, pp. 127–165. doi:10.1007/978-94-009-6542-3_5.

Stallard, R.F., Edmond, J.M. (1983). Geochemistry of the Amazon: 2. The influence of geology and weathering environment on the dissolved load. *Journal of Geophysical Research: Oceans*, **88(C14)**, 9671-9688.

Syvitski, J. P. (2003). Supply and flux of sediment along hydrological pathways: research for the 21st century. *Global and Planetary Change*, **39(1)**, 1-11.

Syvitski, J. P., Vörösmarty, C. J., Kettner, A. J., Green, P. (2005). Impact of humans on the flux of terrestrial sediment to the global coastal ocean. *Science*, **308(5720)**, 376-380.

Syvitski, J. P., Kettner, A. (2011). Sediment flux and the Anthropocene. *Philosophical Transactions of the Royal Society of London A: Mathematical, Physical and Engineering Sciences*, **369(1938)**, 957-975.

Tassinari, C.C., Macambira, M.J. (1999). Geochronological provinces of the Amazonian Craton. *Episodes-Newsmagazine of the International Union of Geological Sciences*, **22(3)**, 174-182.

Tassinari, C.C.G., Bittencourt, J.S., Geraldes, M.C., Macambira, M.J.B., Lafon, J.M. (2000). The Amazon Craton. In: Cordani, U.G., Thomaz-Filho, A., Campos, D.A. (Eds.) Tectonic Evolution of South America. Acad. Bras. Cienc. Spec. Publ. 31st Int. Geol. Cong., pp. 41-95.

Veizer, J. (1989). Strontium isotopes in seawater through time. *Annual Review of Earth and Planetary Sciences*, **17(1)**, 141-167.

Veizer, J., Ala, D., Azmy, K., Bruckschen, P., Buhl, D., Bruhn, F., Carden, G. A. F, Diener, A., Ebneth, S., Godderis, Y., Jasper, T., Korte, C., Pawellek, F., Podlaha, O. G., Strauss, H. (1999). 87Sr/86Sr, δ13C and δ18O evolution of Phanerozoic seawater. *Chemical geology*, **161(1)**, 59-88.

Voigt, I., Henrich, R., Preu, B. M., Piola, A. R., Hanebuth, T. J., Schwenk, T., Chiessi, C. M. (2013). A submarine canyon as a climate archive—interaction of the Antarctic Intermediate Water with the Mar del Plata Canyon (Southwest Atlantic). *Marine Geology*, **341**, 46-57.

Walling, D. E. (2005). Tracing suspended sediment sources in catchments and river systems. *Science of the total environment*, **344(1)**, 159-184.

Walling, D. E. (2009). The impact of global change on erosion and sediment transport by rivers: current progress and future challenges. Unesco.

Walter, H.J., Hegner, E., Diekmann, B., Kuhn, G. (2000). Provenance and transport of terrigenous sediment in the South Atlantic Ocean and their relations to glacial and interglacial cycles: Nd and Sr isotopic evidence. *Geochimica et Cosmochimica Acta*, **64(22)**, 3813-3827.

Wasserburg, G.J., DePaolo, D.J. (1979). Models of earth structure inferred from neodymium and strontium isotopic abundances. *Proceedings of the National Academy of Sciences*, **76(8)**, 3594-3598.

Wei, G., Ma, J., Liu, Y., Xie, L., Lu, W., Deng, W., Ren, Z., Zeng, T., Yang, Y. (2013). Seasonal changes in the radiogenic and stable strontium isotopic composition of Xijiang River water: Implications for chemical weathering. *Chemical Geology*, **343**, 67-75.

Wilson, D. J., Piotrowski, A. M., Galy, A., Clegg, J. A. (2013). Reactivity of neodymium carriers in deep sea sediments: Implications for boundary exchange and paleoceanography. *Geochimica et Cosmochimica Acta*, **109**, 197-221.

Wolf, A. T., Natharius, J. A., Danielson, J. J., Ward, B. S., Pender, J. K. (1999). International river basins of the world. *International Journal of Water Resources Development*, **15(4)**, 387-427.

Chapter 2
Methodology

2.1 Sample collection

This study is based on three different types of samples: i) marine sediment cores (gravity and multi cores) sampled on two expeditions, ii) river suspended particulate matter and iii) riverbank and bed sediments.

2.1.1 Amazon River basin

During RV Maria S. Merian cruise MSM20/3 in 2012 (Mulitza et al., 2013) marine gravity cores GeoB16224-1, GeoB16223-2, GeoB16217-2, GeoB16216-3, GeoB16212-3 and GeoB16211-3 as well as Multicore GeoB16212-2 were collected on the shelf area and continental slope off southern Brazil and French Guiana (Table 1).

Table 1 Location, length, water depth and used sampling device (MUC: Multicorer, GC: Gravity Core) of analyzed marine sediment cores.

Sample name	Device	Location [Lon (°E) / Lat (°N)]	Length [cm]	Water depth [m]
GeoB16211-3	GC	-49.34967 / 2.87817	368	56
GeoB16212-2	MUC	- 49.38817 / 3.10366	34 - 60	77
GeoB16212-3	GC	-49.38800 / 3.1045	605	75
GeoB16216-3	GC	-51.25567 / 6.2405	722	2833
GeoB16217-2	GC	-51.29017 / 6.0695	665	2440
GeoB16223-2	GC	-52.11650 / 6.62717	715	2253
GeoB16224-1	GC	-52.08305 / 6.65638	760	2510

Suspended particulate matter (SPM) samples from the Amazon River channel and mouth as well as from the five main tributaries (Solimões, Madeira, Negro, Tapajós and Xingu) were collected during several sampling campaigns between 2011 and 2015 (Table 2). Samples were taken aboard a small boat in the middle of the river channel. The water column depth of 60 % was determined with a sonar and a submersible pump was fixed to collect the sample. On land, the samples were filtered through 0.45 µm Sartorius® cellulose acetate membrane filter and dried at 50°C overnight in a small portable oven. The average sample size varied between 7 and 800 mg, depending on the SPM amount transported by the river.

Table 2 River name, season, sampling date and location for the suspended particulate matter samples of the Amazon River basin.

Sample name	River	Season	Sampling date	Location [Lon (°E) / Lat (°N)]
MAO-2f	Negro	dry	11/2011	-60.34648/-3.05295
MAO-01	Negro	dry	11/2011	-60.29815/-3.05776
MAO-83	Negro	wet	05/2012	-60.28617/-3.06063
MAO-81A	Negro	wet	05/2012	-60.43856/-3.01876
MAO-25c	Madeira	dry	11/2011	-58.90835/-3.53172
MAO-42	Madeira	wet	05/2012	-58.89843/-3.51745
MAO-10d	Solimões	dry	11/2011	-60.28577/-3.26928
MAO-77	Solimões	wet	05/2012	-60.03926/-3.30969
MAO175	Solimões	dry	10/2015	-67.92626/-3.25742
MAO123	Purus	dry	10/2015	-61.38084/-3.89446
MAO184	Japurá	dry	10/2015	-65.19695/-2.11780
STM-37	Tapajós	dry	11/2012	-54.99278/-2.47124
STM-13	Tapajós	wet	05/2012	-55.07681/-2.80241
XA-26	Xingu	dry	10/2011	-51.97992/-2.64643
XA-73	Xingu	wet	05/2012	-52.16048/-2.21725
MCP-N-MD-P	Amazon mouth (North)	wet	05/2014	-50.98507/-0.06900
MCP-S-ME-P	Amazon mouth (South)	wet	05/2014	-50.63580/-0.13392
MAO-21b	Amazon (up Madeira)	dry	11/2011	-59.027571/-3.247544
MAO-35c	Amazon (down Madeira)	dry	11/2011	-58.552865/-3.208796
MAO-51	Amazon (down Madeira)	wet	05/2012	-58.547846/-3.198223
STM-51	Amazon (up Tapajós)	dry	11/2012	-55.186068/-2.157202
STM-01	Amazon (up Tapajós)	wet	05/2012	-55.510539/-1.931037
STM-60	Amazon (down Tapajós)	dry	11/2012	-54.531682/-2.44886
STM-22	Amazon (down Tapajós)	wet	05/2012	-54.528453/-2.450372
XA-60	Amazon (down Xingu)	wet	05/2012	-52.308108/-1.498309

2.1.2 Río de la Plata drainage basin (LPDB)

During Meteor cruise M46/2 in 1999/2000 (Schulz et al., 2001) marine gravity core GeoB6212-1 was collected on the continental slope off the coast of SE Brazil (Table 3).

Table 3 Location, length, water depth and used sampling device (GC: Gravity Core) of analyzed marine sediment core GeoB6212-1.

Sample name	Device	Location [Lon (°E) / Lat (°N)]	Length [cm]	Water depth [m]
GeoB6212-1	GC	-50.24267 / -32.50517	790	1010

Suspended particulate matter samples for the Brazilian part of the Río de la Plata drainage basin (Uruguay and upper Paraná main channel with five tributaries) were collected during a sampling campaign in February/March 2016 (Table 4). Samples were taken aboard a small boat in the middle of the river channel. The water column depth of 60 % was determined with a sonar and a submersible pump was fixed to collect the sample. On land, the samples were filtered through 0.45 µm Sartorius® cellulose acetate membrane filter and dried at 50°C overnight in a small portable oven. The average sample size varied from 2 to 150 mg,

depending on the SPM amount transported by the river. At each sampling location (11 locations), two 200 ml PP wide-neck containers were filled with river water (already filtered through the 0.45 µm Sartorius® cellulose acetate membrane filter). One water sample was left untreated, the other was acidified with a few drops of concentrated HNO_3.

Table 4 River name, season, sampling date and location for the suspended particulate matter samples of the Río de la Plata drainage basin. A small x together with river name, means the sample was taken after the confluence with the respective river. (*): not analyzed. (+w): two additional river water samples, one acidified and one untreated.

Sample name	River	Season	Sampling date	Location [Lon (°E) / Lat (°N)]
NH PL1(*)	Paraná (Paranaíba x Grande)	wet	02/2016	-51.108688/-20.267283
NH PL2(+w)	Paraná (Paranaíba x Grande)	wet	02/2016	-51.114151/-20.274680
NH PL3	Paraná (Paranaíba x Grande)	wet	02/2016	-51.224997/-20.326559
NH PL4(+w)	Paranaíba	wet	02/2016	-51.012856/-19.981110
NH PL5	Paranaíba	wet	02/2016	-51.016831/-19.969046
NH PL6(*)	Paranaíba	wet	02/2016	-51.011366/-19.996560
NH PL7	Grande	wet	02/2016	-50.900298/-19.989568
NH PL8(+w)	Grande	wet	02/2016	-50.928448/-20.014306
NH PL9(*)	Grande	wet	02/2016	-50.944823/-20.023204
NH PL10	Tietê	wet	02/2016	-50.993525/-20.758754
NH PL11(+w)	Tietê	wet	02/2016	-51.026790/-20.743267
NH PL12(*)	Tietê	wet	02/2016	-51.063918/-20.724644
NH PL13	Paraná (x Tietê, near)	wet	02/2016	-51.625922/-20.868663
NH PL14(+w)	Paraná (x Tietê, near)	wet	02/2016	-51.631453/-20.846659
NH PL15(*)	Paraná (x Tietê, near)	wet	02/2016	-51.634754/-20.813090
NH PL16	Paraná (x Tietê, far)	wet	02/2016	-52.987989/-22.500671
NH PL17(+w)	Paraná (x Tietê, far)	wet	02/2016	-53.013573/-22.523217
NH PL18(*)	Paraná (x Tietê, far)	wet	02/2016	-53.041837/-22.542998
NH PL19	Paraná (x Paranapanema)	wet	02/2016	-53.202515/-22.729315
NH PL20	Paraná (x Paranapanema)	wet	02/2016	-53.178096/-22.713461
NH PL21(*)	Paraná (x Paranapanema)	wet	02/2016	-53.152060/-22.702807
NH PL22	Paranapanema	wet	02/2016	-52.969250/-22.569720
NH PL23(+w)	Paranapanema	wet	02/2016	-52.998194/-22.586447
NH PL24(*)	Paranapanema	wet	02/2016	-53.020715/-22.601778
NH PL25	Paraná (x Iguaçu)	wet	02/2016	-54.650345/-25.664730
NH PL26(+w)	Paraná (x Iguaçu)	wet	02/2016	-54.631823/-25.659656
NH PL27(*)	Paraná (x Iguaçu)	wet	02/2016	-54.603813/-25.667972
NH PL28	Iguaçu	wet	02/2016	-54.497760/-25.615137
NH PL29(+w)	Iguaçu	wet	02/2016	-54.525754/-25.628032
NH PL30(*)	Iguaçu	wet	02/2016	-54.533550/-25.599889
NH PL31	Uruguay	wet	03/2016	-53.146331/-27.150832
NH PL32(*)	Uruguay	wet	03/2016	-53.162390/-27.140298
NH PL33(+w)	Uruguay	wet	03/2016	-53.135689/-27.180072

Water as well as riverbank and bed sediment samples for the Salado drainage basin (Argentinian part of the LPDB) were sampled during a sampling campaign in December 2014 (Table 5). Sediment samples were taken in 50 ml polypropylene (PP) centrifuge tubes, filled between 40 and 95 % with sediment. Wherever possible, river water was sampled into the tubes as well, between 5 to 10 ml. Water samples were taken in 100 ml PP wide-neck containers (filled completely with water and occasionally with 0.25 to 2.5 cm of sediment at the bottom of the container). The riverbank sample of the Paraguay drainage basin (from the Clara River in Brazil) was taken in October 2015 (Table 5). A sediment sample of approximately 500 g (in a plastic bag) and a water sample of 500 ml (in a 0.5 l PE bottle) were taken. Water as well as riverbank and bed sediment from the Pilcomayo and Bermejo drainage basin (Bolivian part of the LPDB) were taken during a sampling campaign in December 2015 (Table 6). Samples were collected either in 100 ml PP wide-neck containers or in 50 ml PP centrifuge tubes. The sampling containers or centrifuge tubes were filled between 40 and 95 % with sediment. Wherever possible, river water was sampled into the containers as well, between 6 and 120 ml. For the water samples, the sampling containers or centrifuge tubes were filled completely with water and occasionally 1 cm sediment at the bottom of the container is present. Furthermore, four samples of the salt flats of the Salar de Uyuni were taken. The 100 ml PP wide-neck containers were filled completely with water and between 1 and 7 cm of salt.

Table 5 River name, sample type, sampling container, sampling date and location for the riverbank and bed sediment, and water samples of the Salado and Paraguay River drainage basin (Río de la Plata drainage basin). 100PP: 100 ml PP wide-neck containers, 50PP: 50 ml PP centrifuge tubes. (+s): there is some additional sediment in the sample container. (*): not analyzed.

Sample name	River	Sample type	Sampling container	Sampling date	Location [Lon (°E) / Lat (°N)]
CAL1(*)	Calchaqui	Water	100PP	12/2014	-65.75332/-25.97407
CAL2	Calchaqui	Sediment	50PP	12/2014	-65.75332/-25.97407
CAL3(*)	Calchaqui	Water	100PP	12/2014	-65.75332/-25.97407
CAL4	Calchaqui	Sediment	50PP	12/2014	-65.75332/-25.97407
CAL5(*)	San Lucas	Water(+s)	100PP	12/2014	-65.95446/-25.85242
CAL6(*)	San Lucas	Water(+s)	100PP	12/2014	-65.95446/-25.85242
CAL7	San Lucas	Sediment	50PP	12/2014	-65.95446/-25.85242
CAL8	San Lucas	Sediment	50PP	12/2014	-65.95446/-25.85242
CAL9(*)	La Salamanka	Water(+s)	100PP	12/2014	-65.64056/-25.62837
CAL10(*)	La Salamanka	Water(+s)	100PP	12/2014	-65.64056/-25.62837
CAL11	La Salamanka	Sediment	50PP	12/2014	-65.64056/-25.62837
CAL12(*)	Calchaqui	Water(+s)	100PP	01/2015	-65.60637/-25.61485
CAL13(*)	Calchaqui	Water(+s)	100PP	01/2015	-65.60637/-25.61485
CAL14	Calchaqui	Sediment	50PP	01/2015	-65.60637/-25.61485
RT1(*)	Toro	Water	100PP	01/2015	-65.49676/-25.03945
RT2(*)	Toro	Water	100PP	01/2015	-65.49676/-25.03945
RT3	Toro	Sediment	50PP	01/2015	-65.49676/-25.03945
TB1	Tolombon	Sediment	50PP	12/2014	-65.91945/-26.21782
TB2(*)	Tolombon	Water(+s)	100PP	12/2014	-65.91945/-26.21782
TB3(*)	Tolombon	Water(+s)	100PP	12/2014	-65.91945/-26.21782
RC	Rio Clara (Brazil, to Rio Paraguay)	Sediment + water(*)	plastic bag + 500 ml PE bottle	10/2015	-56.693915/-16.596967

Table 6 River name, sample type, sampling container, sampling date and location for the riverbank and bed sediment and water samples of the Pilcomayo and Bermejo River drainage basin (Río de la Plata drainage basin). 100PP: 100 ml PP wide-neck containers, 50PP: 50 ml PP centrifuge tubes. (+s): there is some additional sediment in the sample container. (*): not analyzed.

Sample name	River	Sample type	Sampling container	Sampling date	Location [Lon (°E) / Lat (°N)]
RA1(*)	Rio Atocha	Water	100PP	12/2015	-66.20496/-20.95625
RA2	Rio Atocha	Sediment	100PP	12/2015	-66.20496/-20.95625
RBL1	Rio Blanco	Sediment + water(*)	100PP	12/2015	-65.665806/-20.820528
RGD1	Rio Grande	Sediment	100PP	12/2015	-65.497333/-22.962972
RGD2(*)	Rio Grande	Water	100PP	12/2015	-65.45/-22.971111
RGD3	Rio Grande	Sediment + water(*)	100PP	12/2015	-65.45/-22.971111
RP1	Rio Pilcomayo	Sediment + water(*)	100PP	12/2015	-65.903444/-19.393472
RP2(*)	Rio Pilcomayo	Water	100PP	12/2015	-65.903444/-19.393472
RTL1(*)	Rio Tumul	Water(+s)	100PP	12/2015	-65.625167/-20.488
RTZ1	Rio Tupiza	Sediment + water(*)	100PP	12/2015	-65.699417/-21.50975
BM1(*)	Ruta Nacional 34, nahe Embarcacion	Water	50PP	12/2015	-64.139423/-23.247854
BM2(*)	Ruta Nacional 34, nahe Embarcacion	Water	50PP	12/2015	-64.139423/-23.247854
BM3	Ruta Nacional 34, nahe Embarcacion	Sediment	50PP	12/2015	-64.139423/-23.247854
BM4	Ruta Nacional 34, nahe Embarcacion	Sediment	50PP	12/2015	-64.139423/-23.247854
BU1	Salar de Uyuni	Water + salt	100PP	12/2015	-66.98357/-20.31624
BU2(*)	Salar de Uyuni, Ojos de Salar	Water + salt	100PP	12/2015	-66.663889/-20.311944
BU3	Salar de Uyuni, Ojos de Salar	Water + salt	100PP	12/2015	-66.663889/-20.311944
BU4(*)	Salar de Uyuni, north, near volcano	Water + salt	100PP	12/2015	-67.68425/-19.907333

2.2 Sample preparation

2.2.1 Marine sediment cores

2.2.1.1 GeoB16224-1 and GeoB6212-1

The sampling of the working halves of the two gravity cores GeoB16224-1 and GeoB6212-1 took place in the sampling laboratory of the IODP Bremen Core Repository at MARUM – Center for Marine Environmental Sciences. The selection of the sampling depth was based on pre-existing age models, established on AMS radiocarbon dates (Häggi et al., 2017, Campos et al., 2017), to create an even coverage of the radiocarbon dated section of the cores. The wet sediment was sampled into 40 and 70 ml pre-weighed PP container and weighed afterwards. Further sample treatment was conducted in the sample preparation lab of the "Isotope Geochemistry Group" at MARUM – Center for Marine Environmental Sciences. The samples were washed with Milli Q water (18.2 MΩ) to remove residual pore water, dried at 110°C and the dry weight was determined (Table 7). The washing solution was saved in 40 ml PP containers (Labelled 'Porewater') and dried at 110°C. The sample was divided into two fractions by wet sieving. The fraction > 63 µm was dried at 110°C and transferred into 1.5 ml Eppendorf® centrifuge tubes. The fraction < 63 µm was caught in 400 ml PP containers, dried at 110°C and milled to a homogenous powder with an agate mortar. Afterwards, it was transferred into 10 ml centrifuge tubes and is used for further analyses.

Table 7 General information (total number of samples, average wet/dry weight, average water/carbonate content) for the samples of the two marine gravity cores GeoB16224-1 and GeoB6212-1.

	GeoB16224-1	GeoB6212-1
Total number of samples	47	45
Average wet weight [g]	7.6	8.8
Average dry weight [g]	3.0	5.4
Average water content [%]	60.8	38.5
Average volume of fraction > 63µm [%] of total sample	1.7	8.6
Average carbonate content [%]	11.7	11.8

Approximately 150 to 200 mg of the sample were decarbonated with a 15 % acetic acid solution (buffered to pH ~4 with 1 M Na-acetate) in a four-step procedure, to remove the marine carbonates from the detrital material (Gutjahr et al., 2007) (Table 8).

Table 8 Step by step procedure for the sample decarbonization (after Gutjahr et al., 2007)

Steps	mL [added fluid]	Procedure after fluid addition	Supernatant
Step 1	~ 2.5 [CLS]	a) Shake for 2.5 h with 50 rpm b) Centrifuge for 30 min with 4000 rpm	Decant (pipette) into PP beaker; save for further analyses
Step 2	~ 2.5 [50/50; CLS/Milli Q]	c) Shake overnight with 50 rpm d) Centrifuge for 30 min with 4000 rpm	Decant (pipette) into PP beaker; save for further analyses
Step 3	~ 2.5 [Milli Q]	e) Shake for 20 min with 50 rpm f) Centrifuge for 30 min with 4000 rpm	Decant (pipette) into PP beaker; save for further analyses
Step 4	~ 2.5 [Milli Q]	g) Shake for 20 min with 50 rpm h) Centrifuge for 30 min with 4000 rpm	discard

Subsequently the sample was dried at 110°C, weighed and transferred into 15 ml Savillex® beaker. The digestion of the sediment powder was done in the clean laboratory of the "Isotope Geochemistry Group" at MARUM – Center for Marine Environmental Sciences. The detrital material was digested in 2 to 4 ml of a concentrated HF-HNO_3 acid mixture for at least 48 hours in closed Savillex® beakers at 140°C. The cooled samples were dried at 80°C and redissolved in 2 to 4 ml of *aqua regia* (3:1, 6 N HCl : concentrated HNO_3). It reacted for at least 48 hours in closed Savillex® beakers at 140°C. After that, it was dried at 90°C and redissolved in 3 to 4 steps in a H_2O_2 and concentrated HNO_3 acid mixture (between 3.5 and 4.5 ml of total acid volume, the amount of acid and steps depended on the amount of organic matter in the individual sample). After each step, the sample was being left to react for at least 6 to 8 hours and was dried at 50°C. Following, the sample was redissolved in 3 to 4 ml of 6 N HCl. If needed an aliquot for elemental analyses was taken during this step. Finally, the detrital fraction was dried at 95°C and redissolved in 600 to 1000 µl of 2 N HNO_3 for further isotopic analyses. Small particles of hardly soluble graphite or organic matter might remain in the sample solution. They will be separated by centrifugation before the column separation and do not influence the radiogenic isotope signatures.

2.2.1.2 GeoB16223-2, GeoB16217-2, GeoB16216-3, GeoB16212-3, GeoB16212-2 and GeoB16211-3

The bulk material from the sampled part of the cores was powered without any additional sample treatment in a previous study. They were received as a homogenous powder in glass

beakers and no sieving was possible. Material from the upper core section at 2 cm (GeoB16211-3, GeoB16216-3, GeoB16217-2 and GeoB16223-2) and 3 cm (GeoB16212-2) core depth was chosen, to analyze samples with Holocene ages. Additionally, samples from the gravity core GeoB16212-3 were analyzed in 100 cm intervals from 560 to 177 cm. Approximately 100 mg of the samples were decarbonated with a 15 % acetic acid solution (buffered to pH ~4 with 1 M Na-acetate) in a four-step procedure, to remove the marine carbonates from the detrital material (Gutjahr et al., 2007) (Table 8). Afterwards the sample was dried at 110°C, weight and transferred into 15 ml Savillex® beaker for digestion. The average carbonate content was 20.6 %. The digestion of the sediment powder was done as described in section 2.2.1.1, amounts of acids were adjusted to the smaller sample size of approximately 100 mg.

2.2.2 River suspended particulate matter

For each of the five main tributary (Solimões, Madeira, Negro, Tapajós and Xingu) of the Amazon River basin one dry and one wet season sample was chosen for analyses (if possible located close to each other). Additionally, five locations along the Amazon River main channel, between the confluences with the main tributaries, were chosen with one wet and one dry season sample. Finally, two sample from the Amazon River mouth, one from the north and one from the south river channel were chosen (Table 2). For the Río de la Plata drainage basin, two out of three samples for each sampling location were chosen for analyses. Five locations along the Paraná River main channel, the five largest tributaries (Paranaíba, Grande, Tietê, Paranapanema and Iguaçu) and the Uruguay River (Table 4). The filters were cut in half and half of every filter was transferred into pre-weighed 30 ml Teflon Savillex® beaker, filled with Milli Q water (18.2 MΩ) and placed into an ultrasonic bath for 30 min. Afterwards the remaining SPM was removed from filters by scraping. The solution was reduced on a hotplate at 110°C until it could be transferred into 15 ml Teflon Savillex® beaker. Subsequently, it was dried completely at 110°C and the sample weight determined. The cleaned SPM was dissolved in hot acid digestion steps, identical as described in section 2.2.1.1, amounts of acid were adjusted to the sample volume.

2.2.3 Riverbank and bed sediments

All sediment samples and two salt samples were analyzed (Tables 5 and 6). The water samples were not chosen for analyses. If river water was present together with sediment in the sample container, it was pipetted into a separate 40 ml PP container and shelved in a cold storage room at MARUM – Center for Marine Environmental Sciences. The residue was dried at 110°C and between 0.8 to 3.6 g of material was homogenized and powdered with an agate mortar. The powder was transferred into 10 ml centrifuge tubes. Approximately 100 mg were

dissolved in 15 ml Teflon Savillex® beaker in hot acid digestion steps, identical as for the marine sediments described in section 2.2.1.1.

2.2.4 Additional methodological tests

2.2.4.1 Leaching experiments

Five samples of GeoB16224-1 and of GeoB6212-1 were chosen to test the necessary leaching procedure (Table 9).

Table 9: Sample depth, calculated age and sediment supplying river basin for the five selected samples of GeoB16224-1 and GeoB6212-1.

Core	Sample name	Sample depth [cm]	Age [cal ka BP]	River basin
GeoB16224-1	A7	57.0	9.5*	Amazon
	A11	65.0	12.2*	
	A28	354.5	25.9	
	A34	415.0	28.6	
	A46	591.5	39.3	
GeoB6212-1	RP3	50.0	11.0	Río de la Plata
	RP5	75.0	12.2	
	RP13	210.0	17.1	
	RP21	368.0	21.7	
	RP36	630.0	26.3	

*treat ages with caution

The samples are already washed, sieved and powdered as described in section 2.2.1.1. Approximately 100 mg are transferred into 15 ml Teflon Savillex® beaker for hot acid digestion and are called the bulk fraction. Approximately 100 to 200 mg of the sample were decarbonated with a 15 % acetic acid solution (buffered to pH ~4 with 1 M Na-acetate) in a four-step procedure, to remove the marine carbonates from the detrital material (Gutjahr et al., 2007) (Table 8). The leach solution of the decarbonization step (KL fraction) is pipetted into 30 ml Teflon Savillex® beaker and dried at 110°C. The residual decarbonated sample (dc fraction) was dried at 110°C, weighed and transferred into 15 ml Savillex® beaker for hot acid digestion. Approximately 100 to 200 mg of the sample were first decarbonated and subsequently treated with an acid solution (0.05 M hydroxylamine-hydrochloride (HH) / 15 % acetic acid / 0.03 M Na EDTA, buffered to pH 4 with NaOH) in a four-step procedure, to remove potential authigenic Fe-Mn oxyhydroxide coatings (Gutjahr et al., 2007) (Table 10).

Table 10 Step by step procedure for Fe-Mn oxyhydroxide coating leaching on sediments (after Gutjahr et al., 2007)

Steps	mL [added fluid]	Procedure after fluid addition	Supernatant
Step 1	~ 2.5 [FMLS]	a) Shake for 1 h with 50 rpm b) Centrifuge for 30 min with 4000 rpm	Decant (pipette) into PP beaker; save for further analyses
Step 2	~ 2.5 [Milli Q]	c) Shake for 15 min with 50 rpm d) Centrifuge for 30 min with 4000 rpm	Decant (pipette) into PP beaker; save for further analyses
Step 3	~ 2.5 [Milli Q]	e) Shake for 15 min with 50 rpm f) Centrifuge for 30 min with 4000 rpm	Decant (pipette) into PP beaker; save for further analyses
Step 4	~ 2.5 [Milli Q]	g) Shake for 15 min with 50 rpm h) Centrifuge for 30 min with 4000 rpm	discard

The leach solution of the Fe-Mn oxyhydroxide leaching step (FML fraction) is pipetted into 30 ml Teflon Savillex® beaker and dried at 110°C. The residual sample (dt fraction) was dried at 110°C, weighed and transferred into 15 ml Teflon Savillex® beaker for hot acid digestion. This sample treatment produced five fraction (bulk, dc, KL, dt, FML) per sample (Fig. 9).

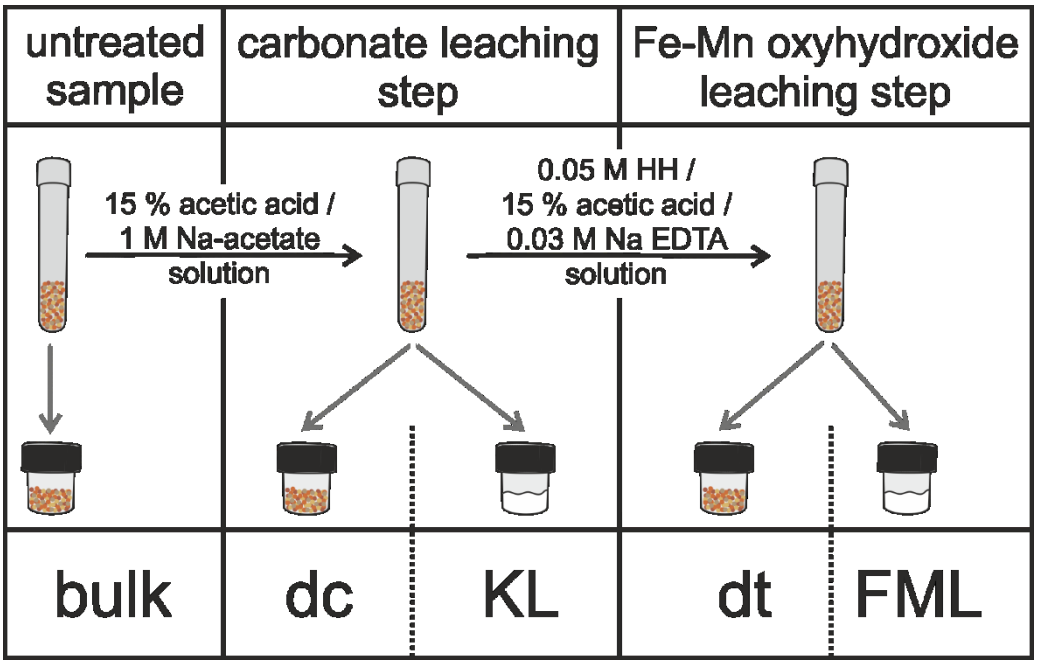

Fig. 9. Schematic overview of the sample treatment. Annotations are described in more detail in the text, bulk: chemically untreated sample, KL: supernatant of carbonate leaching, dc: decarbonated sample, FML: supernatant of Fe-Mn oxyhydroxide leaching and dt: decarbonated and Fe-Mn oxyhydroxide leached sample.

The solid samples (bulk, dc and dt fraction) are digested as described in section 2.2.1.1. The dried leachate solutions (KL and FML fraction) are redissolved in three steps of 2 ml of concentrated HNO_3 and three steps of 2 ml of 6 N HCl. After each individual step, the solution is dried at 95°C and redissolved. An aliquot for elemental analyses is taken in the last 6 N HCl step. Finally, the fraction was evaporated at 95°C and redissolved in 1000 to 1500 µl of 2 N HNO_3 for further isotopic analyses.

2.2.4.2 Unsieved vs. sieved

The widely applied procedure for the analyses of the detrital part of marine sediments is a decarbonization of the sample to remove marine carbonates (and sometimes the sorting out of particles > 63 µm). A fellow PhD student, working on the same marine sediment core (GeoB16224-1), did his analyses without decarbonization or sieving. Therefore, nine samples from marine sediment core GeoB16224-1 were chosen to analyze without sieving and decarbonization and an additional ten samples were sieved but not decarbonated. This way the effect of sieving and decarbonization on the, in this study, used isotopic systems (Sr, Nd and Pb) could be evaluated. Before the whole material of GeoB16224-1 was sieved (described in section 2.2.1.1.) approximately 100 to 200 mg (wbulk fraction) were weighed into 15 ml Teflon Savillex® beaker and digested in hot acid steps as described in section 2.2.1.1. Additionally, approximately 100 mg from the < 63 µm fraction (bulk fraction) were weighed into 15 ml Teflon Savillex® beaker and digested in hot acid steps as described in section 2.2.1.1.

2.2.4.3 Fe-Mn oxyhydroxide leaching of river suspended particulate matter

Four SPM samples from the Amazon River main channel were chosen for Fe-Mn oxyhydroxide leaching. A quarter of each filter was transferred into pre-weighed 15 ml Teflon Savillex® beaker, filled with Milli Q water (18.2 MΩ) and placed into an ultrasonic bath for 30 min. Afterwards the remaining SPM was removed from filters by scraping. The solution was evaporated at 110°C and the sample weight determined (between 33 and 129 mg). The sample was transferred into 10 ml centrifuge tubes and potential authigenic Fe-Mn oxyhydroxide coatings were removed with an acid solution (0.05 M hydroxylamine-hydrochloride (HH) / 15 % acetic acid / 0.03 M Na EDTA, buffered to pH 4 with NaOH) in a four-step procedure (Gutjahr et al., 2007) (Table 10). Afterwards, the sample was dried at 110°C, weighed and transferred into 15 ml Teflon Savillex® beaker for hot acid digestion as described in section 2.2.1.1.

2.3 Chemical separation and thermal ion mass spectrometry

For an accurate and precise isotope measurement of Sr, Nd and Pb a separation from interfering isotopes present in the sample matrix is important and can be achieved by using an ion exchange chromatography technique. The chemical separation was executed in the clean laboratory of the “Isotope Geochemistry Group” at MARUM – Center for Marine Environmental Sciences.

2.3.1 Strontium

The sample, dissolved in 500 to 1000 µl 2N HNO_3, is transferred into 1.5 to 2 ml Eppendorf® centrifuge tubes and centrifuged to avoid loading hardly soluble graphite or organic matter particles remaining in the solution after the digestion. Sr is separated from the matrix elements by using the ion exchange resins Sr.spec™ with a method after Deniel and Pin, 2001 (procedural work chart in Appendix A.1). Approximately 70 µl of Sr.spec™ resin are loaded into self-made columns (lower part of a disposable PE pipette with a frit inserted at the end and a volumetric capacity of approximate 1 ml). The resin is cleaned by consecutive steps of two times one column reservoir of 6 N HCl, four times one column reservoir of Milli Q water (18.2 MΩ) and two times 500 µl of 2 N HNO_3. Afterwards, the sample is loaded onto the column in 100 µl steps and the eluate is collected. The removal of matrix elements (including the rare earth elements (REE)) is achieved by adding 12 times 100 µl of 2 N HNO_3 and the eluate is collected again. Sr is eluted by adding five times 200 µl of 0.05 N HNO_3. 20 µl of 0.1 N H_3PO_4 were added to the Sr fraction and it was dried on the hot plate at 95°C. To remove potential residual resin 70 µl of concentrated HNO_3 are added and subsequently dried on the hot plate at 95°C. To remove potential residual organic matter 40 µl of H_2O_2 are added into the still warm beaker. After some reaction time, the sample is slowly dried on the hotplate at 50 to 60°C. The sample is redissolved in 3 µl of 0.1 N H_3PO_4 and loaded onto a rhenium filament in combination with a tantalum emitter (Birck HB), that is loaded beforehand and afterwards on the filament "sandwiching" the sample (Birck, 1986). Measurements were performed on a ThermoFisher Scientific TRITON Plus thermal ion mass spectrometer (TIMS) at the Isotope Geochemistry Laboratory at MARUM, University of Bremen, Germany. Sr isotope ratios were measured in the dynamic multicollection mode. Instrumental mass fractionation during the Sr measurement was corrected using the stable isotope ratio of $^{86}Sr/^{88}Sr$ (= 0.1194). The measurement accuracy and external long-term reproducibility for $^{87}Sr/^{86}Sr$ of reference material NIST SRM 987 was 0.710246 ± 0.000011 (2SD, n= 24; period: May 2015 to May 2017) and is within the range of 0.710250 ± 0.000034 (2SD, n= 1245, data <0.7102 and > 0.7103 are discarded) calculated from published values analyzed by TIMS (GeoRem data base; query September 2017; http://georem.mpch-mainz.gwdg.de).

2.3.2 Lead

The chemical separation of Pb from the sample matrix is performed by using the ion exchange resins Sr.spec™ (method after Deniel and Pin, 2001; procedural work chart in Appendix A.1) and is subsequently done after the Sr elution on the same columns. The column chemistry is changed to HCl by preconditioning the column with five times 100 µl of 2N HCl. Thereafter, Pb is rinsed from the column with four times 200 µl of 6 N HCl. The resin is discarded. 20 µl of 0.1 N H_3PO_4 were added to the Pb fraction and it was dried on the hot plate at 95°C. To remove potential residual resin 70 µl of concentrated HNO_3 are added and left to react with a closed

lid on the hot plate over night at 140 °C. The cooled sample is dried on the hot plate at 95°C. To remove potential residual organic matter 40 µl of H_2O_2 are added into the still warm beaker. After some reaction time, the sample is slowly dried on the hotplate at 50 to 60°C. The sample is redissolved in 3 µl of 0.1 N H_3PO_4. 6.5 µl of a silicate emitter (Gerstenberger and Haase, 1997) are loaded onto a rhenium filament and evaporated to two thirds of its volume. The sample is added to the still liquid silica emitter drop and the solution is dried completely. Measurements were performed on a ThermoFisher Scientific TRITON Plus thermal ion mass spectrometer (TIMS) at the Isotope Geochemistry Laboratory at MARUM, University of Bremen, Germany. Pb isotope ratios were measured in the static multicollection mode. Pb isotope ratios have been corrected for instrumental mass-fractionation using 0.1 % per atomic mass unit based on the repeated analyses of NIST SRM 981. The reproducibility including the correction for mass-fractionation is better than 0.1 % of the respective ratio, which is the assumed error on the Pb isotope ratios.

2.3.3 Neodymium

Nd is separated from the sample matrix in two parts. The light rare earth elements (LREE) are obtained from the REE using the ion exchange resin TRU.spec™ and Nd is separated from the LREE using the ion exchange resin LN.spec™ (method after Pin et al., 1994; procedural work chart in Appendix A.2 and A.3). First, approximately 250 µl of TRU.spec™ resin are filled into self-made columns (lower part of a disposable PE pipette with a frit inserted at the end and a volumetric capacity of approximate 3.5 ml). The column is preconditioned by consecutive steps of three times one column reservoir of Milli Q water (18.2 MΩ), 2 ml of 0.05 N HNO_3, one column reservoir of Milli Q water (18.2 MΩ) and two times 500 µl of 2 N HNO_3. Afterwards, the sample is loaded onto the column in 500 µl steps. The matrix elements are removed by consecutively adding seven times 500 µl of 2 N HNO_3 and 250 µl of 0.05 N HNO_3. The LREE are rinsed by adding four times 500 µl of 0.05 N HNO_3. The resin is saved and cleaned for reuse. The LN.spec™ resin is preinstalled in glass columns (approximately 1.5 ml of resin and a volumetric reservoir capacity of approximate 6 ml). The columns are preconditioned by consecutive steps of 5 ml of 0.25 N HCl, 5 ml of Milli Q water (18.2 MΩ) and two times 1 ml of 0.05 N HNO_3. Afterwards, the sample is loaded onto the column in 500 µl steps. The removal of matrix elements is achieved by consecutively adding three times 250 µl of 0.25 N HCl, 500 µl of 0.25 N HCl and 2 ml of 0.25 N HCl. Nd is eluted by using 2.5 ml of 0.25 N HCl. In the end, the resin is cleaned for reuse by consecutively adding two times 5 ml of 6 N HCl and two times 5 ml of 0.25 N HCl. 20 µl of 0.1 N H_3PO_4 were added to the Nd fraction and it was dried on the hot plate at 95°C. The sample is redissolved in 3 µl of 0.1 N H_3PO_4 and loaded onto a rhenium filament. Measurements were performed on a ThermoFisher Scientific TRITON Plus thermal ion mass spectrometer (TIMS) at the Isotope Geochemistry Laboratory at MARUM, University of Bremen, Germany. Nd isotope ratios were measured in the static multicollection mode.

Instrumental mass fractionation during the Nd measurement was corrected using the stable isotope ratio of $^{146}Nd/^{144}Nd$ (= 0.7219). The measurement accuracy and external long-term reproducibility for $^{143}Nd/^{144}Nd$ for reference material JNdi-1 was 0.512093 ± 0.000009 (2SD, n= 27; period: May 2015 to May 2017) and is within the calculated range of 0.512106 ± 0.000027 (2 SD, n = 211, data <0.51204 and >0.51217 are discarded) analyzed by TIMS (GeoRem data base; query September 2017; http://georem.mpch-mainz.gwdg.de). The $^{143}Nd/^{144}Nd$ isotope ratio is commonly presented in the ε_{Nd} notation (ε_{Nd} = {[($^{143}Nd/^{144}Nd)_{sample}$ / ($^{143}Nd/^{144}Nd)_{CHUR}$]-1}*10000) relative to the Chondritic Uniform Reservoir (CHUR) with a value of $^{143}Nd/^{144}Nd$= 0.512638 (Wasserburg and DePaolo, 1979).

2.4 Preparation and element analysis

2.4.1 Inductively coupled plasma optical emission spectroscopy (ICP-OES)

During the sample digestion, an aliquot for the element analyses was taken (see section 2.2.1.1). The solution is dried on the hot plate at 95°C and redissolved in 2% HNO_3. The analysis is performed in 1 to 10 ml of a 5,000 to 10,000-fold diluted aliquot. Therefore, the calculated amount to create this dilution is transferred into a 10 ml centrifuge tube and filled up with 2 % HNO_3. The major element concentrations (Al, K, Mg, Ca, Fe, Mn, Ba, P, Ti and Sr) were measured with an inductively coupled plasma optical emission spectrometer (ICP-OES, Agilent Technologies, 700 series) at the Sediment Geochemistry Laboratory, University of Bremen, Germany. The measurement was conducted in a 5,000 to 10,000-fold diluted aliquot in axial configuration.

2.4.2 Inductively coupled plasma mass spectroscopy (ICP-MS)

During the sample digestion, an aliquot for the element analysis was taken (see section 2.2.1.1). The solution is dried on the hot plate at 95°C and redissolved in 2% HNO_3. The analysis is performed in 10 ml of a 20,000-fold diluted aliquot. Therefore, the calculated amount to create this dilution is transferred into a 10 ml centrifuge tubes and filled up with 2 % HNO_3. Sr, Nd and Pb concentrations were measured with a high-resolution inductively coupled plasma mass spectrometer (HR-ICP-MS, Thermo Finnigan Element2, Germany) at the Petrology of the Ocean Crust Laboratory, University of Bremen, Germany. The analyses were conducted in a 20,000-fold diluted aliquot in low-resolution mode using indium and thallium as internal standards. International reference materials (BCR-2, BHVO-2) were used to check for accuracy (< 9 %, 2SD) and precision (< 2.5 %, 2SD).

2.4.3 X-ray diffraction (XRD)

Fifteen samples from marine sediment core GeoB16224-1 were chosen for XRD measurement. For the analysis, approximately 1 g of the washed, sieved and powdered material was decarbonated (see section 2.2.1.1) and once more ground with an agate mortar to a homogenous powder. Mineral assemblages were determined by standard powder X-ray

diffraction (XRD) analyses (Philips X'Peert Pro MD equipped with an X'Celeratir Detector Array) and quantification of mineral phases is based on the full-pattern method QUAX Vers. 2016 (© 2016 Christoph Vogt, Central Laboratory for Crystallography and Applied Material Science, ZEKAM, Geosciences, University Bremen).

2.4.4 Scanning electron microscopy (SEM) with energy-dispersive X-Ray spectroscopy (EDX)

Eight samples from marine sediment core GeoB16224-1 were chosen for SEM/EDX analysis. Four samples of the bulk fraction (only previously washed, sieved and powdered; see section 2.2.1.1), two samples that were decarbonated and two samples that were additionally Fe-Mn oxyhydroxide leached (see section 2.2.4.1). The material was spread on a special metal stub with adhesive. Semi-quantitative element abundances were evaluated using a scanning electron microscope (SEM) with energy-dispersive X-Ray spectroscopy (EDX). Measurements were performed at the Petrology of the Ocean Crust Laboratory, University of Bremen, Germany using a Zeiss SUPRA 40 equipped with a Bruker Modell XFlash 6 | 30 EDX system. EDX analysis were carried out at 15 kV accelerating voltage and with 5 µm beam diameter.

2.5 References

Birck, J. L. (1986). Precision K-Rb-Sr isotopic analysis: application to Rb-Sr chronology. *Chemical Geology*, **56(1-2)**, 73-83.

Campos, M. C., Chiessi, C. M., Voigt, I., Piola, A. R., Kuhnert, H., Mulitza, S. (2017). δ 13 C decreases in the upper western South Atlantic during Heinrich Stadials 3 and 2. *Climate of the Past*, **13(4)**, 345-358.

Deniel, C., Pin, C. (2001). Single-stage method for the simultaneous isolation of lead and strontium from silicate samples for isotopic measurements. *Analytica Chimica Acta*, **426(1)**, 95-103.

Gerstenberger, H., Haase, G. (1997). A highly effective emitter substance for mass spectrometric Pb isotope ratio determinations. *Chemical Geology*, **136(3-4)**, 309-312.

Gutjahr, M., Frank, M., Stirling, C. H., Keigwin, L. D., Halliday, A. N. (2008). Tracing the Nd isotope evolution of North Atlantic deep and intermediate waters in the Western North Atlantic since the Last Glacial Maximum from Blake Ridge sediments. *Earth and Planetary Science Letters*, **266(1)**, 61-77.

Häggi, C., Chiessi, C. M., Merkel, U., Mulitza, S., Prange, M., Schulz, M., Schefuß, E. (2017). Response of the Amazon rainforest to late Pleistocene climate variability. *Earth and Planetary Science Letters*, **479**, 50-59.

Mulitza, S., Chiessi, C.M., Cruz, A.P.S., Frederichs, T., Gomes, J.G., Gurgel, M.H., Haberkern, J., Huang, E., Jovane, L., Kuhnert, H., Pittauerová, D., Reiners, S.-J., Roud, S.C., Schefuß, E., Schewe, F., Schwenk, T.A., Sicoli Seoane, J.C., Sousa, S.H.M., Wagner, D.J., Wiers, S. (2013). Response of Amazon sedimentation to deforestation, land use and climate variability, Cruise No. MSM20/3, February 19–March 11 2012, Recife (Brazil), Bridgetown (Barbados). Berichte, Fachbereich Geowissenschaften, Universität Bremen, Bremen, Germany, 1-86.

Pin, C., Briot, D., Bassin, C., Poitrasson, F. (1994). Concomitant separation of strontium and samarium-neodymium for isotopic analysis in silicate samples, based on specific extraction chromatography. *Analytica Chimica Acta*, **298(2)**, 209-217

Schulz H. D., Ayres Neto A., Boetius A., Enneking K., Fabian K., Feseker T., Funk J., Gorke M., Heidersdorf F., Hensen C., Heuer V., Hill H.G., Hinrichs S., Kasten S., Klann M., Lacerda de Souza C., Martinez Briao A., Meyer S., Mulitza S., Niebler H.-S., Ochsenhirt W.-T., Panteleit B., Pfeifer K., Schewe F., Schwenk T., Senorans J.L., Siemer S., Steinmetz E., Wenzhöfer F. (2001). Report and preliminary results of Meteor Cruise M46/2. Berichte, Fachbereich Geowissenschaften, Universität Bremen, 184, 107.

Wasserburg, G.J., DePaolo, D.J. (1979). Models of earth structure inferred from neodymium and strontium isotopic abundances. *Proceedings of the National Academy of Sciences*, **76(8)**, 3594-3598

Chapter 3

Holocene provenance shift of suspended particulate matter in the Amazon River basin

Natalie Höppner[a]*, Friedrich Lucassen[a], Cristiano M. Chiessi[b], André O. Sawakuchi[c], Simone A. Kasemann[a]

[a] MARUM – Center for Marine Environmental Sciences and Faculty of Geosciences, University of Bremen, Leobener Str. 8, 28359 Bremen, Germany (flucassen@marum.de; skasemann@marum.de)

[b]School of Arts, Sciences and Humanities, University of São Paulo, Av. Arlindo Bettio, 1000, CEP03828-000 São Paulo, Brazil (chiessi@usp.br)

[c]Institute of Geosciences, University of São Paulo, Rua do Lao, 562, CEP05508-080, São Paulo, Brazil (andreos@usp.br)

*corresponding author: nhoeppner@marum.de, telephone: +49 (0) 421 218 65934

3.1 Abstract

The strontium (Sr), neodymium (Nd) and lead (Pb) isotope signatures of suspended particulate matter (SPM) in rivers reflect the radiogenic isotope signatures of the rivers' drainage basin. These signatures are not significantly affected by weathering, transport or depositional cycles, but document the sedimentary contributions of the respective sources. We report new Sr, Nd and Pb isotope ratios and element concentrations of modern SPM from the Brazilian Amazon River basin and document the past evolution of the basin by analyzing radiogenic isotopes of a (i) marine sediment core from the slope off French Guiana archiving the last 40 kyr of Amazon River SPM, and (ii) the Holocene core top section of several sediment cores raised between the Amazon River mouth and the slope off French Guiana. The composition of modern SPM confirms two main source areas, the Andes and the cratonic Shield. The SPM of the rivers draining the Andes (Solimões and Madeira Rivers) has the least radiogenic Sr and Pb and most radiogenic Nd isotope signatures. The SPM of the rivers draining the Brazilian (Tapajós and Xingu Rivers) and Guiana (Negro River) Shields has the most radiogenic Sr and Pb and least radiogenic Nd isotope signatures. Mixing models constrain the contributions of the source areas to the modern SPM (Solimões River ~55-60 %, Madeira River ~35-40 % and Shield rivers ~2-3 %). In the marine sediment core notable changes occurred during the second phase of Heinrich Stadial 1 (i.e. increased proportion of Shield rivers SPM) and during the last deglaciation (i.e. increased proportion of Madeira River SPM) on the background of elsewhere constant source contributions. Furthermore, we report a prominent offset in Sr and Nd isotopic composition between the average core value (ε_{Nd}: -11.7 ± 0.9 (2SD), $^{87}Sr/^{86}Sr$: 0.7229 ± 0.0016 (2SD)) and the average modern Amazon River SPM signal (ε_{Nd}: -10.5 ± 0.5 (2SD), $^{87}Sr/^{86}Sr$: 0.7213 ± 0.0036 (2SD)). We suggest that a permanent change in the Amazon River basin sediment supply during the late Holocene to a more Andean dominated SPM signal was responsible for the offset.

3.2 Introduction

The bulk of solid continental materials is transferred to the oceans as river suspended particulate matter (SPM) (Milliman and Meade, 1983). Other less significant transport mechanisms are aeolian and glacial input (Duce et al., 1991; Hallett et al., 1996). River SPM is deposited in river deltas or along continental margins and may provide valuable archives with high temporal resolution. These deposits record the isotope signatures of their continental sources as well as changes in provenance (Bentahila et al., 2008; Revel et al., 2010, 2014, 2015; Walter et al., 2000; Wei et al., 2013), provided the sediment sources of the individual drainage basins are sufficiently different in their radiogenic strontium (Sr), neodymium (Nd) and lead (Pb) isotope signatures.

The Amazon River drains an area of 6.3 x 10^6 km^2 with contrasting geology and radiogenic isotope composition including old Precambrian shields, Phanerozoic sedimentary deposits,

and the Cenozoic Andean orogen with an active magmatic arc in the west (Fig. 10). The water discharge of the Amazon River accounts for roughly 20 % of the world's river supply into the oceans making it the world's largest river not only in water discharge but also in drainage area (Gibbs, 1967). It supplies an average of 1.1 to 1.3 x 10^9 tons of sediments per year into the Atlantic Ocean (Meade, 1994), which are transported northwestwards and deposited from its mouth along hundreds of kilometers on the continental margin (Gibbs and Konwar, 1986). Two thirds of the drainage basin consists of a broad lowland plain and borders the Cenozoic Andes in the west and the Precambrian cratonic highlands in the north (Guiana Shield) and south (Brazilian Shield) (Gibbs, 1967) (Fig. 10). The five largest tributaries of the Amazon River are (in descending order of drainage area) the Solimões and Madeira (draining the Andes), the Negro, Xingu and Tapajós Rivers (draining the Shield areas) (Gibbs, 1967).

Numerous studies have investigated the chemical and mineralogical composition of the Amazon River and its tributaries' water and sediment load in order to characterize the different source areas and to understand the influence of distinct processes as e.g. sedimentation, transport and weathering on these signatures (e.g. Medeiros Filho et al., 2016; Guyot et al., 2007; Santos et al., 2015; Vital and Stattegger, 2000). In contrast to the elemental composition, the radiogenic isotopes are not influenced by these processes making them particularly suited for provenance studies. The Sr, Nd and Pb isotope composition of SPM from the Amazon River and its tributaries is poorly known and most of the existing data are from the Solimões and Madeira Rivers, both draining the Andes (Allègre et al., 1996; Bouchez et al., 2011; Viers et al., 2008). Only limited values are available for the main channel of the Amazon River and the Shield draining Negro, Tapajós and Xingu Rivers (Allègre et al., 1996; Bouchez et al., 2011). Several studies have shown that the main sediment supplier to the modern Amazon River (Filizola and Guyot, 2004; Meade et al., 1985) and during the late Quaternary (Govin et al., 2014; Milliman et al., 1975) are the Andes. There is, however, evidence for small variations in the proportions of Andean and cratonic Shield material within the Amazon River SPM. Given the continental extension of the Amazon River basin, even small variations may have large paleoenvironmental implications. Horbe et al. (2014) report a shift in Sr and Nd signatures from a more cratonic Shield component in Quaternary floodplain sediments of the Solimões River to more Andean material in modern Solimões River SPM. McDaniel et al. (1997) studied Nd and Pb isotopes on glacial stage sediments from the Amazon fan and suggested that Pleistocene muds have a more cratonic composition. The identification and interpretation of changing source contributions in the past relies on an accurate knowledge of the modern Sr, Nd and Pb isotopic composition of the Amazon River and its tributaries.

Here we present the Sr, Nd and Pb isotopic and elemental composition of SPM from the five main Amazon River tributaries (Solimões, Madeira, Negro, Tapajós and Xingu Rivers), as well

as from the Amazon River main channel and mouth. We applied our isotopic source characterization to a marine sediment core representing the integrated Amazon River basin discharge for the last 40 kyr and a range of marine core top samples representing the late Holocene deposits of the Amazon River. The new data accurately constrain the modern contributions of the Andean highland and cratonic lowland source areas, while the marine deposits indicate a shift toward a more Andean signature during the late Holocene as a response to a change in climate.

3.3 Regional setting

3.3.1 Geological setting

Stallard and Edmond (1983) divided the Amazon River basin into four morphostructural zones (Fig. 10A): The Andean Cordillera, the Subandean foreland, the Precambrian Shield and the Amazon trough. Subzones of the Andean Cordillera include the Eastern Cordillera, the Altiplano and the Western Cordillera. The Amazon trough is mainly filled by Phanerozoic sedimentary rocks (Pc). Its uppermost Neogene and Quaternary sedimentary units (Dino et al., 2012; Rossetti et al., 2005) are a mixture of the material weathered upstream from the principal source areas in the Andes and Brazilian and Guiana Shields. Similarly, the Subandean foreland with the northern (NF) and southern (SF) Amazon foreland basins is mainly composed of Miocene to Pliocene sediments from the same sources (Roddaz et al., 2005). The Precambrian Amazon Craton is subdivided into the Guiana Shield to the north and the Brazilian Shield to the south. The volcano-plutonic and the metamorphic units have ages between 3.7 and 1.0 Ga (da Rosa-Costa et al., 2006; Tassinari and Macambira, 1999; Tassinari et al., 2000). The region of the Andes drained by the Amazon River basin (i.e. Bolivia, Colombia, Ecuador and Peru) is mainly composed of Paleozoic to Cenozoic plutonic, volcanic and sedimentary rocks with the dominance of Cenozoic volcanic rocks at the surface (Jaillard et al., 2000). The Andes can be divided into a northern (0° to 15°S) and a central (10°S to 20°S) sector drained by the headwaters of the Solimões (northern) and Madeira (central) Rivers, respectively.

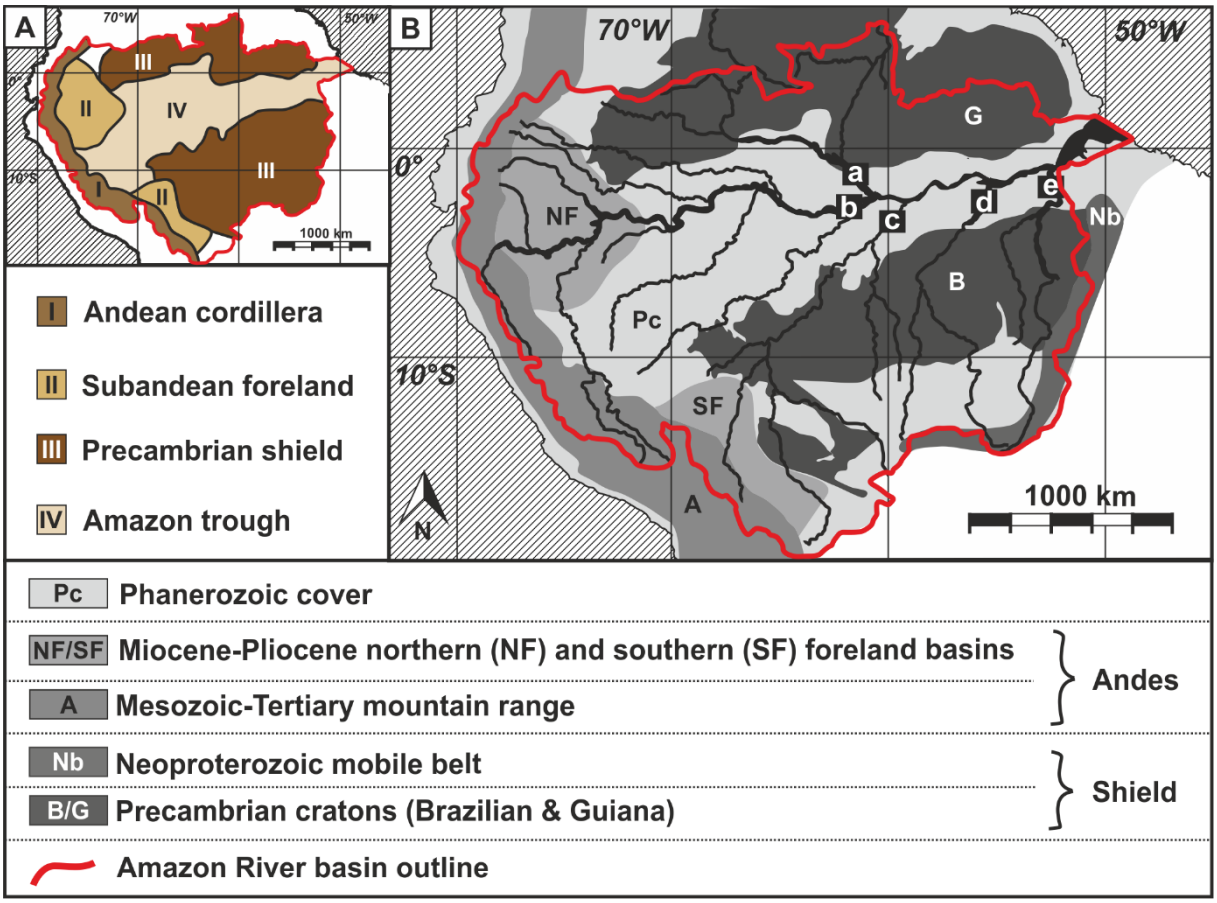

Fig. 10. Panel A: Main morphostructural zones of the Amazon River basin adapted from Stallard and Edmond (1983). Panel B: Major geological units of the Amazon River basin. The outline of the Amazon River basin is shown in red and the main tributaries of the Amazon River are marked with white lowercase letters as follows a: Negro River, b: Solimões River, c: Madeira River, d: Tapajós River and e: Xingu River. Geological units are simplified after Roddaz et al. (2005) and Tassinari and Macambira (1999).

3.3.2 Hydrological setting

The Amazon River has five main tributaries (Fig. 10B): Solimões, Madeira, Negro, Tapajós and Xingu Rivers. Due to differences in the topography and vegetation cover of each tributary basin, they were subdivided into three river types (Sioli, 1984). The Solimões and Madeira Rivers are classified as ‘whitewater’ rivers. They have a high turbidity due to a high SPM load. The Tapajós and Xingu Rivers are classified as ‘clearwater’ rivers with a low turbidity and an accordingly low SPM load. The Negro River is classified as a ‘blackwater’ river, showing also a low turbidity with the olive-brown color resulting from a high amount of fulvic and humic acids in the water (Sioli, 1957). Additionally, the tributaries of the Amazon River basin can be divided in two categories based on the predominant weathering types of each sub-basin (Gibbs, 1967). ‘Mountainous’ rivers drain areas with a steep relief and a high seasonality in temperature and precipitation (Solimões and Madeira Rivers). ‘Tropical’ rivers drain areas with a relatively flat relief and a year-round high temperature, but a high seasonality in precipitation (Negro, Tapajós and Xingu Rivers). The dominant weathering process in the drainage areas of ‘mountainous’ rivers is physical weathering. The steep relief leads to a fast removal of the

weathered products, not leaving enough time for an advanced chemical breakdown of the rocks (Gibbs, 1967). This regime is called ‘weathering-limited’ (Stallard and Edmond, 1983). ‘Tropical’ rivers, on the other hand, are characterized by an intense chemical weathering. The weathered materials have a long residence time due to the flat relief and very low denudation rates (Wittman et al., 2010), leaving enough time for an advanced chemical breakdown (Gibbs, 1967). This regime is called ‘transport-limited’ (Stallard and Edmond, 1983). The main water supplier to the Amazon River basin does not match with the main sediment supplier (Meade, 1994). The Solimões (43 %), Madeira (20 %) and Negro (29 %) Rivers supply about 92 % of the total modern water discharge (Gibbs, 1967). In contrast, the Solimões (41 %) and Madeira (55 %) Rivers alone supply about 96 % of the modern SPM discharge of the Amazon River to the Atlantic Ocean (Meade, 1994)

3.4 Material and methods

3.4.1 Material

The samples investigated in this study are river SPM and marine sediments from gravity and multi cores (Fig. 11).

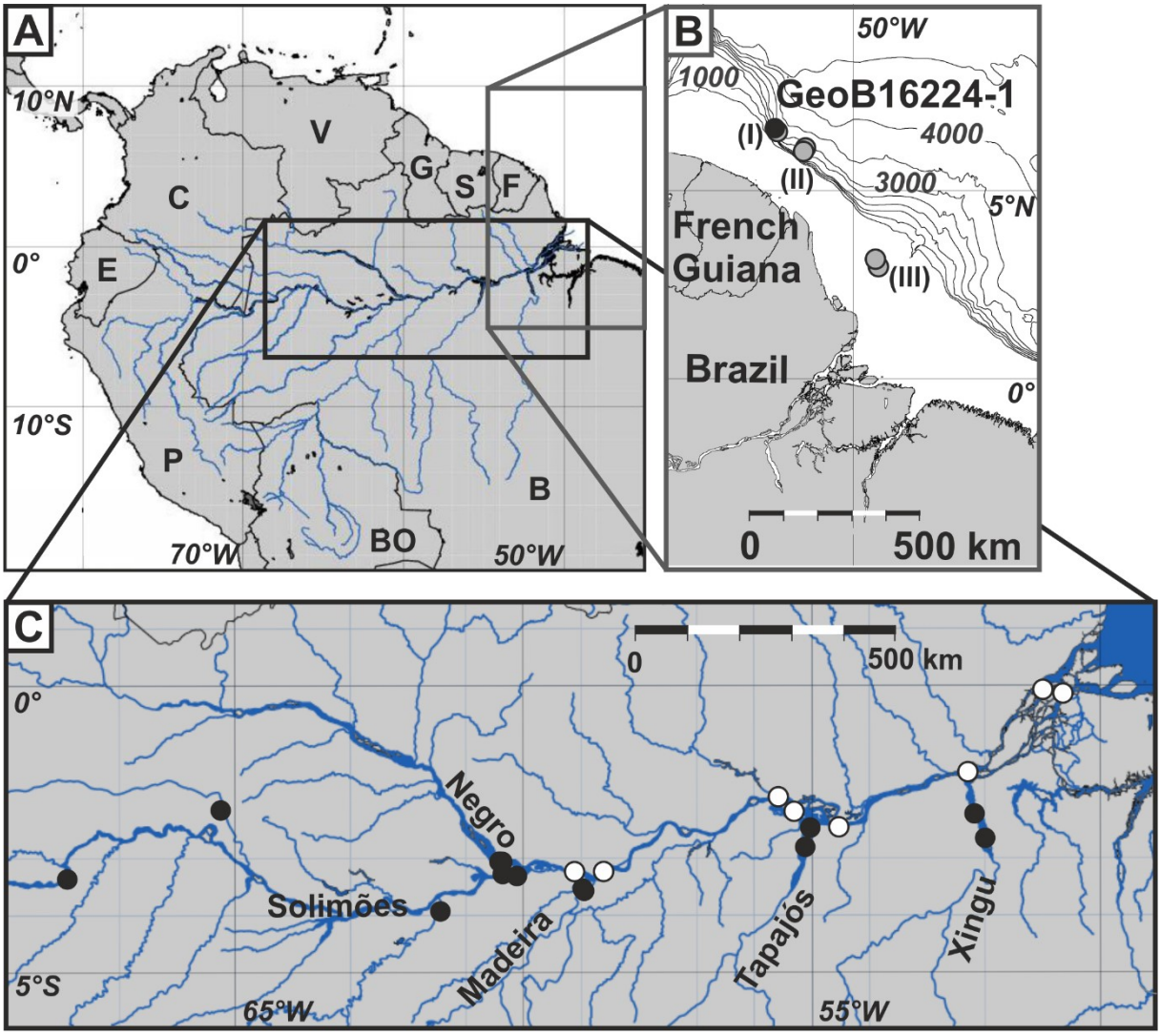

Fig. 11. Location of the sediment samples investigated in this study. Panel A: Northern South America showing the Amazon River Basin and the areas expanded in the other panels. The countries are marked with black uppercase letters as follows B: Brazil, BO: Bolivia, C: Colombia, E: Ecuador, F: French Guiana, G: Guiana, P: Peru, S: Suriname and V: Venezuela. Panel B: Location of marine sediment core GeoB16224-1 (black circle) and of the additionally analyzed marine sediment cores (grey circles; I: GeoB16223-2; II: GeoB16216-3 and GeoB16217-2; III: GeoB16212-2 and GeoB16212-3). Panel C: Location of the suspended particulate matter samples from the different tributaries (black circles) and of the Amazon River main channel and mouth (white circles).

Suspended particulate matter from the main Amazon River tributaries (Solimões, Madeira, Negro, Tapajós and Xingu Rivers) and the main Amazon River channel as well as its mouth were collected during several sampling campaigns between 2011 and 2015 (Table 11, Fig. 11C). For every tributary there is at least one dry and one wet season sample. Samples were

Table 11 Sr, Nd and Pb concentrations for the river suspended particulate matter of the Amazon River basin.

Sample name	River	Season	Sampling date	Location [Lon (°E) / Lat (°N)]	Sr [µg/g]	Nd [µg/g]	Pb [µg/g]
MAO-2f	Negro	dry	11/2011	-60.34648/-3.05295	-	-	-
MAO-01	Negro	dry	11/2011	-60.29815/-3.05776	47	29	35
MAO-83	Negro	wet	05/2012	-60.28617/-3.06063	83	27	42
MAO-81A	Negro	wet	05/2012	-60.43856/-3.01876	-	-	-
MAO-25c	Madeira	dry	11/2011	-58.90835/-3.53172	-	-	-
MAO-42	Madeira	wet	05/2012	-58.89843/-3.51745	127	47	38
MAO-10d	Solimões	dry	11/2011	-60.28577/-3.26928	-	-	-
MAO-77	Solimões	wet	05/2012	-60.03926/-3.30969	133	39	35
MAO175	Solimões	dry	10/2015	-67.92626/-3.25742	75	12	18
MAO123	Purus	dry	10/2015	-61.38084/-3.89446	67	28	23
MAO184	Japurá	dry	10/2015	-65.19695/-2.11780	133	26	23
STM-37	Tapajós	dry	11/2012	-54.99278/-2.47124	-	-	-
STM-13	Tapajós	wet	05/2012	-55.07681/-2.80241	69	51	44
XA-26	Xingu	dry	10/2011	-51.97992/-2.64643	-	-	-
XA-73	Xingu	wet	05/2012	-52.16048/-2.21725	85	25	33
MCP-N-MD-P	Amazon mouth (North)	wet	05/2014	-50.98507/-0.06900	114	28	26
MCP-S-ME-P	Amazon mouth (South)	wet	05/2014	-50.63580/-0.13392	82	19	32
MAO-21b	Amazon (up Madeira)	dry	11/2011	-59.027571/-3.247544	-	-	-
MAO-35c	Amazon (down Madeira)	dry	11/2011	-58.552865/-3.208796	-	-	-
MAO-51	Amazon (down Madeira)	wet	05/2012	-58.547846/-3.198223	83	26	25
STM-51	Amazon (up Tapajós)	dry	11/2012	-55.186068/-2.157202	-	-	-
STM-01	Amazon (up Tapajós)	wet	05/2012	-55.510539/-1.931037	114	35	30
STM-60	Amazon (down Tapajós)	dry	11/2012	-54.531682/-2.44886	-	-	-
STM-22	Amazon (down Tapajós)	wet	05/2012	-54.528453/-2.450372	94	28	35
XA-60	Amazon (down Xingu)	wet	05/2012	-52.308108/-1.498309	49	21	24

taken in the middle of the river channel at 60 % depth of the water column, filtered through 0.45 µm Sartorius® cellulose acetate membrane filter and dried at 50°C overnight. The average sample size varied from 7 to 800 mg, depending on the SPM amount transported by the river.

Gravity core GeoB16224-1 was collected on the continental slope off French Guiana (Table 12, Fig. 11B) during RV Maria S. Merian cruise MSM20/3 in 2012 (Mulitza et al., 2013), northwest of the Amazon River mouth. The SPM of the Amazon River is transported to the northwest by the North Brazil Current (NBC) (Johns et al., 1998). 37 samples with approximately 3 g dry weight were collected from 591 to 17 cm and provide an even coverage of the radiocarbon dated section of the core. Zhang et al. (2015) published 15 AMS radiocarbon (^{14}C) ages based on mixed planktonic foraminifera with a large age gap between 66 and 55 cm suggesting a hiatus. Here we use the age model published by Häggi et al. (2017) for the period between 41.2 (at 600 cm) and 12.6 (at 66 cm) cal ka BP and an extension of that age model for the upper 66 cm of the core based on the extrapolation of two ^{14}C ages using the calibration settings and method of Häggi et al. (2017). However we treat the upper portion (i.e. shallower than 66 cm core depth) of the age model of core GeoB16224-1 with caution.

Table 12 Location, length, water depth and used sampling device (MUC: Multicorer, GC: Gravity corer) of analyzed marine sediment cores.

Sample name	Device	Location [Lon (°E) / Lat (°N)]	Length [cm]	Water depth [m]
GeoB16212-2	MUC	-49.38817 / 3.10366	34 - 60	77
GeoB16212-3	GC	-49.38800 / 3.1045	605	75
GeoB16216-3	GC	-51.25567 / 6.2405	722	2833
GeoB16217-2	GC	-51.29017 / 6.0695	665	2440
GeoB16223-2	GC	-52.11650 / 6.62717	715	2253
GeoB16224-1	GC	-52.08305 / 6.65638	760	2510

Multi core GeoB16212-2 and gravity cores GeoB16212-3, GeoB16216-3, GeoB16217-2 and GeoB16223-2 were collected during the same cruise (Table 12) from the foreset of the submarine Amazon River delta and the Amazon River mudbelt off Brazil and French Guiana (Fig. 11B). Samples from the core tops were taken at 2 cm (GeoB16216-3, GeoB16217-2 and GeoB16223-2) and 3 cm (GeoB16212-2) core depth. Additionally the gravity core GeoB16212-3 was sampled in 100 cm intervals from 560 to 177 cm. All nine samples weighed approximately 100 mg. Gravity cores GeoB16216-3, GeoB16217-2 and GeoB16223-2 have one ^{14}C age at 6 cm core depth each (Table 13), providing maximum ages for the core top samples. Unfortunately, we have no age constrains for cores GeoB16212-2 and GeoB16212-3. Since both cores were raised from the submarine Amazon River delta where accumulation

rates are extremely high reaching up to 10 cm/yr (Kuehl et al., 1986; Nittrouer et al., 1995) it can be assumed that the deepest sample of core GeoB16212-3 at 560 cm has a maximum age that is not older than a century.

Table 13 ^{14}C AMS data and calibrated ages of the cores GeoB16216-3, GeoB16217-2 and GeoB16223-2.

Sediment core	Sample depth [cm]	Species	Lab No.	^{14}C AMS age ± SD [a BP]	Calibrated ages [cal a BP]	
					Min.	Max.
GeoB16216-3	6	Planktonic foraminifera	Poz-50186[1]	2825 ± 30	2469	2696
GeoB16217-2	6	Planktonic foraminifera	Beta-388901[2]	3020 ± 30	2725	2859
GeoB16223-2	6	Planktonic foraminifera	Poz-49096[1]	8160 ± 50	8508	8847

[1] Poz: Poznań Radiocarbon Laboratory, Poznań, Poland

[2] Beta Analytic Radiocarbon Dating Laboratory, Miami, USA

Zhang et al. (2015) published 15 ε_{Nd} values from 430 to 10 cm for core GeoB16224-1 and nine ε_{Nd} values of Holocene core-tops from the sector between the Amazon River mouth and core GeoB16224-1. However, the samples were prepared with a different methodological approach.

3.4.2 Methods

3.4.2.1 ^{14}C ages for GeoB16216-3, GeoB16217-2 and GeoB16223-2

Samples for radiocarbon analyses were wet-sieved, and oven-dried at 50°C overnight. Approximately 10 mg mixed planktonic foraminifera (> 150 µm) from each sample were hand-picked under a binocular microscope for ^{14}C measurements. The AMS radiocarbon analyses were performed at the Poznań Radiocarbon Laboratory, Poland, and at the Beta Analytic Radiocarbon Dating Laboratory, USA (Table 13). The calibrated ages were produced using the R-script Clam (version 2.2; Blaauw and Christen, 2011) with the Marine13 calibration curve (Reimer et al., 2013).

3.4.2.2 Sample preparation and dissolution

3.4.2.2.1 River SPM

The filter were cut in half and one half of each filter was transferred into a Teflon Savillex® beaker, filled with Milli Q water (18.2 MΩ) and placed into an ultrasonic bath for 30 min. Afterwards the remaining SPM was scratched from the filters and the sample was dried on a hot plate. The average analyzed amount varied from 4 to 400 mg. The SPM was digested in 0.5 to 2 ml of a concentrated HF:HNO_3 (5:1) acid mixture, dried and redissolved in 0.5 to 4 ml of *aqua regia* (3:1, 6 N HCl:concentrated HNO_3), dried and redissolved in 3 to 6 ml of a H_2O_2:concentrated HNO_3 (1:1) acid mixture (the amount depending on the amount of organic matter), dried and redissolved in 1 to 4 ml of 6 N HCl. An aliquot for elemental analyses was

taken. Finally, the detrital fraction was dried and redissolved in 500 to 1000 µl of 2 N HNO_3 for further chemical separation for isotopic analyses.

3.4.2.2.2 Marine sediment core GeoB16224-1

The sediment samples (average of 3 g dry weight) were washed two times with Milli Q water (18.2 MΩ) to remove residual pore water, wet sieved to collect the < 63 µm fraction used for further analysis and after drying ground in a mortar to a homogenous powder. Approximately 150 to 200 mg of the powder was decarbonated with a 15 % acetic acid solution (buffered to pH ~4 with 1 M Na-acetate) to remove the marine carbonates from the detrital material (Gutjahr et al., 2007). Leaching with hydroxylamine hydrochloride (HH) and acetic acid to remove potential authigenic Fe-Mn oxyhydroxide coatings on the sediments (Gutjahr et al., 2007) was not carried out, since our investigation of the leach solution revealed insignificant influence of Fe-Mn oxyhydroxide coatings, but dominant leaching of the clay minerals. The detrital material was digested in hot acid digestion steps identical as for the SPM described in section 3.4.2.2.1, amounts of acids were adjusted to the sample volume.

3.4.2.2.3 Marine sediment cores GeoB16212-2, GeoB16212-3, GeoB16216-3, GeoB16217-2 and GeoB16223-2

The samples from the five additional cores GeoB16212-2, GeoB16212-3, GeoB16216-3, GeoB16217-2 and GeoB16223-2 were treated in the same way like the material from GeoB16224-1 described in section 3.4.2.2.2, amounts of acids were adjusted to the sample size of 100 mg. The bulk samples were powdered in the course of a previous study and were therefore not sieved. To test the comparability of sieved and unsieved samples we analyzed 10 bulk samples of GeoB16224-1, but no significant difference between both fractions was detected (Table S1, supplementary data).

3.4.2.3 Chemical separation and mass spectrometry

Sr and Pb were separated from the sample matrix using 70 µl of Sr.spec™ resin (method modified from Deniel and Pin, 2001). Nd was isolated in two steps from the sample matrix using TRU.spec™ for LREE and LN.spec™ for Nd separation (Eichrom®) (method after Pin et al., 1994). Total procedural blanks are <140 pg for Sr, <80 pg for Nd and <60 pg for Pb. Analyses were performed on a ThermoFisher Scientific TRITON Plus thermal ionization mass spectrometer (TIMS) at the Isotope Geochemistry Laboratory at MARUM, University of Bremen, Germany. Nd and Pb isotope ratios were analyzed in the static multicollection mode and Sr isotope ratios in the dynamic multicollection mode.

Instrumental mass fractionation during Sr analyses was corrected using the stable isotope ratio of $^{86}Sr/^{88}Sr$ (= 0.1194). The analytical accuracy and external long-term reproducibility for $^{87}Sr/^{86}Sr$ of reference material NIST SRM 987 was 0.710246 ± 0.000011 (2SD, n= 24; period: May 2015 to May 2017) and is within the range of 0.710250 ± 0.000034 (2SD, n= 1245, data <0.7102 and > 0.7103 are discarded) calculated from published values analyzed by TIMS

(GeoRem data base; query September 2017; http://georem.mpch-mainz.gwdg.de). Instrumental mass fractionation during Nd measurements was corrected using the stable isotope ratio of $^{146}Nd/^{144}Nd$ (= 0.7219). The analytical accuracy and external long-term reproducibility for $^{143}Nd/^{144}Nd$ for reference material JNdi-1 was 0.512093 ± 0.000009 (2SD, n= 27; period: May 2015 to May 2017) and is within the calculated range of 0.512106 ± 0.000027 (2 SD, n = 211, data <0.51204 and >0.51217 are discarded) analyzed by TIMS (GeoRem data base; query September 2017; http://georem.mpch-mainz.gwdg.de). The $^{143}Nd/^{144}Nd$ isotope ratio is commonly presented in the ε_{Nd} notation (ε_{Nd} = {[$(^{143}Nd/^{144}Nd)_{sample}$ / $(^{143}Nd/^{144}Nd)_{CHUR}$]-1}*10000) relative to the Chondritic Uniform Reservoir (CHUR) with a value of $^{143}Nd/^{144}Nd$= 0.512638 (Wasserburg and DePaolo, 1979). Pb isotope ratios have been corrected for instrumental mass fractionation using 0.1 % per atomic mass unit based on the repeated analyses of NIST SRM 981. The reproducibility including the correction for mass fractionation is better than 0.1 % of the respective ratio, which is the assumed uncertainty on the Pb isotope ratios.

Sr, Nd and Pb concentrations of the SPM were measured with a high-resolution inductively coupled plasma mass spectrometer (HR-ICP-MS, Thermo Finnigan Element2, Germany) at the Petrology of the Ocean Crust Laboratory, University of Bremen, Germany. The analyses were conducted in a 20,000-fold diluted aliquot in low resolution mode using indium and thallium as internal standards. International reference materials (BCR-2 and BHVO-2) were used to check for accuracy (< 9 %; 2SD) and precision (< 2.5 %; 2SD).

3.5 Results

Sr, Nd and Pb isotopic compositions and concentrations for the river SPM are listed in Tables 11 and 14. Sr, Nd and Pb isotopic compositions for the detrital fraction of marine sediment core GeoB16224-1 are summarized in Table 15 and of marine sediment cores GeoB16212-2, GeoB16212-3, GeoB16216-3, GeoB16217-2 and GeoB16223-2 in Table 16.

Table 14 Sr, Nd and Pb isotopic composition for the river suspended particulate matter of the Amazon River basin. Uncertainties ($2SD_{mean}$) are given for the last digit.

Sample name	River	$^{87}Sr/^{86}Sr$	$^{143}Nd/^{144}Nd$	ε_{Nd}	$^{206}Pb/^{204}Pb$[a]	$^{207}Pb/^{204}Pb$[a]	$^{208}Pb/^{204}Pb$[a]
MAO-2f	Negro	0.77028(1)	0.511587(6)	-20.5(1)	19.90	15.83	39.51
MAO-01	Negro	0.763838(9)	0.511611(3)	-20.0(1)	19.76	15.82	39.41
MAO-83	Negro	0.730078(9)	0.511756(3)	-17.2(1)	19.46	15.78	39.22
MAO-81A	Negro	0.724546(8)	0.511920(4)	-14.0(1)	19.36	15.74	39.14
MAO-25c	Madeira	0.732227(5)	0.512018(4)	-12.1(1)	18.82	15.67	38.91
MAO-42	Madeira	0.735736(5)	0.512025(5)	-12.0(1)	18.70	15.64	38.83
MAO-10d	Solimões	0.715495(4)	0.512162(6)	-9.3(1)	19.01	15.67	38.96
MAO-77	Solimões	0.715816(6)	0.512191(7)	-8.7(1)	18.95	15.66	38.90
MAO175	Solimões	0.712528(6)	0.512186(4)	-8.8(1)	19.06	15.70	39.06
MAO123	Purus	0.718041(6)	0.512164(4)	-9.2(1)	18.84	15.66	38.87
MAO184	Japurá	0.714720(4)	0.512124(4)	-10.0(1)	19.07	15.71	39.09
STM-37	Tapajós	0.758463(9)	0.51166(1)	-19.1(3)	19.42	15.81	39.34
STM-13	Tapajós	0.753273(9)	0.511657(3)	-19.1(1)	19.40	15.81	39.34
XA-26	Xingu	0.75519(2)	-	-	19.74	15.93	39.99
XA-73	Xingu	0.741124(8)	0.511398(6)	-24.2(1)	19.38	15.86	39.53
MCP-N-MD-P	Amazon mouth (North)	0.720090(4)	0.512105(5)	-10.4(1)	18.93	15.66	38.93
MCP-S-ME-P	Amazon mouth (South)	0.721430(8)	0.512094(4)	-10.6(1)	18.90	15.67	38.91
MAO-21b	Amazon (up Madeira)	0.71665(1)	0.512130(4)	-9.9(1)	19.01	15.67	38.97
MAO-35c	Amazon (down Madeira)	0.71694(1)	0.51213(1)	-9.9(2)	19.01	15.68	38.99
MAO-51	Amazon (down Madeira)	0.721119(8)	0.512109(4)	-10.3(1)	18.93	15.68	38.98
STM-51	Amazon (up Tapajós)	0.718316(6)	0.512120(4)	-10.1(1)	18.97	15.66	38.89
STM-01	Amazon (up Tapajós)	0.721472(5)	0.512084(4)	-10.8(1)	18.87	15.68	38.96
STM-60	Amazon (down Tapajós)	0.718889(5)	0.512108(4)	-10.3(1)	18.98	15.66	38.91
STM-22	Amazon (down Tapajós)	0.722809(4)	0.512077(3)	-10.9(1)	18.84	15.67	38.90
XA-60	Amazon (down Xingu)	0.723199(5)	0.512103(4)	-10.4(1)	18.88	15.68	39.00

[a]Uncertainties ($2SD_{mean}$) are 0.1 %.

Table 15 Sr, Nd and Pb isotopic composition for sediment core GeoB16224-1. Uncertainties ($2SD_{mean}$) are given for the last digit.

Sample depth [cm]	Age [cal ka BP]	$^{87}Sr/^{86}Sr$	$^{143}Nd/^{144}Nd$	ε_{Nd}	$^{206}Pb/^{204}Pb^a$	$^{207}Pb/^{204}Pb^a$	$^{208}Pb/^{204}Pb^a$
17	5.5*	0.723102(7)	0.512027(4)	-11.9(1)	19.07	15.69	39.13
26	5.7*	0.722742(6)	0.512045(6)	-11.6(1)	19.11	15.71	39.18
38	6.0*	0.723661(9)	0.512022(3)	-12.0(1)	19.08	15.70	39.15
53	7.6*	0.72383(2)	0.512039(4)	-11.7(1)	19.06	15.69	39.10
55	8.7*	0.7246(3)	0.512038(6)	-11.7(1)	19.12	15.74	39.27
57	9.7*	0.724438(4)	0.512042(5)	-11.6(1)	19.08	15.68	39.09
59	10.5*	0.723894(4)	0.512033(4)	-11.8(1)	19.09	15.71	39.16
61	11.3*	0.723603(5)	0.512032(9)	-11.8(2)	19.05	15.69	39.06
63	11.8*	0.72367(4)	0.51204(1)	-11.7(2)	19.07	15.70	39.11
65	12.4*	0.723973(8)	0.512061(4)	-11.3(1)	19.08	15.69	39.08
75	13.2	0.723594(4)	0.51204(2)	-11.7(3)	19.11	15.74	39.24
88	13.9	0.723288(7)	0.512013(5)	-12.2(1)	19.07	15.71	39.18
95.5	14.2	0.722993(6)	0.512008(4)	-12.3(1)	19.04	15.69	39.08
127	15.5	0.72256(2)	0.51199(1)	-12.7(2)	19.06	15.71	39.14
147	16.4	0.722633(9)	0.511999(4)	-12.5(1)	19.03	15.69	39.10
157	16.8	0.723612(5)	0.512016(8)	-12.1(2)	19.07	15.71	39.15
168	17.3	0.723301(5)	0.51202(1)	-12.0(2)	19.04	15.69	39.10
186	18.1	0.722823(5)	0.512009(4)	-12.3(1)	19.03	15.69	39.09
208.5	19.1	0.722352(6)	0.512024(5)	-12.0(1)	19.03	15.69	39.11

*treat ages with caution. [a]Uncertainties ($2SD_{mean}$) are 0.1 %.

Table 15 (continued).

Sample depth [cm]	Age [cal ka BP]	$^{87}Sr/^{86}Sr$	$^{143}Nd/^{144}Nd$	ε_{Nd}	$^{206}Pb/^{204}Pb^{a}$	$^{207}Pb/^{204}Pb^{a}$	$^{208}Pb/^{204}Pb^{a}$
261	21.6	0.722477(7)	0.512021(6)	-12.0(1)	19.02	15.69	39.08
317	24.1	0.723226(5)	-	-	19.06	15.74	39.27
354.5	25.9	0.72331(3)	0.512034(4)	-11.8(1)	19.05	15.70	39.11
364.5	26.3	0.72283(2)	0.512048(6)	-11.5(1)	19.05	15.70	39.11
377	26.8	0.722219(7)	0.512052(9)	-11.4(2)	19.12	15.77	39.37
395	27.6	0.721950(7)	0.512028(4)	-11.9(1)	19.03	15.68	39.07
407	28.2	0.722893(4)	0.51205(1)	-11.5(2)	19.06	15.69	39.08
415	28.7	0.723114(6)	0.512035(5)	-11.8(1)	19.06	15.68	39.06
427	29.4	0.722409(5)	0.51204(1)	-11.8(2)	19.02	15.68	39.04
451	30.8	0.72155(1)	0.512041(4)	-11.6(1)	19.06	15.70	39.13
470.5	32.0	0.721868(7)	0.51210(4)	-10.6(8)	19.10	15.71	39.16
491	33.2	0.722241(6)	0.512046(6)	-11.5(1)	19.11	15.76	39.32
512	34.3	0.722244(5)	0.512068(7)	-11.1(1)	19.07	15.69	39.10
531	35.3	0.721012(9)	0.512057(8)	-11.3(2)	19.08	15.69	39.10
543	35.9	0.723120(9)	0.51210(1)	-10.6(2)	19.05	15.69	39.08
551	36.3	0.72237(1)	0.512039(8)	-11.7(2)	19.05	15.70	39.12
571	37.9	0.72214(4)	0.512054(6)	-11.4(1)	19.08	15.70	39.14
591.5	39.5	0.72249(1)	0.512039(4)	-11.7(1)	19.06	15.69	39.08

[a]Uncertainties ($2SD_{mean}$) are 0.1 %.

Table 16 Sr, Nd and Pb isotopic composition for the core GeoB16212-3 and core-tops (GeoB16212-2, GeoB16216-3, GeoB16217-2 and GeoB16223-2). Uncertainties ($2SD_{mean}$) are given for the last digit.

Sample name	Sample depth [cm]	Age [cal ka BP]	$^{87}Sr/^{86}Sr$	$^{143}Nd/^{144}Nd$	ε_{Nd}	$^{206}Pb/^{204}Pb$[a]	$^{207}Pb/^{204}Pb$[a]	$^{208}Pb/^{204}Pb$[a]
GeoB16212-2	3	Last century	0.723944(8)	0.51206(1)	-11.3(2)	19.01	15.69	39.09
GeoB16212-3	177	Last century	0.723747(8)	0.512074(5)	-11.0(1)	19.00	15.66	38.99
GeoB16212-3	230	Last century	0.723639(7)	0.512075(4)	-11.0(1)	19.02	15.68	39.06
GeoB16212-3	320	Last century	0.724317(7)	0.512055(4)	-11.4(1)	19.00	15.67	39.04
GeoB16212-3	430	Last century	0.724619(9)	0.512069(7)	-11.1(1)	19.03	15.68	39.06
GeoB16212-3	560	Last century	0.724102(8)	0.51206(1)	-11.3(2)	19.05	15.69	39.12
GeoB16216-3	2	See table 13	0.72368(1)	0.512036(7)	-11.7(1)	18.99	15.69	39.06
GeoB16217-2	2	See table 13	0.720585(7)	0.512029(7)	-11.9(1)	19.11	15.68	39.17
GeoB16223-2	2	See table 13	0.723597(5)	0.51204(1)	-11.6(2)	19.16	15.68	39.02

[a]Uncertainties ($2SD_{mean}$) are 0.1 %.

3.5.1 Pb isotopic composition of the river SPM

The Pb isotopic composition of the river SPM forms two clusters (Fig. 12). Cluster A consists of samples from Solimões and Madeira Rivers as well as from the Amazon River mouth and main channel with isotopic ratios ranging from 18.70 to 19.06 for $^{206}Pb/^{204}Pb$, from 15.64 to 15.70 for $^{207}Pb/^{204}Pb$ and from 38.83 to 39.06 for $^{208}Pb/^{204}Pb$ (not shown). The Negro, Tapajós and Xingu Rivers samples compose cluster B with isotopic ratios from 19.36 to 19.90 for $^{206}Pb/^{204}Pb$, from 15.74 to 15.93 for $^{207}Pb/^{204}Pb$ and from 39.14 to 39.99 for $^{208}Pb/^{204}Pb$ (not shown). Values of wet and dry season samples are in good agreement, except for Negro and Xingu Rivers were the Pb isotope ratios are more radiogenic for the dry season samples (Table 14) but still within the boundaries of cluster B

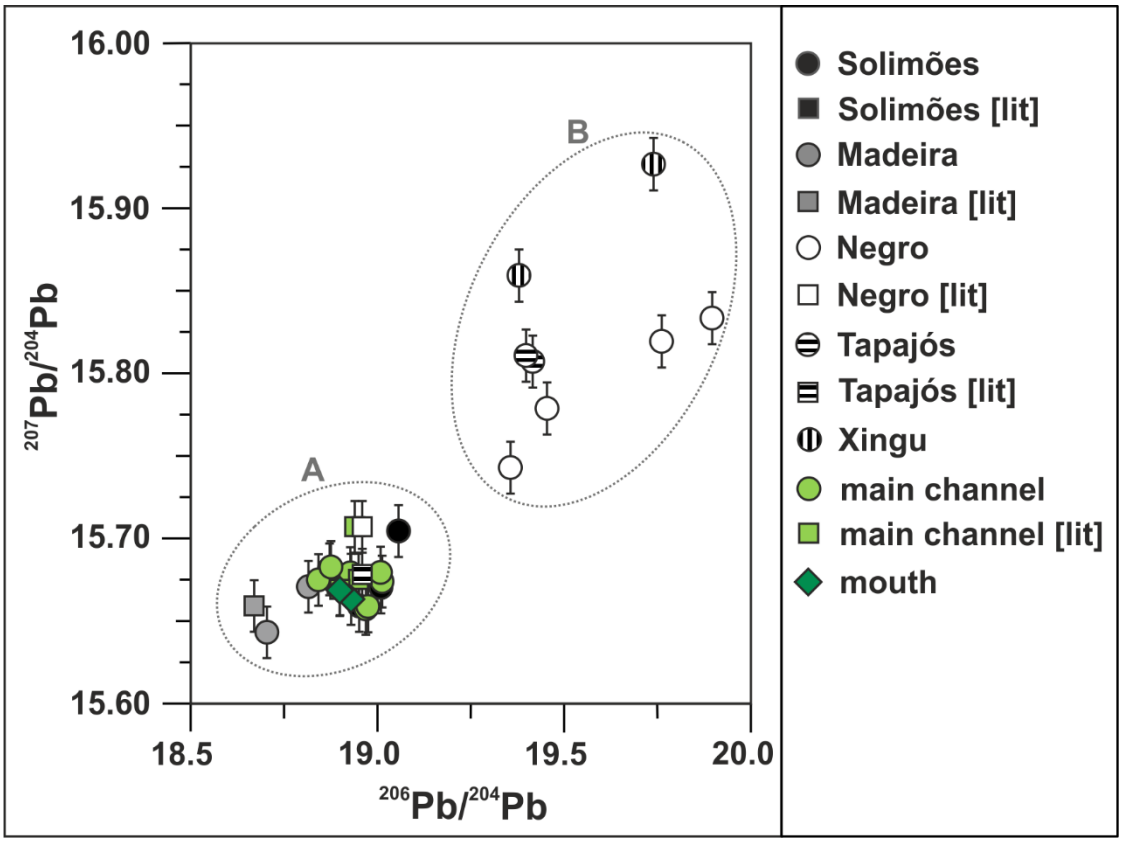

Fig. 12. $^{206}Pb/^{204}Pb$ vs. $^{207}Pb/^{204}Pb$ of river suspended particulate matter samples. The Amazon River tributaries form two clusters: [A] Madeira and Solimões Rivers and [B] Negro, Xingu and Tapajós Rivers. Samples from the Amazon River mouth and main channel plot in cluster [A]. Literature data [lit] are from Allègre et al. (1996) and marked as squares. The literature data for Negro and Tapajós Rivers plot in cluster [A].

3.5.2 Sr and Nd isotopic composition of the river SPM

The SPM samples show large ranges in $^{87}Sr/^{86}Sr$ from 0.713 to 0.770 and in ε_{Nd} from -8.7 to -24.2, with distinctive signatures for each tributary and for the Amazon River mouth and main channel (Fig. 13). The Solimões River has the least radiogenic $^{87}Sr/^{86}Sr$ (average of 0.715 ± 0.004; 2SD) and most radiogenic ε_{Nd} (average of -9.2 ± 1.0; 2SD) isotope ratios. The Madeira River has an intermediate isotope signal with an average $^{87}Sr/^{86}Sr$ of 0.734 ± 0.005 (2SD) and

an average ε_{Nd} of -12.0 ± 0.2 (2SD). The Negro, Tapajós and Xingu Rivers show, with exception of the wet season signal of the Negro River, the most radiogenic $^{87}Sr/^{86}Sr$ (average of 0.757 ± 0.020; 2SD) and least radiogenic ε_{Nd} (average of -20.6 ± 2.1; 2SD) signals. For the Negro River, the dry season signal is more radiogenic in $^{87}Sr/^{86}Sr$ (0.764 to 0.770) and less radiogenic in ε_{Nd} (-20.0 to -20.5) compared to the wet season signal ($^{87}Sr/^{86}Sr$ = 0.725 to 0.730; ε_{Nd} = -14.0 to -17.2). All other dry and wet season signals are in good agreement. The signal of the Amazon River mouth ($^{87}Sr/^{86}Sr$ = 0.720 to 0.721; ε_{Nd} = -10.4 to -10.6) and main channel ($^{87}Sr/^{86}Sr$ = 0.717 to 0.723; ε_{Nd} = -9.9 to -10.9) plot between the Solimões and Madeira Rivers values (Figs. 13 and 14).

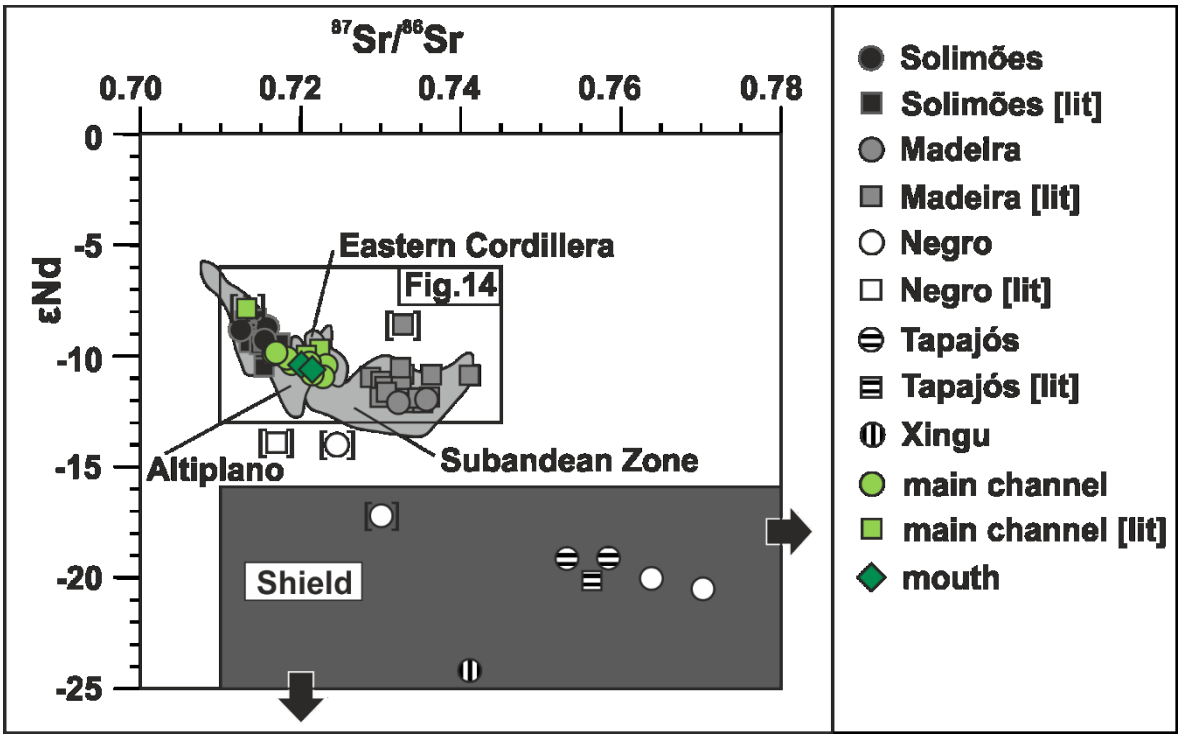

Fig. 13. $^{87}Sr/^{86}Sr$ vs. ε_{Nd} of river suspended particulate matter (SPM) samples and of the Amazon River basin source areas. The different tributaries SPM plot within their drainage basin source, outliers are marked with brackets. Literature [lit] data are marked with squares (Allègre et al., 1996; Bouchez et al., 2011 and Viers et al., 2008). The Shield composition extends beyond the figure (black arrows). Isotopic signatures of Andean sources are for the areas drained by the Amazon River basin. Literature data for the source areas are from Pinto (2003), Macambira et al. (2009), Payolla et al. (2002), da Rosa-Costa et al. (2006) and Santos et al. (2000).

3.5.3 Sr, Nd and Pb isotopic composition of marine sediment core GeoB16224-1

The $^{87}Sr/^{86}Sr$ values range between 0.721 and 0.723 from 590 to 208 cm, shifting to more radiogenic values (maximum of 0.7246 ± 0.0003; $2SD_{mean}$) until 55 cm before turning back to less radiogenic values up to 17 cm (Fig. 15, Table 15). The ε_{Nd} values are uniform (average of -11.6 ± 0.4; 2SD) from the bottom to the top of the core, interrupted by an excursion to more unradiogenic values between -12.0 and -12.7 from 261 to 88 cm (Fig. 15, Table 15). The $^{206}Pb/^{204}Pb$, $^{207}Pb/^{204}Pb$ and $^{208}Pb/^{204}Pb$ are uniform with average values of 19.07 ± 0.05 (2SD), 15.70 ± 0.04 (2SD) and 39.13 ± 0.15 (2SD) excluding five distinct peaks at 490, 377, 317, 75 and 55 cm core depth with values higher than 19.11, 15.71 and 39.18, respectively (Fig. 15, Table 15).

3.5.4 Sr, Nd and Pb isotopic composition of GeoB16212-2, GeoB16212-3, GeoB16216-3, GeoB16217-2 and GeoB16223-2

The ε_{Nd} values range from -11.0 to -11.4 for the core tops younger than 100 years and from -11.6 to -11.9 for the older core tops (8.7 to 2.6 cal ka BP) (Table 16). The Sr and Pb isotopic composition does not show such a clear division of the two sample groups. The $^{87}Sr/^{86}Sr$ varies from 0.7236 to 0.7246 for the younger samples and from 0.7206 to 0.7237 for the older samples. The lead isotope signatures for the core tops vary from 18.78 to 19.16 for $^{206}Pb/^{204}Pb$, from 15.63 to 15.69 for $^{207}Pb/^{204}Pb$ and from 38.68 to 39.17 for $^{208}Pb/^{204}Pb$.

3.6 Discussion

3.6.1 Modern Sr, Nd and Pb isotopic signatures in the Amazon River basin SPM

Viers et al. (2008) showed that the Sr and Nd isotope signals from the SPM of the Solimões and Madeira Rivers are in agreement with the isotopic composition of Andean rocks, where part of their drainage basins are located. The Sr and Nd isotope ratios for the SPM of the Solimões and the Madeira Rivers from our study corroborate these literature values (Figs. 13 and 14) (Allègre et al., 1996; Bouchez et al., 2011; Viers et al., 2008). The SPM of the Solimões River drainage basin (northern Andes, 0°N to 15°S) shows average $^{87}Sr/^{86}Sr$ values around 0.7147 ± 0.0029 (2SD) and the SPM of the Madeira River drainage basin (central Andes, 10°S to 20°S) shows average $^{87}Sr/^{86}Sr$ values around 0.7333 ± 0.0056 (2SD) (Fig. 13) (this study; Allègre et al., 1996; Bouchez et al., 2011; Viers et al., 2008). The Sr and Nd isotopic ratios for the Shield draining rivers (Negro, Xingu and Tapajós Rivers) also correspond to the source characteristics of their drainage basins (Fig. 13). The isotopic signature of the SPM of the Amazon River mouth and main channel is a mixture of SPM from all tributaries. Sediment flux studies have suggested that in the last few decades 90 to 95 % of the SPM supplied by the Amazon River into the Atlantic Ocean originates from the Andes, almost equally distributed between the Solimões and Madeira Rivers (Meade et al., 1985; Meade, 1994). In our study, the Sr and Nd isotope ratios for the SPM from the mouth and main channel of the Amazon River plot on a mixing curve between the Solimões and Madeira Rivers isotope values (Fig.

14). We calculated binary mixing models with the two main SPM suppliers of the Amazon River as endmembers, using a maximum, minimum and mean value of Sr and Nd isotopic composition and content (Table 17). With this compositional variability, the Solimões River supplies ~55 to 60 % of SPM and the Madeira River supplies ~35 to 40 % (Fig. 14). Previously published studies show that the Shield draining rivers (e.g. Negro River) have a small share in the sediment supply (Meade et al., 1985; Meade, 1994).

Table 17 Endmembers for the mixing model calculation based on the Sr and Nd isotopic compositions and concentrations from SPM samples of the Solimões and Madeira Rivers.

	Endmember	$^{87}Sr/^{86}Sr$	Sr [µg/g]	$^{143}Nd/^{144}Nd$	ε_{Nd}	Nd [µg/g]	Reference
min	Madeira	0.741082	83	0.512081	-10.9	22	[4]
min	Solimões	0.714477	177	0.512210	-8.4	36	[3]
mean	Madeira	0.732712	134	0.512036	-11.8	53	[1 – 4]
mean	Solimões	0.714544	193	0.512171	-9.1	44	[1 – 4]
max	Madeira	0.732227	127	0.512018	-12.1	47	[1]
max	Solimões	0.715431	157	0.512101	-10.5	38	[3]

[1]: this study; [2]: Allègre et al., 1996; [3]: Bouchez et al., 2011; [4]: Viers et al., 2008

According to our endmember model the total 1.1 to 1.3 x 10^9 T/yr of SPM (Meade et al., 1985) supplied by the Amazon River to the Atlantic Ocean would split to roughly 7 x 10^8 T/yr for the Solimões River, 4.7 x 10^8 T/yr for the Madeira River. This further confirms that the modern SPM supplied to the Atlantic Ocean largely originates in the Andes with minor influence from the Amazon Shield draining rivers.

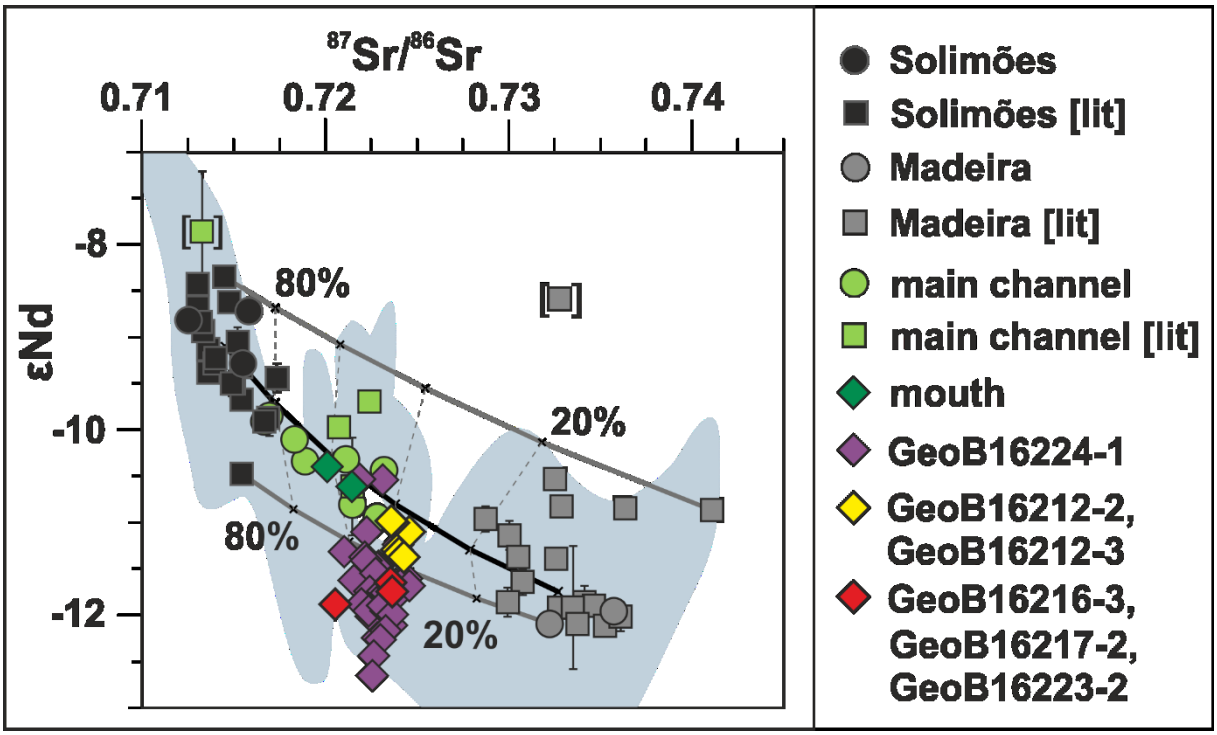

Fig. 14. Mixing curve based on Sr and Nd concentrations and isotopic ratios from suspended particulate matter (SPM) of the Solimões and Madeira Rivers. Sr and Nd isotopic signatures of Solimões and Madeira Rivers and Amazon River mouth and main channel, core GeoB16224-1 and the core tops GeoB16212-2, GeoB16212-3 (young) and GeoB16216-3, GeoB16217-2 and GeoB16223-2 (old). Grey lines show mixing of the respective maximum (upper line) and minimum mixing (lower line) endmembers (Table 17). The thick black line shows mixing of the mean endmember values. The Amazon River mouth and main channel samples plot on the mean mixing line between Solimões and Madeira Rivers SPM. Circles indicate our Sr and Nd isotopic values, squares indicate literature [lit] values (Allègre et al., 1996; Bouchez et al., 2011; Viers et al., 2008) and outlier are marked with brackets. The shaded blue area represents the isotopic signature of the northern and central Andes drained by the Amazon River basin (Pinto, 2003). The samples from marine sediment core GeoB16224-1 plot close to the values from samples of the Amazon River mouth and main channel, but with a shift to less radiogenic ε_{Nd} values.

Sr, Nd and Pb isotopic signatures of the Negro River SPM vary strongly between the wet and dry seasons (Table 14). The wet season samples have a less radiogenic Sr and Pb and more radiogenic Nd signature than the dry season samples. A change in the source region of the Negro River can be ruled out. We explain the wet season shift by a strong backflow of Solimões River SPM up the Negro River channel (Meade et al., 1991). The rainy season in the Solimões River basin starts earlier than in the Negro River basin (Garreaud et al., 2009). Therefore, the Solimões River transports higher volumes of water during this time, which leads to a water pressure imbalance at the confluence between the Solimões and Negro Rivers and the Solimões River, as a whitewater river, carries distinctively more sediment than the Negro River. The samples from the Negro River were taken ca. 50 km upstream the confluence with the Solimões River and are probably influenced by material from the Solimões River during the wet season. A similar situation was described for the confluence between the Amazon River

main channel and the Xingu River (Häggi et al., 2016) as well as for the Tapajós River (Freitas et al., 2017).

3.6.2 Changes in sediment supply during the last 40 kyr

The age model for marine sediment core GeoB16224-1 (Häggi et al., 2017) is well defined for the lower part of the core (i.e. 600 to 66 cm). The upper part of the core (65 to 0 cm) is gradually younger than the sediment below, but a hiatus cannot be excluded. Therefore, the ages shown for the ten samples in the upper part of the core should be treated with caution. Furthermore, we did not plot the Nd data from Zhang et al. (2015) for core GeoB16224-1 into Fig. 6. In contrast to our samples, they were not washed, not decarbonated and not sieved, which can cause a small bias on the isotope composition. The variation of ε_{Nd} in both data sets is small. Despite the similar average GeoB16224-1 ε_{Nd} values of -11.5 ± 0.6 (2SD) from Zhang et al. (2015) and -11.7 ± 0.9 (2SD) from this study, we restrict the interpretation to our ε_{Nd} data from silicate detrital material in order to avoid any ambiguities from different sample treatment.

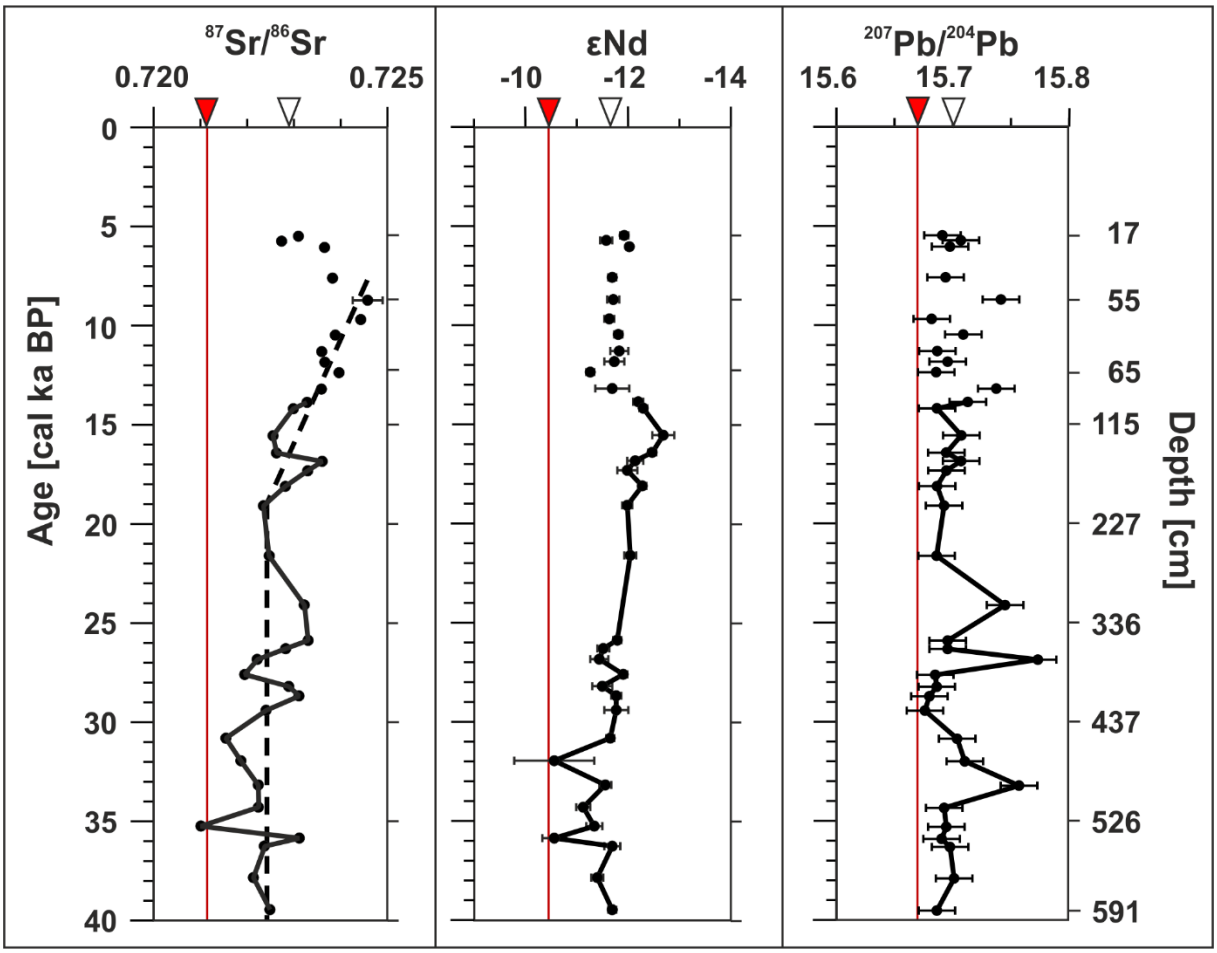

Fig. 15. Down-core changes in $^{87}Sr/^{86}Sr$, ε_{Nd} and $^{207}Pb/^{204}Pb$ of marine sediment core GeoB16224-1. The red triangles and lines mark the modern average Amazon River mouth signal (this study). The white triangles mark the average value for the entire sediment core. The dashed line is used to highlight a dominant shift in the $^{87}Sr/^{86}Sr$ down-core record. Data points connected by a solid black line represent the section of the core with a reliable age model.

3.6.2.1 Sr isotope signal

The $^{87}Sr/^{86}Sr$ signal scatters around 0.7224 ± 0.0012 (2SD) from 40 to 19 cal ka BP and rises to more radiogenic values (up to 0.725) from 19 to 9 cal ka BP (Fig. 15). Around 8 cal ka BP the signal shifts back to less radiogenic (< 0.724) values. We consider the observed shift as a change in the provenance of the material, caused by a supply change between the central and northern Andes during asynchronous deglaciation of the two sectors. The deglaciation of the northern sector of the Andes started at the earliest around 17 cal ka BP (7°S, Bush et al., 2005) corroborated by ages between 16 to 14 cal ka BP from Peru and Ecuador (7°S, Bush et al., 2005; 14°S, Mercer and Palacios, 1977; 13°S, Valencia et al., 2010) and at the latest around 12 cal ka BP (7-8 °S, Birkeland et al., 1989; 11°S, Wright, 1983). In contrast, the deglaciation of the central (16°S to 18°S) sector of the Andes started already around 21 to 19 cal ka BP (Bush et al., 2011 and references therein). The deglaciation led to new areas being exposed to erosion and an increase in meltwater and SPM supply to the Amazon River. As the deglaciation started in the Madeira River drainage basin, the supply of more radiogenic $^{87}Sr/^{86}Sr$ increases (Figs. 14 and 15). The shift back to less radiogenic Sr values (towards the modern Amazon River mouth Sr isotopic values) starts around 8 cal ka BP (Fig. 15) and could be due to the proposed intensification in precipitation of the Amazon River basin during the mid to late Holocene (Cheng et al., 2013). During the Holocene the morphology of the Andes was already very similar to its modern one (Hartley, 2003). The northern Andes are characterized by a narrow mountain range with steep slopes and high precipitation leads to high denudation rates (Wittmann et al., 2011). The central part of the Andes is much wider with the denudation focused in the large river valleys of the Madeira River drainage basin (Montgomery et al., 2001). More precipitation in the Andes leads to higher supply of material from the northern sector and the signal shifts back to less radiogenic $^{87}Sr/^{86}Sr$ values in SPM. This shift in the Sr signature attributed to a deglaciation-based change in provenance between the northern and central Andes is not observed in the Nd and Pb records (Fig. 15). The decoupled signal is likely controlled by the input of (old) micas, known to have markedly radiogenic Sr isotopic signatures (Dickin, 2005) but low Nd and Pb contents (Bea, 1996; White, 2015), hence, little influence on the isotopic composition of Nd and Pb. Micas are one of the main minerals of the Amazon River SPM originating predominantly from the Andean draining rivers (Gibbs, 1967). Additionally, micas are relatively resistant to chemical weathering (Goldich, 1938). This makes them a probable source for the decoupled shift in the Sr signature observed in core GeoB16224-1. Nevertheless, for a definite clarification additional data is needed.

3.6.2.2 Nd isotope signal

The ε_{Nd} signal of GeoB16224-1 is quite uniform (Fig. 15) and only shows one small excursion to less radiogenic values between 17 to 14 cal ka BP. This age range coincides with the age

(ca. 18.1 to 14.7 cal ka BP; Sarnthein et al., 2001; Stríkis et al., 2015) of Heinrich Stadial 1 (HS1). The Amazon River basin experienced higher precipitation rates during HS1 (Zhang et al., 2016 and references therein). Interestingly the shift in ε_{Nd} values does not occur at the very beginning, but rather during a second phase of HS1. Since Andean stalagmite $\delta^{18}O$ records indicate an increase in precipitation at the very beginning of HS1 (Cheng et al., 2013; Kanner et al., 2012), the delayed response in ε_{Nd} suggests a change in the main location of precipitation towards the lowlands (Shield areas) within HS1. This would shift the ε_{Nd} signal to less radiogenic values, as observed in core GeoB16224-1 (Fig. 15). This shift might not appear in the Sr isotopic signal, since the Shield areas and the Andes overlap in their Sr isotopic values (Fig. 13). Additionally, the observed shift in the Sr isotopic signature attributed to a deglaciation-based provenance shift in the Andes between 19 to 9 cal ka BP (section 3.6.2.1) might have overprinted a matching change in the Sr isotopes during the second phase of HS1. Another possibility for this small excursion could be related to changes in sea level from -130 m during the Last Glacial Maximum (LGM) to -90 m at about 14 cal ka BP (Lambeck and Chappell, 2001), leading to the exposure of most of the continental shelf. During times of extreme sea level low stand, part of the Amazon River SPM was directly channeled into the deep sea not reaching our core site (Milliman et al., 1975). Furthermore, the French Guiana rivers discharged more SPM with an average ε_{Nd} value of -19.6 to the continental margin during this period (Pujos et al., 1990). Combined with less material from the Amazon River, this could also be responsible for the small shift in the ε_{Nd} down-core record of GeoB16224-1. However, we do not favor this hypothesis because under lowest sea level (i.e. LGM) a maximum shift in the ε_{Nd} data should be expected and this is not the case.

3.6.2.3 Pb isotope signal

The Pb isotope signal is rather uniform throughout core GeoB16224-1. An exception are five localized peaks with values >15.71 for $^{207}Pb/^{204}Pb$ (Fig. 15) and uniform $^{206}Pb/^{204}Pb$ values pointing to an old high μ component ($\mu = {}^{238}U/^{204}Pb$), typical of old continental crustal rocks, i.e. from the Shield areas (Mattinson, 1990). The $^{207}Pb/^{204}Pb$ peaks are not visible neither in the Sr nor the Nd isotope systems. McDaniel et al. (1997) also found more radiogenic Pb signatures of 15.71 ± 0.03 (2SD) for $^{207}Pb/^{204}Pb$ (larger cratonic contribution) in Amazon fan mud sediments with a decoupled Nd signature of -10.4 ± 1.0 (2SD) (more Andean contribution). The reason behind this decoupling is not yet understood. We propose a nugget effect, caused by minerals rich in Pb with no Sr or Nd such as galena. Nevertheless, the Pb signal shows that the Shield draining rivers indeed have some influence on the final SPM delivered by the Amazon River to the Atlantic Ocean.

3.6.3 Modern Amazon River SPM and the offset to GeoB16224-1

The modern isotope signal from the mouth and main channel of the Amazon River is less radiogenic in Sr and Pb and more radiogenic in Nd than the material from core GeoB16224-1

(Fig. 15). About 90 % of the core samples plot outside the modern mixing curve between Solimões and Madeira Rivers (Fig. 14). To identify the cause for this isotopic offset between the modern Amazon River SPM and sediments from core GeoB16224-1, we analyzed core tops, with different Holocene ages (Fig. 16), along the transport path of the Amazon River SPM from its mouth to the GeoB16224-1 site (Fig. 11). The core tops are divided in two groups, based on age, location and isotope composition: the younger ones are located closer to the Amazon River submarine delta with isotopic signatures plotting on the Andean mixing array, while the older core tops have similar isotopic signatures to core GeoB16224-1 (Figs. 14 and 16).

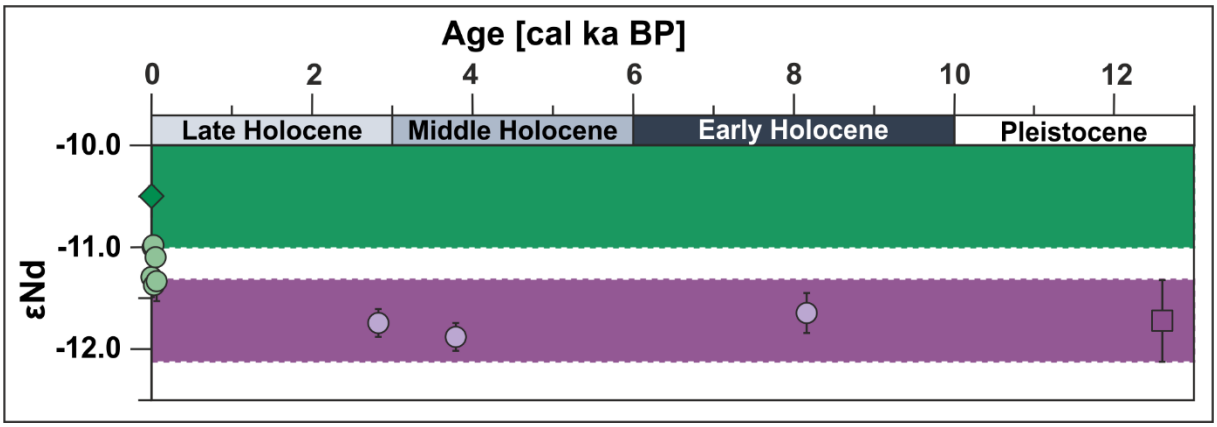

Fig. 16. ε_{Nd} values vs. the age of core tops along the Amazon River suspended particulate matter (SPM) transport path in the Atlantic Ocean. The modern average ε_{Nd} signal of the Amazon River SPM is marked with the dark green diamond and the shaded green bar. The average ε_{Nd} signature of marine sediment core GeoB16224-1 is marked with the dark purple square, plotted at 12.6 cal ka BP (the youngest data point with a reliable age), and the shaded purple bar. The light purple circles represent cores (GeoB16216-3, 16217-2, 16223-2) raised close to GeoB16224-1. The light green circles represent cores GeoB16212-2/-3 raised close to the Amazon River mouth. For the location of the cores see Fig. 11 and Table 12.

A possible cause for the isotopic offsett is a basin internal shift in the Amazon River SPM provenance from Shield signatures (core GeoB16224-1 and older core tops) to a more Andean dominated signature (younger core tops and modern SPM) (Fig. 17). Another possibility could be the deposition of external sources, unrelated to the Amazon River as windblown dust or other rivers, draining the continent with unradiogenic ε_{Nd}, at the GeoB16224-1 core site (Fig. 18B). The distance between the Amazon River mouth and the GeoB16224-1 core location can be excluded as a cause for the isotopic offset, since Nd isotopes are not significantly altered by transport and deposition processes (Miller et al., 2015).

3.6.4 Basin internal shift

The difference between the modern and past isotope signatures can be explained by changing the relative contribution of Andean and Shield SPM to the Amazon River SPM (Fig. 17). The ages of the core tops constrain the time window for the change to modern SPM compositions.

The youngest core top with an ε_{Nd} close to the average ε_{Nd} of GeoB16244-1 is 2.8 cal ka BP (Fig. 16) and provides a maximum age limit for the change to modern values characterized by higher relative input of Andean derived SPM.

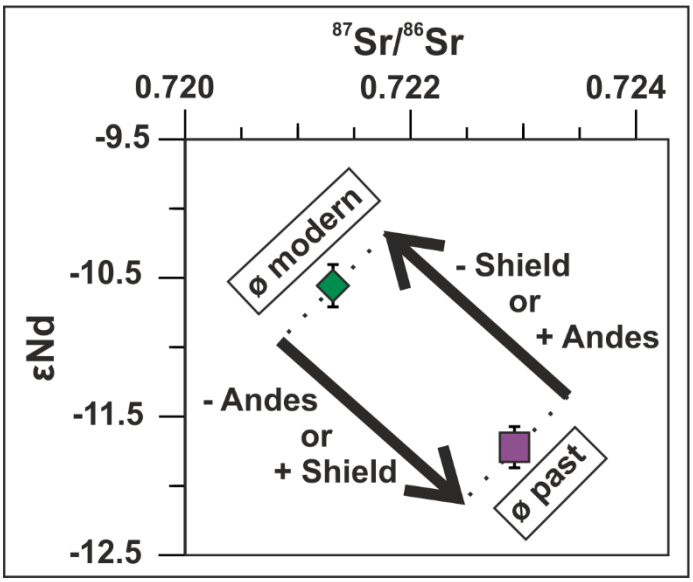

Fig. 17. $^{87}Sr/^{86}Sr$ vs. ε_{Nd} for marine sediment core GeoB16224-1 (purple square) and the modern Amazon River suspended particulate matter (green diamond) signals, illustrating how internal changes to the Amazon River basin (Andean vs. Shield sediment supply) may have shifted the signal.

Indeed, a decrease in precipitation over the eastern sector (Prado et al., 2013; Wang et al., 2017) and an increase over the western sector (Cheng et al., 2013; Govin et al., 2014) of the Amazon River basin occurred from the mid to the late Holocene. Moreover, the last 2.3 kyr were described as the wettest period of the whole Holocene over the Peruvian Andes (Abbot et al., 2003). Physical weathering rates and sediment transport in the Andes increased due to the stronger precipitation compared to the Shield areas. This would lead to a higher sediment supply from the Andes during the late Holocene. Having the less radiogenic Sr and Pb and more radiogenic Nd isotope signatures, the increased SPM supply from the Andes could produce the observed shift in the isotopic signals (Fig. 17).

The younger core tops (with estimated ages of younger than one hundred years) show a shift towards higher Andean input, plot on the Andean mixing array and on the modern Solimões and Madeira Rivers mixing curve. However, they do not have the modern proportion of Solimões and Madeira Rivers input (60:40), but a stronger Madeira River influenced signature (Fig. 14). Therefore, a very recent shift from a Madeira River to a Solimões River influenced SPM signature happened, produced by higher (lower) input from Solimões River (Madeira River) SPM. A possible cause therefore could be a change in SPM input due to dam building. Large dams (for hydroelectric power plants) have been built in the Amazon River basin during the last century, mostly in the southern portion of the basin (Tapajós, Xingu and Madeira River

drainage basins) (Lees et al., 2016). Dams act as a barrier for the SPM transported by the rivers and change the natural balance of the sediment fluxes (Latrubesse et al., 2017). Therefore, the modern SPM has a more Solimões River influenced signal due to a partial blockage of the Madeira River SPM after the dam building. The core tops, being presumably older than the dam building, show a modern unblocked signal.

3.6.5 Possible sediment sources for the Nd shift besides the Amazon River basin

To explain the offset four potential sources for non-Amazonian sediment supply could be considered: rivers from French Guiana (Fig. 18b), the Tocantins River (Fig. 18c) and the Parnaíba River from NE Brazil (Fig. 18d) as well as windblown Saharan dust (Fig. 18e).

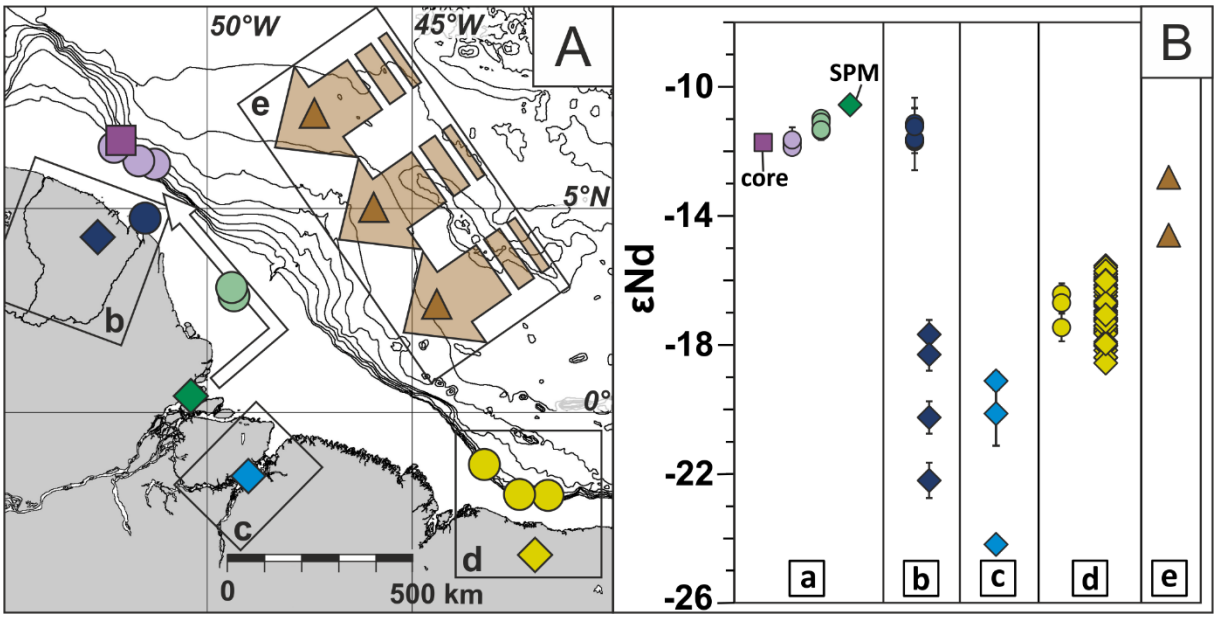

Fig. 18. Panel A: Location of the Amazon River mouth (green diamond), marine sediment core GeoB16224-1 (purple square) and core tops (purple and green circles) along the suspended particulate matter (SPM) transport path from the Amazon River mouth to core site GeoB16224-1. Four additional sources of Nd are marked: (b) estimated French Guiana fluvial input (dark blue diamond) (Allègre et al., 1996) and shelf core tops (blue circle) (Parra and Pujos, 1998); (c) estimated Tocantins River fluvial input (light blue diamond) (this study; Allègre et al., 1996); (d) Parnaíba River fluvial input (yellow diamond) and shelf core tops (yellow circles) (Zhang et al., 2015); (e) Saharan aeolian dust input (brown triangles) (Grousset et al., 1998). Panel B: ε_{Nd} values of the samples shown in panel A. Column (a): modern Amazon River SPM, GeoB16224-1 and core tops; column (b): estimated French Guiana river sediment and shelf core tops (Allègre et al., 1996; Parra and Pujos, 1998); column (c): estimated Tocantins SPM (this study; Allègre et al., 1996); column (d): Parnaíba River SPM and slope core tops (Zhang et al., 2015); column (e): Saharan aeolian dust (Grousset et al., 1998).

All three river systems have modern SPM fluxes into the Atlantic Ocean in the order of 1.7 to 3.1 x 10^6 T/yr (Table 18; da Silva et al., 2015; Prost and Lointier, 1988; Werneck Lima et al., 2003), much smaller than the 1.5 x 10^8 T/yr SPM transported northward from the Amazon River (Eisma et al., 1991). The distance of their river mouths to the GeoB16224-1 core site varies from 250 km (French Guiana rivers) to 1500 km (Parnaíba River) (Fig. 18A). Their ε_{Nd}

isotopic signatures are less radiogenic than the modern Amazon River SPM (Fig. 18B). The Parnaíba River has values between -15.6 and -18.6 (Zhang et al., 2015). Values from Tocantins River and the French Guiana rivers that drain directly into the Atlantic Ocean are not available, but the rivers sample material from the Brazilian (Guyot et al., 2007) and Guiana Shield (Gibbs and Barron, 1993), respectively. Hence, the ε_{Nd} isotopic signature for the Tocantins River is approximately -21 and estimated using the Brazilian Shield rivers (this study; Allègre et al., 1996; supplementary data table S2), and for the French Guiana rivers is approximately -20 using Guiana Shield values from Parra and Pujos (1998) and Guiana Shield draining river data from Allègre et al. (1996) (Supplementary data table S2). These ε_{Nd} signals could theoretically shift the modern Amazon River SPM ε_{Nd} signal to less radiogenic values, as observed in the samples from core GeoB16224-1. However, late Holocene sediments deposited on the French Guiana shelf have a much more radiogenic ε_{Nd} value (-9.0 to -11.5) than the estimated SPM from the French Guiana rivers (Parra and Pujos, 1998; Zhang et al., 2015). The shelf sediments off French Guiana mainly originate from the Amazon River (Andes and Shield areas) (Parra and Pujos, 1998). Core top ε_{Nd} values (-16.4 to -17.5) and Nd concentrations (average 10.2 µg/g) from the slope northwestward of the Parnaíba River mouth, show that the Parnaíba River SPM gets transported along the continental margin being deposited along the way (Zhang et al., 2015). However, similar to the Tocantins River, due to their location to the southeast of the Amazon River mouth (Fig. 18A), a stronger influence is expected at the core tops near the Amazon River mouth than at core GeoB16224-1 site, which is not the case. Additionally, we performed a simplified mixing calculation (Table 18) to estimate the minimum SPM supply for each river to produce the observed offset. Assuming that all the SPM supplied by the respective rivers gets transported and deposited at the GeoB16224-1 core site without sedimentation along the way, all three rivers would have to have supplied at least 5 times more SPM than their modern supply. Hence, we exclude the Tocantins River, the Parnaíba River and the French Guiana rivers SPM as a source for the offset between the GeoB16224-1 sediment and the modern Amazon River SPM ε_{Nd} signals. Deposition of material from these sources at the GeoB16224-1 core site, is still probable but will be of negligible influence in comparison to the Amazon River SPM.

Table 18 Endmembers for the mixing model calculations based on the Nd isotopic composition and concentration and suspended particulate matter (SPM) supply amount of the Amazon, Tocantins, Parnaíba and French Guiana Rivers. The displayed values for the Nd signature and concentrations are calculated averages. For individual values used for the calculation see supplementary data table S2.

Endmember	SPM supply amount [T/yr]	ε_{Nd} ± 2SD	Nd [µg/g]
Amazon River	1.5 x 10^8 [2]	-10.5 ± 0.5 [1]	26 [1]
French Guiana rivers	1.7 x 10^6 [3]	-19.6 ± 4.1 [7,9]	38 [8]
Tocantins River	3.06 x 10^6 [4]	-20.6 ± 4.8 [1,7]	38 [1]
Parnaíba River	2.54 x 10^6 [5]	-16.9 ± 1.7 [6]	43 [6]
GeoB16224-1	-	-11.7 ± 0.9 [1]	28 [1]

[1]: this study; [2]: Eisma et al., 1991; [3]: Prost and Lointier, 1988; [4]: Werneck Lima et al., 2003; [5]: da Silva et al., 2015; [6]: Zhang et al., 2016; [7]: Allègre et al., 1996; [8]: Gaillardet et al., 1997; [9]: Parra and Pujos, 1998

Saharan dust is transported through wind systems westward over the Atlantic Ocean reaching, among other locations, northeastern South America and the Amazon River basin (Fig. 18A) (Prospero et al.,1981; Swap et al., 1992). The annual estimation of transported dust varies two orders of magnitude from 1.3 x 10^7 T/yr (Swap et al., 1992), through 2.5 to 3.4 x 10^7 T/yr (Prospero and Carlson, 1972) up to 1 to 4 x 10^9 T/yr (Prospero et al., 1981). The ε_{Nd} signature of Saharan dust varies from -12.8 to -14.6 and the average Nd concentration ranges from 20 to 30 µg/g (Grousset et al., 1998), being theoretically sufficient to create the observed offset between modern Amazon River SPM and core GeoB16224-1. However, the average North African dust has less radiogenic Sr (Abouchami et al., 2013; Kumar et al., 2014; Skonieczny et al., 2013) and Pb isotopic signatures (Kumar et al., 2014) than the modern Amazon River SPM. An addition of these dust particles would, therefore, shift the Sr and Pb isotopic signature to less radiogenic values, the opposite direction than the observed offset in core GeoB16224-1. As such, the Saharan dust can be excluded for a driver for the observed offset between GeoB16224-1 sediment and the modern Amazon River SPM ε_{Nd} signal.

3.7 Conclusions

We investigated the modern and last 40 kyr supply of Amazon River SPM to the Atlantic Ocean. The radiogenic (Sr, Nd and Pb) isotope SPM signature can be used to distinguish between the two main SPM sources within the Amazon River basin (i.e. Andes vs. Shield). The Andes, compared to the Shield areas, have less radiogenic Sr and Pb and more radiogenic Nd isotope signatures. The ε_{Nd} data of our down-core record document, besides the generally increased precipitation that occurred over the Amazon River basin during HS1, a shift of the precipitation locus from the Andes to the lowlands (Shield areas). Furthermore, marine sediment core GeoB16224-1 covers the last 40 kyr of the Amazon River basin sediment discharge and shows an offset from the modern Amazon River SPM isotopic signature. We

showed that the offset was not produced by external influences, but by a basin internal change of the Amazon River SPM signal. The change in the supply occurred at some point during the late Holocene. This led to a change in the isotopic signal of the river SPM to a more Andean dominated signal (more radiogenic in Nd and less radiogenic in Sr and Pb). We suggest that an increase in precipitation over the western and/or a decrease in the eastern Amazon River basin during the late Holocene increased erosion rates in the Andes and produced the offset. Further, we propose that the shift towards a more Andean dominated signal in the late Holocene was divided into two parts. First the Madeira River SPM dominated the Amazon River SPM and finally the Solimões River SPM dominated the Amazon River SPM.

To further elucidate the late Holocene offset in the Amazon River SPM isotopic signature, additional radiogenic isotope analyses of well-dated late Holocene marine sediment cores raised in the Amazon River continental margin are necessary. It would be particularly important to identify the exact timing of the observed shift.

3.8 Acknowledgments

This work was funded through the DFG-Research Center/Cluster of Excellence “The Ocean in the Earth System” at MARUM – Center for Environmental Sciences, University of Bremen. We thank the RV Maria S. Merian cruise MSM20/3 crew. Sample material has been provided by the GeoB Core Repository at the MARUM – Center for Marine Environmental Sciences, University of Bremen, Germany. The data reported in this paper are archived in Pangaea (www.pangaea.de). NH thanks GLOMAR – Bremen International Graduate School for Marine Sciences for support. CMC acknowledges the financial support from FAPESP (grant 2012/17517-3), CAPES (grant 564/2015), and CNPg (grant 302607/2016 and 422255/2016-5). AOS is supported by CNPg (grant 309223/2014-8). The sampling of sediments in the Amazon Rivers was supported by FAPESP grant 2011/06609-1.

3.9 References

Abbott, M.B., Wolfe, B.B., Wolfe, A.P., Seltzer, G.O., Aravena, R., Mark, B.G., Polissar, P.J., Rodbell, D.T., Rowe, H.D., Vuille, M. (2003). Holocene paleohydrology and glacial history of the central Andes using multiproxy lake sediment studies. *Palaeogeography, Palaeoclimatology, Palaeoecology*, **194(1)**, 123-138.

Abouchami, W., Näthe, K., Kumar, A., Galer, S.J., Jochum, K.P., Williams, E., Horbe, A.M.C., Rosa, J.W.C., William, B., Adams, D., Mezger, K., Andreae, M.O. (2013). Geochemical and isotopic characterization of the Bodélé Depression dust source and implications for transatlantic dust transport to the Amazon Basin. *Earth and Planetary Science Letters*, **380**, 112-123.

Allègre, C.J., Dupré, B., Négrel, P., Gaillardet, J. (1996). Sr-Nd-Pb isotope systematics in Amazon and Congo River systems: constraints about erosion processes. *Chemical Geology*, **131(1-4)**, 93-112.

Bea, F. (1996). Residence of REE, Y, Th and U in granites and crustal protoliths; implications for the chemistry of crustal melts. *Journal of petrology*, **37(3)**, 521-552.

Bentahila, Y., Othman, D.B., Luck, J.M. (2008). Strontium, lead and zinc isotopes in marine cores as tracers of sedimentary provenance: A case study around Taiwan orogen. *Chemical Geology*, **248(1)**, 62-82.

Birkeland, P.W., Rodbell, D.T., Short, S.K. (1989). Radiocarbon dates on deglaciation, Cordillera central, northern Peruvian Andes. *Quaternary Research*, **32(1)**, 111-113.

Blaauw, M., Christen, J.A. (2011) Flexible Paleoclimate Age-Depth Models Using an Autoregressive Gamma Process. *Bayesian Analysis*, **6**, 457-474

Bouchez, J., Gaillardet, J., France-Lanord, C., Maurice, L., Dutra-Maia, P. (2011). Grain size control of river suspended sediment geochemistry: Clues from Amazon River depth profiles. *Geochemistry, Geophysics, Geosystems*, **12(3).**

Bush, M.B., Hansen, B.C.S., Rodbell, D.T., Seltzer, G.O., Young, K.R., León, B., Abbott, M. B., Silman, M.R., Gosling, W.D. (2005). A 17 000-year history of Andean climate and vegetation change from Laguna de Chochos, Peru. *Journal of Quaternary Science*, **20(7-8)**, 703-714.

Bush, M.B., Hanselman, J.A., Hooghiemstra, H. (2011). Andean montane forests and climate change. In Tropical rainforest responses to climatic change (pp. 35-60). Springer Berlin Heidelberg.

Cheng, H., Sinha, A., Cruz, F.W., Wang, X., Edwards, R.L., d'Horta, F.M., Ribas, C.C., Vuille, M., Stott, L.D., Auler, A.S. (2013). Climate change patterns in Amazonia and biodiversity. *Nature communications*, **4**, 1411.

da Rosa-Costa, L.T., Lafon, J.M., Delor, C. (2006). Zircon geochronology and Sm–Nd isotopic study: further constraints for the Archean and Paleoproterozoic geodynamical evolution of the southeastern Guiana Shield, north of Amazonian Craton, Brazil. *Gondwana Research*, **10(3)**, 277-300.

da Silva, A.G.A., Amaro, V.E., Stattegger, K., Schwarzer, K., Vital, H., Heise, B. (2015). Spectral calibration of CBERS 2B multispectral satellite images to assess suspended sediment concentration. *ISPRS Journal of Photogrammetry and Remote Sensing*, **104**, 53-62.

Deniel, C., Pin, C. (2001). Single-stage method for the simultaneous isolation of lead and strontium from silicate samples for isotopic measurements. *Analytica Chimica Acta*, **426(1)**, 95-103.

Dickin, A. P. (2005). Radiogenic Isotope Geology. Cambridge University Press, New York, 492p.

Dino, R., Soares, E.A.A., Antonioli, L., Riccomini, C., Nogueira, A.C.R. (2012). Palynostratigraphy and sedimentary facies of Middle Miocene fluvial deposits of the Amazonas Basin, Brazil. *Journal of South American Earth Sciences*, **34**, 61-80.

Duce, R. A., Liss, P. S., Merrill, J. T., Atlas, E. L., Buat-Menard, P., Hicks, B. B., Miller, J. M., Prospero, J. M., Arimoto, R., Church, T. M., Ellis, W., Galloway, J. N., Hansen, L., Jickells, T. D., Knap, A. H., Reinhardt, K. H., Schneider, B., Soudine, A., Tokos, J. J., Tsunogai, S., Wollast, R., Zhou, M. (1991). The atmospheric input of trace species to the world ocean. *Global biogeochemical cycles*, **5(3)**, 193-259.

Eisma, D., Augustinus, P.G.E.F., Alexander, C. (1991). Recent and subrecent changes in the dispersal of Amazon mud. *Netherlands Journal of Sea Research*, **28(3)**, 181-192.

Filizola, N., Guyot, J.L. (2004). The use of Doppler technology for suspended sediment discharge determination in the River Amazon/L'utilisation des techniques Doppler pour la détermination du transport solide de l'Amazone. *Hydrological Sciences Journal*, **49(1)**, 143-153.

Freitas, P.T.A., Asp, N.E., Souza-Filho, P.W.M., Nittrouer, C.A., Ogston, A.S., Silva, M.S. (2017). Tidal influence on the hydrodynamics and sediment entrapment in a major Amazon River tributary - Lower Tapajós River. *Journal of South American Earth Sciences*, **79**, 189-201.

Gaillardet, J., Dupre, B., Allègre, C. J., Négrel, P. (1997). Chemical and physical denudation in the Amazon River Basin. *Chemical geology*, **142(3-4)**, 141-173.

Garreaud, R.D., Vuille, M., Compagnucci, R., Marengo, J. (2009). Present-day south american climate. *Palaeogeography, Palaeoclimatology, Palaeoecology*, **281(3)**, 180-195.

Gibbs, R.J. (1967). The geochemistry of the Amazon River system: Part I. The factors that control the salinity and the composition and concentration of the suspended solids. *Geological Society of America Bulletin*, **78(10)**, 1203-1232.

Gibbs, R.J., Konwar, L. (1986). Coagulation and settling of Amazon River suspended sediment. *Continental Shelf Research*, **6(1-2)**, 127-149.

Gibbs, A.K., Barron, C.N. (1993) The Geology of the Guiana Shield, Oxford University Press, New York, 246p.

Goldich, S. S. (1938). A study in rock-weathering. *The Journal of Geology*, **46(1)**, 17-58.

Govin, A., Chiessi, C.M., Zabel, M., Sawakuchi, A.O., Heslop, D., Hörner, T., Zhang, Y., Mulitza, S. (2014). Terrigenous input off northern South America driven by changes in Amazonian climate and the North Brazil Current retroflection during the last 250 ka. *Climate of the Past*, **10(2)**, 843-862.

Grousset, F.E., Parra, M., Bory, A., Martinez, P., Bertrand, P., Shimmield, G., Ellam, R.M. (1998). Saharan wind regimes traced by the Sr–Nd isotopic composition of subtropical Atlantic sediments: last glacial maximum vs today. *Quaternary Science Reviews*, **17(4)**, 395-409.

Gutjahr, M., Frank, M., Stirling, C.H., Klemm, V., Van de Flierdt, T., Halliday, A.N. (2007). Reliable extraction of a deepwater trace metal isotope signal from Fe–Mn oxyhydroxide coatings of marine sediments. *Chemical Geology*, **242(3)**, 351-370.

Guyot, J.L., Jouanneau, J.M., Soares, L., Boaventura, G.R., Maillet, N., Lagane, C. (2007). Clay mineral composition of river sediments in the Amazon Basin. *Catena*, **71(2)**, 340-356.

Häggi, C., Sawakuchi, A.O., Chiessi, C.M., Mulitza, S., Mollenhauer, G., Sawakuchi, H.O., Baker, P.A., Zabel, M., Schefuß, E. (2016). Origin, transport and deposition of leaf-wax biomarkers in the Amazon Basin and the adjacent Atlantic. *Geochimica et Cosmochimica Acta*, **192**, 149-165.

Häggi, C., Chiessi, C. M., Merkel, U., Mulitza, S., Prange, M., Schulz, M., Schefuß, E. (2017). Response of the Amazon rainforest to late Pleistocene climate variability. *Earth and Planetary Science Letters*, **479**, 50-59.

Hallet, B., Hunter, L., Bogen, J. (1996). Rates of erosion and sediment evacuation by glaciers: A review of field data and their implications. *Global and Planetary Change*, **12(1-4)**, 213-235.

Hartley, A. (2003). Andean uplift and climate change. *Journal of the Geological Society*, **160(1)**, 7-10

Horbe, A.M.C., da Trindade, I.R., Dantas, E.L., Santos, R.V., Roddaz, M. (2014). Provenance of quaternary and modern alluvial deposits of the Amazonian floodplain (Brazil) inferred from major and trace elements and Pb–Nd–Sr isotopes. *Palaeogeography, Palaeoclimatology, Palaeoecology*, **411**, 144-154.

Jaillard, E., Hérail, G., Monfret, T., Díaz-Martínez, E., Baby, P., Lavenu, A., Dumont, J.F. (2000). Tectonic evolution of the Andes of Ecuador, Peru, Bolivia and northernmost Chile. In: Cordani, U.G., Thomaz-Filho, A., Campos, D.A. (Eds.) Tectonic Evolution of South America. Acad. Bras. Cienc. Spec. Publ. 31st Int. Geol. Cong., pp. 41-95.

Johns, W.E., Lee, T.N., Beardsley, R.C., Candela, J., Limeburner, R., Castro, B. (1998). Annual cycle and variability of the North Brazil Current. J. *Phys. Oceanogr*. **28 (1)**, 103–128.

Kanner, L.C., Burns, S.J., Cheng, H., Edwards, R.L. (2012). High-latitude forcing of the South American summer monsoon during the last glacial. *Science*, **335(6068)**, 570-573.

Kuehl, S.A., DeMaster, D.J., Nittrouer, C.A. (1986). Nature of sediment accumulation on the Amazon continental shelf. *Continental Shelf Research*, **6(1-2)**, 209-225.

Kumar, A., Abouchami, W., Galer, S.J.G., Garrison, V.H., Williams, E., Andreae, M.O. (2014). A radiogenic isotope tracer study of transatlantic dust transport from Africa to the Caribbean. *Atmospheric Environment*, **82**, 130-143.

Lambeck, K., Chappell, J. (2001). Sea level change through the last glacial cycle. *Science*, **292(5517)**, 679-686.

Latrubesse, E.M., Arima, E.Y., Dunne, T., Park, E., Baker, V.R., d'Horta, F.M., Wight, C., Wittmann, F., Zuanon, J., Baker, P.A., Ribas, C.C., Norgaard, R.B., Filizola, N., Ansar, A., Flyvbjerg, B., Stevaux, J.C. (2017). Damming the rivers of the Amazon basin. *Nature*, **546(7658)**, 363-369.

Lees, A.C., Peres, C.A., Fearnside, P.M., Schneider, M., Zuanon, J.A. (2016). Hydropower and the future of Amazonian biodiversity. *Biodiversity and conservation*, **25(3)**, 451-466.

Macambira, M.J.B., Vasquez, M.L., da Silva, D.C.C., Galarza, M.A., de Mesquita Barros, C.E., de Freitas Camelo, J. (2009). Crustal growth of the central-eastern Paleoproterozoic domain, SW Amazonian craton: Juvenile accretion vs. reworking. *Journal of South American Earth Sciences*, **27(4)**, 235-246.

Mattinson, J.M. (1990). Petrogenesis and evolution of the Salinian magmatic arc. *Geological Society of America Memoirs*, **174**, 237-250.

McDaniel, D.K., McLennan, S.M., Hanson, G.N. (1997). Provenance of Amazon fan muds: constraints from Nd and Pb isotopes. In *Proceedings of the Ocean Drilling Program. Scientific Results* (Vol. 155, pp. 169-176). Ocean Drilling Program.

Meade, R.H., Dunne, T., Richey, J.E., Santos, U.D.M., Salati, E. (1985). Storage and remobilization of suspended sediment in the lower Amazon River of Brazil. *Science*, **228(4698)**, 488-490.

Meade, R.H., Rayol, J.M., Da Conceicão, S.C., Natividade, J.R. (1991). Backwater effects in the Amazon River basin of Brazil. *Environmental Geology*, **18(2)**, 105-114.

Meade, R.H. (1994). Suspended sediments of the modern Amazon and Orinoco rivers. *Quaternary International*, **21**, 29-39.

Medeiros Filho, L.C., Lafon, J.M., Souza Filho, P.W.M. (2016). Pb Sr Nd isotopic tracing of the influence of the Amazon River on the bottom sediments in the lower Tapajós River. *Journal of South American Earth Sciences*, **70**, 36-48.

Mercer, J.H., Palacios, O. (1977). Radiocarbon dating of the last glaciation in Peru. *Geology*, **5(10)**, 600-604.

Miller, J. R., Mackin, G., Miller, S. M. O. (2015). Application of geochemical tracers to fluvial sediment. Springer International Publishing, 142 p.

Milliman, J.D., Summerhayes, C.P., Barretto, H.T. (1975). Quaternary sedimentation on the Amazon continental margin: a model. *Geological Society of America Bulletin*, **86(5)**, 610-614.

Milliman, J.D., Meade, R.H. (1983). World-wide delivery of river sediment to the oceans. *The Journal of Geology*, **91(1)**, 1-21.

Montgomery, D.R., Balco, G., Willett, S.D. (2001). Climate, tectonics, and the morphology of the Andes. *Geology*, **29(7)**, 579-582.

Mulitza, S., Chiessi, C.M., Cruz, A.P.S., Frederichs, T., Gomes, J.G., Gurgel, M.H., Haberkern, J., Huang, E., Jovane, L., Kuhnert, H., Pittauerová, D., Reiners, S.-J., Roud, S.C., Schefuß, E., Schewe, F., Schwenk, T.A., Sicoli Seoane, J.C., Sousa, S.H.M., Wagner, D.J., Wiers, S. (2013). Response of Amazon sedimentation to deforestation, land use and climate variability, Cruise No. MSM20/3, February 19–March 11 2012, Recife (Brazil), Bridgetown (Barbados). *Berichte, Fachbereich Geowissenschaften, Universität Bremen, Bremen, Germany*, 1-86.

Nittrouer, C.A., Kuehl, S.A., Sternberg, R.W., Figueiredo, A.G., Faria, L.E. (1995). An introduction to the geological significance of sediment transport and accumulation on the Amazon continental shelf. *Marine Geology*, **125(3-4)**, 177-192.

Parra, M., Pujos, M. (1998). Origin of late Holocene fine-grained sediments on the French Guiana shelf. *Continental shelf research*, **18(13)**, 1613-1629.

Payolla, B.L., Bettencourt, J.S., Kozuch, M., Leite, W.B., Fetter, A.H., Van Schmus, W.R. (2002). Geological evolution of the basement rocks in the east-central part of the Rondônia Tin Province, SW Amazonian Craton, Brazil: U–Pb and Sm–Nd isotopic constraints. *Precambrian Research*, **119(1)**, 141-169.

Pin, C., Briot, D., Bassin, C., Poitrasson, F. (1994). Concomitant separation of strontium and samarium-neodymium for isotopic analysis in silicate samples, based on specific extraction chromatography. *Analytica Chimica Acta*, **298(2)**, 209-217.

Pinto, L. (2003) Traçage de l'érosion Cénozoïc des Andes Centrales à l'aide dela minéralogie et de la géochemie des sediments (Nord du Chili et Nord-Ouest de la Bolivie), PhD, University Paul Sabatier

Prado, L., Wainer, I., Chiessi, C., Ledru, M. P., Turcq, B. (2013). A mid-Holocene climate reconstruction for eastern South America. *Climate of the Past*, **9(5)**, 2117-2133.

Prospero, J.M., Carlson, T.N. (1972). Vertical and areal distribution of Saharan dust over the western equatorial North Atlantic Ocean. *Journal of Geophysical Research*, **77(27)**, 5255-5265.

Prospero, J.M., Glaccum, R.A., Nees, R.T. (1981). Atmospheric transport of soil dust from Africa to South America. *Nature*, **289(5798)**, 570-572.

Prost, M.T., Lointier, M. (1988). Coastal sedimentation and local rivers supply in French Guiana: comparisons with the Amazon. In Chaprnan Conference on the rate of particulate and dissolved components within the Amazon Dispersai System: River and Oceano Nittrouer & DeMaster Ed. Charleston. WIld Dunes. USA (pp. 182-186).

Pujos, M., Bouysse, P., Pons, J.C. (1990). Sources and distribution of heavy minerals in Late Quaternary sediments of the French Guiana continental shelf. *Continental Shelf Research*, **10(1)**, 59-79.

Reimer, P.J., Bard, E., Bayliss, A., Beck, J.W., Blackwell, P.G., Ramsey, C.B., Buck, C.E., Cheng, H., Edwards, R.L., Friedrich, M., Grootes, P.M., Guilderson, T.P., Haflidason, H., Hajdas, I., Hatte, C., Heaton, T.J., Hoffmann, D.L., Hogg, A.G., Hughen, K.A., Kaiser, K. F., Kromer, B., Manning, S.W., Niu, M., Reimer, R.W., Richards, D.A., Scott, E.M., Southon, J.R., Staff, R.A., Turney, C.S.M., van der Plicht, J. (2013). IntCal13 and Marine13 radiocarbon age calibration curves 0–50,000 years cal BP. *Radiocarbon*, **55(4)**, 1869-1887.

Revel M., Ducassou E., Grousset F. E., Bernasconi S. M., Migeon S., Revillon S., Mascle J., Murat A., Zaragosi S., Bosch D. (2010). 100,000 years of African monsoon variability recorded in sediments of the Nile margin. *Quaternary Science Reviews*, **29(11)**, 1342-1362.

Revel, M., Colin, C., Bernasconi, S., Combourieu-Nebout, N., Ducassou, E., Grousset, F.E., Rolland, Y., Migeon, S., Bosch, D., Brunet, P., Zhao, Y., Mascle, J. (2014). 21,000 Years of Ethiopian African monsoon variability recorded in sediments of the western Nile deep-sea fan. *Regional environmental change*, **14(5)**, 1685-1696.

Revel, M., Ducassou, E., Skonieczny, C., Colin, C., Bastian, L., Bosch, D., Migeon, S., Mascle, J. (2015). 20,000 years of Nile River dynamics and environmental changes in the Nile catchment area as inferred from Nile upper continental slope sediments. *Quaternary Science Reviews*, **130**, 200-221.

Roddaz, M., Viers, J., Brusset, S., Baby, P., Hérail, G. (2005). Sediment provenances and drainage evolution of the Neogene Amazonian foreland basin. *Earth and Planetary Science Letters*, **239(1)**, 57-78.

Rossetti, D.F., Toledo, P.M., Góes, A.M. (2005). New geological framework for Western Amazonia (Brazil) and implications for biogeography and evolution. *Quaternary Research,* **63**, 78–89.

Santos, J.O.S., Hartmann, L.A., Gaudette, H.E., Groves, D.I., Mcnaughton, N.J., Fletcher, I.R. (2000). A new understanding of the provinces of the Amazon Craton based on integration of field mapping and U-Pb and Sm-Nd geochronology. *Gondwana Research*, **3(4)**, 453-488.

Santos, R.V., Sondag, F., Cochonneau, G., Lagane, C., Brunet, P., Hattingh, K., Chaves, J.G. (2015). Source area and seasonal 87Sr/86Sr variations in rivers of the Amazon basin. *Hydrological processes*, **29(2)**, 187-197.

Sarnthein, M., Stattegger, K., Dreger, D., Erlenkeuser, H., Grootes, P., Haupt, B.J., Jung, S., Kiefer, T., Kuhnt, W., Pflaumann, U., Schäfer-Neth, C., Schulz, H., Schulz, M., Seidov, D., Simstich, J., van Kreveld, S., Vogelsang, E., Völker, A., Weinelt, M. (2001). Fundamental modes and abrupt changes in North Atlantic circulation and climate over the last 60 ky-Concepts, reconstruction and numerical modeling. In The Northern North Atlantic (pp. 365-410). Springer Berlin Heidelberg.

Sioli, H. (1957). Sedimentation im Amazonasgebiet. *Geologische Rundschau*, **45(3)**, 608-633.

Sioli, H. (1984). The Amazon and its main affluents: Hydrography, morphology of the river courses, and river types, in: Sioli, H. (Ed.), The Amazon: Limnology and Landscape Ecology of a Mighty Tropical River and Its Basin. Springer Netherlands, Dordrecht, pp. 127–165. doi:10.1007/978-94-009-6542-3_5.

Skonieczny, C., Bory, A., Bout-Roumazeilles, V., Abouchami, W., Galer, S.J.G., Crosta, X., Diallo, A., Ndiaye, T. (2013). A three-year time series of mineral dust deposits on the West African margin: sedimentological and geochemical signatures and implications for interpretation of marine paleo-dust records. *Earth and Planetary Science Letters*, **364**, 145-156.

Stallard, R.F., Edmond, J.M. (1983). Geochemistry of the Amazon: 2. The influence of geology and weathering environment on the dissolved load. *Journal of Geophysical Research: Oceans*, **88(C14)**, 9671-9688.

Stríkis, N.M., Chiessi, C.M., Cruz, F.W., Vuille, M., Cheng, H., Souza Barreto, E.A., Mollenhauer, G., Kasten, S., Karmann, I., Edwards, R.L., Bernal, J.P., dos Reis Sales, H. (2015). Timing and structure of Mega-SACZ events during Heinrich Stadial 1. *Geophysical Research Letters*, **42(13)**, 5477.

Swap, R., Garstang, M., Greco, S., Talbot, R., Kållberg, P. (1992). Saharan dust in the Amazon Basin. *Tellus B*, **44(2)**, 133-149.

Tassinari, C.C., Macambira, M.J. (1999). Geochronological provinces of the Amazonian Craton. *Episodes-Newsmagazine of the International Union of Geological Sciences*, **22(3)**, 174-182.

Tassinari, C.C.G., Bittencourt, J.S., Geraldes, M.C., Macambira, M.J.B., Lafon, J.M. (2000). The Amazon Craton. *In:* Cordani, U.G., Thomaz-Filho, A., Campos, D.A. (Eds.) Tectonic Evolution of South America. Acad. Bras. Cienc. Spec. Publ. 31st Int. Geol. Cong., pp. 41-95.

Valencia, B.G., Urrego, D.H., Silman, M.R., Bush, M.B. (2010). From ice age to modern: a record of landscape change in an Andean cloud forest. *Journal of Biogeography*, **37(9)**, 1637-1647.

Viers, J., Roddaz, M., Filizola, N., Guyot, J.L., Sondag, F., Brunet, P., Zouiten, C., Boucayrand, C., Martin, F., Boaventura, G.R. (2008). Seasonal and provenance controls on Nd–Sr isotopic compositions of Amazon rivers suspended sediments and implications for Nd and Sr fluxes exported to the Atlantic Ocean. *Earth and Planetary Science Letters*, **274(3)**, 511-523.

Vital, H., Stattegger, K. (2000). Major and trace elements of stream sediments from the lowermost Amazon River. *Chemical Geology*, **168(1)**, 151-168.

Walter, H.J., Hegner, E., Diekmann, B., Kuhn, G. (2000). Provenance and transport of terrigenous sediment in the South Atlantic Ocean and their relations to glacial and interglacial cycles: Nd and Sr isotopic evidence. *Geochimica et Cosmochimica Acta*, **64(22)**, 3813-3827.

Wang, X., Edwards, R.L., Auler, A.S., Cheng, H., Kong, X., Wang, Y., Cruz, F.W., Dorale, J.A., Chiang, H.W. (2017). Hydroclimate changes across the Amazon lowlands over the past 45,000 years. *Nature*, **541(7636)**, 204-207.

Wasserburg, G.J., DePaolo, D.J. (1979). Models of earth structure inferred from neodymium and strontium isotopic abundances. *Proceedings of the National Academy of Sciences*, **76(8)**, 3594-3598.

Wei, G., Ma, J., Liu, Y., Xie, L., Lu, W., Deng, W., Ren, Z., Zeng, T., Yang, Y. (2013). Seasonal changes in the radiogenic and stable strontium isotopic composition of Xijiang River water: Implications for chemical weathering. *Chemical Geology*, **343**, 67-75.

Werneck Lima, J.E.F., Dos Santos, P.M.C., Carvalho, N.O., da Silva, E.M. (2003). Araguaia-Tocantins: Diagnóstico do fluxo de sedimentos em suspensão na bacia. Brasília: Embrapa, ANEEL, ANA. 116p.

White, W. M. (2015). Isotope geochemistry. John Wiley & Sons, UK, 478p.

Wittmann, H., von Blanckenburg, F., Maurice, L., Guyot, J. L., Filizola, N., Kubik, P. W. (2010). Sediment production and delivery in the Amazon River basin quantified by in situ—produced cosmogenic nuclides and recent river loads. Geological Society of America Bulletin, B30317-1.

Wittmann, H., von Blanckenburg, F., Maurice, L., Guyot, J.L., Kubik, P.W. (2011). Recycling of Amazon floodplain sediment quantified by cosmogenic 26Al and 10Be. *Geology,* **39(5)**, 467-470.

Wright Jr, H.E. (1983). Late-Pleistocene glaciation and climate around the Junin Plain, central Peruvian highlands. Geografiska Annaler. Series A. *Physical Geography*, **35-43**.

Zhang, Y., Chiessi, C.M., Mulitza, S., Zabel, M., Trindade, R.I., Hollanda, M.H.B., Dantas, E.L., Govin, A., Tiedemann, R., Wefer, G. (2015). Origin of increased terrigenous supply to the NE South American continental margin during Heinrich Stadial 1 and the Younger Dryas. *Earth and Planetary Science Letters*, **432**, 493-500.

Zhang, Y., Zhang, X., Chiessi, C.M., Mulitza, S., Zhang, X., Lohmann, G., Prange, M., Behling, H., Zabel, M., Govin, A., Sawakuchi, A.O., Cruz, F.W., Wefer, G. (2016). Equatorial Pacific forcing of western Amazonian precipitation during Heinrich Stadial 1. *Scientific reports*, **6**, 35866.

Table S1 Sr, Nd and Pb isotopic compositions for unsieved and sieved (< 63µm) samples of the bulk fraction of GeoB16224-1. Uncertainties ($2SD_{mean}$) are given for the last digit.

Bulk fraction	Sample depth [cm]	Age [cal ka BP]	$^{87}Sr/^{86}Sr$	$^{143}Nd/^{144}Nd$	ε_{Nd}	$^{206}Pb/^{204}Pb$[a]	$^{207}Pb/^{204}Pb$[a]	$^{208}Pb/^{204}Pb$[a]
unsieved	75	13.2	0.713931(4)	0.512046(3)	-11.55(1)	19.09	15.77	39.32
unsieved	95.5	14.2	0.713522(5)	0.512033(2)	-11.80(1)	19.00	15.67	39.01
unsieved	157	16.8	0.714912(4)	0.512018(4)	-12.09(1)	19.02	15.71	39.14
unsieved	186	18.1	0.714208(4)	0.512036(4)	-11.74(1)	19.01	15.72	39.14
unsieved	241	20.7	0.713935(9)	0.51205(3)	-11.47(1)	18.98	15.70	39.09
unsieved	336.5	25.1	0.713968(4)	0.512057(3)	-11.33(1)	18.96	15.68	38.99
unsieved	364.5	26.3	0.714412(5)	0.512055(3)	-11.37(1)	19.05	15.76	39.29
unsieved	395	27.6	0.713596(6)	0.512062(3)	-11.24(1)	19.07	15.79	39.38
unsieved	427	29.4	0.715869(7)	0.512038(4)	-11.70(1)	18.98	15.67	38.99
sieved [< 63 µm]	53	7.6	0.71606(5)	0.512042(2)	-11.63(1)	19.01	15.67	38.99
sieved [< 63 µm]	57	9.7	0.716062(7)	0.512046(3)	-11.55(1)	19.01	15.67	38.98
sieved [< 63 µm]	61	11.3	0.71588(7)	0.51205(4)	-11.47(1)	19.01	15.67	38.99
sieved [< 63 µm]	63	11.8	0.714306(6)	0.512055(3)	-11.37(1)	19.02	15.68	39.03
sieved [< 63 µm]	65	12.4	0.715627(5)	0.512065(3)	-11.18(1)	19.02	15.68	39.03
sieved [< 63 µm]	354.5	25.9	0.715291(3)	0.512055(4)	-11.37(1)	18.96	15.66	38.95
sieved [< 63 µm]	415	28.7	0.713462(5)	0.512045(4)	-11.57(1)	18.98	15.66	38.96
sieved [< 63 µm]	451	30.8	0.715623(6)	0.512054(1)	-11.39(2)	18.99	15.67	38.98
sieved [< 63 µm]	562	37.2	0.71577(6)	0.512044(4)	-11.59(1)	19.01	15.67	38.99
sieved [< 63 µm]	591.5	39.5	0.715638(8)	0.512034(4)	-11.78(1)	18.98	15.67	38.99

[a]Uncertainties ($2SD_{mean}$) are 0.1 %.

Table S2 Nd isotopic compositions and concentration for the individual values used to calculate the average values for the Tocantins and French Guiana rivers in table 18. Uncertainties ($2SD_{mean}$) are given for the last digit.

Average signature for	Sample	$^{143}Nd/^{144}Nd$	ε_{Nd}	Nd [µg/g]
Tocantins River	Tapajós	0.51166(1)[1]	-19.1(3)	n.a.
	Tapajós	0.511657(3)[1]	-19.1(1)	51[1]
	Xingu	0.511398(6)[1]	-24.2(1)	25[1]
	Tapajós	0.51161(5)[2]	-20(1)	n.a.
			Ø -20.6 ± 4.8	Ø 38
French Guiana rivers	Urucara	0.51173(2)[2]	-17.7(4)	31.7[3]
	Trombetas	0.51150(3)[2]	-22.2(6)	45[3]
	Guiana Shield	0.5116[4]	-20.3	n.a.
	Guiana Shield	0.5117[4]	-18.3	n.a.
			Ø -19.6 ± 4.1	Ø 38

[1] this study; [2]: Allègre et al., 1996; [3] Gaillardet et al., 1997; [4] Parra and Pujos, 1998

Chapter 4

Provenance shift of suspended particulate matter in the Río de la Plata drainage basin over time

Natalie Höppner[1]*, Friedrich Lucassen[1], Cristiano M. Chiessi[2], Raúl A. Becchio[3], Simone A. Kasemann[1]

[1] MARUM – Center for Marine Environmental Sciences and Faculty of Geosciences, University of Bremen, Bremen, Germany (*corresponding author: nhoeppner@marum.de, telephone: +49 (0) 421 218 65934)

[2]School of Arts, Sciences and Humanities, University of São Paulo, São Paulo, Brazil

[3]National University of Salta, Salta, Argentina

4.1 Abstract

Since radiogenic isotopes in riverine sediments reflect the drainage basin geology, sediment transported in rivers can have distinct signatures. These isotopic signatures are not significantly altered by weathering, transport or deposition and hence can document variations in the sediment supply. We present Strontium (Sr), neodymium (Nd) and lead (Pb) isotope values for the Río de la Plata drainage basin, suggesting that the basin has three main sediment source areas (the upper Paraná River, the Uruguay River and the Andean draining rivers) with distinct isotopic signatures. The sediment from the Andean draining rivers (Salado, Pilcomayo and Bermejo Rivers) has the most radiogenic Pb (i.e. >18.5 for $^{206}Pb/^{204}Pb$) and Sr (average of 0.726 ± 0.031; 2SD) isotopic signatures, and least radiogenic ε_{Nd} values (average of -10.5 ± 3.1; 2SD). The upper Paraná and Uruguay Rivers have less radiogenic Pb (i.e. <18.5 for $^{206}Pb/^{204}Pb$) and Sr (average of 0.715 ± 0.003; 2SD) isotopic signatures. The upper Paraná has average ε_{Nd} values of -7.8 ± 1.1 (2SD), the Uruguay River has average ε_{Nd} values of -5.9 ± 0.2 (2SD). Millennial-scale climate events (e.g. Heinrich Stadials, Younger Dryas) have an impact on the sediment supply dynamics of river basins and its individual tributaries. To understand how the Río de la Plata drainage basin sediment supply changed in the past, we present radiogenic isotope signatures (Sr, Nd and Pb) of a marine sediment core archiving the last 30 kyr of the Río de la Plata drainage basin sediment supply history. The core signal shows several pronounced peaks. We suggest that these peaks result from higher precipitation in the Andes (i.e. Heinrich Stadial 1, Younger Dryas) or in the southeastern sector of the Río de la Plata drainage basin (i.e. Bølling-Allerød). The peak at the beginning of the Holocene indicates a change in sea level and ocean current dynamics (i.e. stronger Subantarctic Shelf Water).

4.2 Introduction

The largest percentage of dissolved and solid material delivered into the world oceans originates from rivers, followed (in descending amount) by glacier delivery and atmospheric dust input (Milliman and Meade, 1983). The riverine input impacts the ocean on a multitude of levels. The freshwater input influences ocean density and the circulation dynamics (Dávila et al., 2002), riverine terrestrial organic matter is a very important component of the global carbon cycle (Hedges et a., 1997) and element fluxes imprint on the ocean chemistry. The riverine supply, especially in large river basin, is prone to changes in environmental conditions (i.e. climate). Precipitation variations influence the denudation rate and impact the sediment amount transported in individual tributaries of the river basin, thus changing the sediment composition ultimately supplied into the ocean. Identifying the provenance of the supplied river sediment makes it possible to determine changes in the river drainage basin. Tools to identify sediment provenances are radiogenic isotopes, because they do not change during weathering, transport and deposition and therefore reflect the geology of the drainage basin of the respective river. Due to mineralogical differences in the continental crust as well as different

crustal ages, the distinct isotopic signatures can be used to identify changes in the riverine sediment supply. Marine sediments offshore river deltas and estuaries are a valuable archive of deposited river sediment. Hence, they can be used to study the supply provenances in the past.

The Río de la Plata drainage basin (LPDB) has a drainage area of 3.1 x 10^6 km² and is the second largest river basin in South America (Depetris and Griffin, 1968) and the fifth largest in the world (Milliman and Meade 1983). It is located in northern Argentina, southern Brazil, as well as parts of Uruguay, Paraguay and Bolivia. The LPDB is bordered to the west by the Andes Mountains, to the northeast-east by the Brazilian Plateau and to the southwest by the Argentine Pampas (Depetris and Griffin, 1968). The main rivers of the LPDB are the Paraná River (with its tributary the Salado River), the Paraguay River (with its tributaries the Bermejo River and the Pilcomayo River) and the Uruguay River. At the border of Uruguay and Argentina the Paraná River confluences with the Uruguay River and forms the Río de la Plata River and estuary that flows into the Atlantic Ocean. The modern total annual suspended particulate matter (SPM) discharge of 9.2 x 10^7 t (Depetris et al., 2003) is supplied to 44 % by the Bermejo River alone, that has a total drainage area of about 4 % of the whole basin (Henry et al., 1996). Because most of the studies to date focus on sediments from the estuary (Biscaye and Dasch, 1971; de Mahiques et al. 2008) or on samples from the lower Paraná and Uruguay Rivers near the estuary (Goldstein et al., 1984; Henry et al., 1996), there is only a sparse database of radiogenic isotope signatures of river sediment in the LPDB. However, to identify changes in river sediment supply in the LPDB (i.e. due to climate), it is crucial to have a database of isotopic compositions of the different tributaries of the LPDB.

Several studies to date show the impact of climate variation on the LPDB during the Holocene (Chiessi et al., 2009; Gyllencreutz et al., 2010; de Mahiques et al., 2009; Perez et al., 2016) and with even higher resolution during the last centennial (Amsler and Drago, 2009; Collischonn et al., 2001; Piola et al., 2005). Additionally, a few studies investigated the late Pleistocene (Chiessi et al., 2015; Razik et al., 2013; Voigt et al., 2013), using Nd isotope signatures (Lantzsch et al., 2014). However, there are no studies going further back than 20 cal ka BP and/or using a multi isotope approach. Here we present Sr, Nd and Pb isotopic compositions for SPM and river bed samples for six river drainage basins (Paraná, Uruguay, Paraguay, Pilcomayo, Bermejo and Salado Rivers) in the LPDB. In addition, we applied our Sr, Nd and Pb isotopic source characterization to a marine sediment core representing the integrated Río de la Plata drainage basin discharge for the last 30 kyr. The data allows to identify the modern contribution distribution and helps to understand climate induced shifts in sediment provenances.

4.3 Regional setting

4.3.1 Geological setting

The Río de la Plata drainage basin is adjacent to the Argentinian Pampas to the southwest and flanked by the Andes Mountains to the west and the Brazilian Plateau to the northeast-east (Depetris and Griffin, 1968). A huge section of the drainage basin of the Paraguay River (northern part of the LPDB) is a large swamp called the Pantanal (Berbery and Barros, 2002). The Uruguay River drains primarily tholeiitic flood basalts (Jurassic-Cretacous) and the upper Paraná River drains Jurassic-Cretacous sedimentary rocks. Additionally, both rivers drain parts of Precambrian crystalline basement (Río de la Plata Craton and the Brazilian Shield). The Bermejo, Pilcomayo and Salado Rivers all mainly drain Mesozoic to Tertiary sedimentary and metamorphic Andean rocks (Henry et al., 1996) (Fig. 19).

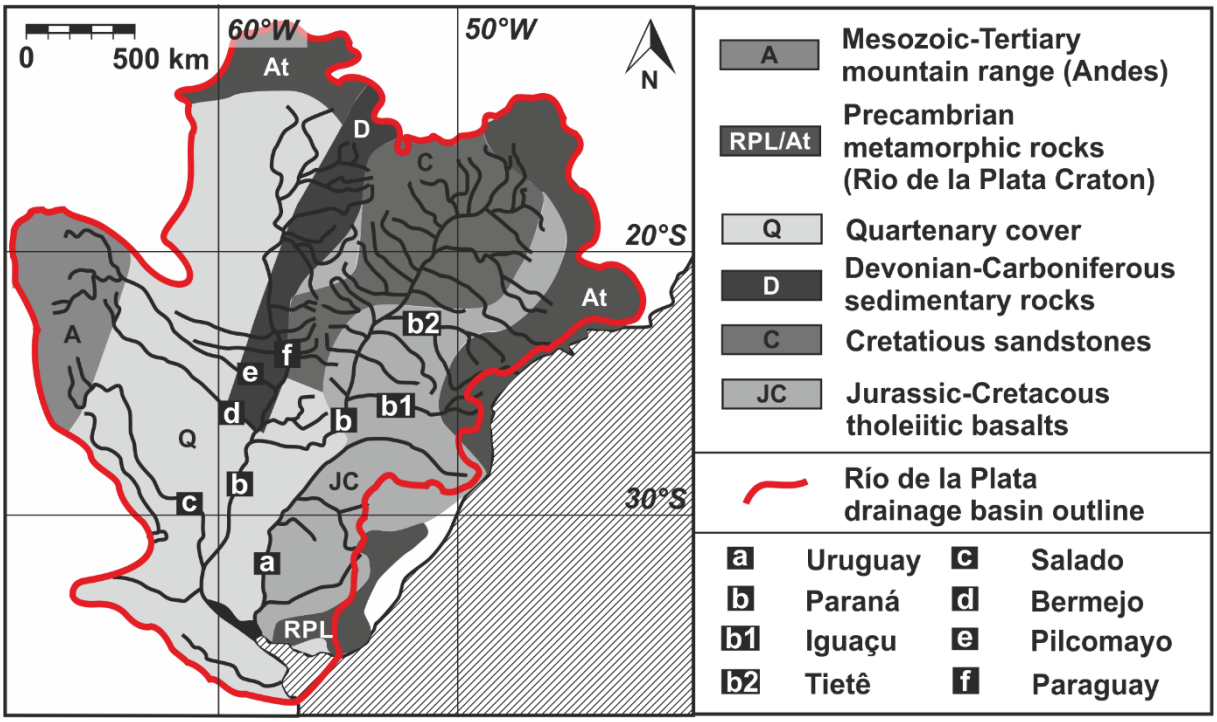

Fig. 19. Major geological units of the Río de la Plata drainage basin. The outline of the Río de la Plata drainage basin is shown in red and the main tributaries are marked with white lowercase letters as follows a: Uruguay, b: Paraná, b1: Iguaçu, b2: Tietê, c: Salado, d: Bermejo, e: Pilcomayo and f: Paraguay. Geological units are simplified after Henry et al. (1996).

4.3.2 Hydrological setting

The Río de la Plata drainage basin has six main rivers (Fig. 19): Uruguay, Paraná, Paraguay, Pilcomayo, Bermejo and Salado. The Paraná River can further be divided into two parts, upper and lower part. The upper part confluences with the Paraguay River near the city of Corientes at the Paraguayan and Argentinian border. The lower part, together with the Uruguay River, forms the Río de la Plata River that flows into the Atlantic Ocean at the Uruguayan and Argentinian border. The upper Paraná River is suppling about 60 % of the total water discharge of the Río de la Plata drainage basin. However, the main supplier of SPM is the Bermejo River

with 50 to 70 % (Depetris et al., 2003), due to its steep slope and sparse vegetation cover (Henry et al., 1996).

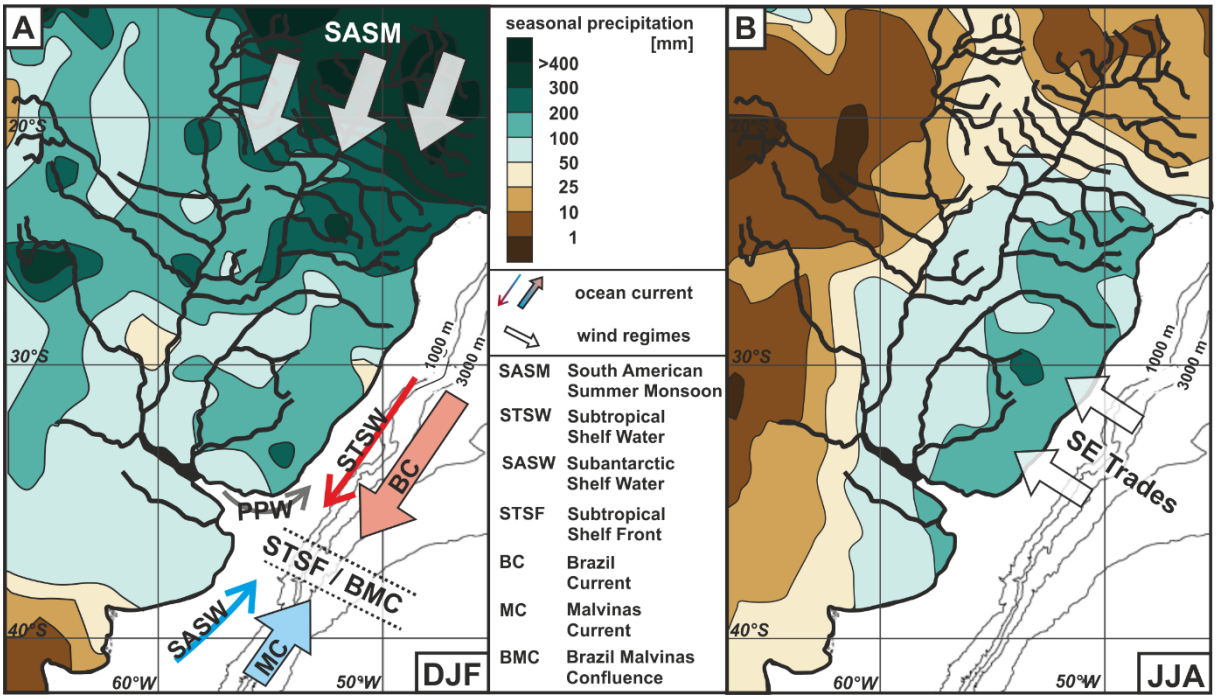

Fig. 20. Seasonal precipitation patterns in austral summer (DJF) and winter (JJA) (after Piovano et al., 2009) and surface ocean currents. Ocean currents are shown in panel (A), shelf currents (SASW and STSW) are marked with thin arrows, offshore currents (BC and MC) are marked with thick arrows; a red color represents warm water, a blue color represents cold water; the arrow head indicated the main transport direction; the confluences of the ocean currents (STSF onshore and BMC offshore) is indicated by two dotted lines. Dominant wind regimes are shown in panel (A) and (B) for their respective season (DJF: SASM and JJA: SE Trades) indicated with thick white arrows, the arrow head highlights the main wind direction. The main tributaries of the LPDB are illustrated in black lines.

The Río de la Plata drainage basin has a west to east precipitation gradient (drier west and wetter east), with an additional precipitation maxima in the northern part of the basin (Berbery and Barros, 2002). During the austral summer (DJF) the Andean foreland as well as the Paraná River drainage basin have the highest precipitation, due to the South American Summer Monsoon (SASM) (Fig. 20). During the austral winter (JJA) the precipitation has a gradient from east (wet) to west (dry) due to the Southeast Trade winds (SE Trades) (Piovano et al., 2009). The climate in southern South America is closely coupled to the Atlantic Meridional Overturning Circulation (AMOC). A strong (weak) AMOC cools (heats) the South Atlantic, leading to a northwards (southwards) migration of the Inter Tropical Convergence Zone (ITCZ). This weakens (strengthens) the convection along the South American Convergence Zone (SACZ), displacing the summer rainfall belt (i.e. the SASM) northwards (southwards) (Chiessi et al., 2009). The shelf area in front of the Río de la Plata estuary is dominated by two ocean currents (Fig. 20). The northeastwards flowing Subantarctic Shelf Water (SASW) and the southwestwards flowing Subtropical Shelf Water (STSW). Their meeting zone is called the

Subtropical Shelf Front (STSF), which is assumed to be the extension of the Brazil-Malvinas Confluence (BMC). The discharge of the Río de la Plata drainage basin gets transported northeastwards by the Plata Plume Water (PPW), mainly driven by the wind (Piola et al., 2000).

4.4 Material and methods

4.4.1 Material

Sample material investigated in this study are river suspended particulate matter, riverbank and bed sediments and sediments from a marine gravity core (Fig. 21).

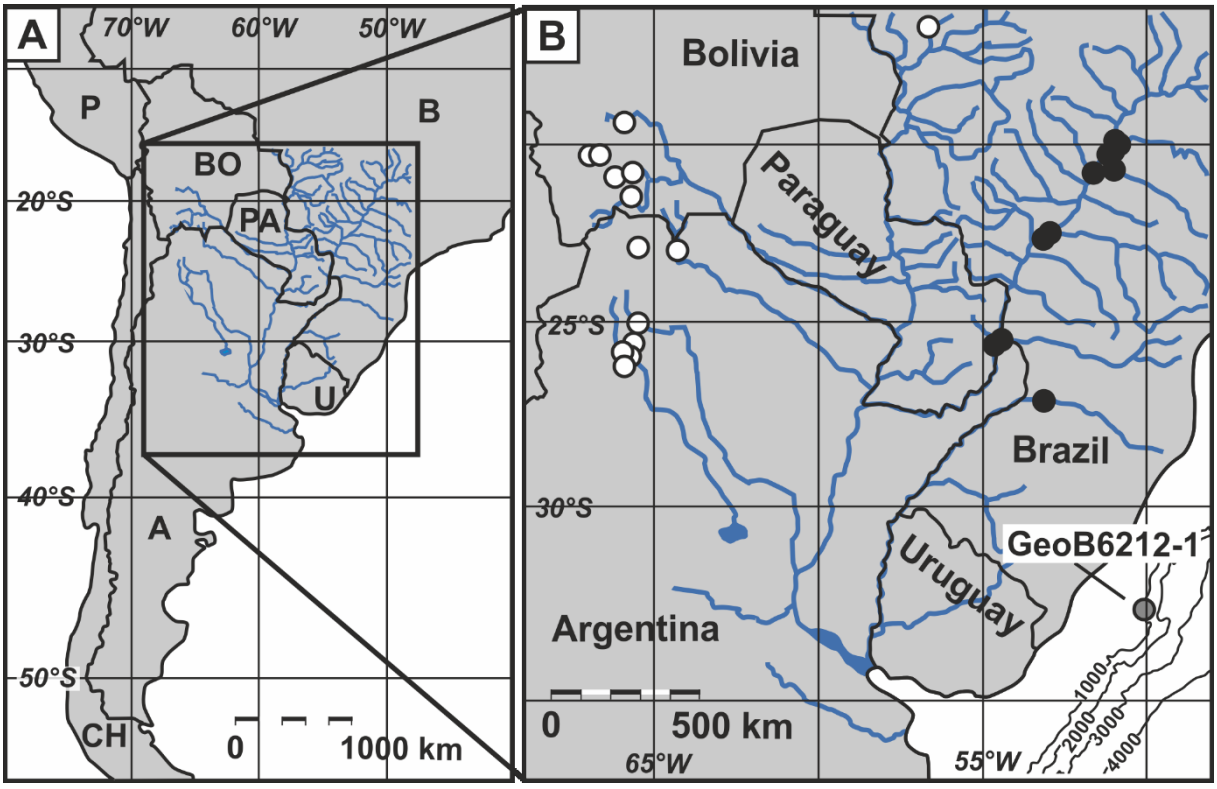

Fig. 21. Location of the sediment samples investigated in this study. Panel A: Southern South America showing the Río de la Plata drainage basin and the area expanded in panel B. The countries are marked with black uppercase letters as follows: A: Argentina, B: Brazil, BO: Bolivia, CH: Chile, P: Peru, PA: Paraguay and U: Uruguay. Panel B: The location of the marine sediment core GeoB6212-1 is marked with a grey circle. The location of the suspended particulate matter samples from the Uruguay River, the Paraná River main channel and it's different tributaries are marked with black circles. The locatin of the river sediment samples from Argentina (Salado River drainage basin), from Bolivia (Bermejo and Pilcomayo Rivers drainage basin) and from the Paraguay River drainage basin (Brazil) are marked with white circles.

Suspended particulate matter (SPM) samples for the Brazilian part of the LPDB (Uruguay River and upper Paraná River main channel with six tributaries) were collected during a sampling campaign in February/March 2016 (Fig 21B, Table 19). Samples were taken in the middle of the river channel at 60 % depth of the water column. They were filtered through 0.45 µm Sartorius® cellulose acetate membrane filter and dried at 50°C overnight. The average sample size varied from 2 to 150 mg, depending on the SPM amount transported by the river. River bed sediment samples for the Salado River drainage basin (Argentinian part of the LPDB) (Fig.

21B, Table 20) were sampled during a sampling campaign in December 2014. Samples were taken in 50 ml PP centrifuge tubes, filled between 40 to 95 % with sediment. Wherever possible, river water was sampled into the tubes as well, between 5 to 10 ml. River bed sediment from the Pilcomayo and Bermejo Rivers drainage basins (Bolivian part of the LPDB) (Fig. 21B, Table 20) was taken during a sampling campaign in December 2015. Samples were collected in 100 ml PP wide-neck containers, filled between 40 to 95 % with sediment. Wherever possible, river water was sampled into the containers as well, between 6 and 120 ml. Additionally, two samples of the salt flats of the Salar de Uyuni were taken of about 12 to 90 cm^3 sample size. The river bed sample of the Paraguay River drainage basin (Fig. 21B, Table 20) was taken in October 2015. A sediment sample of approximately 500 g and a water sample of 500 ml were taken.

Gravity core GeoB6212-1 (790cm; 32°30.31'S 50°14.56'W; 1010 m water depth) was collected on the continental slope off the coast of SE Brazil (Fig 21B) during Meteor cruise M46/2 in 1999/2000 (Schulz et al., 2001). It is located northeast of the Río de la Plata estuary. The northeastwards flowing PPW transports the terrigenous material to the core site (Lantzsch et al., 2014). 45 samples with an average of 5 g dry weight were sampled from 771 to 10 cm to generate an even coverage of the radiocarbon dated section of the core. The age model is based on 14 AMS radiocarbon ages (^{14}C) from planktonic foraminifera (Campos et al., 2017) and dates the sediment between 31.9 (768 cm) to 5.9 (8 cm) cal ka BP.

4.4.2 Methods

4.4.2.1 Sample preparation and dissolution

4.4.2.1.1 River suspended particulate matter

The filter were cut in half and half of every filter was transferred into a Teflon Savillex® beaker, filled with Milli Q water (18.2 MΩ) and placed into an ultrasonic bath for 30 min. Afterwards the remaining SPM was removed from filters by scraping. The solution was dried on a hot plate and the SPM was digested in 0.5 to 4 ml of a concentrated HF:HNO_3 (5:1) acid mixture, dried and redissolved in 0.5 to 4 ml of aqua regia (3:1, 6 N HCl:concentrated HNO_3), dried and redissolved in 3 to 6 ml of a H_2O_2:concentrated HNO_3 (1:1) acid mixture, dried and redissolved in 1 to 4 ml of 6 N HCl. An aliquot for elemental analyses was taken. Finally, the detrital fraction was dried and redissolved in 500 to 1000 µl of 2 N HNO_3 for further chemical separation and isotopic analyses.

Table 19 Sr, Nd and Pb concentrations for river suspended particulate matter of the Brazilian Río de la Plata drainage basin.

Sample name	River	Season	Sampling date	Location [Lon (°E) / Lat (°N)]	Sr [µg/g]	Nd [µg/g]	Pb [µg/g]
NH PL2	Paraná (Paranaíba x Grande)	wet	02/2016	-51.114151/-20.274680	66	35	28
NH PL3	Paraná (Paranaíba x Grande)	wet	02/2016	-51.224997/-20.326559	121	35	21
NH PL4	Paranaíba	wet	02/2016	-51.012856/-19.981110	60	42	42
NH PL5	Paranaíba	wet	02/2016	-51.016831/-19.969046	61	42	22
NH PL7	Grande	wet	02/2016	-50.900298/-19.989568	68	27	14
NH PL8	Grande	wet	02/2016	-50.928448/-20.014306	156	40	16
NH PL10	Tietê	wet	02/2016	-50.993525/-20.758754	820	132	120
NH PL11	Tietê	wet	02/2016	-51.026790/-20.743267	56	12	9
NH PL13	Paraná (x Tietê, near)	wet	02/2016	-51.625922/-20.868663	142	20	13
NH PL14	Paraná (x Tietê, near)	wet	02/2016	-51.631453/-20.846659	245	77	53
NH PL16	Paraná (x Tietê, far)	wet	02/2016	-52.987989/-22.500671	72	41	46
NH PL17	Paraná (x Tietê, far)	wet	02/2016	-53.013573/-22.523217	71	38	22
NH PL19	Paraná (x Paranapanema)	wet	02/2016	-53.202515/-22.729315	73	49	28
NH PL20	Paraná (x Paranapanema)	wet	02/2016	-53.178096/-22.713461	50	37	20
NH PL22	Paranapanema	wet	02/2016	-52.969250/-22.569720	43	37	20
NH PL23	Paranapanema	wet	02/2016	-52.998194/-22.586447	42	36	21
NH PL25	Paraná (x Iguaçu)	wet	02/2016	-54.650345/-25.664730	58	42	25
NH PL26	Paraná (x Iguaçu)	wet	02/2016	-54.631823/-25.659656	53	35	21
NH PL28	Iguaçu	wet	02/2016	-54.497760/-25.615137	56	45	21
NH PL29	Iguaçu	wet	02/2016	-54.525754/-25.628032	51	39	21
NH PL31	Uruguay	wet	03/2016	-53.146331/-27.150832	30	29	16
NH PL33	Uruguay	wet	03/2016	-53.135689/-27.180072	46	31	15

Table 20 Sr, Nd and Pb concentrations for riverbank and bed sediments of the Argentinian and Bolivian part of the Río de la Plata drainage basin and the Paraguay River drainage basin.

Sample name	River	Sampling date	Location [Lon (°E) / Lat (°N)]	Sr [µg/g]	Nd [µg/g]	Pb [µg/g]
CAL2	Calchaqui	12/2014	-65.75332/-25.97407	57	5	13
CAL4	Calchaqui	12/2014	-65.75332/-25.97407	37	4	12
CAL7	San Lucas	12/2014	-65.95446/-25.85242	43	8	13
CAL8	San Lucas	12/2014	-65.95446/-25.85242	54	10	13
CAL11	La Salamanka	12/2014	-65.64056/-25.62837	52	7	12
CAL14	Calchaqui	01/2015	-65.60637/-25.61485	90	26	15
RT3	Toro	01/2015	-65.49676/-25.03945	48	17	12
TB1	Tolombon	12/2014	-65.91945/-26.21782	101	17	15
RC	Rio Clara (Brazil, to Rio Paraguay)	10/2015	-56.693915/-16.596967	26	32	22
RA2	Rio Atocha	12/2015	-66.20496/-20.95625	375	10	10
RBL1	Rio Blanco	12/2015	-65.665806/-20.820528	230	31	30
RGD1	Rio Grande	12/2015	-65.497333/-22.962972	108	19	12
RGD3	Rio Grande	12/2015	-65.45/-22.971111	157	17	15
RP1	Rio Pilcomayo	12/2015	-65.903444/-19.393472	321	27	19
RTZ1	Rio Tupiza	12/2015	-65.699417/-21.50975	207	54	48
BM3	Ruta Nacional 34, nahe Embarcacion	12/2015	-64.139423/-23.247854	66	31	14
BM4	Ruta Nacional 34, nahe Embarcacion	12/2015	-64.139423/-23.247854	70	35	14
BU1	Salar de Uyuni	12/2015	-66.98357/-20.31624	-	-	-
BU3	Salar de Uyuni, Ojos de Salar	12/2015	-66.663889/-20.311944	-	-	-

4.4.2.1.2 Riverbank and bed sediment

If river water was present in the sample containers it was pipetted into a separate container and stored. The sediments were dried and homogenized to a powder in an agate mortar. Approximately 100 mg were dissolved with hot acid, identical as described in section 4.4.2.1.1, acid amounts were adjusted to the sample volume.

4.4.2.1.3 Marine sediment core GeoB6212-1

The sediment samples (average of 5 g dry weight) were washed two times with Milli Q water (18.2 MΩ) to remove residual pore water and wet sieved to collect the < 63 µm fraction used for further analyses. Approximately 100 mg of the sieved sediment fraction was decarbonated with a 15 % acetic acid solution (buffered to pH ~4 with 1 M Na-acetate) to remove the marine carbonates from the detrital material (Gutjahr et al. 2007). Leaching with hydroxylamine hydrochloride (HH) and acetic acid to remove potential authigenic Fe-Mn oxyhydroxide coatings on the sediments (Gutjahr et al. 2007) was not carried out, since leaching tests revealed no Fe-Mn oxyhydroxide coatings on the sediments, but rather a leaching of dolomite and detrital material. The detrital material was digested with hot acid, identical as described in section 4.4.2.1.1, acid amounts were adjusted to the sample volume.

4.4.2.2 Chemical separation and mass spectrometry

Sr and Pb were separated from the sample matrix using 70 µl of Sr.spec™ resin (method modified from Deniel and Pin, 2001). Nd was isolated in two steps from the sample matrix using TRU.spec™ for LREE and LN.spec™ for Nd separation (Eichrom®) (method after Pin et al., 1994). Analyses were performed on a ThermoFisher Scientific TRITON Plus thermal ionization mass spectrometer (TIMS) at the Isotope Geochemistry Laboratory at MARUM, University of Bremen, Germany. Nd and Pb isotope ratios were analyzed in the static multicollection mode and Sr isotope ratios in the dynamic multicollection mode.

Instrumental mass fractionation during Sr analyses was corrected using the stable isotope ratio of $^{86}Sr/^{88}Sr$ (= 0.1194). The analytical accuracy and external long-term reproducibility for $^{87}Sr/^{86}Sr$ of reference material NIST SRM 987 was 0.710246 ± 0.000011 (2SD, n= 24; period: May 2015 to May 2017) and is within the range of 0.710250 ± 0.000034 (2SD, n= 1245, data <0.7102 and > 0.7103 are discarded) calculated from published values analyzed by TIMS (GeoRem data base; query September 2017; http://georem.mpch-mainz.gwdg.de). Instrumental mass fractionation during Nd measurements was corrected using the stable isotope ratio of $^{146}Nd/^{144}Nd$ (= 0.7219). The analytical accuracy and external long-term reproducibility for $^{143}Nd/^{144}Nd$ for reference material JNdi-1 was 0.512093 ± 0.000009 (2SD, n= 27; period: May 2015 to May 2017) and is within the calculated range of 0.512106 ± 0.000027 (2 SD, n = 211, data <0.51204 and >0.51217 are discarded) analyzed by TIMS (GeoRem data base; query September 2017; http://georem.mpch-mainz.gwdg.de).

The $^{143}Nd/^{144}Nd$ isotope ratio is commonly presented in the ε_{Nd} notation (ε_{Nd} = {[($^{143}Nd/^{144}Nd$)$_{sample}$ / ($^{143}Nd/^{144}Nd$)$_{CHUR}$]-1}*10000) relative to the Chondritic Uniform Reservoir (CHUR) with a value of $^{143}Nd/^{144}Nd$= 0.512638 (Wasserburg and DePaolo, 1979). Pb isotope ratios were corrected for instrumental mass fractionation using 0.1 % per atomic mass unit based on the repeated analyses of NIST SRM 981. The reproducibility including the correction for mass fractionation is better than 0.1 % of the respective ratio, which is the assumed uncertainty on the Pb isotope ratios.

Sr, Nd and Pb concentrations of the SPM were measured with a high-resolution inductively coupled plasma mass spectrometer (HR-ICP-MS, Thermo Finnigan Element2, Germany) at the Petrology of the Ocean Crust Laboratory, University of Bremen, Germany. The analyses were conducted in a 20,000-fold diluted aliquot in low resolution mode using indium and thallium to correct for instrumental mass bias. International reference materials (BCR-2, BHVO-2) were used to check for accuracy (< 9 %, 2SD) and precision (< 2.5 %, 2SD).

4.5 Results

Sr, Nd and Pb isotopic compositions and concentrations for the river SPM are listed in Table 19 and 21 and for the riverbank and bed sediments in Table 20 and 22. Sr, Nd and Pb isotopic compositions for the detrital fraction of marine gravity core GeoB6212-1 are summarized in Table 23.

Table 21 Sr, Nd and Pb isotopic compositions for river suspended particulate matter of the Brazilian Río de la Plata drainage basin. Uncertainties ($2SD_{mean}$) are given for the last digit.

Sample name	River	Sub drainage basin	$^{87}Sr/^{86}Sr$	$^{143}Nd/^{144}Nd$	ε_{Nd}	$^{206}Pb/^{204}Pb$[a]	$^{207}Pb/^{204}Pb$[a]	$^{208}Pb/^{204}Pb$[a]
NH PL2	Paraná (Paranaíba x Grande)	upper Paraná	0.714894(6)	0.512199(4)	-8.6(1)	18.37	15.59	38.32
NH PL3	Paraná (Paranaíba x Grande)	upper Paraná	0.714243(6)	0.51223(1)	-7.9(3)	18.38	15.60	38.31
NH PL4	Paranaíba	upper Paraná	0.716344(6)	0.512227(5)	-8.0(1)	18.27	15.56	38.11
NH PL5	Paranaíba	upper Paraná	0.716598(7)	0.512234(6)	-7.9(1)	18.35	15.60	38.30
NH PL7	Grande	upper Paraná	0.713174(5)	0.51222(1)	-8.2(2)	18.31	15.58	38.33
NH PL8	Grande	upper Paraná	0.712944(8)	0.51222(1)	-8.2(2)	18.36	15.61	38.48
NH PL10	Tietê	upper Paraná	0.713168(6)	0.51211(4)	-10.3(8)	18.43	15.61	38.39
NH PL11	Tietê	upper Paraná	0.713106(6)	0.51190(1)	-14.3(2)	18.38	15.58	38.27
NH PL13	Paraná (x Tietê, near)	upper Paraná	0.713868(8)	0.51207(1)	-11.0(3)	18.41	15.62	38.36
NH PL14	Paraná (x Tietê, near)	upper Paraná	0.714908(7)	0.51189(1)	-14.6(2)	18.40	15.61	38.33
NH PL16	Paraná (x Tietê, far)	upper Paraná	0.716289(6)	-	-	18.00	15.56	37.90
NH PL17	Paraná (x Tietê, far)	upper Paraná	0.71663(5)	0.512153(4)	-9.5(1)	18.31	15.60	38.41
NH PL19	Paraná (x Paranapanema)	upper Paraná	0.716959(7)	0.512217(8)	-8.2(2)	18.35	15.59	38.36
NH PL20	Paraná (x Paranapanema)	upper Paraná	0.716982(4)	0.51224(2)	-7.7(3)	18.39	15.58	38.37
NH PL22	Paranapanema	upper Paraná	0.715716(5)	0.51227(2)	-7.2(3)	18.37	15.58	38.35
NH PL23	Paranapanema	upper Paraná	0.715660(6)	0.512272(6)	-7.1(1)	18.34	15.57	38.30
NH PL25	Paraná (x Iguaçu)	upper Paraná	0.715550(6)	0.512214(8)	-8.3(2)	18.40	15.59	38.38
NH PL26	Paraná (x Iguaçu)	upper Paraná	0.715368(6)	0.512228(7)	-8.0(1)	18.40	15.58	38.37
NH PL28	Iguaçu	upper Paraná	0.713136(5)	0.512286(5)	-6.9(1)	18.42	15.57	38.39
NH PL29	Iguaçu	upper Paraná	0.712635(5)	0.512288(8)	-6.8(2)	18.28	15.55	38.20
NH PL31	Uruguay	Uruguay	0.710902(6)	0.512339(3)	-5.8(1)	18.43	15.57	38.40
NH PL33	Uruguay	Uruguay	0.712899(6)	0.512331(6)	-6.0(1)	18.58	15.62	38.61

[a]Uncertainties ($2SD_{mean}$) are 0.1 %.

Table 22 Sr, Nd and Pb isotopic compositions for river bed sediment of the Argentinian and Bolivian part of the Río de la Plata drainage basin and the Paraguay drainage basin. Uncertainties ($2SD_{mean}$) are given for the last digit.

Sample name	River	Sub drainage basin	$^{87}Sr/^{86}Sr$	$^{143}Nd/^{144}Nd$	ε_{Nd}	$^{206}Pb/^{204}Pb$[a]	$^{207}Pb/^{204}Pb$[a]	$^{208}Pb/^{204}Pb$[a]
CAL2	Calchaqui	Salado	0.723398(5)	0.512164(8)	-9.2(2)	18.56	15.59	38.26
CAL4	Calchaqui	Salado	0.728250(5)	0.51216(2)	-9.3(3)	18.50	15.63	38.37
CAL7	San Lucas	Salado	0.727262(6)	0.51216(2)	-9.3(3)	19.08	15.64	38.75
CAL8	San Lucas	Salado	0.727075(5)	0.512148(7)	-9.6(1)	18.56	15.62	38.55
CAL11	La Salamanka	Salado	0.727159(7)	0.512149(9)	-9.5(2)	18.57	15.61	38.36
CAL14	Calchaqui	Salado	0.721163(6)	-	-	18.98	15.63	39.21
RT3	Toro	Salado	0.728616(7)	0.512064(4)	-11.2(1)	18.91	15.64	39.01
TB1	Tolombon	Salado	0.715001(5)	0.512137(4)	-9.8(1)	18.89	15.63	39.13
RC	Rio Clara (Brazil, to Rio Paraguay)	Paraguay	0.77954(3)	0.511946(5)	-13.5(1)	19.10	15.70	39.12
RA2	Rio Atocha	Pilcomayo	0.711210(5)	0.512250(5)	-7.6(1)	18.89	15.63	38.95
RBL1	Rio Blanco	Pilcomayo	0.715833(6)	0.512061(4)	-11.3(1)	18.79	15.62	38.81
RGD1	Rio Grande	Bermejo	0.721047(6)	0.512114(4)	-10.2(1)	18.82	15.62	38.80
RGD3	Rio Grande	Bermejo	0.721129(7)	0.512129(6)	-9.9(1)	18.71	15.61	38.60
RP1	Rio Pilcomayo	Pilcomayo	0.713099(7)	0.512089(5)	-10.7(1)	18.84	15.63	38.91
RTZ1	Rio Tupiza	Pilcomayo	0.715715(5)	0.512041(4)	-11.6(1)	18.73	15.64	38.85
BM3	Ruta Nacional 34, nahe Embarcacion	Bermejo	0.733542(8)	0.512018(4)	-12.1(1)	19.11	15.66	39.15
BM4	Ruta Nacional 34, nahe Embarcacion	Bermejo	0.733073(6)	0.511981(5)	-12.8(1)	19.41	15.68	39.69
BU1	Salar de Uyuni	-	0.709162(6)	-	-	-	-	-
BU3	Salar de Uyuni, Ojos de Salar	-	0.71037(5)	-	-	18.47	15.60	38.51

[a]Uncertainties ($2SD_{mean}$) are 0.1 %.

Table 23 Sr, Nd and Pb isotopic composition for sediment core GeoB16224-1. Uncertainties ($2SD_{mean}$) are given for the last digit.

Sample depth [cm]	Age [cal ka BP]	$^{87}Sr/^{86}Sr$	$^{143}Nd/^{144}Nd$	ε_{Nd}	$^{206}Pb/^{204}Pb$[a]	$^{207}Pb/^{204}Pb$[a]	$^{208}Pb/^{204}Pb$[a]
10	9.8	0.712068(6)	0.512248(6)	-7.6(1)	18.69	15.70	38.82
30	10.3	0.711125(6)	0.512250(7)	-7.6(1)	18.70	15.65	38.78
50	11.0	0.718930(4)	0.512128(3)	-9.9(1)	18.70	15.63	38.72
65	11.6	0.717509(6)	0.512154(5)	-9.4(1)	18.68	15.64	38.70
75	12.2	0.718628(5)	0.512132(4)	-9.9(1)	18.61	15.62	38.58
85	12.7	0.717885(6)	0.512133(4)	-9.9(1)	18.68	15.63	38.69
95	13.3	0.7245(3)	0.512145(6)	-9.6(1)	18.72	15.66	38.80
110	14.1	0.717627(4)	0.512124(6)	-10.0(1)	18.65	15.63	38.67
130	14.6	0.717957(8)	0.512138(3)	-9.8(1)	18.73	15.64	38.75
150	15.0	0.718010(4)	0.512154(4)	-9.4(1)	18.52	15.62	38.45
170	15.6	0.717224(5)	0.512125(3)	-10.0(1)	18.70	15.63	38.71
191	16.4	0.717074(7)	0.512138(3)	-9.8(1)	18.71	15.63	38.74
210	17.1	0.715802(7)	0.512151(4)	-9.5(1)	18.70	15.62	38.70
230	17.8	0.716174(6)	0.512151(4)	-9.5(1)	18.73	15.63	38.75
250	18.5	0.718016(6)	0.512103(5)	-10.4(1)	18.82	15.65	39.01
270	19.1	0.717502(5)	0.512061(5)	-11.3(1)	18.91	15.66	39.05
294	19.8	0.713977(9)	0.512160(4)	-9.3(1)	18.64	15.62	38.59
309	20.3	0.715888(4)	0.512159(4)	-9.3(1)	18.71	15.63	38.74
328	20.8	0.716273(6)	0.512151(5)	-9.5(1)	18.62	15.61	38.59
348	21.2	0.717392(5)	0.512179(7)	-9.0(1)	18.69	15.61	38.66
368	21.7	0.715643(6)	0.512141(6)	-9.7(1)	18.73	15.63	38.77
392	22.1	0.713380(4)	0.512156(4)	-9.4(1)	18.63	15.61	38.58
410	22.4	0.715754(4)	0.512143(6)	-9.7(1)	18.71	15.61	38.68

[a]Uncertainties ($2SD_{mean}$) are 0.1 %.

Table 23 (continued).

Sample depth [cm]	Age [cal ka BP]	$^{87}Sr/^{86}Sr$	$^{143}Nd/^{144}Nd$	ε_{Nd}	$^{206}Pb/^{204}Pb^{a}$	$^{207}Pb/^{204}Pb^{a}$	$^{208}Pb/^{204}Pb^{a}$
430	22.7	0.716667(7)	0.512118(2)	-10.1(1)	18.72	15.63	38.80
450	23.0	0.718534(5)	0.512129(5)	-9.9(1)	18.67	15.63	38.67
465	23.3	0.715955(6)	0.512149(3)	-9.5(1)	18.70	15.64	38.71
476	23.5	0.716169(8)	0.512148(6)	-9.6(1)	18.71	15.65	38.78
485	23.6	0.715023(5)	0.512157(7)	-9.4(1)	18.68	15.65	38.70
495	23.8	0.714787(6)	0.512159(5)	-9.3(1)	18.70	15.63	38.70
510	24.1	0.716864(5)	0.512153(4)	-9.5(1)	18.73	15.65	38.80
530	24.5	0.715194(4)	0.512175(4)	-9.0(1)	18.68	15.67	38.74
550	24.9	0.71469(1)	0.51214(1)	-9.6(2)	18.70	15.64	38.75
570	25.3	0.714688(6)	0.512161(6)	-9.3(1)	18.69	15.62	38.64
591	25.7	0.714298(4)	0.512191(4)	-8.7(1)	18.68	15.62	38.71
610	26.0	0.716064(4)	0.512145(5)	-9.6(1)	18.67	15.61	38.64
630	26.3	0.713607(7)	0.512183(5)	-8.9(1)	18.71	15.64	38.71
650	26.6	0.714772(6)	0.512169(7)	-9.1(1)	18.70	15.62	38.70
670	26.9	0.713662(5)	0.512174(5)	-9.1(1)	18.70	15.66	38.75
695	27.4	0.713509(4)	0.512195(6)	-8.6(1)	18.73	15.62	38.71
710	27.7	0.712845(4)	0.512221(6)	-8.1(1)	18.70	15.63	38.66
730	28.1	0.712366(8)	0.512201(6)	-8.5(1)	18.71	15.62	38.66
740	28.4	0.711835(4)	0.51224(1)	-7.7(2)	18.72	15.62	38.68
750	28.6	0.712023(5)	0.51225(2)	-7.6(3)	18.69	15.62	38.62
760	28.8	0.712699(6)	0.512228(6)	-8.0(1)	18.68	15.62	38.61
771	29.0	0.713191(4)	0.51220(1)	-8.6(2)	18.71	15.61	38.65

4.5.1 Pb isotopic composition of the river SPM and river bed sediments

The Pb isotopic composition of the sediments of the LPDB forms two clusters (Fig. 22). Cluster A consists of the samples from Salado, Bermejo, Pilcomayo and Paraguay Rivers with isotopic signatures of >= 18.5 for $^{206}Pb/^{204}Pb$ and >= 15.61 for $^{207}Pb/^{204}Pb$. Their $^{208}Pb/^{204}Pb$ value varies from 38.3 to 39.7. The upper Paraná and Uruguay Rivers samples form cluster B with isotopic signatures of < 18.50 for $^{206}Pb/^{204}Pb$ and < 15.62 for $^{207}Pb/^{204}Pb$. Their $^{208}Pb/^{204}Pb$ value varies between 37.9 and 38.6.

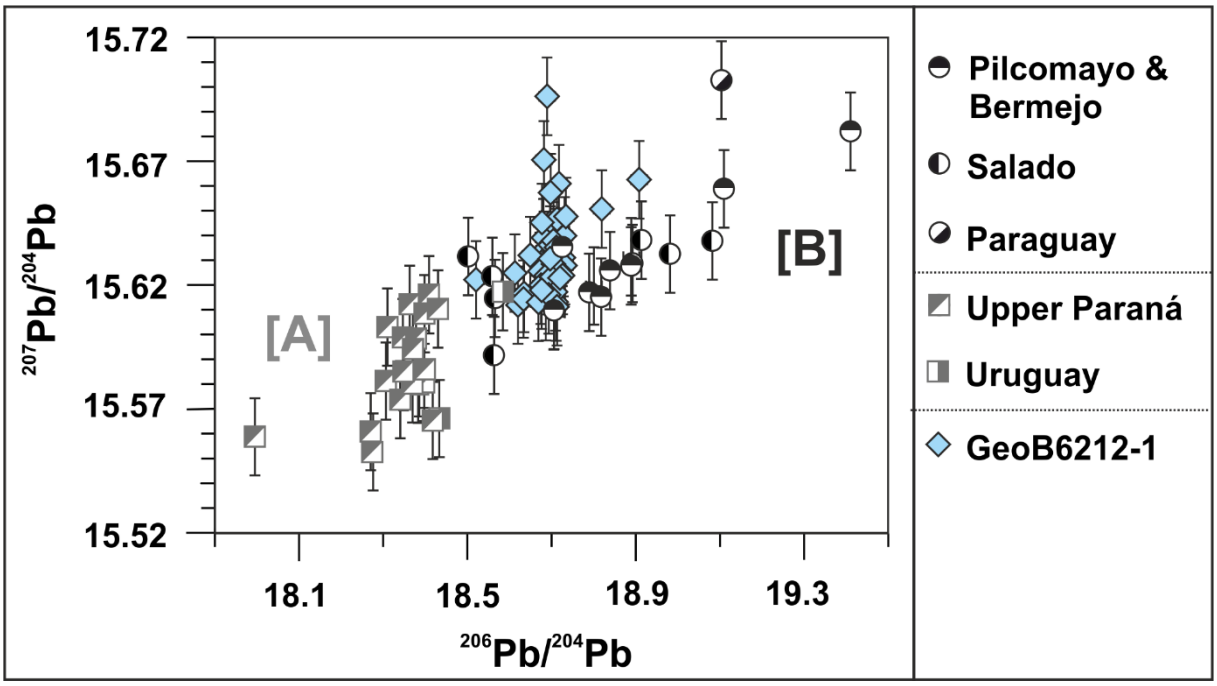

Fig. 22. $^{206}Pb/^{204}Pb$ vs.$^{207}Pb/^{204}Pb$ of river suspended particulate matter, river bed sediments and marine sediment core GeoB6212-1. The Río de la Plata drainage basin tributaries form two clusters: [A] Salado, Bermejo, Pilcomayo and Paraguay Rivers and [B] upper Paraná and Uruguay Rivers. Samples from GeoB6212-1 plot in cluster [B].

4.5.2 Nd and Sr isotopic composition of the river SPM and river bed sediments

The Salado River drainage basin sediments have ε_{Nd} values with an average of -9.5 ± 0.4 (2SD), with an outlier of -11.2 ± 0.1 ($2SD_{mean}$). The Pilcomayo and Bermejo Rivers drainage basin sediments have average ε_{Nd} values of -11.2 ± 2.1 (2SD) with an outlier of -7.6 ± 0.1 ($2SD_{mean}$) (Fig. 23). The samples from the upper Paraná River main channel as well as its tributaries have ε_{Nd} values between -7.1 and -8.6. An exceptions are the samples from the Iguaçu River with an average ε_{Nd} value of -5.9 ± 0.2 (2SD) and the samples from the Tietê River (including the upper Paraná River main channel samples in proximity to the confluence) with ε_{Nd} varying from -9.5 to -14.6. The samples from the Uruguay River drainage basin have the most radiogenic ε_{Nd} values (average of -5.9 ± 0.1; 2SD). The sample from the Paraguay River drainage basin has an unradiogenic ε_{Nd} values of -13.5 ± 0.1 ($2SD_{mean}$) and the most radiogenic $^{87}Sr/^{86}Sr$ of 0.77954 ± 0.00003 ($2SD_{mean}$). The samples from the Pilcomayo and Bermejo Rivers drainage basin show a wide spread in their $^{87}Sr/^{86}Sr$ isotopic signature from

0.711 to 0.734. The Salado River drainage basin samples have an average $^{87}Sr/^{86}Sr$ value of 0.726 ± 0.006 (2SD), with an outlier of 0.715001 ± 0.000005 ($2SD_{mean}$). The upper Paraná River drainage basin samples have average $^{87}Sr/^{86}Sr$ isotopic signatures of 0.715 ± 0.003 (2SD). The Uruguay River drainage basin samples have the least radiogenic $^{87}Sr/^{86}Sr$ values (average of 0.712 ± 0.003; 2SD).

4.5.3 Sr, Nd, Pb isotopic composition of detrital sediment (core GeoB6212-1)

The $^{87}Sr/^{86}Sr$ isotopic composition (Fig. 24) has the least radiogenic values (average of 0.7119 ± 0.0009; 2SD) from 750 to 730 and from 30 to 10 cm. The most radiogenic value of 0.7245 ± 0.0003 ($2SD_{mean}$) occurs at 95 cm. From 730 to 450 cm the signal continuously shifts from less radiogenic (0.71237 ± 0.00001; $2SD_{mean}$) to more radiogenic values (0.71853 ± 0.00001; $2SD_{mean}$). From 450 to 50 cm the $^{87}Sr/^{86}Sr$ signal has an average of 0.717 ± 0.004 (2SD), with two small peaks with values of < 0.714 at 392 and 294 cm. From 730 to 430 cm the Nd isotope signal has a continuous shift from radiogenic (-8.5 ± 0.1; $2SD_{mean}$) to less radiogenic (-10.1 ± 0.1; $2SD_{mean}$) ε_{Nd} values (Fig. 24). From 410 to 50 cm the ε_{Nd} signal has an average of -9.7 ± 0.9 (2SD), with a peak to the least radiogenic value of -11.3 ± 0.1 ($2SD_{mean}$) at 270 cm. The most radiogenic ε_{Nd} values <= -8.0 are from 760 to 740 and from 30 to 10 cm. The Pb isotope curve has average values of 18.70 ± 0.11 (2SD) for $^{206}Pb/^{204}Pb$, of 15.63 ± 0.03 (2SD) for $^{207}Pb/^{204}Pb$ and of 38.71 ± 0.20 (2SD) for $^{208}Pb/^{204}Pb$ (Fig. 24). Additionally, from 270 to 250 cm a peak to the most radiogenic values of > 18.73 for $^{206}Pb/^{204}Pb$ and of > 38.82 for $^{208}Pb/^{204}Pb$ and at 150 cm a peak to the least radiogenic of < 18.61 for $^{206}Pb/^{204}Pb$ and of < 38.58 for $^{208}Pb/^{204}Pb$. These peaks are not visible in the $^{207}Pb/^{204}Pb$ isotope curve, but there is a shift to the most radiogenic value of > 15.67 at 10 cm.

4.6 Discussion

4.6.1 Modern Sr, Nd and Pb isotopic signatures of the Río de la Plata drainage basin

Surface sediment samples from the Río de la Plata estuary have average ε_{Nd} values of -9.6 ± 1.5 (2SD) and average Pb isotope values of 18.67 ± 0.12 (2SD) for $^{206}Pb/^{204}Pb$, of 15.65 ± 0.02 (2SD) for $^{207}Pb/^{204}Pb$, and of 38.70 ± 0.16 (2SD) for $^{208}Pb/^{204}Pb$ (de Mahiques et al., 2008). They plot in the area of the Andean draining river signature conducted in this study (Salado, Pilcomayo and Bermejo Rivers) (Fig. 23), which confirms that the main sediment supplier (50 to 70 % of the SPM load) for the LPDB today are the Andes (Depetris et al., 2003). The literature Sr isotopic signatures for the Río de la Plata estuary varies from 0.73 to 0.71 (Biscaye and Dasch, 1971) matching with the Andean river signature as well.

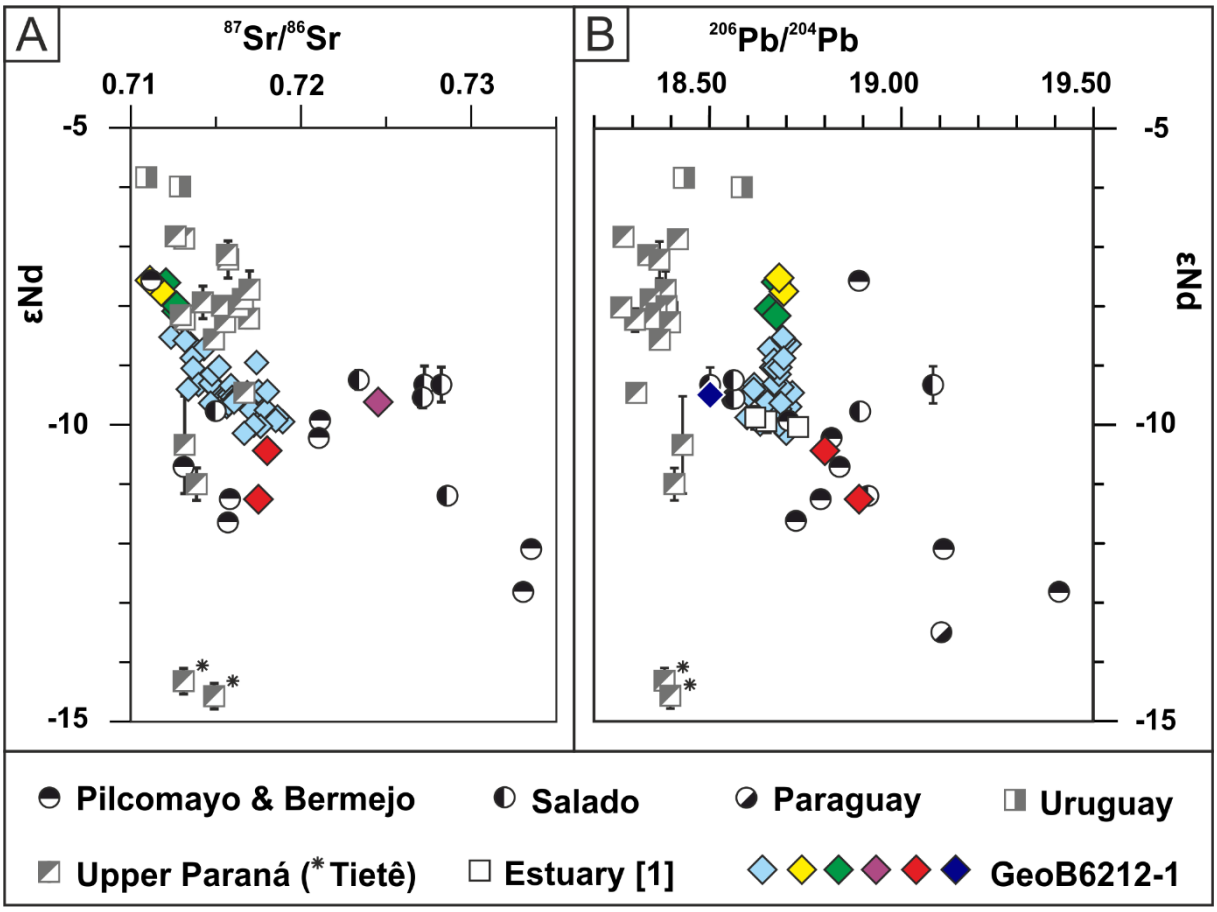

Fig. 23. Panel A: $^{87}Sr/^{86}Sr$ vs. ε_{Nd} of river suspended particulate matter, river bed sediment and marine sediment core GeoB6212-1. Panel B: $^{206}Pb/^{204}Pb$ vs. ε_{Nd} of river suspended particulate matter, river bed sediment and marine sediment coreGeoB6212-1. Pb and Nd literature values of the estuary [1] are from de Mahiques et al. (2008). Diamonds represent the GeoB6212-1 results with the average core values marked with a light blue diamond. Distinct peaks in the down-core record are marked in yellow, green, purple, red and dark blue, also highlighted in Fig. 24.

4.6.2 Changes in sediment supply during the last 30 kyr

The prominent shift in the Sr and Nd isotopic signatures around 10 cal ka BP (Fig. 24) can also be seen in ε_{Nd} results of marine sediment core GeoB6211-2 (measured by Lantzsch et al., 2014; Fig. S1, supplementary data). However, there is an offset between the calculated ages of the shift of about 1,500 years. Either there is a lack in sediment deposition between core site GeoB6211-2 and GeoB6212-1 or the age models are not in total agreement with each other.

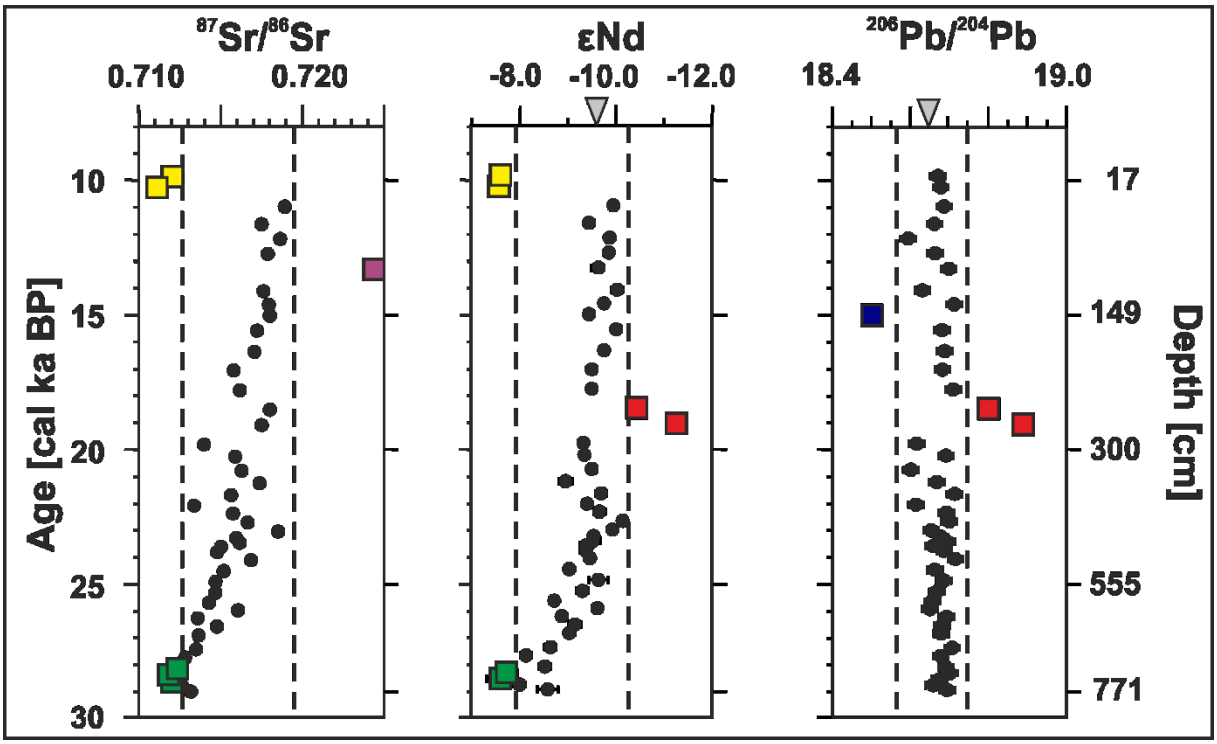

Fig. 24. Down-core changes in $^{87}Sr/^{86}Sr$, ε_{Nd} and $^{206}Pb/^{204}Pb$ of marine sediment core GeoB6212-1. The dotted line is used to highlight dominant shifts in the down-core records. The colored squares (green, red, dark blue, purple and yellow) highlight distinct peaks and are additionally marked in Fig. 23. The grey triangles mark the modern average Río de la Plata estuary sediment signal (de Mahiques et al., 2008).

4.6.2.1 10 cal ka BP shift – Sediment input from southern Argentina

At around 10 cal ka BP years there is an abrupt shift from 0.718930 ± 0.000004 ($2SD_{mean}$) to 0.711125 ± 0.000006 ($2SD_{mean}$) for $^{87}Sr/^{86}Sr$ and from -9.9 ± 0.1 ($2SD_{mean}$) to -7.6 ± 0.1 ($2SD_{mean}$) for ε_{Nd} (Fig. 24). The $^{206}Pb/^{204}Pb$ and $^{208}Pb/^{204}Pb$ signals have no significant variation. However, the $^{207}Pb/^{204}Pb$ signal, shows a shift to more radiogenic values of > 15.65. The time period at 10 cal ka BP marks the end of the Late Glacial and the beginning of the Holocene (Early Holocene). Comparing the shift in the core signal with the isotopic signatures of the different source areas of the Río de la Plata drainage basin, the shift points towards a higher input from the Uruguay River drainage basin (southeast sector of the LPDB) (Fig. 23). During the late Pleistocene (14.8 to 10.0 cal ka BP) the southeastern part of Uruguay had dry and cool climate conditions. With the onset of the Holocene the conditions changed and the early

Holocene (10.0 to 6.6 cal ka BP) was warmer and more humid (Iriarte, 2006). This could have led to higher precipitation rates and therefore higher physical erosion rates, allowing the Uruguay River to supply more sediment to the Río de la Plata estuary. However, there are several studies indicating a wetter episode starting at some time between 10.0 and 7.3 cal ka BP in whole southcentral Brazil and northeastern Argentina (Stevaux et al., 2000 and therein). This implies, that not only the Uruguay River, but also the Paraná and Paraguay Rivers would supply more sediment during this time hence and a shift would not be visible. Furthermore, a signal shift due to a higher sediment supply should correlate with an increase in the sedimentation rate. At 10 cal ka BP the sedimentation rate for core GeoB6212-1 has an abrupt decrease (Campos et al., 2017). Higher sediment supply due to higher precipitation from a different part of the LPDB can be excluded for the observed shift at 10 cal ka BP. During the rising sea level at the Early to Middle Holocene boundary, sediment from further down the coast of Argentina (transported by the Subantarctic shelf water (SASW)) got deposited at the Rio Grande cone (Lantzsch et al., 2014; Razik et al., 2013). The shift observed at 10 cal ka BP in our Sr and Nd curve looks matches well with the shift in the Nd data that Lantzsch et al. (2014) published. Sediment transported from southern Argentina has average ε_{Nd} values of -3.2 ± 1.1 (2SD) (Lantzsch et al., 2014). Mixed with the average LPDB river sediment it would shift the signals in the right direction. Hence, we agree with Lantzsch et al. (2014) that this shift is due to the addition of material transported from southern Argentina. However, we suggest that the deposit of Argentinian sediments already started around 10 to 9 cal ka BP.

4.6.2.2 Sr peak at 13.5 cal ka BP - Strong SASM in the Younger Dryas

Around 13.5 cal ka BP the Sr curve has a peak to its most radiogenic value of 0.7245 ± 0.0003 ($2SD_{mean}$) for $^{87}Sr/^{86}Sr$ (Fig. 24). Comparing this value with possible source areas of the LPDB (Fig. 23), the Andean draining rivers, more precisely a higher input from the Argentinian part of the Andes (Salado River), are a possible source area. The peak is not visible in the Nd and Pb curve, as the sediment from the Salado River drainage basin has similar Nd and Pb isotopic signatures to the isotopic signature of the final mixed sediment supplied to the Atlantic Ocean. At 14.5 cal ka BP a sudden global warming (Bølling-Allerød interstadial, B/A) started that forced large melting events of the Pleistocene ice sheets in the Northern Hemisphere (Severinghaus and Brook, 1999). This event was probably induced by a strong AMOC (Chiessi et al., 2008). A strong AMOC would lead to a northwards shift of the ITCZ and SASM, reducing the amount of precipitation in the northern part of the LPDB (Fig. 25). Therefore, we believe that the Sr peak does not represent the B/A, but the Younger Dryas (12.9 to 11.7 cal ka BP) (Brauer et al., 2008; Rasmussen et al., 2006). During the Younger Dryas it was very humid in South America (Wang et al., 2006). A weak AMOC induced a southwards shift of the ITCZ (Kienast et al., 2006), inducing higher precipitation in the northern part of the LPDB (Fig. 25). Higher precipitation led to higher physical erosion and higher sediment amounts in the rivers,

especially in rivers with a high relief like the Andean draining rivers. Marine sediment core GeoB6211-2, located very close to GeoB6212-1, does not show any paleoclimate signal during the Younger Dryas (Razik et al., 2013). However, the investigation was done using magnetic properties. The sediments transported by the Andean draining rivers (especially the Bermejo River) are mostly diamagnetic quartz and feldspar. Those minerals would have limited to no influence on the rock magnetic properties. If a paleoclimate event like the YD would lead to more precipitation in the Andes, thus more sediment supply from these areas, it would not be visible using rock magnetic properties.

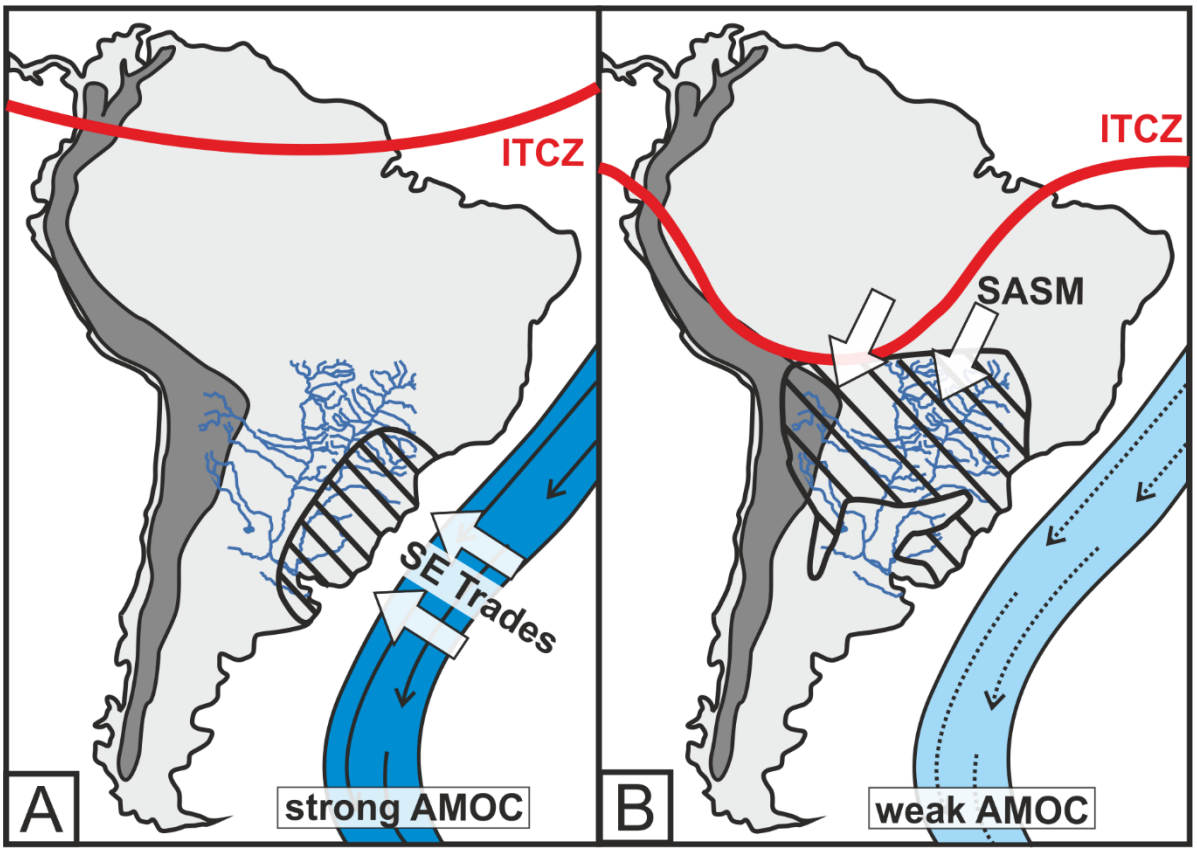

Fig. 25. Interaction of the Atlantic Meridional Overturning Circulation (AMOC), the Intertropical Convergence Zone (ITCZ) and the precipitation in the Río de la Plata drainage basin (LPDB). The AMOC is shown as a broad blue (representing cold water) bar, with arrows indicating the main flow direction. The rivers of the LPDB are outlined in blue. The Andes are highlighted in dark grey. Panel A: During strong AMOC the ITCZ (red line) migrates northward. The southeast trade winds (SE Trades, white arrows) bring precipitation (shaded area) to the southeastern part of the LPDB. Panel B: During weak AMOC the ITCZ (red line) migrates southward. The South American Summer Monsoon (SASM, white arrows) brings precipitation (shaded area) to the northern part of the LPDB.

4.6.2.3 Pb Peak at 15 cal ka BP - Strong SE Trades in the Bølling-Allerød

At 15 cal ka BP the Pb signal has a peak to the least radiogenic values of 18.52 ± 0.02 ($2SD_{mean}$) for $^{206}Pb/^{204}Pb$ and of 38.45 ± 0.04 ($2SD_{mean}$) for $^{208}Pb/^{204}Pb$ (Fig. 24). During this time the sedimentation rate records an increase from 25 to 65 cm/ka (Campos et al., 2017). The sediment from the eastern part of the basin (Upper Paraná and Uruguay Rivers drainage

basin) has average values of < 18.5 for $^{206}Pb/^{204}Pb$. A higher input from this area could produce the observed shift and would also explain the higher sedimentation rate. The Sr signal for these drainage areas has some overlap with the Andean draining rivers (Fig. 23), a shift would not necessarily be visible. However, with higher input from the upper Paraná and Uruguay Rivers drainage basins, the Nd signal should indicate a shift to more radiogenic ε_{Nd} values, which is not the case. The upper Paraná River drainage basin has one tributary (the Tietê River) that has similar Sr and Pb signatures than the other Paraná River tributaries, but the Nd signature is less radiogenic (Fig. 23). Therefore, a higher input from the Tietê River (with an unradiogenic ε_{Nd} signature) mixed with the remaining upper Paraná River tributaries and the Uruguay River (with a radiogenic ε_{Nd} signature) would mask a possible shift in the Nd curve. At the start of the Bølling-Allerød (B/A) interstadial (14.7 cal ka BP) the temperature rise in the Northern Hemisphere reinstated the AMOC (Thiagarajan et al., 2014). A strong AMOC induces the northwards shift of the ITCZ leading to dryer condition in the norther part of the LPDB (Fig. 25). Concomitantly, in the second part of the B/A the SE trade winds were strengthened (Kim et al., 2003), bringing more moisture to the southeastern part (Uruguay, Iguaçu and Tietê Rivers) of the LPDB.

4.6.2.4 Peaks at 20 to 18 cal ka BP - Strong SASM in the Heinrich Stadial 1

The Nd and Pb signal show distinct peaks to less (ε_{Nd}: -11.3 ± 0.1, $2SD_{mean}$) and more ($^{206}Pb/^{204}Pb$: 18.91 ± 0.02, $2SD_{mean}$) radiogenic values. The peak in the Sr signal (to more radiogenic values; $^{87}Sr/^{86}Sr$: 0.717502 ± 0.000005, $2SD_{mean}$) is smaller but still significant (Fig. 24). The Heinrich Stadial 1 (HS1) is dated from 18.1 to 14.7 cal ka BP (Sarnthein et al., 2001). The peaks appear a little earlier, but we assume some age model uncertainties and associate this peaks with the HS1. A possible source area in the LPDB for this peak are the Andean draining rivers, more precisely the Bermejo and Pilcomayo Rivers (draining the Bolivian Andes) (Fig. 23). During the HS1 the SASM was strong (Chiessi et al., 2015; Campos et al., 2017). A strong SASM means a high amount of precipitation in the western (Andes) and northeastern (Paraná River drainage basin) part of the LPDB. Higher precipitation in areas prone to physical erosion, like the Andes with a high relief, leads to higher sediment amounts being transported in the respective rivers. A higher sediment input from the Andes during the HS1 is very reasonable. The peaks are more pronounced in Nd and Pb and smaller in Sr, because the Andean draining rivers (Pilcomayo, Bermejo and Salado Rivers) and the upper Paraná River drainage basin have differences in the Nd and Pb isotopic signature and overlaps in the Sr isotopic signature.

4.6.2.5 29 to 28 cal ka BP shift (Strong SE Trades, strong AMOC)

At 29 to 28 cal ka BP the $^{87}Sr/^{86}Sr$ has values of < 0.712 and ε_{Nd} values of > -8 and shows a gradual development to more radiogenic Sr values ($^{87}Sr/^{86}Sr$: 0.716169 ± 0.000008; $2SD_{mean}$) and less radiogenic Nd values (ε_{Nd}: -9.6 ± 0.1; $2SD_{mean}$) until 23.5 cal ka BP (Fig. 24). The shift

looks similar to the shift at 10 cal ka BP in the down-core record. In contrast to the rising sea level in the Holocene, at 30 cal ka BP the sea level was around 80 m below today and further regressed until 27 cal ka BP to 120 m below today (Peltier and Fairbanks, 2006). The Subtropical shelf water (STSW) was strong during that time period (Lantzsch et al., 2014), making the deposit of sediment from southern Argentina to the GeoB6212-1 core site relatively unreasonable. We eliminate sediment from southern Argentina as the source for the observed shift at 29 to 28 cal ka BP. The sedimentation rate for core GeoB6212-1 increased from 10 cm/ka to 110 cm/ka between 30 and 26 cal ka BP (Campos et al., 2017), pointing to a high amount of sediment being deposited at the core site during that time. Excluding the material from southern Argentina, due to the low sea level and strong STSW current, it's probable to assume the high amount of sediment came from the LPDB itself. During low sea level stands the LPDB material was transported through the Río de la Plata paleo valley (Lantzsch et al., 2014). To shift the signal to the observed values the eastern part of the basin (southeastern Brazil, drainage basin of the Uruguay River) would be a good provenance fit (Fig. 23). Stronger precipitation in this area during 29 to 28 cal ka BP would lead to a higher sediment supply. During austral winter precipitation, the SE trade winds bring moisture to the southeastern part of Brazil. Therefore, this part of the LPDB has the highest seasonal precipitation during winter (Piovano et al., 2009) (Fig. 20). Additionally, a strong Atlantic Meridional Overturning Circulation (AMOC) induces a northwards migration of the Intertropical Convergence Zone (ITCZ), weakening the convection along the South American Convergence Zone (SACZ), displacing the major part of the South American Summer Monsoon (SASM) precipitation north (outside) of the LPDB (Chiessi et al., 2009) (Fig. 25). A weak AMOC occurs during Heinrich Stadials, due to warmer climate in the Northern Hemisphere that inputs freshwater cooling the North Atlantic in the high latitudes (Campos et al., 2017). Therefore, it is viable to assume that in contrast a strong AMOC occurs during cold periods, for example in between Heinrich Stadials. Our observed shift occurs in between Heinrich Stadial 3 (32.7 to 29.0 cal ka BP) and Heinrich Stadial 2 (26.5 to 23.4 cal ka BP) (Goni and Harrison, 2010; Sarntheim et al., 2001).

4.7 Conclusions

In this paper, we provided a first extensive database for the radiogenic isotope signatures of the river sediment of the Río de la Plata drainage basin. The Sr, Nd and Pb isotope results distinguish three main sediment supply areas with distinct signatures: The upper Paraná River, the Uruguay River and the Andean draining rivers (Salado, Pilcomayo and Bermejo Rivers). Using those results we investigated the sediment supply situation from 30 to 10 cal ka BP for the LPDB, archived in marine sediment core GeoB6212-1. We propose a weakened AMOC and a consequential southwards shift of the ITCZ, strengthening the SASM, leading to more sediment supply from the Bolivian (HS1) and Argentinian (YD) Andes. A strengthened AMOC from 29 to 28 cal ka BP (between HS3 and HS2) and around 15 cal ka BP (B/A) led to a

northwards shifts of the ITCZ and a strengthening of the SE trades, increasing the sediment supply from the southeastern part (Uruguay, Iguaçu and Tietê Rivers drainage basin) of the LPDB. We confirm that the shift around 10 cal ka BP (to a less radiogenic Sr and more radiogenic Nd signature) is a result of additional material from southern Argentina deposited at the core site, due to a high sea level and a strong SASW.

To investigate this issue further, we recommend additional radiogenic isotope analyses of river sediment from the LPDB to better constrain the provenances. Additionally, it would be very interesting to apply radiogenic isotope analyses on marine sediment cores reaching further back in time.

4.8 Acknowledgments

This work was funded through the DFG-Research Center/Cluster of Excellence “The Ocean in the Earth System” at MARUM – Center for Environmental Sciences, University of Bremen. We thank the Meteor cruise M46/2 crew. Sample material has been provided by the GeoB Core Repository at the MARUM – Center for Marine Environmental Sciences, University of Bremen, Germany. The data reported in this paper are archived in Pangaea (www.pangaea.de). NH thanks GLOMAR – Bremen International Graduate School for Marine Sciences for support and the DAAD – German Academic Exchange Service for financial support. Furthermore, NH thanks Maria C. Catunda for her help during the sampling campaign of the Brazilian Part of the LPDB and André O. Sawakuchi for lending the sampling equipment. Prof. Dr. Simone A. Kasemann is thanked for providing the samples for the Argentinian and Bolivian part of the LPDB and Dr. Gustavo Macedo Paula-Santos is thanked for providing the sample of the Paraguay drainage basin.

4.9 References

Amsler, M. L., & Drago, E. C. (2009). A review of the suspended sediment budget at the confluence of the Paraná and Paraguay Rivers. *Hydrological Processes*, **23(22)**, 3230-3235.

Berbery, E. H., Barros, V. R. (2002). The hydrologic cycle of the La Plata basin in South America. *Journal of Hydrometeorology*, **3(6)**, 630-645.

Biscaye, P. E., & Dasch, E. J. (1971). The rubidium, strontium, strontium-isotope system in deep-sea sediments: Argentine Basin. *Journal of Geophysical Research*, **76(21)**, 5087-5096.

Brauer, A., Haug, G. H., Dulski, P., Sigman, D. M., Negendank, J. F. (2008). An abrupt wind shift in western Europe at the onset of the Younger Dryas cold period. *Nature Geoscience*, **1(8)**, 520-523.

Campos M. C., Chiessi C. M., Voigt I., Piola A. R., Kuhnert H., Mulitza S. (2017). δ 13 C decreases in the upper western South Atlantic during Heinrich Stadials 3 and 2. *Climate of the Past*, **13(4)**, 345-358.

Chiessi, C. M., Mulitza, S., Paul, A., Pätzold, J., Groeneveld, J., Wefer, G. (2008). South Atlantic interocean exchange as the trigger for the Bølling warm event. *Geology*, **36(12)**, 919-922.

Chiessi, C. M., Mulitza, S., Pätzold, J., Wefer, G., Marengo, J. A. (2009). Possible impact of the Atlantic Multidecadal Oscillation on the South American summer monsoon. *Geophysical Research Letters*, **36(21)**.

Chiessi, C. M., Mulitza, S., Mollenhauer, G., Silva, J. B., Groeneveld, J., Prange, M. (2015). Thermal evolution of the western South Atlantic and the adjacent continent during Termination 1. *Climate of the Past*, **11(6)**, 915.

Collischonn, W., Tucci, C. E. M., Clarke, R. T. (2001). Further evidence of changes in the hydrological regime of the River Paraguay: part of a wider phenomenon of climate change?. *Journal of Hydrology*, **245(1)**, 218-238.

Dávila, P. M., Figueroa, D., Müller, E. (2002). Freshwater input into the coastal ocean and its relation with the salinity distribution off austral Chile (35–55 S). *Continental shelf research*, ***22*(3)**, 521-534.

de Mahiques, M. M., Tassinari, C. C. G., Marcolini, S., Violante, R. A., Figueira, R. C. L., da Silveira, I. C. A., Burone, L., e Sousa, S. H. D. M. (2008). Nd and Pb isotope signatures on the Southeastern South American upper margin: Implications for sediment transport and source rocks. *Marine Geology*, **250(1)**, 51-63.

de Mahiques, M. M., Wainer, I. K. C., Burone, L., Nagai, R., e Sousa, S. H. D. M., Figueira, R. C. L., da Silveira, I. C. A., Bícego, M. C., Alves, D. P. V., Hammer, Ø. (2009). A high-resolution Holocene record on the Southern Brazilian shelf: paleoenvironmental implications. *Quaternary International*, **206(1)**, 52-61.

Deniel C., Pin C. (2001). Single-stage method for the simultaneous isolation of lead and strontium from silicate samples for isotopic measurements. *Analytica Chimica Acta*, **426(1)**, 95-103.

Depetris, P. J., Griffin, J. J. (1968). Suspended load in the Río de la Plata drainage basin. *Sedimentology*, **11(1-2)**, 53-60.

Depetris, P. J., Probst, J. L., Pasquini, A. I., Gaiero, D. M. (2003). The geochemical characteristics of the Paraná River suspended sediment load: an initial assessment. *Hydrological Processes*, **17(7)**, 1267-1277.

Goldstein, S. L., O'nions, R. K., Hamilton, P. J. (1984). A Sm-Nd isotopic study of atmospheric dusts and particulates from major river systems. *Earth and planetary Science letters*, **70(2)**, 221-236.

Goni, M. F. S., Harrison, S. P. (2010). Millennial-scale climate variability and vegetation changes during the Last Glacial: Concepts and terminology Introduction. *Quaternary Sci. Rev.*, **29**, 2823-2827

Gutjahr M., Frank M., Stirling C. H., Klemm V., Van de Flierdt T., Halliday A. N. (2007). Reliable extraction of a deepwater trace metal isotope signal from Fe–Mn oxyhydroxide coatings of marine sediments. *Chemical Geology*, **242(3)**, 351-370.

Gyllencreutz, R., Mahiques, M. M., Alves, D. V. P., & Wainer, I. K. C. (2010). Mid-to late-Holocene paleoceanographic changes on the southeastern Brazilian shelf based on grain size records. *The Holocene*, **20(6)**, 863-875.

Hedges, J. I., Keil, R. G., Benner, R. (1997). What happens to terrestrial organic matter in the ocean?. *Organic geochemistry*, **27(5)**, 195-212.

Henry, F., Probst, J. L., Thouron, D., Depetris, P. J., Garçon, V. (1996). Nd-Sr isotopic compositions of dissolved and particulate material transported by the Parana and Uruguay rivers during high (december 1993) and low (september 1994) water periods. *Sciences Géologiques, Bulletin*, **49(1-4)**, 89-100.

Iriarte, J. (2006). Vegetation and climate change since 14,810 14 C yr BP in southeastern Uruguay and implications for the rise of early Formative societies. *Quaternary Research*, **65(1)**, 20-32.

Kienast, M., Kienast, S. S., Calvert, S. E., Eglinton, T. I., Mollenhauer, G., François, R., Mix, A. C. (2006). Eastern Pacific cooling and Atlantic overturning circulation during the last deglaciation. *Nature*, **443(7113)**, 846.

Kim, J. H., Schneider, R. R., Mulitza, S., & Müller, P. J. (2003). Reconstruction of SE trade-wind intensity based on sea-surface temperature gradients in the Southeast Atlantic over the last 25 kyr. *Geophysical Research Letters*, **30(22)**.

Lantzsch, H., Hanebuth, T. J., Chiessi, C. M., Schwenk, T., & Violante, R. A. (2014). The high-supply, current-dominated continental margin of southeastern South America during the late Quaternary. *Quaternary Research*, **81(2)**, 339-354.

Milliman, J. D., & Meade, R. H. (1983). World-wide delivery of river sediment to the oceans. *The Journal of Geology*, **91(1)**, 1-21.

Peltier, W. R., & Fairbanks, R. G. (2006). Global glacial ice volume and Last Glacial Maximum duration from an extended Barbados sea level record. *Quaternary Science Reviews*, **25(23)**, 3322-3337.

Perez, L., García-Rodríguez, F., Hanebuth, T. J. J. (2015). Variability in terrigenous sediment supply offshore of the Rio de la Plata (Uruguay) recording the continental climatic history over the past 1200 years. *Climate of the Past Discussions*, **11(2)**.

Pin C., Briot D., Bassin C., Poitrasson F. (1994). Concomitant separation of strontium and samarium-neodymium for isotopic analysis in silicate samples, based on specific extraction chromatography. *Analytica Chimica Acta*, **298(2)**, 209-217.

Piola, A. R., Campos, E. J., Möller, O. O., Charo, M., Martinez, C. (2000). Subtropical shelf front off eastern South America. *Journal of Geophysical Research: Oceans*, **105(C3)**, 6565-6578.

Piola, A. R., Matano, R. P., Palma, E. D., Möller, O. O., Campos, E. J. (2005). The influence of the Plata River discharge on the western South Atlantic shelf. *Geophysical Research Letters*, **32(1)**.

Piovano, E. L., Ariztegui, D., Córdoba, F., Cioccale, M., Sylvestre, F. (2009). Hydrological variability in South America below the Tropic of Capricorn (Pampas and Patagonia, Argentina) during the last 13.0 Ka. In Past climate variability in South America and surrounding regions (pp. 323-351). Springer Netherlands.

Rasmussen, S. O., Andersen, K. K., Svensson, A. M., Steffensen, J. P., Vinther, B. M., Clausen, H. B., Siggaard-Andersen, M.-L., Johnsen, S. L., Larsen, L. B., Dahl-Jensen, D., Bigler, M., Röthlisberger, R., Fischer, H., Goto-Azuma, K., Hansson, M. E., Ruth, U. (2006). A new Greenland ice core chronology for the last glacial termination. *Journal of Geophysical Research: Atmospheres*, **111(D6)**.

Razik, S., Chiessi, C. M., Romero, O. E., & von Dobeneck, T. (2013). Interaction of the South American Monsoon System and the Southern Westerly Wind Belt during the last 14kyr. *Palaeogeography, Palaeoclimatology, Palaeoecology*, **374**, 28-40.

Sarnthein, M., Stattegger, K., Dreger, D., Erlenkeuser, H., Grootes, P., Haupt, B. J., Jung, S., Kiefer, T., Kuhnt, W., Pflaumann, U., Schäfer-Neth, C., Schulz, H., Schulz. M., Seidov, D., Simstich, J., van Kreveld, S., Vogelsang, E., Völker, A., Weinelt, M. (2001). Fundamental modes and abrupt changes in North Atlantic circulation and climate over the last 60 ky—Concepts, reconstruction and numerical modeling. In The Northern North Atlantic (pp. 365-410). Springer Berlin Heidelberg.

Schulz H. D., Ayres Neto A., Boetius A., Enneking K., Fabian K., Feseker T., Funk J., Gorke M., Heidersdorf F., Hensen C., Heuer V., Hill H.G., Hinrichs S., Kasten S., Klann M., Lacerda de Souza C., Martinez Briao A., Meyer S., Mulitza S., Niebler H.-S., Ochsenhirt W.-T., Panteleit B., Pfeifer K., Schewe F., Schwenk T., Senorans J.L., Siemer S., Steinmetz E., Wenzhöfer F. (2001). Report and preliminary results of Meteor Cruise M46/2. Berichte, Fachbereich Geowissenschaften, Universität Bremen, 184, 107.

Severinghaus, J. P., Brook, E. J. (1999). Abrupt climate change at the end of the last glacial period inferred from trapped air in polar ice. *Science*, **286(5441)**, 930-934.

Stevaux, J. C. (2000). Climatic events during the late Pleistocene and Holocene in the upper Parana River: Correlation with NE Argentina and South-Central Brazil. *Quaternary International*, **72(1)**, 73-85.

Thiagarajan, N., Subhas, A. V., Southon, J. R., Eiler, J. M., Adkins, J. F. (2014). Abrupt pre-Bølling-Allerød warming and circulation changes in the deep ocean. *Nature*, **511(7507)**, 75.

Voigt, I., Henrich, R., Preu, B. M., Piola, A. R., Hanebuth, T. J., Schwenk, T., Chiessi, C. M. (2013). A submarine canyon as a climate archive—interaction of the Antarctic Intermediate Water with the Mar del Plata Canyon (Southwest Atlantic). *Marine Geology*, **341**, 46-57.

Wang, X., Auler, A. S., Edwards, R. L., Cheng, H., Ito, E., Solheid, M. (2006). Interhemispheric anti-phasing of rainfall during the last glacial period. *Quaternary Science Reviews*, **25(23)**, 3391-3403.

Wasserburg G. J., DePaolo D. J. (1979). Models of earth structure inferred from neodymium and strontium isotopic abundances. *Proceedings of the National Academy of Sciences*, **76(8)**, 3594-3598.

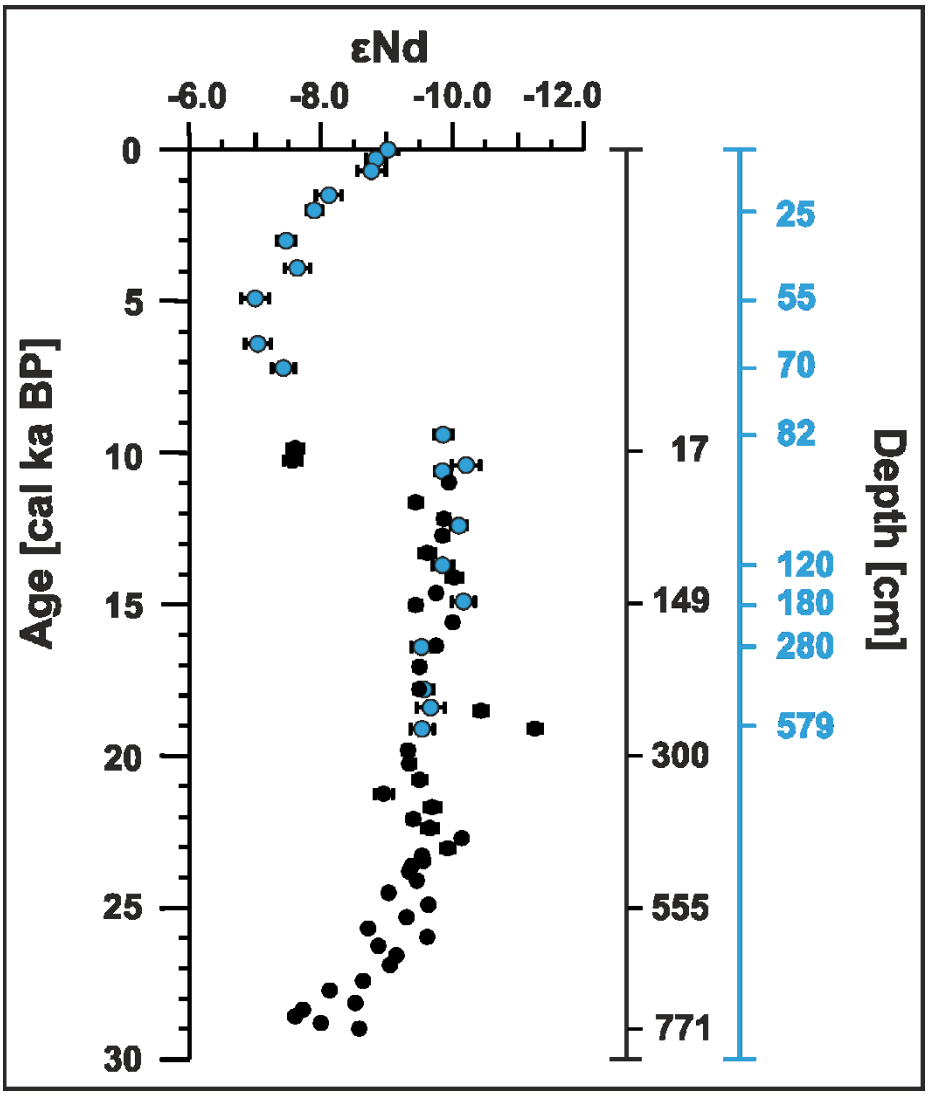

Fig. S1. Down-core ε_{Nd} record of marine sediment core GeoB6212-1 (black circles) and of marine sediment core GeoB6211-2 (blue circles) from Lantzsch et al. (2014).

Chapter 5

Chemical leaching of bulk marine sediment under riverine influence – Radiogenic isotope signatures of different fractions and the challenges of interpretation

Natalie Höppner[1]*, Friedrich Lucassen[1], Simone A. Kasemann[1]

[1] MARUM – Center for Marine Environmental Sciences and Faculty of Geosciences, University of Bremen, Germany (*corresponding author: nhoeppner@marum.de, telephone: +49 (0) 421 218 65934)

5.1 Abstract

The radiogenic isotope signature of different marine sediment components (i.e. detrital, biogenic, authigenic) records paleo seawater circumstances (i.e. the isotopic signature of seawater, the source of detrital material). This signature is not significantly influenced by precipitation, transport or depositional processes. To get these individual signatures, the different marine components have to be separated mechanically or chemically. We report major element concentrations and strontium (Sr), neodymium (Nd) and lead (Pb) isotopic signatures of the bulk and detrital fractions as well as carbonate and Fe-Mn oxyhydroxide leachate fractions of two marine sediment cores. Core GeoB16224-1 is influenced by the Amazon River basin (A), core GeoB6212-1 is influenced by the Río de la Plata drainage basin (RP). The carbonate fraction in both cores has the highest Sr concentration (A: ~900 to 1000 µg/g; RP: ~200 to 400 µg/g) of all fractions and an $^{87}Sr/^{86}Sr$ isotopic signature (A: 0.70921 ± 0.0003 (2SD); RP: 0.70925 ± 0.00006 (2SD)) close to the modern seawater value (0.70916). The $^{87}Sr/^{86}Sr$ isotopic signature of the bulk fraction (A: 0.715 ± 0.02 (2SD); RP: 0.714 ± 0.02 (2SD)) is less radiogenic than the detrital fraction (A: 0.723 ± 0.02 (2SD); RP: 0.717 ± 0.04 (2SD)), showing that the Sr isotopic signature is heavily influenced by the unradiogenic marine seawater signal that needs to be separated to obtain a valid detrital signature. The Fe-Mn oxyhydroxide fraction of the Amazon core (GeoB16224-1) shows a correlation between iron (Fe) and manganese (Mn) pointing to the existence of Fe-Mn oxyhydroxide coatings on the sediments. Additionally, the correlation between phosphorous (P) and Fe and the good match with the Sr and Nd isotopic signature of the Fe-Mn oxyhydroxide fraction of Amazon River suspended particulate matter, indicate that the Fe-Mn oxyhydroxide coatings are not authigenic, but have been pre-formed in the river environment. The Fe-Mn oxyhydroxide fraction of the Río de la Plata core (GeoB6212-1) has a strong correlation of magnesium (Mg) and calcium (Ca), pointing to the dissolution of dolomite. Additionally, a contamination of detrital clay minerals is present. In both cores, the radiogenic isotope signatures of the Fe-Mn oxyhydroxide fraction do not reflect a paleo seawater signal. We hypothesize that for marine sediments under the influence of large rivers a Fe-Mn oxyhydroxide leaching is redundant. It either leaches detrital components (i.e. clay minerals) or pre-formed river borne Fe-Mn oxyhydroxide coatings, both belonging to the primary detrital signal. However, we suggest that for every sample set each leach fraction (bulk, detrital, carbonates and Fe-Mn oxyhydroxides) should be investigated thoroughly to identify possible contamination problems that influence the conclusions.

5.2 Introduction

Marine sediments are a mixture of different components (Chester and Hughes, 1967): detrital, biogenic and authigenic. The detrital material is mainly terrigenous clastic material transported into the ocean through rivers, glaciers or wind (Milliman and Meade, 1983). The biogenic components are either calcareous or siliceous (Sverdrup et al., 1942), with the modern calcium carbonate fraction mainly consisting out of pelagic plants (i.e. coccolithophores) and animals (i.e. foraminifera, pteropods, heteropods) (Morse and McKenzie, 1990). Authigenic particles are inorganic minerals directly formed in the seawater or on marine sediment through the reaction with seawater (i.e. evaporates, hydrogenous Fe-Mn oxyhydroxides or ferromanganese nodules) (Rothwell, 2012). The radiogenic isotope signature (strontium, neodymium and lead) of these different components record an array of processes and environmental conditions. However, there is a high potential of mutual overprinting, therefore the different components (detrital, biogenic and authigenic) should be separated before analysis (Chester and Hughes, 1966). Calcium carbonate ($CaCO_3$) is commonly dissolved in Hydrochloric acid (HCl). Ray et al. (1957) found that HCl is too aggressive on bulk sediment, because it leaches some of the easily removable elements from clay minerals. They suggested acetic acid as a new leaching agent that is most frequently used for bulk sediment decarbonizing today (i.e. Bayon et al., 2002; Gutjahr et al., 2007). To obtain the Fe-Mn oxyhydroxide signal the most widely used method today is acid reductive leaching with hydroxylamine hydrochloride (HH) (Bayon et al., 2002; Gutjahr et al., 2007; Martin et al., 2010; Wilson et al., 2013).

The radiogenic isotope signature of detrital particles is not significantly affected by weathering, transport or depositional cycles. Therefore, it can be used to determine the provenance or transport mechanism of the analyzed particle, allowing the reconstruction of past environments (i.e. river supply, wind regimes, ocean currents) (Bayon et al., 2002 and therein). Marine carbonate organism can be used to determine the age of deep sea sediments directly (Morse and McKenzie, 1990) using radiocarbon (^{14}C) dating. Additionally, calcareous organisms incorporate strontium (Sr) into their shells, due to the chemical similarity to calcium (Ca), without isotopic fractionation (Veizer, 1989). Therefore, the Sr isotopic composition of past seawater can be obtained from marine rocks and carbonate skeletons (Veizer et al., 1999). The residence time of Sr in seawater is much longer (≥ 4 Myr) than the ocean mixing time (~ 10^3 yr) (Veizer, 1989), leading to a global $^{87}Sr/^{86}Sr$ isotopic value for the world oceans (the modern value is 0.70917; Henderson et al., 1994). The Sr content in the ocean is a mixture of radiogenic continental weathering and non-radiogenic hydrothermal input (Edmond, 1992). A change in the Sr isotopic composition is mostly due to changes in continental weathering and tectonics (Henderson et al., 1994), therefore, Sr can be additionally used as a proxy for the tectonic evolution (Veizer et al., 1999).

Precipitation of the Fe-Mn oxide coatings happen at the sediment water interface (Roberts 2010). Fe-Mn oxyhydroxides scavenge ions from solution (Goldberg, 1954) and record the Nd, Sr (Bayon et al., 2002) and Pb (Crocket et al., 2012) isotopic composition of seawater during the time of formation. In contrast to Sr, Pb has a very short residence time (~ 20 to 30 yr) in the Atlantic Ocean compared to the mixing time of the ocean and is used as a proxy for studies of local continental input (Crocket et al., 2012). Compared to Pb, the residence time of Nd is longer (about ~600 to 2000 years; Frank et al., 2002), but still shorter than the mixing time of the deep ocean (Wilson et al., 2013). Therefore, the modern seawater ε_{Nd} value is not globally homogenous, but has variations in the scale of ocean basins. The Atlantic Ocean has ε_{Nd} values between -9 and -14, the Pacific Ocean has ε_{Nd} values between -1 and -6 and the Indian Ocean has ε_{Nd} between -7 and -8.5 (Albarède and Goldstein, 1992). Additionally, smaller water masses, like individual ocean currents, vary inside these values. For example, modern seawater ε_{Nd} values from the Demerara Rise (a submarine plateau off the coast of Suriname and French Guiana) show a variation between -10 to -12, coupled to the individual ocean currents occurring in different depth (i.e. Antarctic Intermediate Water, North Atlantic Deep Water and Antarctic Bottom Water) (Huang et al., 2014). Therefore, the Nd isotopic signature extracted from Fe-Mn oxyhydroxides (Burton et al., 1999; Gutjahr et al., 2007; Xie et al., 2014) can be used as a tracer for inter/intra basin water mass mixing (Wilson et al., 2013) and has for many years been a quasi-conservative tracer of bottom water circulation. However, in the last years the theory emerged that Nd might reflect the pore water composition instead (Du et al., 2016).

The isotopic composition of past seawater can be obtained from several different phases like foraminifera (Howe et al., 2016), fish teeth (Martin and Haley, 2000; Martin et al., 2010), and Fe-Mn crusts/noodles (Frank et al., 2002; O'Nions et al., 1998). However, all of those do not occur regularly and are quite labor intensive (Du et al., 2016). In contrast, the leaching of Fe-Mn oxyhydroxide coatings from bulk sediment has no restriction in spatial coverage and is not as time consuming (Blaser et al., 2016; Chester and Hughes, 1967; Gutjahr et al., 2007; Pahnke et al., 2008; Wilson et al., 2013). However, this leaching procedure contains some challenges. Contamination due to partial leaching of the bulk fraction (Elmore et al., 2011; Howe et al., 2006; Piotrowski et al., 2012; Wilson et al., 2013) is one problem. Furthermore, some authors (Bayon et al, 2004; Kraft et al., 2013) raised the concern that bulk leaching might not be reliable at settings with strong river influences, due to pre-formed river borne Fe-Mn oxyhydroxide coatings that are leached during this step.

In this study we applied the widely used carbonate and Fe-Mn oxyhydroxide leaching methods on bulk material of two marine sediment cores from settings with strong riverine influence (GeoB16224-1: Amazon River basin; GeoB6212-1: Río de la Plata drainage basin). We

present major element concentration data and radiogenic isotope signatures (Sr, Nd and Pb) for the bulk, the detrital, the carbonate and the Fe-Mn oxyhydroxide fraction. We obtained the necessary steps to receive a detrital signature, tested the hypothesis of pre-formed Fe-Mn oxyhydroxides and checked the representability of the Fe-Mn oxyhydroxide fraction as a paleo seawater signal for these two regions.

5.3 Regional setting

5.3.1 Continental setting

The Amazon River basin and Río de la Plata drainage basin are located in northern and southern South America, respectively (Fig. 26). The Amazon River drains an area of ~ 6.3 x 10^6 km^2 (Gibbs, 1967) and supplies 1.1 to 1.3 x 10^9 tons of suspended particulate matter (SPM) annually into the Atlantic Ocean (Meade, 1994). The Río de la Plata drainage basin drains an area of 3.1 x 10^6 km^2 (Depetris and Griffin, 1968) and supplies about 9.2 x 10^7 tons of SPM per year into the Atlantic Ocean (Depetris et al., 2003). They are the largest (Amazon) and fifth largest (Río de la Plata) rivers of the world (Gibbs, 1967; Milliman and Meade, 1983). Both river basins drain the Andes and old Precambrian shield areas (Gibbs, 1967; Henry et al., 1996) and large parts of both basins have a tropical climate (Henry et al., 1996; Longinelli and Edmond, 1983).

5.3.2 Oceanic setting

Both basins have large density controlled freshwater plumes stretching several kilometers along the coast, influencing the seawater chemistry (i.e. salinity) (Gibbs and Konwar, 1986; Guerrero et al., 1996). The freshwater and suspended particulate matter from the Amazon River mouth is transported northwestward along the coast by the North Brazil Current (NBC) (Johns et al., 1998). The intermediate and deep water close to the Amazon River mouth are influenced by the southward flowing North Atlantic Deep Water (NADW) and the northward flowing Antarctic Intermediate Water (AAIW), with ε_{Nd} values measured at the Demerara rise for the AAIW of -10 to -11 and for the NADW of -11 to -12 (Huang et al., 2014). Freshwater and material from the Río de la Plata estuary is transported northeastwards by the Plata Plume Water (PPW) driven mainly by the wind (Piola et al., 2000). Similar to the Amazon River setting, the intermediate and deep water in front of the Río de la Plata estuary are influenced by the southward flowing North Atlantic Deep Water (NADW) and the northward flowing Antarctic Intermediate Water (AAIW) (Voigt et al., 2013). The modern ε_{Nd} values measured from the Atlantic sector of the Southern Ocean are for the NADW -10 to -11 and for the AAIW an average of -8.1 ± 0.2 (Stichel et al., 2012).

5.4 Material and methods

5.4.1 Material

Samples investigated in this study are from marine gravity core GeoB16224-1 and GeoB6212-1 (Fig. 26).

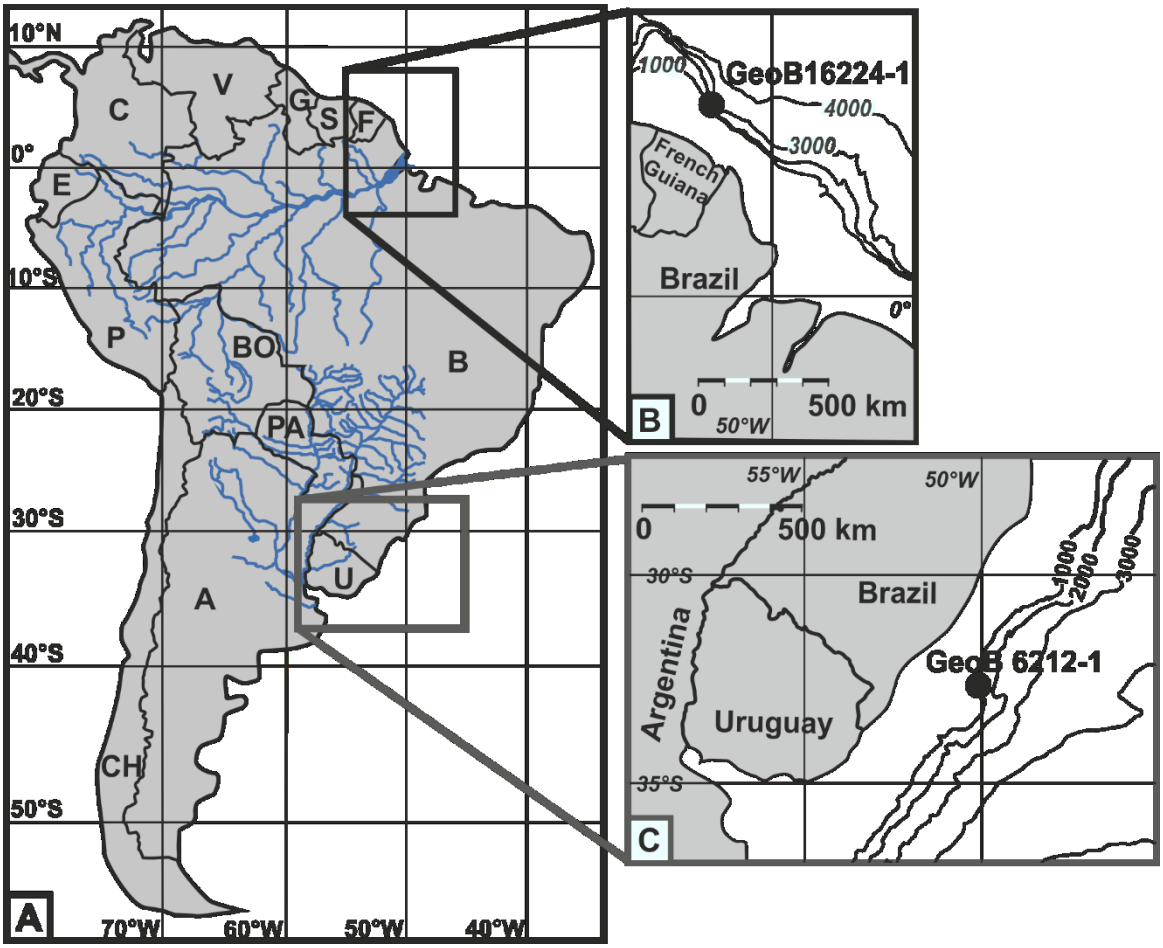

Fig. 26. Location of the marine sediment cores investigated in this study. Panel A: South America showing the Amazon River and Río de la Plata drainage basins and the areas expanded in panel B and C. The countries are marked with black uppercase letters as follows: A: Argentina, B: Brazil, BO: Bolivia, C: Colombia, CH: Chile, E: Ecuador, F: French Guiana, G: Guiana, P: Peru, PA: Paraguay, S: Suriname, U: Uruguay and V: Venezuela. Panel B: Location of the marine sediment core GeoB16224-1 (black circle). Panel C: Location of the marine sediment core GeoB6212-1 (black circle).

Gravity core GeoB16224-1 (Table 24) was collected on the continental slope off French Guiana (Fig. 26) during RV Maria S. Merian cruise MSM20/3 in 2012 (Mulitza et al., 2013). Due to its location northwest of the Amazon River mouth, it receives terrigenous material from the Amazon River that gets transported northwestward by the North Brazil Current (NBC) (Johns et al., 1998). Five samples with an average of 3 g dry weight were chosen (Table 2) to generate an even coverage of the radiocarbon dated section of the core. Zhang et al. (2015) published 15 AMS radiocarbon (^{14}C) ages based on mixed planktonic foraminifera with a large age gap between 66 and 55 cm suggesting a hiatus. Here we use the age model published by Häggi

et al. (2017) for the period between 41.2 (at 600 cm) and 12.6 (at 66 cm) cal ka BP and an extension of that age model for the upper 66 cm of the core based on the extrapolation of two ^{14}C ages using the calibration settings and method of Häggi et al. (2017). However we treat the upper portion (i.e. shallower than 66 cm core depth) of the age model of core GeoB16224-1 with caution.

Gravity core GeoB6212-1 (Table 24) was collected on the continental slope off the coast of SE Brazil (Fig. 26) during Meteor cruise M46/2 in 1999/2000 (Schulz et al. 2001). It is located northeast of the Río de la Plata estuary. The northeastwards flowing PPW transports the terrigenous material to the core site (Lantzsch et al. 2014). Five samples with an average of 5 g dry weight were chosen (Table 25) to generate an even coverage of the radiocarbon dated section of the core. The age model is based on 14 AMS radiocarbon ages (^{14}C) from planktonic foraminifera (Campos et al., 2017) and dates the sediment between 31.9 (768 cm) to 5.9 (8 cm) cal ka BP.

Table 24 Location, core length, water depth and sediment supplying river basin for the two analyzed marine sediment cores GeoB16224-1 and GeoB6212-1.

Sample name	Location [Lon (°E) / Lat (°N)]	Length [cm]	Water depth [m]	Sediment supplying river basin
GeoB16224-1	-52.08305 / 6.65638	760	2510	Amazon River basin
GeoB6212-1	-32.505 / -50.242	790	1010	Río de la Plata drainage basin

5.4.2 Methods

5.4.2.1 Sample preparation and dissolution

An average amount of 7 – 9 g of wet sample was taken from the sediment core. The sample was washed two times with Milli Q water (18.2 MΩ) to remove the residual pore water and wet sieved to collect the < 63µm fraction used for further analyses. Five samples, equally spread throughout the core to cover the whole radiocarbon dated age range, were chosen for GeoB16224-1 and GeoB6212-1, respectively (Table 25).

Table 25 Sample depth, calculated age and sediment supplying river basin for the five selected samples of GeoB16224-1 and GeoB6212-1.

Core	Sample name	Sample depth [cm]	Age [cal ka BP]	River basin
GeoB16224-1	A7	57.0	9.5*	Amazon
	A11	65.0	12.2*	
	A28	354.5	25.9	
	A34	415.0	28.6	
	A46	591.5	39.3	
GeoB6212-1	RP3	50.0	11.0	Río de la Plata
	RP5	75.0	12.2	
	RP13	210.0	17.1	
	RP21	368.0	21.7	
	RP36	630.0	26.3	

*treat ages with caution.

A schematic overview of the further sample treatment is shown in Fig. 27. The untreated sample is called bulk fraction. The next step is the decarbonization of the sample. Approximately 100 to 200 mg of the sample were treated with a 15 % acetic acid solution (buffered to pH ~4 with 1 M Na-acetate), in the following referred to as Carbonate-Leach-Solution (CLS), in a four-step procedure (Gutjahr et al., 2007) to remove the marine carbonates from the detrital fraction (Table 26).

Table 26 The step by step procedure for decarbonization of sediments (after Gutjahr et al., 2007).

Steps	mL [added fluid]	Procedure after fluid addition	Supernatant
Step 1	~ 2.5 [CLS]	a) Shake for 2.5 h with 50 rpm b) Centrifuge for 30 min with 4000 rpm	Decant (pipette) into PP beaker; save for further analyses
Step 2	~ 2.5 [50/50; CLS/Milli Q]	c) Shake overnight with 50 rpm d) Centrifuge for 30 min with 4000 rpm	Decant (pipette) into PP beaker; save for further analyses
Step 3	~ 2.5 [Milli Q]	e) Shake for 20 min with 50 rpm f) Centrifuge for 30 min with 4000 rpm	Decant (pipette) into PP beaker; save for further analyses
Step 4	~ 2.5 [Milli Q]	g) Shake for 20 min with 50 rpm h) Centrifuge for 30 min with 4000 rpm	discard

The residual decarbonated sediment sample is called dc fraction. The collected supernatant of the decarbonization steps is called KL fraction (Fig. 27). Both fractions are dried at 110°C. The next step is the removal of potential authigenic Fe-Mn oxyhydroxide coatings on the sediment. For this the sample is treated with an acid solution (0.05 M hydroxylamine-hydrochloride (HH) / 15 % acetic acid / 0.03 M Na EDTA, buffered to pH 4 with NaOH), in the following referred to as Fe-Mn-Leach-Solution (FMLS), in a four-step procedure (Gutjahr et al., 2007) (Table 27).

Table 27 The step by step procedure for Fe-Mn oxyhydroxide coating leaching on sediments (after Gutjahr et al., 2007).

Steps	mL [added fluid]	Procedure after fluid addition	Supernatant
Step 1	~ 2.5 [FMLS]	a) Shake for 1 h with 50 rpm b) Centrifuge for 30 min with 4000 rpm	Decant (pipette) into PP beaker; save for further analyses
Step 2	~ 2.5 [Milli Q]	c) Shake for 15 min with 50 rpm d) Centrifuge for 30 min with 4000 rpm	Decant (pipette) into PP beaker; save for further analyses
Step 3	~ 2.5 [Milli Q]	e) Shake for 15 min with 50 rpm f) Centrifuge for 30 min with 4000 rpm	Decant (pipette) into PP beaker; save for further analyses
Step 4	~ 2.5 [Milli Q]	g) Shake for 15 min with 50 rpm h) Centrifuge for 30 min with 4000 rpm	discard

The residual sediment sample is called dt fraction. The collected supernatant of the Fe-Mn oxyhydroxide leaching steps is called FML fraction (Fig. 27). Both fractions are dried at 110°C.

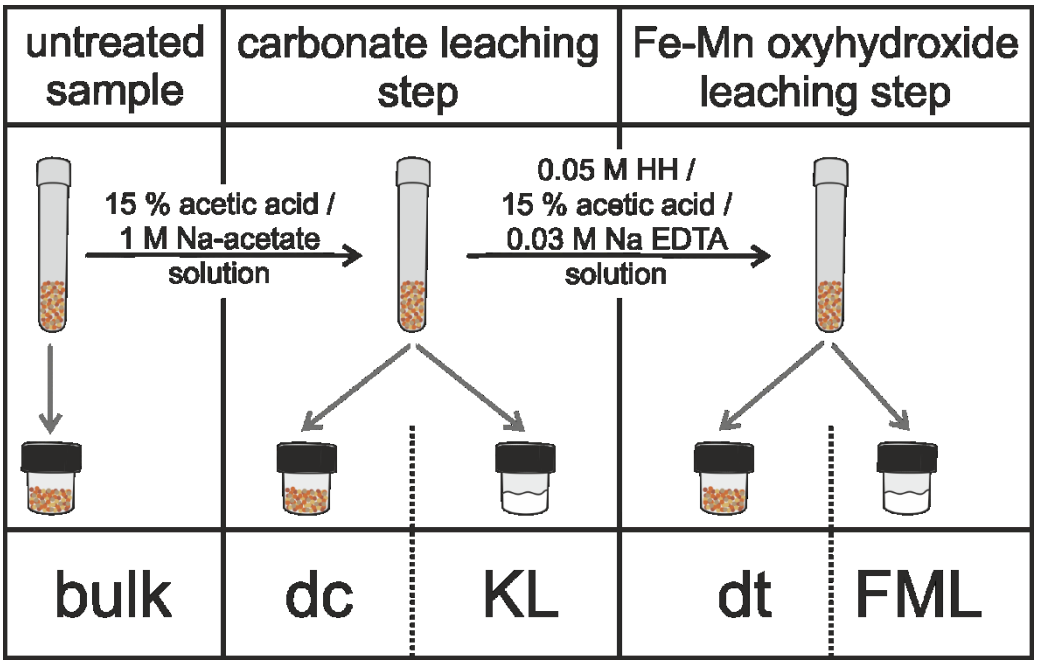

Fig. 27. Schematic overview of the sample treatment. Annotations are described in more detail in the text, bulk: chemically untreated sample, KL: supernatant of carbonate leaching, dc: decarbonated sample, FML: supernatant of Fe-Mn oxyhydroxide leaching and dt: decarbonated and Fe-Mn oxyhydroxide leached sample.

5.4.2.2 Chemical separation and mass spectrometry

The material from the five fractions (bulk, dc, KL, dt and FML) (Fig. 27) is digested in hot acid. The solid samples (bulk, dc and dt) are digested in 2 to 3 ml of a concentrated HF:HNO_3 (5:1) acid mixture, dried and redissolved in 2 to 3 ml of aqua regia (3:1, 6 N HCl:concentrated HNO_3), dried and redissolved in 4 to 5 ml of a H_2O_2:concentrated HNO_3 (1:1) acid mixture, dried and redissolved in 3 to 5 ml of 6 N HCl. An aliquot for elemental analyses was taken. Finally, the detrital fraction was dried and redissolved in 600 to 800 µl of 2 N HNO_3 for further isotopic analyses. The Leachates are dissolved in 3 steps of 2 ml concentrated HNO_3 and 3 steps of 2 ml 6 N HCl, dried and redissolved after each step. An aliquot for elemental analyses is taken in the last 6N HCl step. Finally, the fraction was evaporated and redissolved in 1000 to 1500 µl of 2N HNO_3 for further isotopic analyses.

Sr and Pb were separated from the sample matrix using 70 µl of Sr.spec^{TM} resin (method modified from Deniel and Pin, 2001). Nd was isolated in two steps from the sample matrix using TRU.spec^{TM} for LREE and LN.spec^{TM} for Nd separation (Eichrom®) (method after Pin et al., 1994). Analyses were performed on a ThermoFisher Scientific TRITON Plus thermal ionization mass spectrometer (TIMS) at the Isotope Geochemistry Laboratory at MARUM, University of Bremen, Germany. Nd and Pb isotope ratios were analyzed in the static multicollection mode and Sr isotope ratios in the dynamic multicollection mode.

Instrumental mass fractionation during Sr analyses was corrected using the stable isotope ratio of $^{86}Sr/^{88}Sr$ (= 0.1194). The analytical accuracy and external long-term reproducibility for

$^{87}Sr/^{86}Sr$ of reference material NIST SRM 987 was 0.710246 ± 0.000011 (2SD, n= 24; period: May 2015 to May 2017) and is within the range of 0.710250 ± 0.000034 (2SD, n= 1245, data <0.7102 and > 0.7103 are discarded) calculated from published values analyzed by TIMS (GeoRem data base; query September 2017; http://georem.mpch-mainz.gwdg.de). Instrumental mass fractionation during Nd measurements was corrected using the stable isotope ratio of $^{146}Nd/^{144}Nd$ (= 0.7219). The analytical accuracy and external long-term reproducibility for $^{143}Nd/^{144}Nd$ for reference material JNdi-1 was 0.512093 ± 0.000009 (2SD, n= 27; period: May 2015 to May 2017) and is within the calculated range of 0.512106 ± 0.000027 (2 SD, n = 211, data <0.51204 and >0.51217 are discarded) analyzed by TIMS (GeoRem data base; query September 2017; http://georem.mpch-mainz.gwdg.de). The $^{143}Nd/^{144}Nd$ isotope ratio is commonly presented in the ε_{Nd} notation (ε_{Nd} = {[$(^{143}Nd/^{144}Nd)_{sample}$ / $(^{143}Nd/^{144}Nd)_{CHUR}$]-1}*10000) relative to the Chondritic Uniform Reservoir (CHUR) with a value of $^{143}Nd/^{144}Nd$= 0.512638 (Wasserburg and DePaolo, 1979). Pb isotope ratios have been corrected for instrumental mass fractionation using 0.1 % per atomic mass unit based on the repeated analyses of NIST SRM 981. The reproducibility including the correction for mass fractionation is better than 0.1 % of the respective ratio, which is the assumed uncertainty on the Pb isotope ratios.

Sr, Nd and Pb concentrations of the SPM were measured with a high-resolution inductively coupled plasma mass spectrometer (HR-ICP-MS, Thermo Finnigan Element2, Germany) at the Petrology of the Ocean Crust Laboratory, University of Bremen, Germany. The analyses were conducted in a 20,000-fold diluted aliquot in low resolution mode using indium and thallium as internal standards. International reference materials (BCR-2 and BHVO-2) were used to check for accuracy (< 9 %; 2SD) and precision (< 2.5 %; 2SD).

The major element concentrations were measured with an inductively coupled plasma optical emission spectroscopy (ICP-OES, Agilent Technologies, 700 series) at the Sediment Geochemistry Laboratory, University of Bremen, Germany. The measurement was conducted in a 5,000 to 10,000-fold diluted aliquot in axial configuration.

5.5 Results

The major element concentrations of the five fractions (bulk, dc, dt, Kl and FML) are displayed in Table 28 for GeoB16224-1 (A) and in Table 29 for GeoB6212-1 (RP). The Sr, Nd and Pb isotopic signatures for all five fractions (bulk, dc, dt, Kl and FML) are displayed in Table 30 for GeoB16224-1 (A) and in Table 31 for GeoB6212-1 (RP).

Table 28 Major element concentrations for the fractions (dc, dt, KL, FML) of GeoB16224-1.

Sample name	Sample fraction	Al [%]	K [%]	Mg [%]	Ca [%]	Fe [%]	Mn [µg/g]	Ba [µg/g]	P [µg/g]	Ti [µg/g]	Sr [µg/g]
A7	bulk	n.a.	n.a.	n.a.	n.a.	n.a.	n.a.	n.a.	n.a.	n.a.	n.a.
A11	bulk	n.a.	n.a.	n.a.	n.a.	n.a.	n.a.	n.a.	n.a.	n.a.	n.a.
A28	bulk	n.a.	n.a.	n.a.	n.a.	n.a.	n.a.	n.a.	n.a.	n.a.	n.a.
A34	bulk	n.a.	n.a.	n.a.	n.a.	n.a.	n.a.	n.a.	n.a.	n.a.	n.a.
A46	bulk	n.a.	n.a.	n.a.	n.a.	n.a.	n.a.	n.a.	n.a.	n.a.	n.a.
A7	dc	9.7	1.9	0.9	0.13	4.8	190	229	215	4100	59
A11	dc	8.7	1.7	0.7	0.10	4.9	172	239	326	4802	44
A28	dc	9.4	1.9	0.8	0.12	5.5	206	276	405	4726	50
A34	dc	8.3	1.6	0.7	0.11	5.5	214	182	255	4042	42
A46	dc	8.8	1.8	0.8	0.11	5.3	239	271	349	4878	50
A7	dt	10.0	2.0	0.9	0.06	5.0	183	343	247	4623	59
A11	dt	9.1	1.9	0.8	0.08	5.0	185	335	266	4677	56
A28	dt	9.6	2.3	0.9	0.08	5.6	199	388	405	5262	71
A34	dt	9.8	2.2	1.0	0.08	5.6	232	298	280	4737	76
A46	dt	8.6	2.0	0.9	0.07	5.3	245	103	252	4305	56
A7	KL	0.6	1.5	2.0	16.3	1.0	374	688	1134	4	975
A11	KL	0.5	1.4	1.8	18.3	0.8	374	647	1051	n.a.	1008
A28	KL	0.5	1.3	2.1	15.3	2.0	926	575	1266	3	926
A34	KL	0.3	0.9	1.4	19.5	1.1	888	467	896	1	1037
A46	KL	0.5	1.9	1.9	14.1	1.3	891	801	1319	n.a.	917
A7	FML	1.0	1.6	2.8	0.9	1.8	678	192	1265	93	64
A11	FML	0.7	1.3	2.3	1.0	1.3	616	212	1135	63	64
A28	FML	1.2	1.8	2.3	1.2	2.6	1010	261	2224	121	81
A34	FML	1.5	1.9	2.3	1.6	2.7	1313	463	2249	137	113
A46	FML	1.8	2.6	4.0	1.4	3.1	1809	993	2361	186	143

Table 29 Major element concentration for the fractions (bulk, dc, dt, KL, FML) of GeoB6212-1.

Sample name	Sample fraction	Al [%]	K [%]	Mg [%]	Ca [%]	Fe [%]	Mn [µg/g]	Ba [µg/g]	P [µg/g]	Ti [µg/g]	Sr [µg/g]
RP3	bulk	6.7	1.9	0.9	1.3	4.3	305	290	605	5295	90
RP5	bulk	6.5	2.0	1.0	1.4	4.1	305	320	565	5030	85
RP13	bulk	7.6	2.1	1.0	0.9	4.3	325	350	505	5105	120
RP21	bulk	7.5	2.0	0.9	1.0	4.0	340	355	520	5290	115
RP36	bulk	6.6	1.8	0.9	1.1	3.9	355	305	575	5335	95
RP3	dc	8.4	2.2	1.0	0.5	4.5	305	350	300	5365	90
RP5	dc	8.4	2.3	1.1	0.5	4.6	320	355	295	5530	90
RP13	dc	7.8	2.0	0.9	0.6	4.4	295	340	365	5575	105
RP21	dc	7.1	1.8	0.8	0.5	4.0	285	325	335	5375	70
RP36	dc	7.0	1.8	0.8	0.7	4.0	320	320	315	5465	90
RP3	dt	7.4	2.1	0.9	0.3	4.5	280	310	250	5400	75
RP5	dt	8.3	2.2	1.0	0.4	4.4	290	350	255	5090	90
RP13	dt	7.4	1.8	0.8	0.5	4.2	265	320	295	5360	85
RP21	dt	6.9	1.8	0.8	0.5	3.9	260	330	250	5550	75
RP36	dt	8.0	1.9	0.9	0.7	4.1	305	345	325	5650	105
RP3	KL	0.4	1.6	1.2	7.4	0.5	245	180	1970	45	395
RP5	KL	0.4	1.4	1.1	7.2	0.4	250	175	1725	35	395
RP13	KL	0.4	1.6	1.1	2.9	0.8	250	110	2000	45	205
RP21	KL	0.5	1.9	1.3	4.5	1.1	410	160	2500	70	295
RP36	KL	0.5	1.4	1.0	3.0	0.7	350	120	1950	70	195
RP3	FML	1.2	0.9	1.2	0.9	1.2	385	55	1620	370	50
RP5	FML	0.9	0.7	0.8	0.7	0.9	280	45	1105	320	35
RP13	FML	1.0	0.5	0.7	0.5	1.1	215	30	1085	390	25
RP21	FML	0.8	0.5	0.6	0.6	0.9	235	30	1245	265	25
RP36	FML	0.9	0.4	0.8	0.7	1.0	315	35	1315	345	30

Table 30 Sr, Nd and Pb isotopic compositions for the fractions (dc, dt, KL, FML) of GeoB16224-1. Uncertainties ($2SD_{mean}$) are given for the last digit.

Sample name	Sample fraction	$^{87}Sr/^{86}Sr$	$^{143}Nd/^{144}Nd$	ε_{Nd}	$^{206}Pb/^{204}Pb$[a]	$^{207}Pb/^{204}Pb$[a]	$^{208}Pb/^{204}Pb$[a]
A7	bulk	0.716062(7)	0.512046(3)	-11.5(1)	18.99	15.64	38.86
A11	bulk	0.715627(5)	0.512065(3)	-11.2(1)	19.00	15.65	38.91
A28	bulk	0.715291(3)	0.512055(4)	-11.4(1)	18.94	15.63	38.84
A34	bulk	0.713462(5)	0.512045(4)	-11.6(1)	18.96	15.63	38.84
A46	bulk	0.715638(8)	0.512034(4)	-11.8(1)	18.96	15.64	38.87
A7	dc	0.724438(4)	0.512042(5)	-11.6(1)	19.06	15.65	38.97
A11	dc	0.723973(8)	0.512061(4)	-11.3(1)	19.06	15.65	38.97
A28	dc	0.72331(3)	0.512034(4)	-11.8(1)	19.03	15.66	38.99
A34	dc	0.723114(6)	0.512035(5)	-11.8(1)	19.04	15.65	38.94
A46	dc	0.72249(1)	0.512039(4)	-11.7(1)	19.04	15.65	38.97
A7	dt	0.724676(9)	0.512021(4)	-12.0(1)	19.12	15.71	39.15
A11	dt	0.724590(4)	0.512055(8)	-11.4(2)	19.09	15.68	39.07
A28	dt	0.723162(4)	0.512022(6)	-12.0(1)	19.06	15.67	39.03
A34	dt	0.723143(6)	0.512019(5)	-12.1(1)	19.09	15.67	39.05
A46	dt	0.723692(5)	0.51203(1)	-12.0(2)	19.07	15.68	39.05
A7	KL	0.709196(8)	0.512109(3)	-10.3(1)	18.82	15.62	38.69
A11	KL	0.709198(5)	0.512111(4)	-10.3(1)	n.a.	n.a.	n.a.
A28	KL	0.709207(7)	0.512111(7)	-10.3(1)	n.a.	n.a.	n.a.
A34	KL	0.709237(7)	0.512089(4)	-10.7(1)	n.a.	n.a.	n.a.
A46	KL	0.709202(8)	0.512067(4)	-11.1(1)	18.86	15.64	38.79
A7	FML	0.71071(6)	0.512191(5)	-8.7(1)	18.84	15.64	38.78
A11	FML	0.71059(8)	0.512188(5)	-8.8(1)	18.86	15.65	38.82
A28	FML	0.71037(1)	0.512187(5)	-8.8(1)	18.88	15.67	38.91
A34	FML	0.710035(8)	0.512176(4)	-9.0(1)	18.88	15.66	38.87
A46	FML	0.71038 (2)	0.512131(6)	-9.9(1)	18.86	15.63	38.78

[a] Uncertainties ($2SD_{mean}$) are 0.1 %.

Table 31 Sr, Nd and Pb isotopic composition for the fractions (bulk, dc, dt, KL, FML) of GeoB6212-1. Uncertainties ($2SD_{mean}$) are given for the last digit.

Sample name	Sample fraction	$^{87}Sr/^{86}Sr$	$^{143}Nd/^{144}Nd$	ε_{Nd}	$^{206}Pb/^{204}Pb$[a]	$^{207}Pb/^{204}Pb$[a]	$^{208}Pb/^{204}Pb$[a]
RP3	bulk	0.715587(6)	0.512173(5)	-9.1(1)	18.66	15.69	38.75
RP5	bulk	0.71537(2)	0.512199(8)	-8.6(2)	18.44	15.57	38.20
RP13	bulk	0.714602(8)	0.512189(4)	-8.8(1)	18.57	15.59	38.41
RP21	bulk	0.714107(8)	0.512187(6)	-8.8(1)	18.59	15.59	38.45
RP36	bulk	0.712598(6)	0.512205(4)	-8.4(1)	18.57	15.61	38.48
RP3	dc	0.718930(4)	0.512128(3)	-9.9(1)	18.69	15.60	38.60
RP5	dc	0.718628(5)	0.512132(4)	-9.9(1)	18.59	15.59	38.47
RP13	dc	0.715802(7)	0.512151(4)	-9.5(1)	18.68	15.59	38.58
RP21	dc	0.715643(6)	0.512141(6)	-9.7(1)	18.71	15.60	38.65
RP36	dc	0.713607(7)	0.512183(5)	-8.9(1)	18.69	15.60	38.59
RP3	dt	0.718851(5)	0.512111(7)	-10.3(1)	18.72	15.61	38.66
RP5	dt	0.718500(5)	0.512127(5)	-10.0(1)	18.60	15.60	38.47
RP13	dt	0.715812(4)	0.512156(5)	-9.4(1)	18.68	15.59	38.58
RP21	dt	0.715414(4)	0.512151(4)	-9.5(1)	18.71	15.60	38.63
RP36	dt	0.713526(7)	0.512168(5)	-9.2(1)	18.68	15.60	38.58
RP3	KL	0.709263(6)	0.512302(4)	-6.6(1)	18.42	15.58	38.22
RP5	KL	0.709271(6)	0.512310(4)	-6.4(1)	18.33	15.58	38.07
RP13	KL	0.709255(6)	0.512301(4)	-6.6(1)	18.43	15.59	38.24
RP21	KL	n.a.	0.512298(4)	-6.6(1)	18.42	15.57	38.19
RP36	KL	0.709202(6)	0.512289(4)	-6.8(1)	18.40	15.57	38.15
RP3	FML	0.711910(8)	0.51229(1)	-6.9(2)	18.47	15.59	38.34
RP5	FML	0.712815(9)	n.a.	n.a.	18.37	15.58	38.15
RP13	FML	0.713567(8)	0.512269(9)	-7.2(2)	18.50	15.61	38.40
RP21	FML	0.712165(8)	0.512306(8)	-6.5(2)	18.48	15.59	38.35
RP36	FML	0.71180(1)	0.512307(6)	-6.5(1)	18.45	15.58	38.28

[a]Uncertainties ($2SD_{mean}$) are 0.1 %.

5.5.1 Major element concentrations

In the fractions dc and dt the element concentrations are very similar for both cores. Compared to the other fractions they display the highest aluminum (Al), iron (Fe), titanium (Ti) and barium (Ba) concentrations. The KL fraction is dominated by calcium (Ca) and the highest strontium (Sr) concentration compared to all other fractions. The phosphorus (P) concentration is highest in the FML and KL fraction. Ti has the lowest concentrations in the KL fraction. In most of the concentration distributions of the different fractions the Amazon (GeoB16224-1) and Río de la Plata (GeoB6212-1) show a very similar pattern. An exception is the manganese (Mn) concentration. It is very similar in all fraction of GeoB6212-1, but in GeoB16224-1 it is higher in the KL and FML fraction than in the dc and dt fraction and has the highest concentration in the FML fraction. Additionally, the potassium (K) concentration is very similar in all GeoB16224-1 fractions, in GeoB6212-1 most fractions are also similar, except the FML with lower concentrations.

5.5.2 Sr, Nd and Pb isotopic compositions

The $^{87}Sr/^{86}Sr$ isotopic composition of the KL fraction of both cores is very similar with an average of 0.70921 ± 0.00003 (2SD) for GeoB16224-1 and 0.70925 ± 0.00006 (2SD) for GeoB6212-1 (Fig. 28). The ε_{Nd} isotope composition of the KL fraction of GeoB6212-1 is more radiogenic (average of -6.6 ± 0.3; 2SD) than the ε_{Nd} isotope composition of GeoB16224-1 (average of -10.5 ± 0.8; 2SD). The $^{87}Sr/^{86}Sr$ isotopic composition of the FML fraction is in both cores more radiogenic than the KL fraction, but less radiogenic than the dc, dt and bulk fractions. In GeoB6212-1 the ε_{Nd} isotopic composition of the FML fraction (average of -6.8 ± 0.7; 2SD) is very similar to the KL fraction (average of -6.6 ± 0.3; 2SD). For GeoB16224-1 the FML fraction (average of -9.0 ± 1.0; 2SD) is more radiogenic than the KL fraction (average of -10.5 ± 0.8; 2SD). The isotopic signatures of the dt and dc fractions of both cores are quite close together. The dt and dc fraction of GeoB16224-1 have more radiogenic $^{87}Sr/^{86}Sr$ values (0.723 to 0.724) and less radiogenic ε_{Nd} values (-11.6 to -11.9) than the dt and dc fraction of GeoB6212-1 ($^{87}Sr/^{86}Sr$: 0.716 to 0.717; ε_{Nd}: -9.6 to -9.7). All fractions of GeoB6212-1 have less radiogenic Pb isotopic signatures (maximum of 18.72 ± 0.2 ($2SD_{mean}$) for $^{206}Pb/^{204}Pb$, of 15.69 ± 0.2 ($2SD_{mean}$) for $^{207}Pb/^{204}Pb$, and of 38.75 ± 0.4 ($2SD_{mean}$) for $^{208}Pb/^{204}Pb$) compared to the Pb isotopic signatures of GeoB16224-1 (minimum of 18.82 ± 0.2 ($2SD_{mean}$) for $^{206}Pb/^{204}Pb$, of 15.62 ± 0.2 ($2SD_{mean}$) for $^{207}Pb/^{204}Pb$, and of 38.69 ± 0.4 ($2SD_{mean}$) for $^{208}Pb/^{204}Pb$). In both cores, the dt and dc fraction are more radiogenic than the KL and FML fraction.

5.6 Discussion

5.6.1 Detrital (dc) fraction

There is a clear difference in the Sr, Nd and Pb isotopic composition between the bulk, the detrital (dc) and the carbonate (KL) fraction in both cores, with the bulk fraction being less radiogenic than the detrital fraction and more radiogenic than the carbonate fraction (Fig. 28).

Therefore, the bulk fraction represents a mixed signature of the carbonate and the detrital material. To get the detrital signature it is of utmost importance to decarbonate the sample, especially for the Sr signature.

The isotopic difference between dc (sample after the decarbonization step) and dt (sample after the Fe-Mn oxyhydroxide leaching step) is small (Fig. 28). Additionally, the Fe-Mn oxyhydroxide leaching step is not recommended, due to a probable leaching of detrital material in this leaching step (detailed description see section 5.6.3) that produces a result with an offset of the real detrital value.

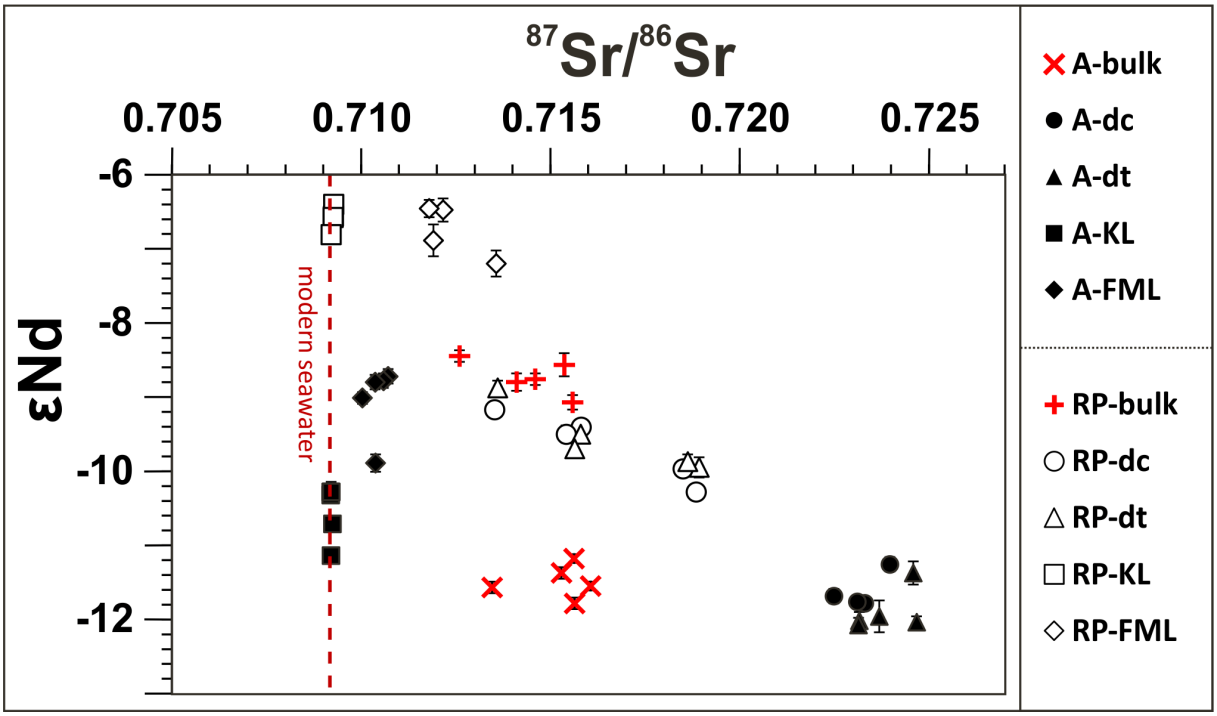

Fig. 28. $^{87}Sr/^{86}Sr$ vs. ε_{Nd} of all five fractions (bulk, dc, dt, KL and FML) for marine sediment core GeoB16224-1 (A) and GeoB6212-1 (RP). The modern $^{87}Sr/^{86}Sr$ seawater value of 0.70917 (Henderson et al., 1994) is marked as a red dashed line.

5.6.2 Carbonate (KL) fraction

The carbonate (KL) fraction of marine sediments is leached with buffered acetic acid (Bayon et al., 2002; Gutjahr et al., 2007) that should not destroy the clay minerals (Ray et al., 1957), but might leach easily exchangeable ions associated with the clay minerals. Element concentration measurements of the KL fraction show the presence of a number of additional elements (i.e. Al, K, Fe) next to the expected Ca concentration. If those elements are incorporated into the carbonate lattice, there should be a correlation between Ca and the respective element. A correlation is observed for Ca and Sr in both cores and for Ca and P in core GeoB16224-1. The other elements have no correlation and are probably leached from an independent source (i.e. the clay minerals). Furthermore, the Fe/Mg and Al/Mg ratios indicate

clay mineral presence (Wei et al., 2007). The KL fraction of both cores is contaminated by a small amount of leached clay minerals.

5.6.2.1 Sr isotopic signature

The Sr isotopic composition of the KL fraction has $^{87}Sr/^{86}Sr$ isotopic values (A: 0.70921 ± 0.0003 (2SD); RP: 0.70925 ± 0.00006 (2SD)) very close to the modern seawater value of 0.70917 (Henderson et al., 1994). A much higher Sr concentration in the carbonates compared to detrital material, inhibits a significant shift of the Sr isotopic signal due to the clay mineral contamination, but could explain the small offset to the modern seawater value. Additionally, the Ca/(Ca+Fe) ratio is a tool, to identify the marine against the detrital composition of a sediment sample (Govin et al., 2012). The results of the KL fraction plot between 0.75 and 1 and henceforth display a marine signal (Fig. 29). The Sr isotopic signature of the KL fraction can be trusted to represent (paleo) seawater values.

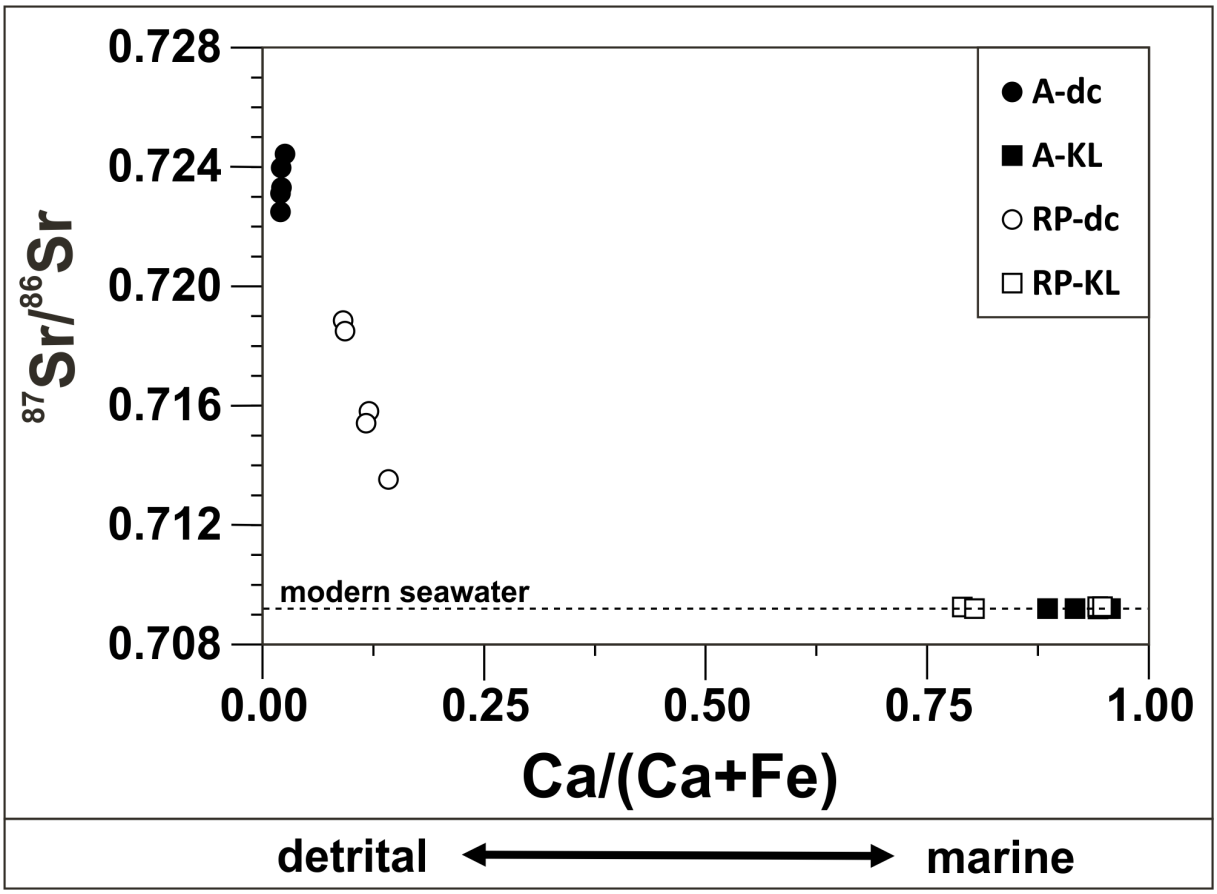

Fig. 29. $^{87}Sr/^{86}Sr$ vs. Ca/(Ca+Fe) of the dc and KL fraction of marine sediment core GeoB16224-1 (A) and GeoB6212-1 (RP). The modern $^{87}Sr/^{86}Sr$ seawater value of 0.70917 (Henderson et al., 1994) is marked as a black dashed line.

5.6.2.2 Nd isotopic signature

The KL fraction of GeoB16224-1 (Amazon River) has an average ε_{Nd} value of -10.5 ± 0.8 (2SD) that is in good agreement with modern seawater values from the nearby Demerara Rise (average ε_{Nd} values between -10 and -12) and with paleo seawater values determined on

foraminifera from a marine sediment core spanning the last 25 cal ka BP (average ε_{Nd} values between -9 and -12; Huang et al., 2014). Therefore, the Nd isotopic signature of the KL fraction could represent (paleo) seawater values. However, the Nd (and Pb) concentrations in biogenic carbonates (carbonate shells and tests) is quite low compared to detrital material (Blaser et al., 2016; Tachikawa et al., 2014), the observed clay mineral contamination on the KL fraction could influence the Nd isotopic signal. The modern Amazon River SPM, source area of the clay minerals, has an average ε_{Nd} value of -10.5 ± 0.5 (2SD) that is in good agreement with the ε_{Nd} signature of the KL fraction (similar for the Pb isotopic signal). An influence of the clay minerals would not be visible in the ε_{Nd} signal of the KL fraction. Therefore, the interpretation of the ε_{Nd} isotopic signature of the KL fraction of GeoB16224-1 as a (paleo) seawater value should be handled carefully.

The KL fraction of GeoB6212-1 (Río de la Plata) has an average ε_{Nd} value of -6.6 ± 0.3 (2SD). It is not in agreement with nearby modern seawater values of -9.2 ± 1.5 (Jeandel, 1993) or the paleo seawater value determined on foraminifera from a marine sediment core spanning the last 25 cal ka BP (average ε_{Nd} values between -8 and -10; Howe et al., 2016). Compared to the modern sediment from the Río de la Plata estuary with average ε_{Nd} values of -9.6 ±1.5 (2SD) (de Mahiques et al., 2008), the ε_{Nd} signal from the KL fraction is also more radiogenic. A leaching of these less radiogenic clay minerals would not produce the observed more radiogenic shift in the KL fraction, unless there would be preferential leaching of more radiogenic particles from the detrital fraction as proposed by Wilson et al. (2013). The ε_{Nd} isotopic signature correlates with the FML fraction of this study and with the FML fraction of a marine sediment core nearby with average ε_{Nd} values between -5.5 and -7.5 (Howe et al., 2016; Pahnke et al. 2008). These results show that the ε_{Nd} signature of the KL fraction of GeoB6212-1 does not represent the ε_{Nd} signature of (paleo) seawater.

5.6.3 Fe-Mn oxyhydroxide (FML) fraction

During the last years many authors discovered that the isotopic signature (especially the Nd isotopic signature) of the authigenic Fe-Mn oxyhydroxide coatings leached from the bulk sediment fraction can be easily contaminated with a non-authigenic or non-seawater derived signal (Bayon et al., 2004; Elmore et al. 2011; Gutjahr et al., 2008; Huang et al., 2014; Kraft et al., 2013; Piotrowski et al., 2012; Wilson et al., 2013; Xie et al., 2014). The screening for clay mineral presence using the Al/Fe, Fe/Mg and Al/Mg ratios (Wei et al., 2007) showed some clay mineral contamination in the FML fraction.

5.6.3.1 GeoB16224-1 (Amazon River basin)

Additional to the correlation of Fe with Al and Ti (clay mineral contamination), Fe has a correlation with Mn and P (Fig. 30). The correlation with Mn points to the presence of Fe-Mn oxyhydroxide coatings.

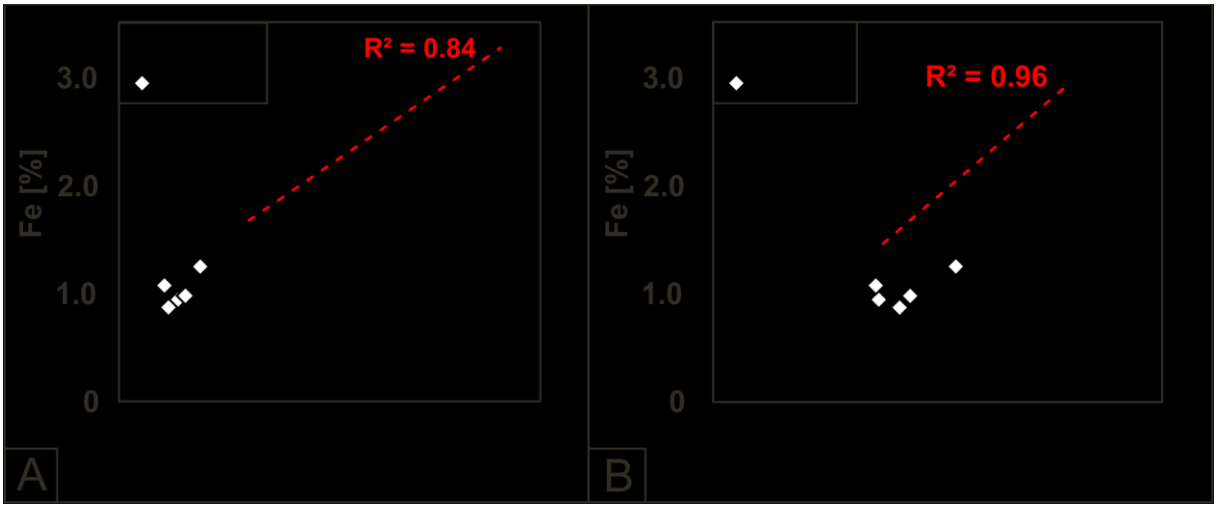

Fig. 30. Panel A: Mn vs. Fe concentrations for the FML fraction of GeoB16224-1 (A) and GeoB6212-1 (RP). The regression line (simple linear regression) for the FML fraction results of GeoB16224-1 (A) is marked as a red dashed line and the coefficient of determination (R^2) is 0.84. Panel B: P vs. Fe concentrations for the FML fraction of GeoB16224-1 (A) and GeoB6212-1 (RP). The regression line (simple linear regression) for the FML fraction results of GeoB16224-1 (A) is marked as a red dashed line and the coefficient of determination (R^2) is 0.96.

The $^{87}Sr/^{86}Sr$ composition of the FML fraction (average of 0.7104 ± 0.005; 2SD) is close to the modern seawater value (0.70917; Henderson et al., 1994) (Fig. 28) and the small but significant offset to a more radiogenic value could be explained by the contamination of clay minerals (Clay has a more radiogenic Sr isotopic signature). The Sr isotopic signal could show a marine signature recorded in Fe-Mn oxyhydroxide coatings. However, the ε_{Nd} signature does not fit to nearby paleo (last 25 cal ka BP) seawater signatures with average ε_{Nd} values between -9 and -12 (Huang et al., 2014). Most of the ε_{Nd} values of the FML fraction are smaller than -9.0 (more radiogenic). Therefore, the ε_{Nd} value, in contrast to the Sr isotopic signature, would speak against a marine signature recorded in the Fe-Mn oxyhydroxide coatings, creating a conundrum between the Sr and Nd isotopic signature. A correlation of Fe and P could point to

the origin of the Fe-Mn oxyhydroxide coatings being river borne, as suggested before by some authors (Bayon et al., 2004; Kraft et al., 2013). Fe and P have a strong correlation in the river SPM, however once deposited in a marine environment the sediment has an independent Fe and P relationship (Rao and Berner, 1993). We propose that this correlation might be preserved in the Fe-Mn oxyhydroxide coatings even after deposition. Rivers with a high organic content (like the Negro River in the Amazon River basin) have a high potential for river borne Fe-Mn oxyhydroxide coatings on the SPM (Allard et al. 2004; Bergquist and Boyle, 2006). The FML fraction of the SPM from the Amazon River main channel has Sr and Nd isotopic signatures similar to the FML fraction of GeoB16224-1 (Fig. 31, Tables 32 and 33). Additionally, the Nd and Pb isotopic signal of the FML fraction fits to the isotopic signatures of the Solimões River (Nd) and Amazon River main channel (Pb) SPM. The leaching of river borne Fe-Mn oxyhydroxide coatings in combination with clay minerals from the main SPM would probably produce the observed isotopic signatures in the FML fraction. We propose that the FML fraction of core GeoB16224-1 does show the isotopic signal of leached Fe-Mn oxyhydroxide coatings, however they are river borne and did not record a paleo seawater signal.

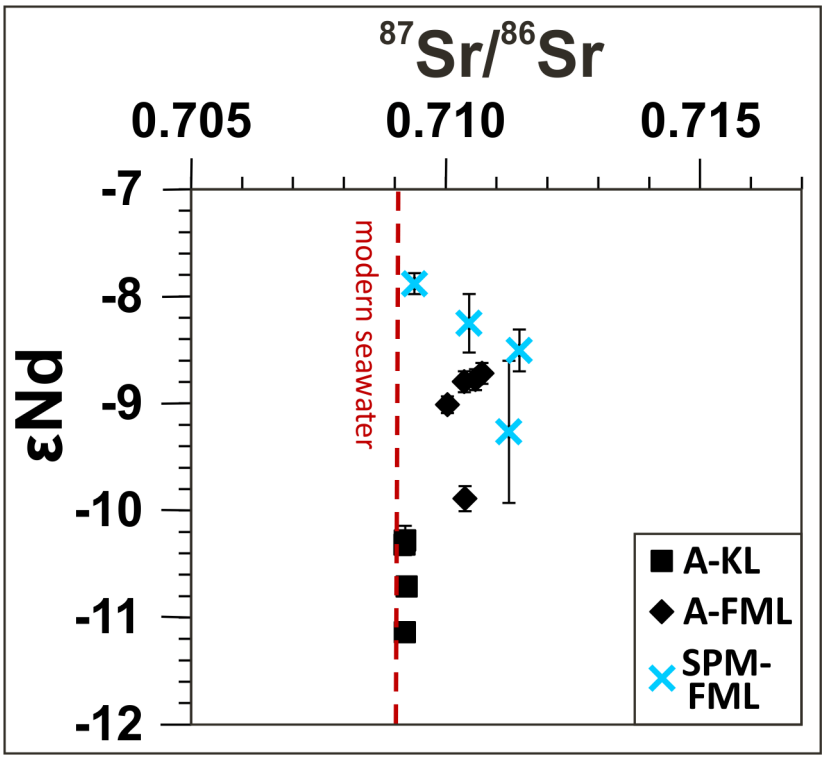

Fig. 31. $^{87}Sr/^{86}Sr$ vs. ε_{Nd} of the KL and FML fraction from GeoB16224-1 (A) and the FML fraction of Amazon River main channel suspended particulate matter. The modern $^{87}Sr/^{86}Sr$ seawater value of 0.70917 (Henderson et al., 1994) is marked as a red dashed line.

Table 32 River name, sampling season, sampling date and sampling location of the four Amazon River main channel suspended particulate matter samples that were Fe-Mn oxyhydroxide leached.

Sample name	River	Season	Sampling date	Location [Lon (°E) / Lat (°N)]
MAO-21b	Amazon (up Madeira)	dry	11/2011	-59.027571/-3.247544
MAO-51	Amazon (down Madeira)	wet	05/2012	-58.547846/-3.198223
STM-01	Amazon (up Tapajós)	wet	05/2012	-55.510539/-1.931037
XA-60	Amazon (down Xingu)	wet	05/2012	-52.308108/-1.498309

Table 33 Sr, Nd and Pb isotopic compositions for the Fe-Mn oxyhydroxide fraction of four Amazon River main channel suspended particulate matter samples. Uncertainties ($2SD_{mean}$) are given for the last digit.

Sample name	$^{87}Sr/^{86}Sr$	$^{143}Nd/^{144}Nd$	ε_{Nd}	$^{206}Pb/^{204}Pb^{a}$	$^{207}Pb/^{204}Pb^{a}$	$^{208}Pb/^{204}Pb^{a}$
MAO-21b	0.709388(7)	0.512234(5)	-7.9(1)	18.77	15.62	38.63
MAO-51	0.710462(6)	0.512215(14)	-8.3(3)	18.75	15.62	38.67
STM-01	0.711244(7)	0.512163(34)	-9.3(7)	18.57	15.62	38.50
XA-60	0.711448(6)	0.512202(10)	-8.2(2)	18.70	15.63	38.64

[a] Uncertainties ($2SD_{mean}$) are 0.1 %.

5.6.3.2 GeoB6212-1 (Río de la Plata drainage basin)

The Fe and Al correlation shows clay mineral contamination in the FML fraction. In contrast to the FML fraction from the GeoB16224-1 core, there is no correlation between Fe and Mn in the FML fraction of GeoB6212-1, speaking against the presence of Fe-Mn oxyhydroxides. There is a correlation between Ca and Mg (Fig. 32) and Ca and Sr in the FML fraction. The Mg/Ca ratio of ~1 points to the presence of dolomite (a calcium and magnesium carbonate, $CaMg(CaCO_3)_2$). The correlation of Ca and Mn supports this, because the Mn^{2+} ion can easily substitute Ca^{2+} or Mg^{2+} ions and can be associated with dolomite (Arunachalam et al., 1996).

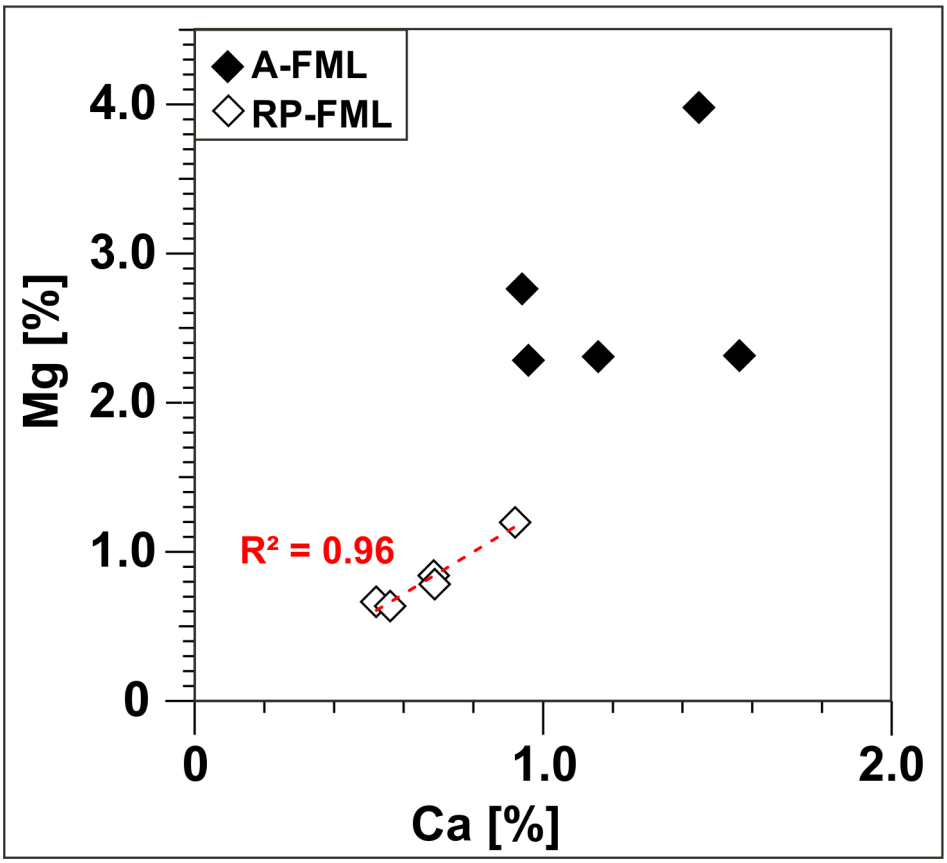

Fig. 32. Ca vs. Mg concentrations of the FML fraction of GeoB16224-1 (A) and GeoB6212-1 (RP). The regression line (simple linear regression) for the FML fraction results of GeoB6212-1 (RP) is marked as a red dashed line and the coefficient of determination (R^2) is 0.96.

The $^{87}Sr/^{86}Sr$ of the FML fraction (average of 0.7125 ± 0.0015; 2SD) is more radiogenic than the modern seawater value of 0.70917 (Henderson et al., 1994). The ε_{Nd} value (-6.8 ± 0.7; 2SD) does neither fit to nearby modern ε_{Nd} values from the eastern South Atlantic (-9.2 ±1.5, Jendel, 1993), nor to paleo ε_{Nd} seawater values determined on Fe-Mn oxyhydroxides of foraminifera from a marine sediment core from the southern Brazil margin spanning the last 25 cal ka BP (between -8 and -10, Howe et al., 2016). However, the ε_{Nd} values correlate with literature FML fractions from bulk sediment of a marine sediment core of the nearby Brazilian margin (average values between -5.5 and -7.5, Howe et al., 2016; Pahnke et al., 2008) and

overlap with the ε_{Nd} values of the Fe-Mn oxyhydroxide coatings from Cenozoic foraminifera from the nearby Rio Grande Rise (values between -6.4 to -9.2, Palmer and Elderfield, 1986). Additionally, they are similar to the ε_{Nd} isotopic signature of the KL fraction (average of -6.6 ± 0.3, 2SD) of this study. This points to the leaching of a similar component in the KL and FML fraction in GeoB6212-1.

Authigenic carbonates (i.e. dolomite) have higher amounts of Nd and lower amounts of Sr compared to biogenic carbonates (i.e. foraminifera) (Banner et al., 1988; Blaser et al., 2016). In the KL fraction a dominant leaching of carbonates, especially biogenic carbonates, takes place. The additional start of dolomite dissolution would not affect the Sr isotopic signature much, but drastically imprint on the Nd isotopic signature. Dolomite starts to get dissolved with the widely used buffered acetic acid leaching procedure (Veizer, 1989), and gets probably completely dissolved during the acetic acid buffered hydroxylamine hydrochloride (HH) leaching step. Therefore, the ε_{Nd} isotopic signature of the FML fraction would be dominated by the same source (i.e. dolomite) as the KL fraction, with high Nd concentrations in the dolomite. The Sr isotopic signature of the authigenic dolomite would have seawater values, however, due to much lower Sr concentrations, a clay mineral contamination would shift the Sr isotopic signal towards more radiogenic values. The KL fraction would not be that strongly influenced by the clay contamination, due to the dominance of biogenic carbonates with a high Sr concentration. A dolomite presence in the samples, would therefore probably produce a very similar ε_{Nd} signal for the KL and FML fraction, while the Sr isotopic signature of the KL fraction can show values close to modern seawater and the Sr isotopic signature of the FML fraction can show values between modern seawater and the detrital fraction (dolomite: seawater signal, clay: detrital signature).

The core site is located at the border of the Antarctic Intermediate Water (AAIW) and the North Atlantic Deep Water (NADW). A probable explanation for the much more radiogenic ε_{Nd} values of the authigenic dolomite could be a higher influence of the AAIW in the past. The modern ε_{Nd} of the AAIW is -8.1 ± 0.2 (Stichel et al., 2012), however, a complete record of the paleo ε_{Nd} signature does not exist to date (Howe et al., 2016). Therefore, a more radiogenic value influenced by the ε_{Nd} of the Antarctic current (-6.5 to -10) or the Pacific (-1 to -6) (Albarède and Goldstein, 1992) might be possible. The Sr isotopic signature of authigenic dolomite would not change from the modern seawater value, due to the long residence time of Sr in the ocean. This hypothesis should also be reflected in the Fe-Mn oxyhydroxide coatings of other authigenic phases (i.e. foraminifera). However the Fe-Mn oxyhydroxide coatings of foraminifera from Howe et al. (2016) show a less radiogenic paleo (last 25 cal ka BP) ε_{Nd} seawater signal of -8 to -9, similar to a modern seawater ε_{Nd} signal. In contrast ε_{Nd} values of the Fe-Mn oxyhydroxide coatings from Cenozoic foraminifera from the nearby Rio Grande Rise

(values between -6.4 to -9.2, Palmer and Elderfield, 1986) reach similar values. An explanation for this difference might be a less constant ε_{Nd} signal of the global water mass endmembers (Roberts et al. 2015; Wilson et al., 2014) or a much more complicated and less conservative mixing behavior of the water masses (Lacan and Jeandel, 2005).

If we assume, that the less radiogenic ε_{Nd} values of the Fe-Mn oxyhydroxide coatings of foraminifera (Howe et al., 2016; Palmer and Elderfield, 1986) represent the true paleo seawater ε_{Nd} values, one possibility might be that the authigenic dolomite we leach does not record the seawater signal but a pore water signal. Pore water and early diagenesis have a strong influence on Nd, while Sr is relative insensitive and reflects the bottom water signal leading to a decoupling of the two isotope signals (Du et al., 2016). Additionally, some authors suggested that a more radiogenic ε_{Nd} value in the FML fraction is due to a contamination of radiogenic volcanogenic minerals that are easily leached during the acetic acid buffered hydroxylamine hydrochloride (HH) leaching step (Elmore et al., 2011; Palmer and Elderfield, 1986). The Río de la Plata, with one of its main sediment sources located in the Andes, could supply volcanogenic material. We agree that this might explain the ε_{Nd} signature of the FML fraction. However, the volcanogenic minerals would have needed to be dissolved additionally already in the buffered acetic acid leaching step, to explain the similar ε_{Nd} values for the KL fraction observed in this study. We prefer the hypothesis that the volcanogenic minerals might affect the pore water signature in situ due to boundary exchange (Elmore et al., 2011) and influence the ε_{Nd} isotopic signature of the authigenic dolomite. Another theory that would exclude the dolomite as a dominant influence on the ε_{Nd} signature, would be a preferential leaching of radiogenic particles from the detrital fraction shifting the ε_{Nd} values in the FML fraction towards more radiogenic values (Howe et al., 2016). We do observe clay mineral contamination in the KL and FML fraction in our study, this hypothesis might therefore explain the equal ε_{Nd} values of both fractions.

To date, the interaction of water and sediment in combination with the Nd isotopic signature of the oceans is still poorly understood (Du et al., 2016). With the current data set, it is not possible to conclusively solve the reason behind the radiogenic ε_{Nd} signature of the FML fraction of the sediment in the area close to the Río de la Plata estuary. The study does however show, how important a comprehensive study of the leaching fractions is for the interpretation.

5.7 Conclusions

We examined the bulk, the detrital, the carbonate and the Fe-Mn oxyhydroxide fraction of two marine sediment cores influenced by large river systems (GeoB16224-1: Amazon River basin; GeoB6212-1: Río de la Plata drainage basin). The Sr isotopic signature of the bulk fraction is highly influenced by the carbonate fraction. Therefore, for a detrital signature the decarbonization step is strongly necessary. During the carbonate leaching step, detrital

material (i.e. clay minerals) can contaminate the Nd isotopic signal, the Sr isotopic signal is largely unaffected and represents a (paleo) seawater signature. We confirm that the Fe-Mn oxyhydroxide fraction should be treated carefully in respect to the interpretation as a paleo seawater signal. In our study the Fe-Mn oxyhydroxide fraction of core GeoB16224-1 reflects pre-formed river borne Fe-Mn oxyhydroxide coatings and clay contamination. The Fe-Mn oxyhydroxide fraction of core GeoB6212-1 reflects dolomite and clay mineral contamination. There is no large variation between the radiogenic isotope signal of the decarbonated and further Fe-Mn oxyhydroxide leached fraction. Therefore, we strongly argue against the application of the Fe-Mn oxyhydroxide leaching step on marine sediments influenced by large river systems. Furthermore, if analyses on the Fe-Mn oxyhydroxide fraction are made, it is very important to check if it really does represent authigenic Fe-Mn oxyhydroxide coatings of marine sediments.

5.8 Acknowledgments

This work was funded through the DFG-Research Center/Cluster of Excellence “The Ocean in the Earth System” at MARUM – Center for Environmental Sciences, University of Bremen. We thank the RV Maria S. Merian cruise MSM20/3 crew. Sample material has been provided by the GeoB Core Repository at the MARUM – Center for Marine Environmental Sciences, University of Bremen, Germany. The data reported in this paper are archived in Pangaea (www.pangaea.de). NH thanks GLOMAR – Bremen International Graduate School for Marine Sciences for support.

5.9 References

Albarède, F., Goldstein, S. L. (1992). World map of Nd isotopes in sea-floor ferromanganese deposits. *Geology*, **20(8)**, 761-763.

Allard, T., Menguy, N., Salomon, J., Calligaro, T., Weber, T., Calas, G., Benedetti, M. F. (2004). Revealing forms of iron in river-borne material from major tropical rivers of the Amazon Basin (Brazil) 1*. Geochimica et Cosmochimica Acta*, **68(14)**, 3079-3094.

Arunachalam, J., Emons, H., Krasnodebska, B., Mohl, C. (1996). Sequential extraction studies on homogenized forest soil samples. *Science of the Total Environment*, **181(2)**, 147-159.

Banner, J. L., Hanson, G. N., Meyers, W. J. (1988). Rare earth element and Nd isotopic variations in regionally extensive dolomites from the Burlington-Keokuk Formation (Mississippian): Implications for REE mobility during carbonate diagenesis. *Journal of Sedimentary Research*, **58(3)**.

Bayon, G., German, C. R., Boella, R. M., Milton, J. A., Taylor, R. N., Nesbitt, R. W. (2002). An improved method for extracting marine sediment fractions and its application to Sr and Nd isotopic analysis. *Chemical Geology*, **187(3)**, 179-199.

Bayon, G., German, C. R., Burton, K. W., Nesbitt, R. W., Rogers, N. (2004). Sedimentary Fe–Mn oxyhydroxides as paleoceanographic archives and the role of aeolian flux in regulating oceanic dissolved REE. *Earth and Planetary Science Letters*, **224(3)**, 477-492.

Bergquist, B. A., Boyle, E. A. (2006). Iron isotopes in the Amazon River system: weathering and transport signatures. *Earth and Planetary Science Letters*, **248(1)**, 54-68.

Berner, R. A., Rao, J. L. (1994). Phosphorus in sediments of the Amazon River and estuary: Implications for the global flux of phosphorus to the sea. *Geochimica et Cosmochimica Acta*, **58(10)**, 2333-2339.

Blaser, P., Lippold, J., Gutjahr, M., Frank, N., Link, J. M., Frank, M. (2016). Extracting foraminiferal seawater Nd isotope signatures from bulk deep sea sediment by chemical leaching. *Chemical geology*, **439**, 189-204.

Burton, K. W., Lee, D. C., Christensen, J. N., Halliday, A. N., Hein, J. R. (1999). Actual timing of neodymium isotopic variations recorded by Fe Mn crusts in the western North Atlantic. *Earth and Planetary Science Letters*, **171(1)**, 149-156.

Campos, M. C., Chiessi, C. M., Voigt, I., Piola, A. R., Kuhnert, H., Mulitza, S. (2017). δ 13 C decreases in the upper western South Atlantic during Heinrich Stadials 3 and 2. *Climate of the Past*, **13(4)**, 345-358.

Chester, R., Hughes, M. J. (1966). The distribution of manganese, iron and nickel in a North Pacific deep-sea clay core. *Deep Sea Research and Oceanographic Abstracts*, **13(4)**, 627-634

Chester, R., Hughes, M. J. (1967). A chemical technique for the separation of ferro-manganese minerals, carbonate minerals and adsorbed trace elements from pelagic sediments. *Chemical geology*, **2**, 249-262.

Crocket, K. C., Vance, D., Foster, G. L., Richards, D. A., Tranter, M. (2012). Continental weathering fluxes during the last glacial/interglacial cycle: insights from the marine sedimentary Pb isotope record at Orphan Knoll, NW Atlantic. *Quaternary Science Reviews*, **38**, 89-99.

de Mahiques, M. M., Tassinari, C. C. G., Marcolini, S., Violante, R. A., Figueira, R. C. L., da Silveira, I. C. A., Burone, L., e Sousa, S. H. D. M. (2008). Nd and Pb isotope signatures on the Southeastern South American upper margin: Implications for sediment transport and source rocks. *Marine Geology*, **250(1)**, 51-63.

Deniel, C., Pin, C. (2001). Single-stage method for the simultaneous isolation of lead and strontium from silicate samples for isotopic measurements. *Analytica Chimica Acta*, **426(1)**, 95-103.

Depetris, P. J., Griffin, J. J. (1968). Suspended load in the Río de la Plata drainage basin. *Sedimentology*, **11(1-2)**, 53-60.

Depetris, P. J., Probst, J. L., Pasquini, A. I., Gaiero, D. M. (2003). The geochemical characteristics of the Paraná River suspended sediment load: an initial assessment. *Hydrological Processes*, **17(7)**, 1267-1277.

Du, J., Haley, B. A., Mix, A. C. (2016). Neodymium isotopes in authigenic phases, bottom waters and detrital sediments in the Gulf of Alaska and their implications for paleo-circulation reconstruction. *Geochimica et Cosmochimica Acta*, **193**, 14-35.

Edmond, J. M. (1992). Himalayan tectonics, weathering processes, and the strontium isotope record in marine limestones. SCIENCE-NEW YORK THEN WASHINGTON-, 258, 1594-1594.

Elmore, A. C., Piotrowski, A. M., Wright, J. D., Scrivner, A. E. (2011). Testing the extraction of past seawater Nd isotopic composition from North Atlantic deep sea sediments and foraminifera. *Geochemistry, Geophysics, Geosystems*, **12(9).**

Frank, M., Whiteley, N., Kasten, S., Hein, J. R., O'Nions, K. (2002). North Atlantic Deep Water export to the Southern Ocean over the past 14 Myr: Evidence from Nd and Pb isotopes in ferromanganese crusts. *Paleoceanography,* **17(2)**.

Gibbs, R. J. (1967). The geochemistry of the Amazon River system: Part I. The factors that control the salinity and the composition and concentration of the suspended solids. *Geological Society of America Bulletin*, **78(10)**, 1203-1232.

Gibbs, R. J., Konwar, L. (1986). Coagulation and settling of Amazon River suspended sediment. *Continental Shelf Research*, **6(1-2)**, 127-149.

Goldberg, E. D. (1954). Marine geochemistry 1. Chemical scavengers of the sea. *The Journal of Geology*, **62(3)**, 249-265.

Govin, A., Holzwarth, U., Heslop, D., Ford Keeling, L., Zabel, M., Mulitza, S., Collins, J. A., Chiessi, C. M. (2012). Distribution of major elements in Atlantic surface sediments (36 N–49 S): Imprint of terrigenous input and continental weathering. *Geochemistry, Geophysics, Geosystems*, **13(1)**.

Guerrero, R. A., Acha, E. M., Framin, M. B., Lasta, C. A. (1997). Physical oceanography of the Río de la Plata Estuary, Argentina. *Continental Shelf Research*, **17(7)**, 727-742.

Gutjahr, M., Frank, M., Stirling, C. H., Klemm, V., Van de Flierdt, T., Halliday, A. N. (2007). Reliable extraction of a deepwater trace metal isotope signal from Fe–Mn oxyhydroxide coatings of marine sediments. *Chemical Geology*, **242(3)**, 351-370.

Gutjahr, M., Frank, M., Stirling, C. H., Keigwin, L. D., Halliday, A. N. (2008). Tracing the Nd isotope evolution of North Atlantic deep and intermediate waters in the Western North Atlantic since the Last Glacial Maximum from Blake Ridge sediments. *Earth and Planetary Science Letters*, **266(1)**, 61-77.

Häggi, C., Chiessi, C. M., Merkel, U., Mulitza, S., Prange, M., Schulz, M., Schefuß, E. (2017). Response of the Amazon rainforest to late Pleistocene climate variability. *Earth and Planetary Science Letters*, **479**, 50-59.

Henderson, G. M., Martel, D. J., O'Nions, R. K., Shackleton, N. J. (1994). Evolution of seawater 87Sr86Sr over the last 400 ka: the absence of glacial/interglacial cycles. *Earth and Planetary Science Letters*, **128(3-4)**, 643-651.

Henry, F., Probst, J. L., Thouron, D., Depetris, P. J., Garçon, V. (1996). Nd-Sr isotopic compositions of dissolved and particulate material transported by the Parana and Uruguay rivers during high (december 1993) and low (september 1994) water periods. *Sciences Géologiques, Bulletin*, **49(1-4)**, 89-100.

Howe, J. N., Piotrowski, A. M., Oppo, D. W., Huang, K. F., Mulitza, S., Chiessi, C. M., Blusztajn, J. (2016). Antarctic intermediate water circulation in the South Atlantic over the past 25,000 years. *Paleoceanography*, **31(10)**, 1302-1314.

Huang, K. F., Oppo, D. W., Curry, W. B. (2014). Decreased influence of Antarctic intermediate water in the tropical Atlantic during North Atlantic cold events. *Earth and Planetary Science Letters*, **389**, 200-208.

Jeandel, C. (1993). Concentration and isotopic composition of Nd in the South Atlantic Ocean. Earth and Planetary Science Letters, **117(3-4)**, 581-591.

Johns, W. E., Lee, T. N., Schott, F. A., Zantopp, R. J., Evans, R. H. (1990). The North Brazil Current retroflection: Seasonal structure and eddy variability. *Journal of Geophysical Research: Oceans*, **95(C12)**, 22103-22120.

Kraft, S., Frank, M., Hathorne, E. C., Weldeab, S. (2013). Assessment of seawater Nd isotope signatures extracted from foraminiferal shells and authigenic phases of Gulf of Guinea sediments. *Geochimica et Cosmochimica Acta*, **121**, 414-435.

Lacan, F., Jeandel, C. (2005). Neodymium isotopes as a new tool for quantifying exchange fluxes at the continent–ocean interface. *Earth and Planetary Science Letters*, **232(3)**, 245-257.

Lambelet, M., van de Flierdt, T., Crocket, K., Rehkämper, M., Kreissig, K., Coles, B., Rijkenberg, M. J. A., Gerringa, L. A. A., de Baar, H. J. W., Steinfeldt, R. (2016). Neodymium isotopic composition and concentration in the western North Atlantic Ocean: results from the GEOTRACES GA02 section. *Geochimica et Cosmochimica Acta*, **177**, 1-29.

Lantzsch, H., Hanebuth, T. J., Chiessi, C. M., Schwenk, T., Violante, R. A. (2014). The high-supply, current-dominated continental margin of southeastern South America during the late Quaternary. *Quaternary Research*, **81(2)**, 339-354.

Longinelli, A., Edmond, J. M. (1983). Isotope geochemistry of the Amazon basin: a reconnaissance. *Journal of Geophysical Research: Oceans*, **88(C6)**, 3703-3717.

Martin, E. E., Haley, B. A. (2000). Fossil fish teeth as proxies for seawater Sr and Nd isotopes. *Geochimica et Cosmochimica Acta*, **64(5)**, 835-847.

Martin, E. E., Blair, S. W., Kamenov, G. D., Scher, H. D., Bourbon, E., Basak, C., Newkirk, D. N. (2010). Extraction of Nd isotopes from bulk deep sea sediments for paleoceanographic studies on Cenozoic time scales. *Chemical Geology*, **269(3)**, 414-431.

Meade, R. H. (1994). Suspended sediments of the modern Amazon and Orinoco rivers. *Quaternary International*, **21**, 29-39.

Milliman, J. D., Meade, R. H. (1983). World-wide delivery of river sediment to the oceans. *The Journal of Geology*, **91(1)**, 1-21.

Morse, J. W., Mackenzie, F. T. (1990). Geochemistry of sedimentary carbonates (Vol. 48). Elsevier.

Mulitza, S., Chiessi, C.M., Cruz, A.P.S., Frederichs, T., Gomes, J.G., Gurgel, M.H., Haberkern, J., Huang, E., Jovane, L., Kuhnert, H., Pittauerová, D., Reiners, S.-J., Roud, S.C., Schefuß, E., Schewe, F., Schwenk, T.A., Sicoli Seoane, J.C., Sousa, S.H.M., Wagner, D.J., Wiers, S. (2013). Response of Amazon sedimentation to deforestation, land use and climate variability, Cruise No. MSM20/3, February 19–March 11 2012, Recife (Brazil), Bridgetown (Barbados). Berichte, Fachbereich Geowissenschaften, Universität Bremen, Bremen, Germany, 1-86.

O'nions, R. K., Frank, M., Von Blanckenburg, F., Ling, H. F. (1998). Secular variation of Nd and Pb isotopes in ferromanganese crusts from the Atlantic, Indian and Pacific Oceans. *Earth and Planetary Science Letters*, **155(1)**, 15-28.

Palmer, M. R., Elderfield, H. (1985). Sr isotope composition of sea water over the past 75 Myr. *Nature*, **314(6011)**, 526-528.

Palmer, M. R., Elderfield, H. (1986). Rare earth elements and neodymium isotopes in ferromanganese oxide coatings of Cenozoic foraminifera from the Atlantic Ocean∗∗ Cambridge Earth Sciences Series, Contribution No. 651. *Geochimica et Cosmochimica Acta*, **50(3)**, 409-417.

Pahnke, K., Goldstein, S. L., Hemming, S. R. (2008). Abrupt changes in Antarctic Intermediate Water circulation over the past 25,000 years. *Nature Geoscience*, **1(12)**, 870.

Pin, C., Briot, D., Bassin, C., Poitrasson, F. (1994). Concomitant separation of strontium and samarium-neodymium for isotopic analysis in silicate samples, based on specific extraction chromatography. *Analytica Chimica Acta*, **298(2)**, 209-217.

Piola, A. R., Campos, E. J., Möller, O. O., Charo, M., Martinez, C. (2000). Subtropical shelf front off eastern South America. *Journal of Geophysical Research: Oceans*, **105(C3)**, 6565-6578.

Piotrowski, A. M., Galy, A., Nicholl, J. A. L., Roberts, N., Wilson, D. J., Clegg, J. A., Yu, J. (2012). Reconstructing deglacial North and South Atlantic deep water sourcing using foraminiferal Nd isotopes. *Earth and Planetary Science Letters*, **357**, 289-297.

Rao, J. L., Berner, R. A. (1993). Phosphorus dynamics in the Amazon river and estuary. *Chemical geology*, **107(3-4)**, 397-400.

Ray, S., Gault, H. R., Dodd, C. G. (1957). The separation of clay minerals from carbonate rocks. *Am. Mineral*, **42**, 681-686.

Roberts, N. L., Piotrowski, A. M., McManus, J. F., Keigwin, L. D. (2010). Synchronous deglacial overturning and water mass source changes. *Science*, **327(5961)**, 75-78.

Roberts, N. L., Piotrowski, A. M. (2015). Radiogenic Nd isotope labeling of the northern NE Atlantic during MIS 2. *Earth and Planetary Science Letters*, **423**, 125-133.

Rothwell, R. G. (Ed.). (2012). Minerals and mineraloids in marine sediments: an optical identification guide. Springer Science & Business Media.

Schulz H. D., Ayres Neto A., Boetius A., Enneking K., Fabian K., Feseker T., Funk J., Gorke M., Heidersdorf F., Hensen C., Heuer V., Hill H.G., Hinrichs S., Kasten S., Klann M., Lacerda de Souza C., Martinez Briao A., Meyer S., Mulitza S., Niebler H.-S., Ochsenhirt W.-T., Panteleit B., Pfeifer K., Schewe F., Schwenk T., Senorans J.L., Siemer S., Steinmetz E., Wenzhöfer F. (2001). Report and preliminary results of Meteor Cruise M46/2. Berichte, Fachbereich Geowissenschaften, Universität Bremen, 184, 107.

Stichel, T., Frank, M., Rickli, J., Haley, B. A. (2012). The hafnium and neodymium isotope composition of seawater in the Atlantic sector of the Southern Ocean. *Earth and Planetary Science Letters*, **317**, 282-294.

Sverdrup, H. U., Johnson, M. W., Fleming, R. H. (1942). The Oceans: Their physics, chemistry, and general biology (Vol. 7). New York: Prentice-Hall.

Tachikawa, K., Athias, V., Jeandel, C. (2003). Neodymium budget in the modern ocean and paleo-oceanographic implications. *Journal of Geophysical Research: Oceans*, **108(C8)**.

Veizer, J. (1989). Strontium isotopes in seawater through time. *Annual Review of Earth and Planetary Sciences*, **17(1)**, 141-167.

Veizer, J., Ala, D., Azmy, K., Bruckschen, P., Buhl, D., Bruhn, F., Carden, G. A. F, Diener, A., Ebneth, S., Godderis, Y., Jasper, T., Korte, C., Pawellek, F., Podlaha, O. G., Strauss, H. (1999). 87Sr/86Sr, δ13C and δ18O evolution of Phanerozoic seawater. *Chemical geology*, **161(1)**, 59-88.

Voigt, I., Henrich, R., Preu, B. M., Piola, A. R., Hanebuth, T. J., Schwenk, T., Chiessi, C. M. (2013). A submarine canyon as a climate archive—interaction of the Antarctic Intermediate Water with the Mar del Plata Canyon (Southwest Atlantic). *Marine Geology*, **341**, 46-57.

Wasserburg, G.J., DePaolo, D.J. (1979). Models of earth structure inferred from neodymium and strontium isotopic abundances. *Proceedings of the National Academy of Sciences*, **76(8)**, 3594-3598.

Wei, G., Deng, W., Liu, Y., Li, X. (2007). High-resolution sea surface temperature records derived from foraminiferal Mg/Ca ratios during the last 260 ka in the northern South China Sea. *Palaeogeography, Palaeoclimatology, Palaeoecology*, **250(1)**, 126-138.

Wilson, D. J., Piotrowski, A. M., Galy, A., Clegg, J. A. (2013). Reactivity of neodymium carriers in deep sea sediments: Implications for boundary exchange and paleoceanography. *Geochimica et Cosmochimica Acta*, **109**, 197-221.

Wilson, D. J., Crocket, K. C., Flierdt, T., Robinson, L. F., Adkins, J. F. (2014). Dynamic intermediate ocean circulation in the North Atlantic during Heinrich Stadial 1: A radiocarbon and neodymium isotope perspective. *Paleoceanography*, **29(11)**, 1072-1093.

Xie, R. C., Marcantonio, F., Schmidt, M. W. (2014). Reconstruction of intermediate water circulation in the tropical North Atlantic during the past 22,000 years. *Geochimica et Cosmochimica Acta*, **140**, 455-467.

Zhang, Y., Chiessi, C.M., Mulitza, S., Zabel, M., Trindade, R.I., Hollanda, M.H.B., Dantas, E.L., Govin, A., Tiedemann, R., Wefer, G. (2015). Origin of increased terrigenous supply to the NE South American continental margin during Heinrich Stadial 1 and the Younger Dryas. *Earth and Planetary Science Letters*, **432**, 493-500.

Chapter 6
Conclusion and Outlook

The primary aim of this thesis was to study the sediment supply evolution and modern situation of the Amazon River and Río de la Plata drainage basins. Sr, Nd and Pb isotopes were determined on modern river sediments and marine sediment cores, archiving the river sediment for the past 30 to 40 cal ka BP. The radiogenic isotope signatures proved valuable to establish the modern sediment sources and identify prominent shifts in the sediment supply histories of the respective basins. The use of a multi isotope approach made it possible to differentiate between most source areas even with overlapping isotopic signature in one or another isotope system. However, some areas, like the northern (Guiana Shield) and southern (Brazilian Shield) Precambrian Amazon Craton could not be differentiated, due to similar geology and thus overlapping radiogenic isotope signatures in all isotope systems.

Two major sediment sources (the Andes and the cratonic Shields) could be confirmed for the Amazon River basin, with the Andes being the main sediment supplier today and in the last 40 kyr. Additionally, the ε_{Nd} isotopic signature of the down-core record suggests a shift in the precipitation locus during the second part of the Heinrich Stadial 1 from the Andes to the cratonic Shields. Furthermore, all three radiogenic isotope systems have a prominent offset between the modern and paleo value of the Amazon River SPM. An external influence causing the shift could be excluded through literature data. We propose a basin internal shift changing the radiogenic isotope signature. Holocene core top analyses established the time of the shift at some point during the late Holocene. The offset indicates a modern more Andean dominated SPM signal compared to the past. Therefore, we suggest a decrease in precipitation over the eastern or an increase of precipitation over the western sector of the Amazon River basin causing higher erosion rate in the Andes. Additionally, we hypothesize that the building of large dams in the Madeira River basin led to a small sediment source shift in the last decades.

The results for the radiogenic isotope signatures of the Río de la Plata drainage basin sediments established three main source areas, (i) the upper Paraná River drainage basin, (ii) the Uruguay River and (iii) the Andean draining rivers (Salado, Bermejo and Pilcomayo Rivers). Pronounced shifts in the down-core record indicate changes in the sediment provenance that could be linked to millennial scale climate events. A dominant sediment input from the Andean draining rivers of the Río de la Plata drainage basin during the Heinrich Stadial 1 and the Younger Dryas suggests a strong South American Summer Monsoon that intensified the precipitation in the Andes. A provenance shift towards a dominant sediment input from the southeastern sector (Uruguay River basin) of the Río de la Plata drainage basin implies a strong Atlantic Meridional Overturning Circulation that shifts the Intertropical Convergence Zone northward and strengthens the southeast trade winds leading to higher precipitation in this basin sector. Additionally, our results confirm that a sea level rise at the beginning of the Holocene allowed the deposition of external material from southern Argentina at the

GeoB6212-1 core location, also observed in a nearby marine sediment core by Lantzsch et al. (2014). This specific shift in the down-core record once more clarifies how important a multi isotope approach can be, as the external ε_{Nd} signature of the Argentinian sediment is very similar to the basin internal ε_{Nd} signature of the Uruguay River basin. The Sr and Pb isotopic signature however, excluded the Uruguay River basin as a possible sediment source.

The study of different leaching fractions clearly establishes that the decarbonization of marine sediment is vital to obtain the detrital sediment signature. Due to a high Sr concentration in marine carbonates, the detrital Sr isotopic signature is otherwise overprinted. Additionally, the Fe-Mn oxyhydroxide leaching procedure on marine sediments was found to be redundant to obtain the detrital signal, as it already predominantly leached parts of the detrital components (i.e. clay minerals). Furthermore, the radiogenic isotope signatures and major element concentrations of the Fe-Mn oxyhydroxide fraction were challenging to interpret. However, it was clear that in this study it did not represent a paleo seawater signal, as is often assumed in the literature. It was shown, that a contamination from detrital particles poses a high risk. The results of the Fe-Mn oxyhydroxide fraction of core GeoB16224-1 (influenced by Amazon River basin sediments) revealed that Fe-Mn oxyhydroxide coatings were present, but they were probably river borne. These findings support the theory of Bayon et al. (2004) and Kraft et al. (2013) that settings with strong riverine influence might have pre-formed river borne Fe-Mn oxyhydroxide coatings. Further, the study could confirm that the Sr isotopic signature of leached carbonates represents a paleo seawater signature. However, the Nd isotopic signature should be treated carefully, because of a contamination sensitivity due to much lower Nd concentrations in carbonates compared to detrital material. Overall, the leaching study showed that the interpretation of leaching fractions should be treated with caution, a thorough examination of all fractions is key to a credible interpretation.

This PhD project confirms that radiogenic isotopes are an effective tool to identify the provenance of sediments, if the source areas are sufficiently different in their radiogenic isotope signatures. The results reveal the impact of natural (i.e. climate) events on the sediment dynamic of large river basins and demonstrate what possible consequences future naturally or anthropogenically induced climate changes (i.e. precipitation locus shifts) might have. The newly produced radiogenic isotope river sediment data, especially for the tributaries of the Río de la Plata drainage basin, will give future researchers in these areas the possibility to easily and more accurately identify the provenance of their analyzed material. Nonetheless, to make well founded conclusions, especially about large and highly dynamic systems (i.e. large river basins), additional research is needed and a profound database is highly beneficial.

Therefore, following are several suggestions for future research:

- Additional samples of river suspended particulate matter from both river basins should be taken to extend the existing database and to allow an even more precise provenance interpretation in the future. Especially SPM samples of the Río de la Plata estuary are needed to get the modern radiogenic isotope signature of the sediment supplied into the Ocean missing from this PhD thesis.
- Well-dated core material from the Amazon River mouth and the Río de la Plata estuary could be analyzed to get a high-resolution Holocene record, and be able to determine possible anthropogenic impacts (i.e. damming of the tributaries) and identify the exact timing of the SPM provenance shift observed in the Amazon River basin in this study.
- To determine whether pre-formed river borne Fe-Mn oxyhydroxide coatings are present in other river influenced settings, river suspended particulate matter (especially from the river mouth or estuary) should be submitted to Fe-Mn oxyhydroxide leaching.
- A similar study on other large river basins would be interesting to reveal common and contrasting features. One recommendation would be the Congo River basin. It is the second largest in the world and has similar morphological (a large flat plain flanked by highlands) and climatic (large parts are covered by rain forest) settings (Runge, 2008) like the Amazon River basin. Furthermore Bayon et al. (2004) hypothesized about the influence of river borne Fe-Mn oxyhydroxides on analyzed marine sediments in front of the Congo River basin. Another recommendation would be the Orinoco River basin. It would complement this PhD thesis very well, as the Orinoco is the third largest river basin in South America (Milliman and Meade, 1983) and is closely coupled to the Amazon River basin.

6.1 References

Bayon, G., German, C. R., Burton, K. W., Nesbitt, R. W., Rogers, N. (2004). Sedimentary Fe–Mn oxyhydroxides as paleoceanographic archives and the role of aeolian flux in regulating oceanic dissolved REE. *Earth and Planetary Science Letters*, **224(3)**, 477-492.

Kraft, S., Frank, M., Hathorne, E. C., Weldeab, S. (2013). Assessment of seawater Nd isotope signatures extracted from foraminiferal shells and authigenic phases of Gulf of Guinea sediments. *Geochimica et Cosmochimica Acta*, **121**, 414-435.

Lantzsch, H., Hanebuth, T. J., Chiessi, C. M., Schwenk, T., Violante, R. A. (2014). The high-supply, current-dominated continental margin of southeastern South America during the late Quaternary. *Quaternary Research*, **81(2)**, 339-354.

Milliman, J. D., & Meade, R. H. (1983). World-wide delivery of river sediment to the oceans. *The Journal of Geology*, **91(1)**, 1-21.

Runge, J. (2008). The Congo River, Central Africa. Large Rivers: Geomorphology and Management. Chichester, John Wiley and Sons Ltd, 293-309.

Acknowledgement

First and foremost, I would like to thank my supervisor Prof. Dr. Simone A. Kasemann for her support and encouragement during the last three years. I truly appreciate you reading my drafts endless times, your excitement about my data even when I wasn't excited and all the helpful discussions we had. Above all, thank you in particular for always showing understanding for personal matters.

Further I want to thank Prof. Dr. Cristiano M. Chiessi. I benefited greatly from the fruitful discussions and your constructive comments and ideas. Thanks for always answering your Emails so quickly and especially for all your help with the field trip.

Sincere thanks go to Dr. Friedrich Lucassen and Annette Meixner for listening to loads and loads of test talks, sharing their vast experience with me and their support in various technical and practical issues in the lab.

I also would like to thank Dr. Enno Schefuß for being part of my thesis committee and for helping me with not losing the bigger picture through his outsider perspective. In this context I would like to thank GLOMAR for the training and financial support.

Dr. André O. Sawakuchi is thanked for providing the sampling equipment for the field trip in Brazil and his valuable feedback on my first manuscript.

Special thanks are given to Barbara Muntz for the administrative help and her cheerful personality.

An enormous thank you to Carolina. I had a wonderful time with you during the field trip in Brazil. Thanks for driving with me for hours and hours and hours through Brazil, sitting in tiny boats, explaining to puzzled boatmen what the heck we are doing and for being my voice while I was the bank. Additionally, I am lucky to have found a dear friend in you, obrigada!

My Isotope Girls: Rieke, Lera, Gustavo and Aneka. The best office mates in the world that grew into great friends. A tremendous thank you for all the awesome conversations, the dancing in clean room suits, the dreaming of being lottery winners and traveling the world. Thanks for all your heartfelt advice and loving comfort. I will forever treasure the time we had together… when I go ooh shooby doo doo lang!

I also would like to thank Timo and Lina for being my lunch buddies.

Here is a good place to thank my friends from Bremen. I am particular grateful to Johanna. Thanks for helping me through tough times and being the understanding and loving person that you are. Jula, Helen, Daniel and Geesche, thanks for providing me once a month with a

phenomenal three course meal at our Kochroulette and thanks for introducing me to cool new sports (Bouldering and Roller Derby). Thank you, Melanie, for all the coffee breaks and wonderful conversations. Special thanks go to the whole queerfilm team. I am very glad that I decided to join you. It was a welcome weekly distraction and greatly improved my work-life balance, especially during the final phase of the thesis. Astrid, thanks for always reminding me about everything!

And of course, I can also not forget my friends from Lüneburg. Marina, thanks for always being there, listening and giving excellent advice. Vanessa, thanks for constantly introducing me to amazing new things and thoughts.

And now to my family, my mum, my sister and my grandpa. I am forever grateful for your everlasting love and support. We endured some tough times in the last years, grew closer together and got stronger. Thanks for always being there for me, loving me the way I am and accepting my faults. I know my dad would have been very proud of me and he will always be in my heart.

Finally, Leo, I am so enormously thankful that you came into my life this year. Thanks for hitting your head on your trunk lid. I will forever cherish the (late night) walks with Nako, the marvelous weekend trips and all the new experiences we made together. Thanks for being patient with me when I am overwhelmed, always making me giggle and keeping me calm. rawr rawr rawr!

Appendices

A.1 Column Procedure – Separation of Sr and Pb on a single Sr.spec column.

a) **Column preparation**
   - Load ~ 70 µl Sr.spec with Milli Q onto the column

b) **Precondition the column (dispose eluate)**
   - 2 x full reservoir of 6 N HCl
   - 4 x full reservoir of Milli Q
   - 2 x 500 µl of 2 N HNO_3

c) **Sample addition (collect eluate for REE separation)**
   - Add the sample in 100 µl steps

d) **Rinse (collect eluate for REE separation)**
   - 12 x 100 µl of 2 N HNO_3

e) **Elution of Sr**
   - 5 x 200 µl of 0.05 N HNO_3

f) **Change column chemistry (dispose eluate)**
   - 5 x 100 µl of 2 N HCl

g) **Elution of Pb**
   - 4 x 200 µl of 6 N HCl

➔ Add 20 µl of 0.1 N H_3PO_4 and dry the Sr and Pb elution on a hotplate at 80 to 100 °C
➔ Add 70 µl of concentrated HNO_3 (to remove possible resin remains)
➔ Dry Sr elution at 80 to 100 °C
➔ Leave Pb elution on the hotplate with a closed lid over night at 140 °C, dry the next day at 100°C
➔ Add 40 µl of H_2O_2 into the warm beaker (to remove possible organic matter remains)
➔ Observe reaction and dry at 50 to 60°C

➔ Clean columns with Milli Q and discard the used Sr.spec

A.2 Column Procedure – Separation of LREE on TRU.spec columns.

a) **Column preparation**
   - Load ~ 250 µl TRU.spec with Milli Q onto the column

b) **Precondition the column (dispose eluate)**
   - 3 x full reservoir of Milli Q
   - 2 ml of 0.05 N HNO_3
   - 1 x full reservoir of Milli Q
   - 2 x 0.5 ml of 2 N HNO_3

c) **Sample addition (dispose eluate)**
   - Add the sample in 500 µl steps

d) **Rinse (dispose eluate)**
   - 7 x 0.5 ml of 2 N HNO_3
   - 1 x 0.25 ml of 0.05 N HNO_3

e) **Elution of LREE (collect eluate for Nd separation)**
   - 4 x 0.5 ml of 0.05 N HNO_3

➔ Clean the columns with Milli Q, save the resin for reuse after cleaning

A.3 Column Procedure – Separation of Nd on LN.spec columns.

➔ The LN.spec resin is preinstalled in glass columns

a) **Precondition the column (dispose eluate)**
   - 1 x 5 ml of 0.25 N HCl
   - 1 x 5 ml of Milli Q
   - 2 x 1 ml of 0.05 N HNO_3

b) **Sample addition (dispose eluate)**
   - Add the sample in 500 µl steps

c) **Rinse (dispose eluate)**
   - 3 x 0.25 ml of 0.25 N HCl
   - 1 x 0.5 ml of 0.25 N HCl
   - 1 x 2 ml of 0.25 N HCl

d) **Elution of Nd**
   - 1 x 2.5 ml of 0.25 N HCl

e) **Column cleaning**
   - 2 x 5 ml of 6 N HCl
   - 2 x 5 ml of 0.25 N HCl

➔ Add 20 µl of 0.1 N H_3PO_4 and dry the Nd elution on a hotplate at 80 to 100 °C

➔ Put the columns in their storage container in 0.25 N HCl (Column should not fall dry!)

B.1 $^{87}Sr/^{86}Sr$ isotope ratios of reference materials.

Measurement # on the TIMS	Standard	Date	$^{87}Sr/^{86}Sr$	± $2SD_{mean}$
241	NIST 987	19.05.2015	0.710251	0.000006
241	NIST 987	20.05.2015	0.710255	0.000008
249	NIST 987	10.07.2015	0.710245	0.000008
249	NIST 987	13.07.2015	0.710239	0.000007
257	NIST 987	13.08.2015	0.710251	0.000008
258	NIST 987	15.08.2015	0.710245	0.000006
269	NIST 987	24.09.2015	0.710251	0.000006
270	NIST 987	28.09.2015	0.710241	0.000006
272	NIST 987	09.10.2015	0.710252	0.000006
280	NIST 987	23.11.2015	0.710249	0.000005
285	NIST 987	07.12.2015	0.710249	0.000008
294	NIST 987	26.01.2016	0.710244	0.000007
303	NIST 987	02.05.2016	0.710248	0.000005
314	NIST 987	07.07.2016	0.710245	0.000006
318	NIST 987	15.08.2016	0.710246	0.000007
325	NIST 987	28.11.2016	0.710249	0.000008
327	NIST 987	06.12.2016	0.710238	0.000006
328	NIST 987	09.12.2016	0.710239	0.000006
329	NIST 987	19.12.2016	0.710237	0.000006
335	NIST 987	02.02.2017	0.710255	0.000005
339	NIST 987	20.03.2017	0.710255	0.000006
341	NIST 987	27.03.2017	0.710242	0.000009
350	NIST 987	17.05.2017	0.710249	0.000005
353	NIST 987	31.05.2017	0.710239	0.000006
	Average: 0.710246 ± 0.000011 (2SD)			
314	B8	07.07.2016	0.711914	0.000005
329	B8	20.12.2016	0.711932	0.000008
353	B8	01.06.2017	0.711600	0.000008
314	TB	08.07.2016	0.734844	0.000007
329	TB	21.12.2016	0.734708	0.000008
353	TB	01.06.2017	0.734653	0.000011

B.2 Pb isotope ratios of reference materials.

Measurement # on the TIMS	Standard	Date	$^{206}Pb/^{204}Pb$[a]	$^{207}Pb/^{204}Pb$[a]	$^{208}Pb/^{204}Pb$[a]
242	NIST 981	22.05.2015	16.8986(6)	15.4403(7)	36.537(2)
242	NIST 981	22.05.2015	16.9072(8)	15.452(1)	36.575(3)
249	NIST 981	13.07.2015	16.8945(5)	15.4351(4)	36.521(1)
250	NIST 981	14.07.2015	16.8931(4)	15.4335(4)	36.5160(9)
260	NIST 981	24.08.2015	16.8954(6)	15.4369(6)	36.527(2)
273	NIST 981	16.10.2015	16.8947(5)	15.4359(5)	36.524(1)
280	NIST 981	24.11.2015	16.9043(5)	15.4487(5)	36.564(1)
280	NIST 981	24.11.2015	16.913(2)	15.461(2)	36.603(8)
281	NIST 981	25.11.2015	16.9138(6)	15.4619(5)	36.606(1)
281	NIST 981	25.11.2015	16.9127(4)	15.4601(4)	36.6003(8)
285	NIST 981	08.12.2015	16.9001(7)	15.4427(7)	36.544(2)
286	NIST 981	09.12.2015	16.8938(5)	15.4345(5)	36.521(1)
295	NIST 981	01.02.2016	16.8954(8)	15.4368(9)	36.527(2)
296	NIST 981	03.02.2016	16.8992(5)	15.4418(6)	36.542(2)
301	NIST 981	27.04.2016	16.929 (2)	15.482(2)	36.667(6)
302	NIST 981	30.04.2016	16.919(1)	15.469(2)	36.629(6)
315	NIST 981	11.07.2016	16.904(1)	15.449(1)	36.568(2)
319	NIST 981	22.08.2016	16.912(1)	15.459(1)	36.598(2)
321	NIST 981	01.09.2016	16.9142(7)	15.4621(7)	36.606(2)
326	NIST 981	02.12.2016	16.943(2)	15.501(2)	36.729(6)
327	NIST 981	07.12.2016	16.9028(7)	15.447(8)	36.560(2)
330	NIST 981	22.12.2016	16.8895(7)	15.4293(6)	36.504(1)
336	NIST 981	08.02.2017	16.8865(5)	15.4246(5)	36.488(1)
340	NIST 981	23.03.2017	16.8943(7)	15.4355(7)	36.523(2)
347	NIST 981	08.05.2017	16.9024(9)	15.4463(9)	36.557(2)
348	NIST 981	10.05.2017	16.8968(7)	15.4384(7)	36.532(2)
Average: 16.904 ± 0.025 (2SD), 15.449 ± 0.035 (2SD), 36.564 ± 0.109 (2SD)					
315	B8	11.07.2016	18.7640(9)	15.6175(8)	38.682(2)
330	B8	23.12.2016	18.7670(7)	15.6016(6)	38.633(1)
348	B8	10.05.2017	18.7745(8)	15.6052(7)	38.650(2)
315	TB	11.07.2016	19.444(1)	15.6395(8)	40.387(2)
330	TB	23.12.2016	19.615(3)	15.655(3)	40.420(6)
348	TB	10.05.2017	19.422(1)	15.6452(8)	40.418(2)

[a]Uncertainties ($2SD_{mean}$) are given for the last digit.

B.3 $^{143}Nd/^{144}Nd$ isotope ratios of reference materials.

Measurement # on the TIMS	Standard	Date	$^{143}Nd/^{144}Nd$	± $2SD_{mean}$
241	JNdi-1	21.05.2015	0.512093	0.000006
242	JNdi-1	22.05.2015	0.512097	0.000005
250	JNdi-1	14.07.2015	0.512101	0.000004
258	JNdi-1	17.08.2015	0.512094	0.000003
259	JNdi-1	19.08.2015	0.512097	0.000009
269	JNdi-1	25.09.2015	0.512091	0.000004
272	JNdi-1	14.10.2015	0.512096	0.000004
281	JNdi-1	25.11.2015	0.512093	0.000004
286	JNdi-1	10.12.2015	0.512086	0.000011
295	JNdi-1	02.02.2016	0.512095	0.000006
296	JNdi-1	03.02.2016	0.512094	0.000005
301	JNdi-1	27.04.2016	0.512095	0.000006
302	JNdi-1	01.05.2016	0.512093	0.000007
304	JNdi-1	09.05.2016	0.512089	0.000009
315	JNdi-1	12.07.2016	0.512097	0.000008
321	JNdi-1	01.09.2016	0.512085	0.000006
323	JNdi-1	10.10.2016	0.512088	0.000004
327	JNdi-1	06.12.2016	0.512090	0.000004
328	JNdi-1	09.12.2016	0.512093	0.000005
329	JNdi-1	20.12.2016	0.512093	0.000003
330	JNdi-1	22.12.2016	0.512092	0.000006
337	JNdi-1	09.02.2017	0.512096	0.000006
337	JNdi-1	10.02.2017	0.512097	0.000003
339	JNdi-1	20.03.2017	0.512090	0.000004
347	JNdi-1	08.05.2017	0.512084	0.000012
348	JNdi-1	10.05.2017	0.512101	0.000008
350	JNdi-1	18.05.2017	0.512086	0.000008
Average: 0.512093 ± 0.000009 (2SD)				
315	B8	12.07.2016	0.512098	0.000004
329	B8	20.12.2016	0.512099	0.000007
350	B8	19.05.2017	0.512098	0.000044
321	TB	01.09.2016	0.511908	0.000003
330	TB	22.12.2016	0.511936	0.000006
350	TB	19.05.2017	0.511967	0.000020

C.1 XRD results for core GeoB16224-1.

Sample depth [cm]	Age [cal ka BP]	Quartz	Plagioclase	K-feldspar	Sum: Phyllosillicates	Montmorillo-nites & smectites	Mixed layer clays	Illites & micas	Kaolinite	Chlorite	Clino-pyroxene	Ortho-pyroxene
		[wt %]	[wt %]	[wt %]	[wt %]	[wt %]	[wt %]	[wt %]	[wt %]	[wt %]	[wt %]	[wt %]
		± 1	± 2 to 5	± 2 to 5	± 5	± 5	± 5 to 10	± 5	± 2 to 5	± 2 to 5	± 2 to 5	± 2 to 5
17	5.4	19.4	8.6	3.2	49.8	4.9	21.4	8.7	8.0	6.8	1.2	0.0
53	7.5	16.4	9.2	3.8	45.7	3.0	25.4	7.2	6.0	4.2	4.7	2.5
55	8.7	16.5	6.5	3.2	47.0	5.3	21.1	11.7	5.0	4.0	1.3	0.0
65	12.2	14.2	8.5	3.4	47.3	1.7	21.0	13.3	7.6	3.7	1.0	3.2
75	13.2	16.9	5.8	1.9	50.0	0.7	31.1	9.6	7.4	1.4	0.7	4.4
88	13.9	13.9	8.1	3.3	57.3	3.3	16.6	29.8	7.1	0.6	1.6	4.3
95.5	14.2	13.0	5.1	1.9	55.2	6.5	20.1	18.7	6.4	3.5	0.9	2.7
127	15.5	12.7	7.5	1.9	56.6	10.1	20.1	19.6	5.9	0.9	2.1	2.2
147	16.4	14.3	8.5	2.4	49.8	6.1	24.6	8.8	9.9	0.4	0.0	0.0
157	16.8	13.6	10.3	2.1	55.7	3.9	39.3	6.0	6.0	0.6	1.4	3.1
317	24.1	14.4	6.3	2.4	61.9	1.3	25.9	24.5	5.4	4.9	0.0	1.2
377	26.9	15.6	9.7	2.7	44.8	2.0	17.1	18.4	6.1	1.3	4.2	0.7
427	29.4	14.1	7.9	8.3	54.3	1.0	21.8	22.7	7.9	0.8	5.2	0.3
491	33.2	16.1	10.9	5.6	54.2	4.6	37.8	4.6	6.6	0.6	1.1	0.0
531	35.4	17.2	8.1	2.4	49.7	0.6	28.7	12.1	5.7	2.7	1.6	3.8

C.1 (continued).

Sample depth [cm]	Age [cal ka BP]	Garnet, olivine, corundum	Epidote	Magnetite	Spinell	Pyrites	Fe-Oxides Fe-Hydroxides, manganit	Rutile, anatas	SiO2 nearly amorphous (Opal, glass)	Calcite
		[wt %]	[wt %]	[wt %]	[wt %]	[wt %]	[wt %]	[wt %]	[wt %]	[wt %]
		± 2 to 5	± 2 to 5	± 2 to 5	± 2 to 5	± 2 to 5	± 5 to 10	± 2 to 5		± 1
17	5.4	0.9	0.0	0.0	0.0	1.1	0.3	1.8	8.7	0.0
53	7.5	0.2	2.3	0.6	1.0	3.1	0.0	2.3	5.7	0.3
55	8.7	0.4	4.7	0.0	0.3	3.0	0.0	1.8	8.6	0.2
65	12.2	0.2	4.0	0.6	0.0	3.3	2.9	0.6	8.2	0.0
75	13.2	1.5	0.0	0.0	0.0	6.7	3.4	2.9	4.6	0.0
88	13.9	1.2	2.6	0.0	0.0	0.0	0.3	1.6	0.0	0.0
95.5	14.2	0.1	3.8	0.0	1.2	0.7	1.6	1.3	9.6	0.0
127	15.5	1.0	0.0	0.0	0.0	0.0	3.5	0.4	7.5	0.0
147	16.4	1.6	4.5	3.0	1.2	0.0	0.4	2.1	6.6	0.0
157	16.8	0.0	1.6	0.0	0.1	0.8	1.3	0.8	8.6	0.0
317	24.1	2.1	2.9	0.5	0.2	2.6	0.4	1.4	0.0	0.0
377	26.9	4.1	2.0	0.3	0.8	5.0	1.0	0.3	0.9	0.0
427	29.4	0.6	0.0	0.6	0.5	0.2	0.2	0.4	0.0	0.7
491	33.2	0.0	0.6	2.7	0.0	2.6	0.0	1.6	0.0	0.4
531	35.4	1.3	3.7	0.0	0.2	5.1	0.0	1.3	3.7	0.0

C.2 Major element concentrations for the Río de la Plata drainage basin suspended particulate matter.

Sample name	Al [%]	Fe [%]	K [%]	Ca [%]	Mg [%]	Na [%]	P [%]	Mn [µg/g]	Ba [µg/g]	Sr [µg/g]	Li [µg/g]
NH PL2	11.6	6.9	0.49	0.69	0.47	0.19	0.18	965	410	60	40
NH PL3	11.6	7.3	1.03	1.46	0.74	0.53	0.46	2345	645	115	50
NH PL4	14.1	9.8	0.77	0.57	0.65	0.13	0.25	650	380	55	40
NH PL5	13.2	8.1	0.62	0.59	0.54	0.10	0.16	730	335	60	35
NH PL7	6.5	5.3	0.43	0.74	0.31	0.29	0.20	2355	325	65	20
NH PL8	9.4	7.9	1.03	1.95	0.61	0.90	0.25	4500	590	140	30
NH PL10	21.2	27.4	5.94	12.29	3.44	10.95	6.44	159875	6550	750	113
NH PL11	1.9	2.7	0.33	0.75	0.21	0.62	0.38	15755	810	55	10
NH PL13	6.1	4.3	1.60	2.38	0.71	1.55	0.70	2287	438	134	69
NH PL14	21.1	15.8	2.76	3.59	1.37	2.42	0.79	5759	1103	231	68
NH PL16	13.6	6.3	0.84	0.73	0.67	0.34	0.16	875	415	70	35
NH PL17	12.4	5.9	0.88	0.77	0.62	0.31	0.14	520	380	70	45
NH PL19	17.9	10.3	0.80	0.68	0.63	0.20	0.15	605	445	70	50
NH PL20	14.5	9.6	0.44	0.43	0.42	0.08	0.11	490	330	50	35
NH PL22	13.2	9.9	0.17	0.28	0.29	0.03	0.10	475	205	30	30
NH PL23	14.6	10.2	0.30	0.37	0.36	0.04	0.10	530	260	40	35
NH PL25	15.8	10.7	0.44	0.57	0.47	0.13	0.15	795	350	55	55
NH PL26	14.1	9.5	0.38	0.58	0.43	0.13	0.13	755	315	50	40
NH PL28	12.0	14.6	0.29	0.53	0.46	0.11	0.19	2065	395	55	30
NH PL29	11.8	12.9	0.29	0.53	0.42	0.10	0.17	2105	360	50	30
NH PL31	10.1	11.4	0.21	0.26	0.34	0.09	0.25	1155	295	30	35
NH PL33	12.4	11.7	0.34	0.49	0.48	0.11	0.17	3455	375	45	35

C.3 Rb, Sr, Nd and Pb concentrations for sediment cores GeoB16211-3, GeoB16212-2, GeoB16212-3, GeoB16216-3, GeoB16217-2 and GeoB16223-2.

Sample name	Sample depth [cm]	Rb [µg/g]	Sr [µg/g]	Nd [µg/g]	Pb [µg/g]
GeoB16211-3	2	53	124	14	10
GeoB16212-2	3	64	44	5	12
GeoB16212-3	320	39	61	16	8
GeoB16216-3	2	42	70	12	15
GeoB16217-2	2	39	70	10	12
GeoB16223-2	2	61	74	16	15

C.4 Sr, Nd and Pb isotopic compositions of GeoB16211-3.

Sample name	Sample depth [cm]	$^{87}Sr/^{86}Sr$	$^{143}Nd/^{144}Nd$	ε_{Nd}	$^{206}Pb/^{204}Pb^a$	$^{207}Pb/^{204}Pb^a$	$^{208}Pb/^{204}Pb^a$
GeoB16211-3	2	0.714799(4)	0.512114(5)	-10.2(1)	18.76	15.60	38.57

Uncertainties ($2SD_{mean}$) are given for the last digit. [a]Uncertainties ($2SD_{mean}$) are 0.1 %.

C.5 SEM pictures and EDX spectrum for six samples from core GeoB16224-1.

Sample name	Sample depth [cm]	Sample treatment	SEM picture	EDX spectrum
NH A11	65	Bulk	x	
NH A19	127	Decarbonated	x	x
NH A28	354.5	Bulk	x	
NH A34	415	Bulk	x	
NH A44	543	Decarbonated	x	x
NH A46	591.5	Bulk	x	x

NH A11:

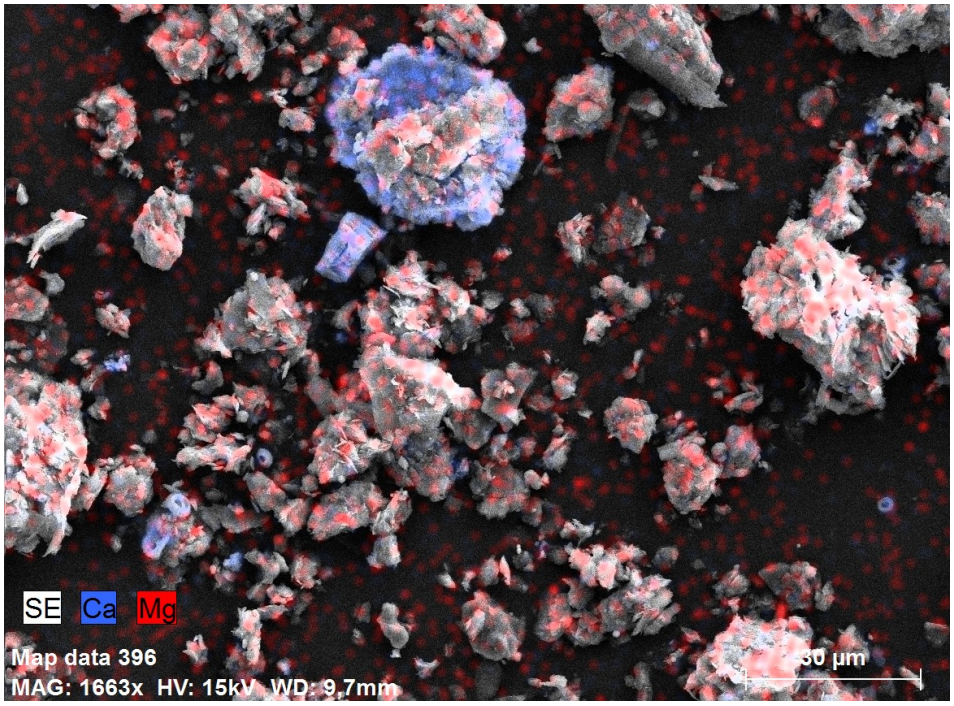

Map data 396; Date: 26.10.2015 09:02:08; Picture size: 1164 x 858
Mag: 1663,40649x; HV: 15,0kV

NH A19:

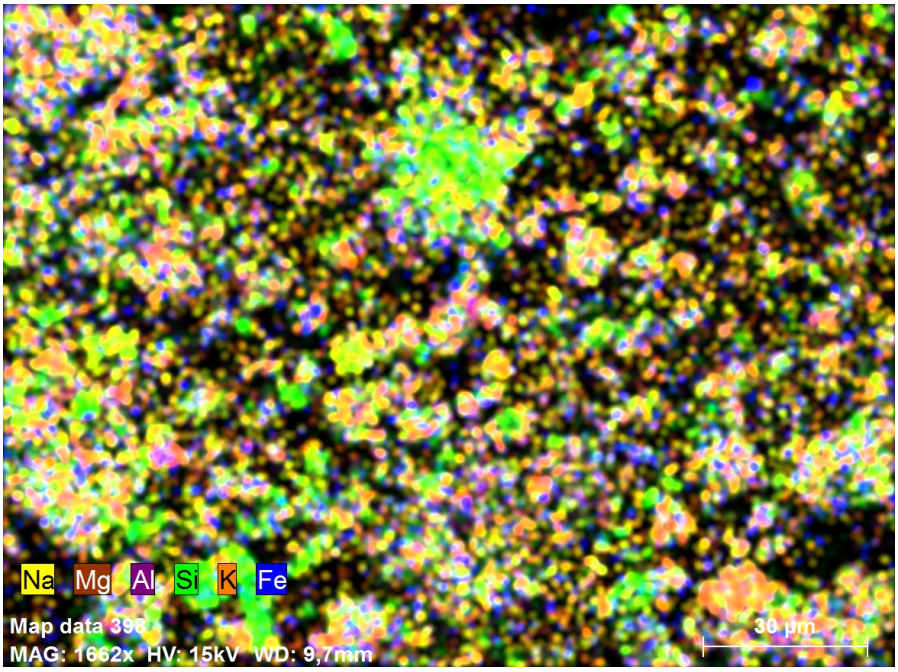

Map data 398; Date: 26.10.2015 09:27:33; Picture size: 1168 x 868
Mag: 1662,13147x; HV: 15,0kV

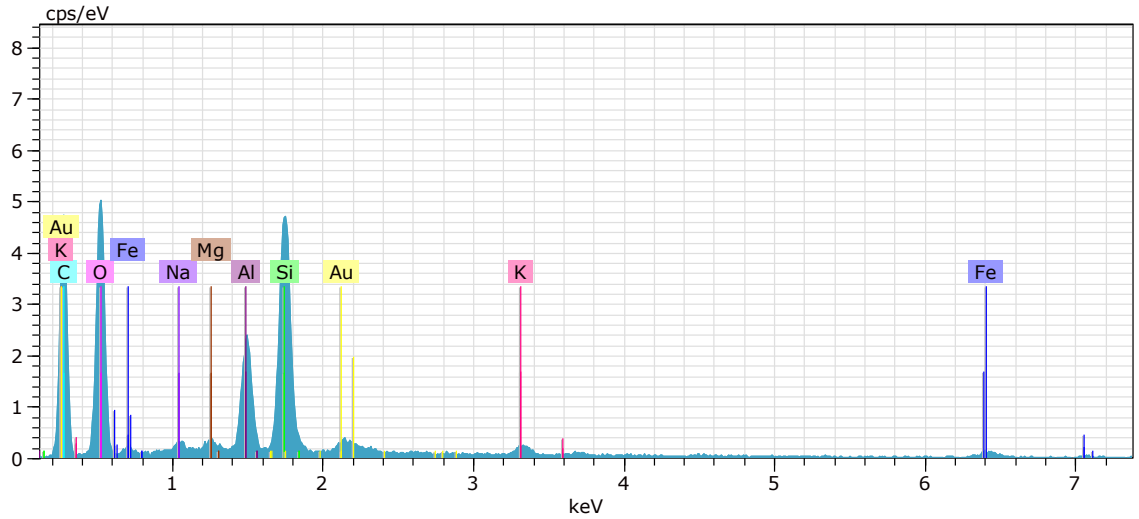

Spektrum Date: 26.10.2015 09:25:47 HV: 15,0kV ImpD.: 2,27kcps

El	OZ	Serie	unn. C [Gew.%]	norm. C [Gew.%]	Atom. C [At.%]	Fehler (1 Sigma) [Gew.%]
C	6	K-Serie	37,97	41,95	53,06	5,55
O	8	K-Serie	35,56	39,28	37,30	5,05
Na	11	K-Serie	0,45	0,50	0,33	0,07
Mg	12	K-Serie	0,39	0,43	0,27	0,06
Al	13	K-Serie	4,01	4,43	2,50	0,23
Si	14	K-Serie	9,45	10,43	5,64	0,44
K	19	K-Serie	0,71	0,79	0,31	0,07
Fe	26	K-Serie	1,99	2,19	0,60	0,14
Au	79	M-Serie	0,00	0,00	0,00	0,00
		Summe:	90,52	100,00	100,00	

NH A28:

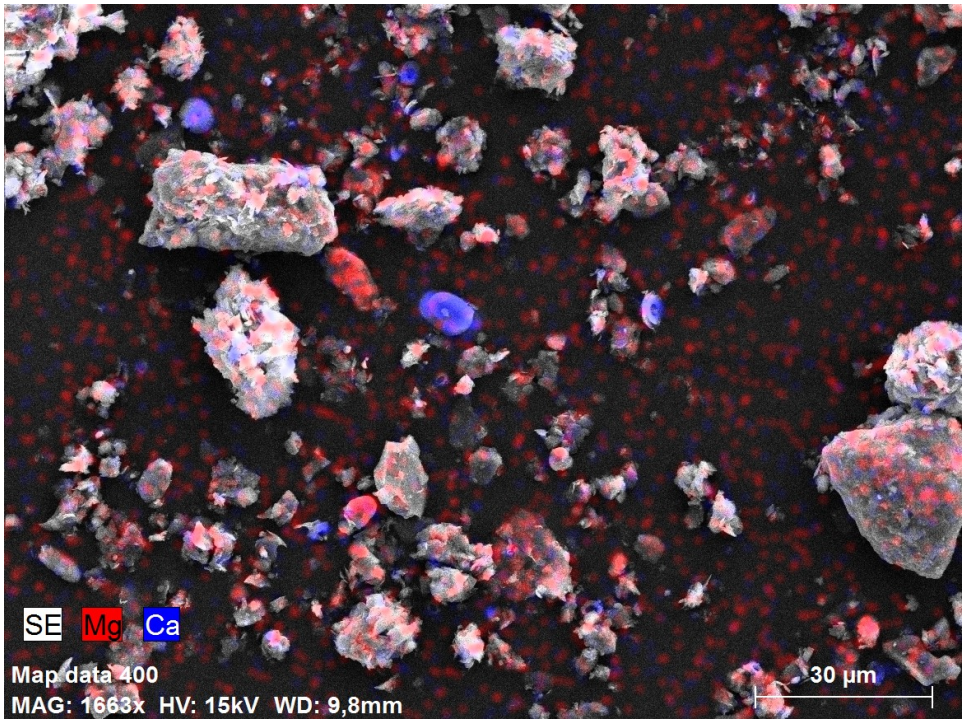

Map data 400; Date: 26.10.2015 09:43:40; Picture size:1 164 x 868
Mag: 1663,40649x; HV: 15,0kV

NH A34:

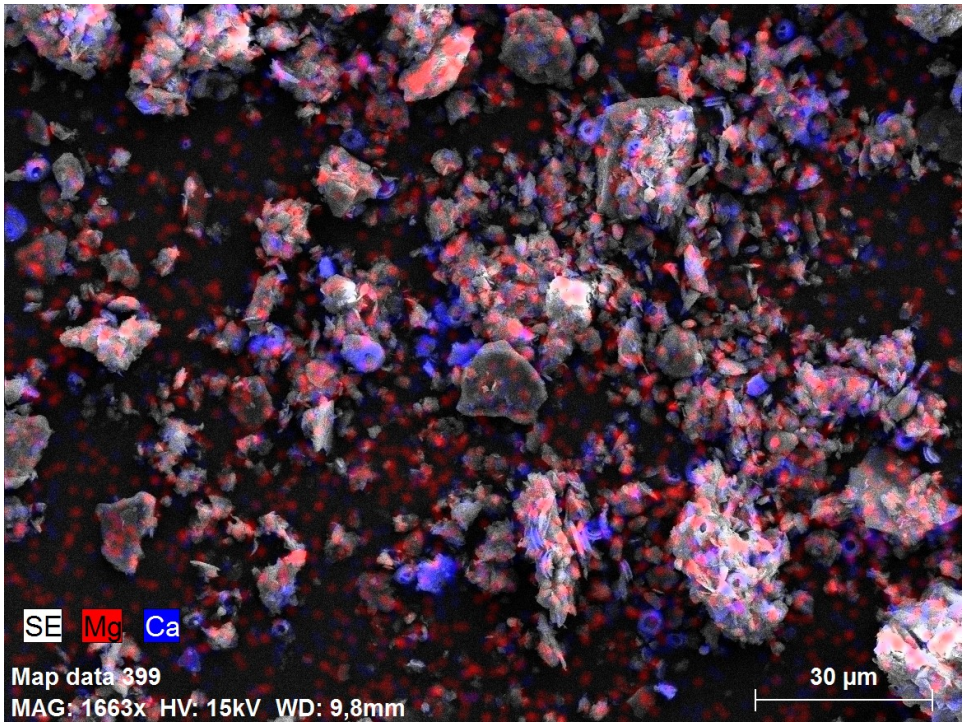

Map data 399; Date: 26.10.2015 09:36:19; Picture size: 1164 x 872
Mag: 1663,40649x; HV: 15,0kV

NH A44:

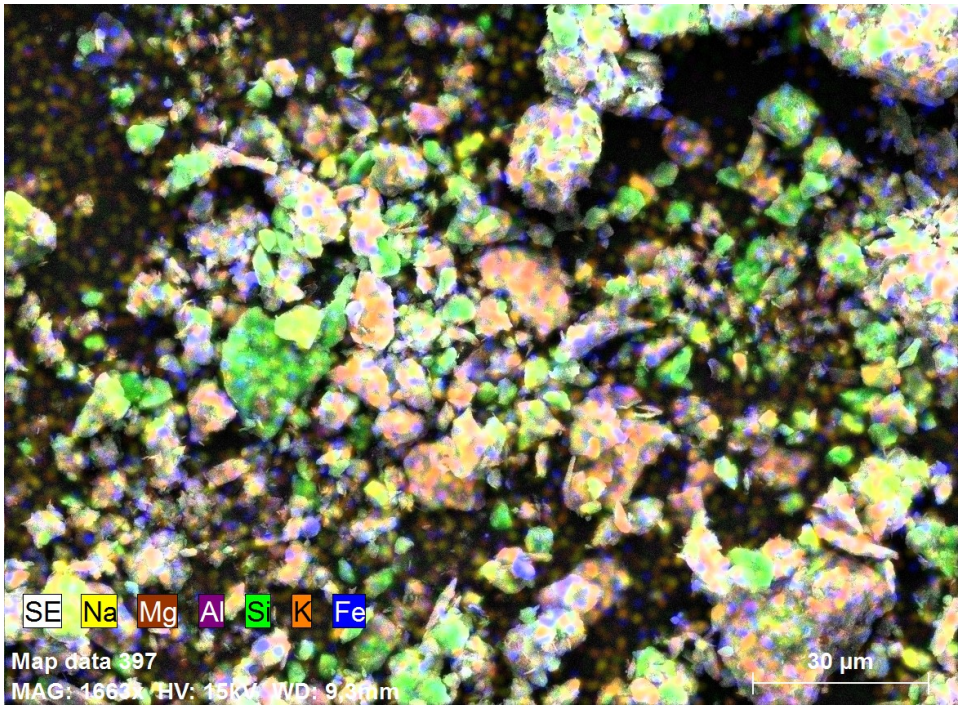

Map data 397; Date: 26.10.2015 09:18:31; Picture size: 1168 x 858
Mag: 1663,40649x; HV: 15,0kV

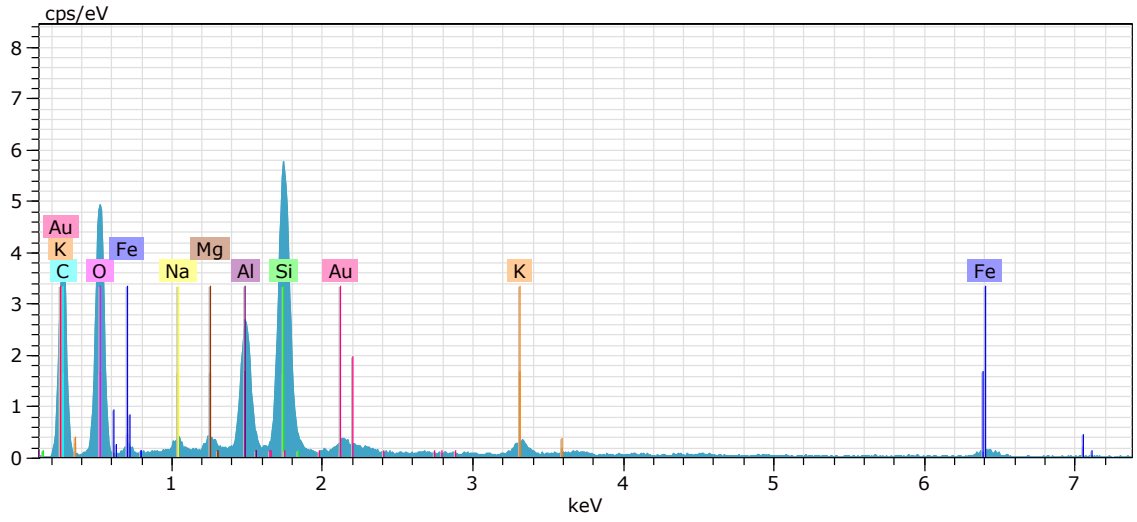

Spektrum Date: 26.10.2015 09:16:45 HV: 15,0kV ImpD.: 2,42kcps

El	OZ	Serie	unn. C [Gew.%]	norm. C [Gew.%]	Atom. C [At.%]	Fehler (1 Sigma) [Gew.%]
C	6	K-Serie	38,97	39,23	50,74	5,83
O	8	K-Serie	38,32	38,57	37,45	5,44
Na	11	K-Serie	0,74	0,75	0,50	0,09
Mg	12	K-Serie	0,56	0,56	0,36	0,07
Al	13	K-Serie	5,08	5,11	2,94	0,28
Si	14	K-Serie	12,55	12,63	6,98	0,57
K	19	K-Serie	1,15	1,15	0,46	0,08
Fe	26	K-Serie	1,99	2,00	0,56	0,14
Au	79	M-Serie	0,00	0,00	0,00	0,00
		Summe:	99,35	100,00	100,00	

NH A46:

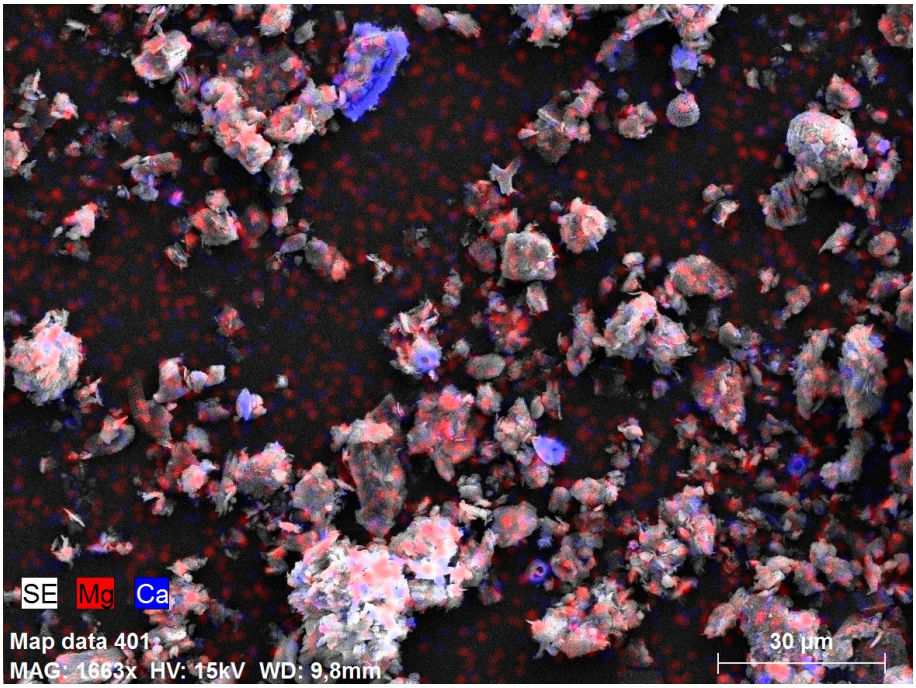

Map data 401; Date: 26.10.2015 09:52:35; Picture size: 1172 x 876
Mag: 1663,40649x; HV: 15,0kV

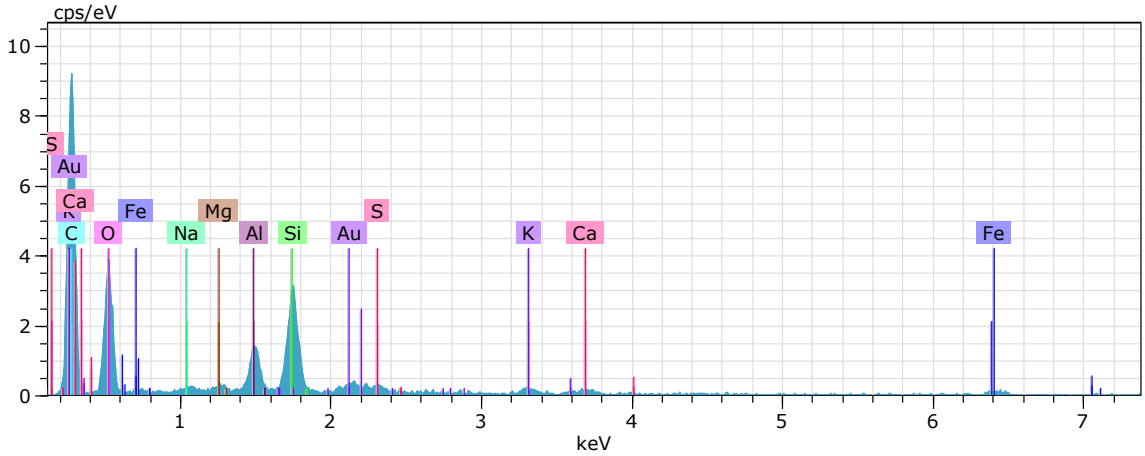

Spektrum Date: 26.10.2015 09:52:05 HV: 15,0kV ImpD.: 2,14kcps

El	OZ	Serie	unn. C [Gew.%]	norm. C [Gew.%]	Atom. C [At.%]	Fehler (1 Sigma) [Gew.%]
C	6	K-Serie	52,29	55,45	65,58	8,03
O	8	K-Serie	30,68	32,53	28,89	5,46
Na	11	K-Serie	0,24	0,25	0,16	0,06
Mg	12	K-Serie	0,27	0,29	0,17	0,06
Al	13	K-Serie	2,22	2,35	1,24	0,16
Si	14	K-Serie	5,32	5,64	2,85	0,29
S	16	K-Serie	0,37	0,40	0,18	0,06
K	19	K-Serie	0,72	0,76	0,28	0,09
Ca	20	K-Serie	0,63	0,67	0,24	0,08
Fe	26	K-Serie	1,57	1,66	0,42	0,16
Au	79	M-Serie	0,00	0,00	0,00	0,00
		Summe:	94,31	100,00	100,00	